Nuclear Magnetic Resonance Spectroscopy of Paramagnetic Metal-Acetylacetonate Complexes in the Solid State

By

Kirill Levin

A Thesis submitted to the Faculty of Graduate Studies of the University of Manitoba in partial fulfillment of the requirements of the degree of

Doctor of Philosophy

Department of Chemistry

University of Manitoba

Winnipeg

Table of Contents

Table of Contents ii

List of Figures viii

List of Tables xvi

Abstract xviii

Acknowledgements xix

Chapter 1: Introduction 1

1.1 Development History of Paramagnetic NMR 1

1.2 Application of Solid-State NMR 7

1.2.1 Method Development 7

1.2.2 Paramagnetic Tags 10

1.2.3 Battery Materials 11

1.2.4 Glasses 12

1.2.5 Metal Organic Frameworks (MOFs) 12

1.3 Metal Acetylacetonate compounds 13

1.3.1 $Ti(acac)_3$ 15

1.3.2 $V(acac)_3$ 16

1.3.3 $Cr(acac)_3$ 17

1.3.4 $Mn(acac)_3$ 18

1.3.5 $Fe(acac)_3$ 20

1.3.6 $Cu(acac)_2$ 20

1.3.7 $Co(acac)_2{\cdot}2H_2O$ and $Ni(acac)_2{\cdot}2H_2O$ 22

1.3.8 $VO(acac)_2$ 23

1.3.9 $[Cu(CH_3COO)_2]_2(H_2O)_2$ 24

1.4 Purpose 25

Chapter 2: Theory of NMR for Crystalline Diamagnetic and Paramagnetic Solids 26

2.1 Introduction to NMR 26

2.1.1 Origin of NMR Signal 26

2.1.2 Observation of NMR Signal 28

2.1.3 Relaxation of NMR Signal in Single Pulse Experiment 29

2.2 Nuclear Magnetic Interactions 35

2.2.1 Nuclear Shielding Interaction 35

2.2.2 Nuclear Dipolar Interaction 37

2.2.3 Quadrupolar Interaction 38

2.2.4 Magic Angle Spinning 39

2.3 Hyperfine Interaction 42

2.3.1 Origin of Fermi Coupling 48

2.3.2 Key Molecular Orbital Interactions 49

2.4 Paramagnetic Relaxation 56

2.4.1 Fermi Coupling 56

2.4.2 Electron-Nuclear Dipolar Coupling 57

2.5 NMR and EPR of Paramagnetic Molecules 58

2.5.1 Measures of Electronic Environment 59

2.5.2 Experimental Conditions in NMR and EPR 60

2.5.3 Electron-Spin Relaxation 61

Chapter 3: Materials and Methods 63

3.1 Samples 63

3.1.1 $Al(acac)_3$ 63

3.1.2 $Zn(acac)_2 \cdot 2H_2O$ 63

3.1.3 $Ti(acac)_3$ 63

3.1.4 $V(acac)_3$ 64

3.1.5 $Mn(acac)_3$ 64

3.1.6 $Fe(acac)_3$ 65

3.1.7 $Co(acac)_2 \cdot 2H_2O$ 65

3.1.8 $Cu(acac)_2$ 65

3.1.9 $VO(acac)_2$, $V(acac)_3$, $Cr(acac)_3$, $Mn(acac)_3$, $[Cu(Ac)_2H_2O]_2$, $Ni(acac)_2 \cdot 2H_2O$ 66

3.2 Powder X Ray Diffraction 66

3.3 Single Crystal X Ray Diffraction 66

3.3.1 $Ti(acac)_3$ 67

3.3.2 $V(acac)_3$ 67

3.4 NMR Methods 68

3.4.1 NMR Experimental Conditions 68

3.4.2 Hahn-Echo Experiment 69

3.4.3 Adiabatic Double-Echo Experiment 70

3.4.4 $^{13}C\{^1H\}$ REDOR 71

3.4.5 $^{13}C\{^1H\}$CP MAS NMR 72

3.5 Software 74

3.5.1 Gaussian 09 74

3.5.2 Mathematica. SpinDynamica 75

3.5.3 Vesta 76

3.5.4 DMfit 76

Chapter 4: Tris(2,4-pentanedionato)metal (d^1 – d^3) 77

4.1 Tris(2,4-pentanedionato)titanium, d^1 77

4.1.1 Molecular Orbital Formalism 78

4.1.2 ^{13}C MAS NMR 82

4.1.3 $^{13}C\{^1H\}$ REDOR 89

4.1.4 ^1H MAS NMR 89

4.1.5 Summary of Computational Assignments 92

4.1.6 Effect of Structural Variation with Temperature on Fermi Coupling 94

4.2 Tris(2,4-pentanedionato)vanadium, d^2 95

4.2.1 ^{13}C MAS NMR 96

4.2.2 ^{1}H MAS NMR 100

4.2.3 ^{1}H-^{13}C 1D CP MAS NMR 101

4.2.4 Crystallographic Assignment with NMR 103

4.3 Tris(2,4-pentanedionato)chromium, d^3 107

4.3.1 ^{13}C MAS NMR 108

4.3.2 ^{1}H MAS NMR 110

4.3.3 Summary of Computational Assignment 111

4.4 Effect of t_{2g} Orbitals on Spin Density in M(acac)$_3$ (M = Ti, V, Cr) 112

4.5 Nuclear Transverse Relaxation in M(acac)$_3$ (M = Ti, V, Cr) 114

4.6 Conclusion 115

Chapter 5: Exploring Jahn-Teller Effects in Tris(2,4-pentanedionato)manganese(III) with Solid-State NMR 116

5.1 ^{13}C MAS NMR 117

5.2 ^{13}C{^{1}H} REDOR 121

5.3 Spin-Density Maps 123

5.4 ^{1}H NMR as a Phase Indicator 128

5.5 Effect of Elongation vs Compression in Mn(acac)$_3$ 133

5.6 Effect of d_{z^2} Orbital on Spin Density in Equatorial Ligand 136

5.7 Conclusion 139

Chapter 6: Bis(2,4-pentanedionato)metal (d^9 – d^7) 139

6.1 Cu(acac)$_2$, d^9 140

6.1.1 ^{13}C MAS NMR 140

6.1.2 Spin-Density Distribution 142

6.1.3 Theoretical Treatment of Paramagnetic Shifts 145

6.1.4 ^{1}H NMR Interpretation 148

6.2 Ni(acac)$_2$·2H$_2$O, d^8 150

6.2.1 ^{13}C NMR and Assignments 150

6.2.3 Spin-Density Distribution 152

6.2.3 ^{1}H NMR Interpretation 153

6.3 $Co(acac)_2 \cdot 2H_2O$, d^7 157

6.3.1 ^{13}C MAS NMR 156

6.3.2 Spin-Density Distribution 159

6.3.3 Beyond The Spin-Only Approximation 161

6.3.4 ^{1}H MAS NMR 165

Chapter 7: Oxobis(2,4-pentanedionato)vanadium(IV) and tetra-μ2-acetatodiaquadicopper(II) 169

7.1 $VO(acac)_2$ 169

7.1.1 ^{13}C and ^{1}H MAS NMR spectra 170

7.1.2 Spin-Density Distribution 176

7.2 $[Cu(Ac)_2H_2O]_2$, $d^9 + d^9$ 178

7.2.1 ^{13}C and ^{1}H MAS NMR spectra 179

7.2.2 Spin-Density Distribution 183

7.2.3 Description of The Fermi shift in a Coupled Spin-State 185

Chapter 8: Understanding signal width in paramagnetic coordination compounds 188

8.1 Multiple-point-dipole model 188

8.2 Modeling NMR Signal Width in $Ti(acac)_3$ 191

8.2.1 ^{13}C MAS NMR 191

8.2.2 ^{1}H MAS NMR 194

8.3 Modeling NMR Signal Width in β-$V(acac)_3$ 196

8.4 Modeling NMR Signal Width in $Cr(acac)_3$ 198

8.5 Modeling NMR Signal Width in γ-$Mn(acac)_3$ 200

8.6 Modeling NMR Signal Width in $Fe(acac)_3$ 202

8.7 Modeling NMR Signal Width in $Co(acac)_2 \cdot 2H_2O$ 203

8.8 Modeling NMR Signal Width in $Ni(acac)_2 \cdot 2H_2O$ 205

8.9 Modeling NMR Signal Width in $Cu(acac)_2$ 206

8.10 Modeling NMR Signal Width in $VO(acac)_2$ 207

8.11 Modeling NMR Signal Width in $[Cu(ac)_2H_2O]_2$ 208

8.12 Conclusion 209

Chapter 9: Spin-density arithmetics **211**

9.1 Expressing spin-density of the d_{z^2} orbital 211

9.2 Signal width and spin density in paramagnetic NMR 215

Chapter 10: Conclusions and Outlook **219**

10.1 Impact on solid-state NMR of paramagnetic materials 219

10.2 Future studies 220

Bibliography **223**

Appendix **240**

List of Figures

1.1	Molecular structures of 2,4 – pentanedione (top) and its complex with a metal (bottom) illustrating major diatomic orbital interactions	14
1.2	Crystal-field splitting of $Ti(acac)_3$ approximated by an octahedral field	15
1.3	Crystal-field splitting of $V(acac)_3$ approximated by an octahedral field	16
1.4	Crystal-field splitting of $Cr(acac)_3$ approximated by an octahedral field	17
1.5	Crystal-field splitting of $Mn(acac)_3$ approximated by an octahedral field	18
1.6	Model structure of $Mn(acac)_3$ illustrating different types of Jahn-Teller (JT) distortion. Structure is JT-elongated for $r_{ax} > r_{eq}$ and JT-contracted for $r_{ax} < r_{eq}$	19
1.7	Crystal-field splitting of $Fe(acac)_3$ approximated by an octahedral field	20
1.8	Three $Cu(acac)_2$ molecules illustrating the packing arrangement in a solid	21
1.9	Crystal-field splitting of $Cu(acac)_2$ approximated by a square-planar field	21
1.10	Molecular structure of $Co(acac)_2 \cdot 2H_2O$ and $Ni(acac)_2 \cdot 2H_2O$	22
1.11	Crystal packing arrangement of $VO(acac)_2$	23
1.12	Molecule of $[Cu(CH_3COO)_2]_2(H_2O)_2$	24
2.1	Illustration of magnetization transformation under pulses with various tip angles	29
2.2	Relaxation processes: a) transverse (T_2) relaxation; b) longitudinal (T_1) relaxation	30
2.3	Single pulse NMR experiment	31
2.4	Effect of dead time on NMR signal with short and long T_2, corresponding to a) paramagnetic and b) diamagnetic samples, respectively	33
2.5	Effect of dead time delay of 5 μs on NMR signal intensity for resonances with different intrinsic width. Range of signal widths are typical of a) paramagnetic and b) diamagnetic systems	34
2.6	Examples of NMR chemical shift anisotropy of solid powdered samples. Anisotropies follow a) oblate; b) spherical and c) prolate symmetries	37
2.7	Effects of different MAS rates on a solid-state NMR spectrum with anisotropic broadening. Ω is the span of the signal. MAS rates are equivalent to a) static; b) $^1/_{20}$ Ω; c) $^3/_{20}$ Ω; d) $^1/_2$ Ω and e) Ω. All simulations are vertically scaled to match intensities of the most prominent signal	40
2.8	Effect of various MAS speeds on intensity of the most prominent signal with a span of Ω	42

List of Figures

2.9	Zeeman energy splitting of a) electron spin, and b) nuclear spin c) with hyperfine interaction for a system of a spin-½ electron and a spin-½ nucleus	44
2.10	Theoretical NMR spectra of a) J-coupled system of two spins, b) hyperfine coupling according to Figure 2.9c) assuming slow electronic relaxation and c) fast electronic relaxation	46
2.11	m_l orbitals that correspond to l = 0, 1 and 2	51
2.12	Two-center molecular-orbital interactions for a transition-metal coordination complex in octahedral coordination. Metal orbitals of *s*-, *p*- and *d*-symmetry are interacting with *s*- and *p*-orbitals of the ligand	53
2.13	Two-center molecular orbital energy diagrams with different relative energies of atomic orbitals: a) $E(\psi_A) > E(\psi_B)$; b) $E(\psi_A) = E(\psi_B)$; c) $E(\psi_A) < E(\psi_B)$	54
2.14	Polarization of a σ bond ($\Psi_{\uparrow\downarrow}$) with another orbital containing positive spin density ($\Psi_{\uparrow}$). Black dots indicate nuclear positions, arrows and colors indicate unpaired electron spins	55
3.1	Schematic representation of the Hahn-Echo MAS pulse sequence	70
3.2	Schematic representation of the adiabatic double-echo MAS pulse sequence	70
3.3	Schematic representation of the $^{13}C\{^1H\}$ REDOR pulse sequence	71
3.4	Schematic representation of the $^{13}C\{^1H\}$ CP MAS pulse sequence. τ_{inc} is the delay used for the second dimension	73
4.1	ORTEP diagram of $Ti(acac)_3$ structure measured at 328 K and Ti-O bond length	78
4.2	Ligand-field theory energy diagram for σ-bonded ligands coordinating to Ti^{3+} in an octahedral field. Encapsulated energy levels represent the crystal-field splitting	79
4.3	Linear combination of atomic orbitals with π-symmetry between one of the metal d_{xy}, d_{xz}, d_{yz} orbitals and the *p*-orbitals of ligands.	80
4.4	a) Reference axis system for interpretation of MO diagrams; b) a molecule of $Ti(acac)_3$ in the reference system	81
4.5	a) ^{13}C Hahn-Echo MAS NMR of $Ti(acac)_3$. Assignment of functional groups is based on DFT. "^" indicate a diamagnetic impurity thought to be $TiO(acac)_2$ [57]. Horizontal bars indicate calculated ranges for signal assignment. b) Signal fitting of CH_3 and CH groups in 2:1 ratio is depicted with solid lines. The dashed line presents the sum fit	83
4.6	a) Spin-density distribution in $Ti(acac)_3$; spin-density isosurface, b) in-plane spin-density contour plot of one of the ligands, c) atomic labels of the contour plot. Blue regions represent positive spin-density, red are used for negative spin-density	84

List of Figures

4.7	Spin-density contour-map from Figure 4.6b showing the dominant contribution to the observed pattern. a) Spin density between metal and carbonyl group; b) spin density between carbonyl and methine groups; c) spin density between carbonyl and methyl groups	86
4.8	$^{13}C\{^{1}H\}$ REDOR MAS NMR of $Ti(acac)_3$. The black trace was acquired in absence of dipolar recoupling, the red spectrum was acquired with dipolar recoupling	89
4.9	^{1}H Hahn-Echo MAS NMR of $Ti(acac)_3$. Proposed signal positions are listed according to DFT calculation, where expected signal regions are indicated	90
4.10	Polarization of the AB bond with unpaired electron in *p*-orbital of atom A	91
4.11	Change in computed ^{13}C Fermi coupling constants between the -173 ºC and 55 ºC structures of $Ti(acac)_3$. The change is calculated as $(A^{-173\,ºC} – A^{55\,ºC})/A^{55\,ºC}$	95
4.12	^{13}C Hahn-Echo MAS NMR of α-$V(acac)_3$ a) and β-$V(acac)_3$ b). Horizontal bars indicate calculated regions of functional groups. "^" indicates the impurity signal of $VO(acac)_2$.	97
4.13	$^{13}C\{^{1}H\}$ REDOR MAS NMR of α-$V(acac)_3$. The black spectrum was acquired without dipolar recoupling; the red spectrum was acquired with dipolar recoupling	97
4.14	Spin density isosurface and contour plots of the ligands of α-$V(acac)_3$ and β-$V(acac)_3$. Ligand 1 is in the xy-plane, ligand 2 is in the yz-plane and ligand 3 is in the xz-plane	99
4.15	^{1}H Hahn-Echo MAS NMR of (a) α-$V(acac)_3$ and (b) β-$V(acac)_3$. Proposed signal positions are listed according to the DFT calculation as used in Figure 4.10. "^"indicates the impurity signal of $VO(acac)_2$ (This complex is discussed in Chapter 7 of the thesis)	101
4.16	$^{1}H – ^{13}C$ 2D CP MAS NMR of (a) α-$V(acac)_3$ and (b) β-$V(acac)_3$ at 9.39 T field and MAS of 14 kHz. Asterisks represent MAS artifacts	102
4.17	^{1}H-^{13}C 2D-CP of β-$V(acac)_3$ at 11.74 T field with MAS of 28 kHz	103
4.18	^{13}C Hahn-Echo MAS NMR of $Cr(acac)_3$. Assignment of functional groups is based on the DFT calculation, Table 4.5. Asterisks indicate the artifacts of MAS	109
4.19	Spin-density a) isosurface and (b) contour-plot of one of the ligands of $Cr(acac)_3$	109
4.20	^{1}H Hahn-Echo MAS NMR of $Cr(acac)_3$. Proposed signal positions are listed according to DFT calculation as used in Figure 4.18. Signals from methyl groups are averaged to simulate fast rotation. Asterisk indicate the artifacts of MAS. "^" indicates the signal from the rotor material	110

4.21	Relation between spin density in the t_{2g} orbital in the ligand plane and spin density at carbon nuclei of the ligand for $M(acac)_3$ (M = Ti, V, Cr). Squares denotes the carbonyl group, circles denote the methine group and triangles denote the methyl group	113
5.1	^{13}C Hahn-Echo MAS NMR of commercial $Mn(acac)_3$. Transmitter frequency at a) -1000 ppm, b) 100 ppm, c) 1000 ppm; d) ^{13}C Adiabatic Double-Echo MAS NMR of commercial $Mn(acac)_3$ with transmitter frequency at 1000 ppm. Asterisks indicate spinning sidebands, "^" indicates an impurity signal (see below)	118
5.2	Variable temperature ^{13}C adiabatic double echo MAS NMR of γ-$Mn(acac)_3$ at a) 65˚C, b) 55˚C and c) 45˚C. Red line indicates isotropic signals with negative Fermi shift, blue line passes through signals with positive shifts. Asterisks indicate artifacts of MAS.	120
5.3	^{13}C {^{1}H} REDOR NMR at a) 50 kHz MAS, 100 ppm offset and 55°C sample temperature; b) 55 kHz MAS, 1000 ppm offset and 55°C sample temperature; c) 60 kHz MAS, 1000 ppm offset and 68°C sample temperature	122
5.4	Detailed crystallographic assignment of ^{13}C NMR of γ-$Mn(acac)_3$ with equatorial elongation (r_{eq}) as illustrated in the reference diagram (top right). Contour plots (middle) and calculated resonance shifts (left, black bars) are presented for each of the three ligands in the reference-axis system, where a) is the xy-plane ligand, b) is the xz-plane ligand and c) is the yz-plane ligand. Red contours signify regions of negative spin density, blue contours signify regions of positive spin density	124
5.5	^{1}H MAS NMR of γ-$Mn(acac)_3$ at 55˚C. Proposed signal assignment regions are indicated according to DFT calculation as used in Figure 5.4 and Table 5.2, where signals from individual mehyl hydrogens are averaged to simulate fast rotation	129
5.6	^{1}H NMR of γ-$Mn(acac)_3$ at 55˚C of a) experimental spectrum, b) deconvolution fit, c) CH_3[4] + CH_3[6] + CH_3[1]+ CH_3[2], d) CH[12], e) CH[34], f) CH[56] and g) CH_3[3] + CH_3[5]. (see Table 5.3)	130
5.7	^{1}H NMR of $Mn(acac)_3$ at 55˚C: a) as-made sample; b, c) two trials of N_2(*l*) cooling of commercial sample; d) original sample from Alfa Aesar; e) Alfa Aesar sample after extended air exposure.	131
5.8	^{13}C NMR of $Mn(acac)_3$ at 55˚C. a) Hahn-Echo of synthesized sample corresponding to Figure 7a (transmitter at 300 ppm); b) adiabatic double-echo of sample in Figure 5.7b; c) adiabatic double-echo of the original sample from Alfa Aesar, Figure 5.7d	133
5.9	Representative spin-densities of Jahn-Teller elongated and compressed forms of $Mn(acac)_3$. Both axial ligands show similar spin-densities in	134

	either form of distortion, thus a single plot is provided for each case. The direction of the distortion is indicated with the z-axis	
5.10	Ranges of calculated chemical shifts for individual functional groups from all molecules in five known crystal structures of $Mn(acac)_3$. Notation follows the reference system in Figure 5.4	136
5.11	Relation between spin density in the t_{2g} orbital in the ligand plane and spin density at carbon nuclei of the ligand for $M(acac)_3$, where M = Ti, V, Cr in dark. Blue data points are added from the equatorial ligand of γ - $Mn(acac)_3$ that include the effect of the d_{z^2} orbital. Squares denotes the carbonyl group, circles denote the methine group and triangles denote the methyl group	138
5.12	Delocalization of the unpaired electron spin density from the d_{z^2} orbital to the acac ligand in the equatorial plane. Dark and light colors indicate orbital phases. All orbital interactions are outlined as antibonding σ*-type	138
6.1	^{13}C MAS Hahn-Echo of $Cu(acac)_2$ with bars indicating calculated shift regions	141
6.2	$^{13}C\{^1H\}$ REDOR of $Cu(acac)_2$. The spectrum in black indicates no dephasing, whereas the spectrum in green has introduced a ^1H recoupling pulse	142
6.3	Spin-density of $Cu(acac)_2$: a) isosurface, b) contour-plot in the plane of the ligand	143
6.4	Delocalization of the unpaired electron spin-density from the $d_{x^2-y^2}$ orbital. Dark and light colors indicate orbital phases. All orbital interactions are outlined as anti-bonding σ*. The green "X" indicates a node.	144
6.5	Illustration of pseudoaxial symmetry in $Cu(acac)_2$ with the relevant angle for the pseudocontact shift calculation	147
6.6	^{13}C MAS Hahn-Echo of $Cu(acac)_2$ with intensity fitting	149
6.7	^{13}C MAS Hahn-Echo of $Ni(acac)_2{\cdot}2H_2O$ with bars indicating calculated shift regions. Asterisks indicate artifacts of MAS	151
6.8	$^{13}C\{^1H\}$ REDOR of $Ni(acac)_2{\cdot}2H_2O$. The spectrum in black indicates no dephasing, whereas the spectrum in red results from an introduced 1H recoupling pulse	151
6.9	Spin-density distribution of $Ni(acac)_2{\cdot}2H_2O$: a) isosurface, b) contour plot in the plane of the ligand	152
6.10	Regions of the ^1H MAS Hahn-Echo spectrum of $Ni(acac)_2{\cdot}2H_2O$.	153
6.11	Molecular structure of $[Ni(acac)_2{\cdot}2H_2O]{\cdot}H_2O$. Image does not include the external water molecule	155
6.12	Spin-density contour-plots of the water molecule with a direct coordination to the nickel metal for a) $Ni(acac)_2{\cdot}2H_2O$ where water is	156

	perpendicular to the ligand and b) $[Ni(acac)_2 \cdot 2H_2O] \cdot H_2O$ where water is parallel to the ligand	
6.13	^{13}C MAS Hahn-Echo NMR of $Co(acac)_2 \cdot 2H_2O$ at 60 kHz MAS rate with calculated shift ranges. Asterisks indicate spinning sidebands	158
6.14	$^{13}C\{^1H\}$ REDOR NMR of $Co(acac)_2 \cdot 2H_2O$ at 50 kHz MAS rate Spectrum in black indicates no dephasing, spectrum in red has introduced ^1H recoupling pulse	158
6.15	Electron-density distribution in the metal valence orbitals of $Co(acac)_2 \cdot 2H_2O$ calculated with the level of theory used in Figure 6.13	159
6.16	Unpaired spin-density distribution in $Co(acac)_2 \cdot 2H_2O$: a) isosurface, b) contour plot in the plane of the ligand	160
6.17	$Co(acac)_2 \cdot 2H_2O$ with the xy-plane and the tilted plane of the ligand	161
6.18	^1H MAS Hahn-Echo NMR of $Co(acac)_2 \cdot 2H_2O$ with insets illustrating differences in spinning-sideband intensity	166
7.1	Illustration of the distortion of the ligand plane with respect to the plane normal to the z-axis	170
7.2	^{13}C MAS Hahn-Echo of $VO(acac)_2$ with calculated assignment regions	171
7.3	^{13}C $\{^1H\}$ REDOR of $VO(acac)_2$. The spectrum in black has no recoupling, whereas the spectrum in red is acquired with ^1H recoupling	172
7.4	^{13}C MAS Hahn-Echo spectra of $VO(acac)_2$, a) Experiment, b), with deconvolution fit that consists of, c), three methyl groups d), a single methyl group and, e), two methine groups.	173
7.5	^1H MAS Hahn-Echo of $VO(acac)_2$. Signals at 30-50 ppm are attributed to an impurity signal of β - $V(acac)_3$. A low intensity signal at 1.5 ppm is attributed to an unknown impurity	174
7.6	a) Spin-density isosurface and b) a contour plot of one of the acac ligands in $VO(acac)_2$	176
7.7	Relation between spin density in the t_{2g} orbital in the ligand plane and spin density at carbon nuclei of the ligand for $M(acac)_3$, where M = Ti, V, Cr in dark. Spin density with added vanadyl data points uses red markers. Hollow markers indicate calculated predictions that are not observed experimentally	178
7.8	Schematic energy diagram illustrating antiferromagnetic in $[Cu(CH_3COO)_2]_2(H_2O)_2$	179
7.9	^{13}C adiabatic double-echo MAS NMR of $[Cu(CH_3COO)_2]_2(H_2O)_2$. Calculated regions are presented based on susceptibility,χ, formulation from Table 7.2	180
7.10	^1H MAS Hahn-Echo of $[Cu(CH_3COO)_2]_2(H_2O)_2$	181

7.11	Anisotropic ^{1}H shift of M(acac)x where M = Ti, V, VO, Cr, Mn, Ni, Co, Cu under the Herzfeld-Berger convention as a function of the square of the effective magnetic moment	182
7.12	Spin-density map of $[Cu(CH_3COO)_2]_2(H_2O)_2$. Selected spin-density contours in the center; isosurface on the left	184
8.1	Interaction sphere in $Cr(acac)_3$ crystal that includes the first molecular coordination sphere [59]	190
8.2	Modeling dipolar paramagnetic contribution to isotropic ^{13}C signal width in $Cr(acac)_3$. Comparison between point-dipole and multiple-point-dipole models	190
8.3	a) ^{13}C Fermi coupling constants in $Ti(acac)_3$. b) Comparison of the two model schemes for the signal width in ^{13}C MAS NMR of $Ti(acac)_3$. Presented widths are from the experiment (Exp), point-dipole model (PDM) and multiple-point-dipole model (MPDM). Detailed values are given in Appendix in Tables 8.1 and 8.2.	192
8.4	a) ^{1}H Fermi coupling constants in $Ti(acac)_3$ and b) the comparison of the two modeling schemes for the signal width, $\upsilon_{½}$, in ^{1}H MAS NMR of $Ti(acac)_3$. Detailed values are presented in Appendix Tables 8.3, 8.4	195
8.5	a) ^{13}C and c) ^{1}H Fermi coupling constants in β-$V(acac)_3$ and the comparison of the two modeling schemes for the signal width in b) ^{13}C and d) ^{1}H MAS NMR of β-$V(acac)_3$. Detailed values are presented in Appendix Tables 8.5 – 8.8.	197
8.6	a) ^{13}C and c) ^{1}H Fermi coupling constants in $Cr(acac)_3$ and the comparison of the two modeling schemes for the signal width in b) ^{13}C and d) ^{1}H MAS NMR of $Cr(acac)_3$. Detailed values are presented in Appendix Table 9.9 – 9.12	199
8.7	a) ^{13}C and c) ^{1}H Fermi coupling constants in $Mn(acac)_3$ and the comparison of the two modeling schemes for the signal width in b) ^{13}C and d) ^{1}H MAS NMR of $Mn(acac)_3$. Detailed values are presented in Appendix Tables 8.13 – 8.16	201
8.8	a) ^{1}H Fermi coupling constants in $Fe(acac)_3$ and the comparison of the two modeling schemes for the signal width in b) ^{1}H and c) ^{13}C MAS NMR of $Fe(acac)_3$. Detailed values are presented in Appendix Tables 8.17 – 8.19	203
8.9	a) ^{13}C and c) ^{1}H Fermi coupling constants in $Co(acac)_2 \cdot 2H_2O$ and the comparison of the two modeling schemes for the signal width in b) ^{13}C and d) ^{1}H MAS NMR of $Co(acac)_2 \cdot 2H_2O$. Detailed values are presented in Appendix Tables 8.20 – 8.23	204
8.10	a) ^{13}C and c) ^{1}H Fermi coupling constants in $Ni(acac)_2 \cdot 2H_2O$ and the comparison of the two modeling schemes for the signal width in b) ^{13}C	205

	and d) ^{1}H MAS NMR of $Ni(acac)_2 \cdot 2H_2O$. Detailed values are presented in Appendix Tables 8.24 – 8.27	
8.11	a) ^{13}C and c) ^{1}H Fermi coupling constants in $Cu(acac)_2$ and the comparison of the two modeling schemes for the signal width in b) ^{13}C and d) ^{1}H MAS NMR of $Cu(acac)_2$. Detailed values are presented in Appendix Tables 9.28 – 9.31	206
8.12	a) ^{13}C and c) ^{1}H Fermi coupling constants in $VO(acac)_2$ and the comparison of the two modeling schemes for the signal width in b) ^{13}C and d) ^{1}H MAS NMR of $VO(acac)_2$. Detailed values are presented in Appendix Tables 9.32 – 9.35	208
8.13	a) ^{13}C and c) ^{1}H Fermi coupling constants in $[Cu(ac)_2H_2O]_2$ and the comparison of the two modeling schemes for the signal width in b) ^{13}C and d) ^{1}H MAS NMR of $[Cu(ac)_2H_2O]_2$, Detailed values are presented in Appendix Tables 8.36 – 8.39	209
9.1	Pictorial representation of d_{z^2} orbital interacting with the ligand in the xy-plane. Values of $A_{iso} \cdot S/g_{iso}$ are presented from Table 9.1, where values in bold come from experiment and italicized values are calculated	214
9.2	Fermi contribution to isotropic signal width in a) S = 0.5; b) S = 1; c) S = 1.5; d) S = 2; e) S = 2.5 spin states in relation to the Fermi coupling constant and the electronic relaxation time. Dashed contours indicate regions with 10 kHz and 30 kHz marks. Solid lines pass through SA = 4 mark, which signifies equivalent $\rho_{\alpha\beta}$	216

List of Tables

4.1	$\pi^*(d-p)$ interactions in the octahedral field with the reference-axis system in Figure 4.4a	81
4.2	^{13}C and ^{1}H NMR of $Ti(acac)_3$ and DFT calculation. Calculated and experimental shifts are in ppm at a sample temperature of 55 ˚C. ^{1}H and ^{13}C NMR shifts from the same functional groups are indicated and appear in the order listed	93
4.3	^{13}C and ^{1}H NMR of α - $V(acac)_3$ and DFT calculation.[a)] Calculated and experimental shifts are in ppm at a sample temperature of 55 ˚C. ^{1}H and ^{13}C shifts from the same functional groups are indicated and appear in the order as listed	104
4.4	^{13}C and ^{1}H NMR of β - $V(acac)_3$ and DFT calculation.[a)] Calculated and experimental shifts are in ppm at a sample temperature of 55 ˚C. ^{1}H and ^{13}C shifts from the same functional groups are indicated and appear in the order as listed	105
4.5	^{13}C and ^{1}H NMR of $Cr(acac)_3$ and DFT calculation.[a)] Calculated and experimental shifts are in ppm at a sample temperature of 55 ˚C. ^{1}H and ^{13}C shifts from the same functional groups are indicated and appear in the order as listed	112
5.1	Selected molecular-orbital symmetries in O_h field	125
5.2	^{13}C and ^{1}H NMR of γ-$Mn(acac)_3$ and DFT calculation. Calculated and experimental shifts are in ppm at a sample temperature of 55 ˚C. ^{1}H and ^{13}C shifts from the same functional groups are indicated and appear in the order as listed	126
5.3	^{1}H NMR fit parameters from Figure 5.6. Fitting included spinning sideband manifold, not shown in Figure 5.6. Assignments from Table 5.2, group labels from Figure 5.4	130
6.1	^{13}C and ^{1}H NMR of $Cu(acac)_2$ and DFT calculations. Calculated[a)] and experimental shifts are in ppm at a sample temperature of 55 ˚C. ^{1}H and ^{13}C shifts from the same functional groups are indicated and appear in the order as listed	146
6.2	^{13}C and ^{1}H NMR of of $Ni(acac)_2{\cdot}2H_2O$ and DFT calculation. Calculated and experimental shifts are in ppm at a sample temperature of 55 ˚C. ^{1}H and ^{13}C shifts from the same functional groups are indicated and appear in the order as listed	154
6.3	^{13}C and ^{1}H NMR of $Ni(acac)_2{\cdot}2H_2O$ and DFT calculation of $[Ni(acac)_2{\cdot}2H_2O]{\cdot}H_2O$. Calculated and experimental shifts are in ppm at the sample temperature of 55 ˚C. ^{1}H and ^{13}C shifts from the same functional groups are indicated and appear in the order as listed	155

List of Tables

6.4	^{13}C MAS NMR of $Co(acac)_2 \cdot 2H_2O$ and DFT calculation. Calculated and experimental shifts are in ppm at a sample temperature of 55 ˚C. Values are presented at different levels of theoretical treatment. M-A stands for Martin-Autschbach formalism, equations 6.4, 6.5	164
6.5	^{1}H of $Co(acac)_2 \cdot 2H_2O$ and DFT calculation. Calculated and experimental shifts are in ppm at the sample temperature of 55 ˚C. Values are presented at different levels of theoretical treatment. M-A stands for Martin-Autschbach formalism, equations 6.4, 6.5	167
7.1	^{13}C and ^{1}H NMR of $VO(acac)_2$ and DFT calculation. Calculated and experimental shifts are in ppm at sample temperature of 55 ˚C. ^{1}H and ^{13}C shifts from the same functional groups are indicated and appear in the order as listed	175
7.2	^{13}C NMR of $[Cu(CH_3COO)_2]_2(H_2O)_2$ and DFT calculation. Calculated and experimental shifts are in ppm at sample temperature of 55 ˚C	185
7.3	Fermi coupling constants of ^{13}C sites in $[Cu(CH_3COO)_2]_2(H_2O)_2$ as derived with equation 7.2	187
9.1	Estimation of d_{z2} orbital contribution to the Fermi contact spin density using the principles of spin arithmetics. When no experimental value is available, italicized calculated values are provided	213

Abstract

This work is addresses the issue of signal acquisition in solid-state Nuclear Magnetic Resonance (NMR) of paramagnetic coordination complexes and provides a comprehensive overview of a methodology of signal assignment. Model coordination complexes include a series of bis/tris(acetylacetonate)metals, where the metal is varied across the transition metals from titanium to copper. Additionally, a coupled spin system of copper acetate is studied to demonstrate the effect of the magnetic coupling on the solid-state NMR signal. ^{13}C and ^{1}H NMR spectra of these compounds are acquired and interpreted in terms of molecular orbital interactions and valence bond theory with the aid of Density Functional Theory (DFT) calculations. The influence of electronic configuration on the detectability of ^{13}C and ^{1}H resonances is addressed. Based on these results, a general methodology for signal acquisition and assignment emerges, which allows chemists to probe magnetically unquenched electronic environments and potentially exploit paramagnetic interactions for molecular structural elucidation. Finally, the electronic characteristics of paramagnetic solids favorable for the acquisition and interpretation of high-quality, structurally informative NMR spectra are identified.

Acknowledgements

This thesis can be regarded as a major milestone in my life-long journey to knowledge. I could not have walked this path alone, without an appreciable support. Here I would like to acknowledge some of the most memorable contributions by people who have helped me over the years to reach one of my early life goals: to obtain a highest academic degree in Chemistry. I would like to thank my supervisor, Dr. Scott Kroeker, for his guidance and knowledge throughout my undergraduate years as one of my first chemistry teachers in thermodynamics and inorganic chemistry classes. Later, when I became his undergraduate summer student, I got a feel for the real research experience, which further cemented my will to pursue a career in research. I would like to thank Scott for his encouragement and support for me to attend numerous conferences throughout the years and around the world, which would serve to shape my understanding of the field and provide opportunities to hear and communicate with great minds in the field. I would like to thank Dr. John Wren, who was a Ph.D. student in the group at the time, for providing me with opportunities for endless discussions about chemistry. His enthusiasm for NMR of unconventional nuclei deepened my understanding and appreciation for the link between physical and chemical concepts in NMR. I am grateful to previous group members Brandon J. Greer and Dr. Randi Christensen for their support in the early stages of my research, as well as former undergraduate students Alex Patterson, David Snider and Heather Cavers. During my graduate studies I have received appreciable help and support from my fellow Ph.D. student Arun Krishnamurthy. I would like to thank more recent undergraduate students Yaroslav Germanov, Jordan Perillo and Daniel Padeanu for their help testing my program, and fruitful discussions on the nature of paramagnetic interactions. I am grateful to

have been present during the era of Dr. Kirk Marat, our departmental NMR guru, from whom I learned a great deal about the NMR instrument capabilities, both during undergraduate classes and the course of my graduate research. I am thankful to Dr. David Davidson for providing technical support in the last stages of my degree. I would like to thank Dr. James Xidos not only for introducing me to the world of computational chemistry in the undergraduate period, but also with a continued support, both technical and theoretical, throughout my Ph.D. program. I would like to thank Dr. Peter Budzelaar and Dr. Victor Nemykin for fruitful discussions on computational and experimental aspects of my work. I am grateful to Dr. Paul Sidhu, who started research on metal acetylacetonates in this group, and left a legacy of samples and NMR spectra. I would like to thank the Faculty of Graduate Studies and the Faculty of Science, the Department of Chemistry, CGSA and GSA for providing me with funding support both for research and travel. I would like to thank my committee members: Dr. Jennifer Van Wijngaarden, Dr. Joe O'Neil, Dr. Frank Hawthorne and Dr. Gang Wu for their influence and support in creating this document. I would like to additionally thank Dr. Van Wijngaarden for introducing me to the world of quantum chemistry in my early undergraduate years, a course that set my future interest in the field and eventually helped me better understand solid-state NMR.

None of this could have been possible without the idea, the goal and the love of chemistry as a discipline that was inspired and supported by my grandmother, Lidia, a head chemical analyst at a nitrogen-capture fertilizer plant in Nevinnomyssk, Russia for over 40 years. Combined with my passion for chemistry, my grandparents Vitali and Violetta, both high school math teachers, provided me with a mathematician's way of thinking and the courage to tackle problems of any size in a systematic way. Finally, I would like to thank my parents, Andrey and

Acknowledgements

Julia for providing me with the opportunity to learn English as a second language, and the support to pursue my passion in Canada, at the University of Manitoba.

Chapter 1: Introduction

Nuclear magnetic resonance (NMR) spectroscopy is a popular method for the elucidation of molecular properties at the atomic scale. One of the major advantages of this technique is the ability to *tune* to different types of nuclei in the system and *listen* to their signals in separate experiments. In these terms, NMR spectroscopy can be thought of as a way to record signals from various “radio stations”. With this analogy, different nuclei broadcast encoded information about the local chemical and magnetic environments of the atom. One can argue that NMR of a different nucleus is a completely new experiment in itself, thus NMR of multiple nuclei of the same system can provide the analyst with enough pieces of the puzzle to obtain comprehensive insight into desired structural detail [1].

1.1 Development history of paramagnetic NMR

Nuclear magnetic resonance (NMR) spectroscopy has seen major development since the first reports of NMR in bulk materials by the independent groups of Purcell and Bloch in late 1946 [2]. This discovery earned both of them a Nobel Prize in Physics in 1952. A year later, Albert Overhauser described the effect of unpaired electrons on the nuclear spin resonance signal [3] and proposed a mechanism to enhance NMR signals via magnetization transfer from conducting electrons, the nuclear Overhauser effect (NOE). This led to the development of a new branch of magnetic resonance: dynamic nuclear polarization (DNP) [4].

Conventional NMR provides a probe for the local environment of a specific atom and enables detailed structural elucidation. The majority of studies are done on diamagnetic species, i.e., those that have no unpaired electrons. Studies of paramagnetic systems that have an

unquenched magnetic moment began in the 1950's, led by physicists such as Overhauser. The major limitation of NMR studies of paramagnetic samples is the overwhelming magnetic contribution of the unpaired electron to the nuclear resonance signal. The electron-nuclear interaction significantly degrades resolution and sensitivity, making the interpretation of the NMR spectrum more difficult. This perturbation stems from the greater magnetic moment of an unpaired electron compared to any spin-active nucleus, by at least three orders of magnitude (Chapter 1 in [5]).

Early experimental investigations of paramagnetic interactions can be dated to the late 1940's, in the works of Bloembergen, Purcell and Pound [6], and Knight [7]. In 1955, Solomon published the first comprehensive theoretical account of dipolar-based relaxation processes for a system of two spins [8]. This paper marked the inception of the **point-dipole model (PDM)**, the same model is used to this day to interpret paramagnetic interactions using the distance between the nucleus and the paramagnetic centre. The formulation of nuclear relaxation that was suggested by Solomon provided the necessary understanding of the contributions of electronic properties to the paramagnetic NMR spectra in both solids and solutions. Nuclear spin relaxation has a direct influence on NMR signal width, thus the ability to estimate relaxation provides a handle for estimating the signal detectability. It is no surprise that this publication is one of the most cited works in the paramagnetic NMR literature, approaching nearly 2900 citations by 2017 [9].

In 1955, Kozyrev [10] presented results of an electron paramagnetic resonance experiment on a dilute solution of VO^{2+}. He was able to resolve 13 resonances that manifest the paramagnetic interaction. A year after Kozyrev's publication, McConnell published an early description of the ^{1}H NMR signal of an aromatic free radical on the basis of molecular-orbital

interactions. Observed resonances suggested the presence of the **polarization** mechanism [11], which is described in detail in the Theory section of this thesis. This was an early attempt to provide an assignment of paramagnetic spectra using only molecular-orbital interactions.

In the following years, there were many publications that investigated the relaxation aspect of paramagnetic NMR in the solution state. Among the most notable works was Bloembergen and Morgan (1961) that used ^{1}H NMR to compare electronic relaxation derived from the point-dipole model applied to the direct relaxation measurement with electron paramagnetic resonance (EPR) spectroscopy [12]. The authors found satisfactory agreement, which confirmed the validity of Solomon's model.

The 1960s marked a rising interest in paramagnetic NMR and its potential application to solid samples with unquenched magnetic moments. This decade saw a number of theoretical and experimental investigations of different aspects of NMR experiments and their relation to specific electronic properties. Golding [13] discussed the theory of the temperature dependence of NMR spectra in paramagnetic octahedral complexes. This work was the first account of the effects of spin-orbit coupling in NMR experiments, an important property of unpaired electrons, and is now used to describe pathways of electron transfer or conductivity [14]. The work is largely based on the book by Griffith "The Theory Of Transition Metal Ions" published in 1961 [15]. This book contains a detailed account of magnetic-susceptibility measurements and spin-orbit coupling theory. This theory was modified to account for spin-orbit coupling effects on paramagnetic NMR shifts by Golding (1964) [13].

In 1965, the first NMR investigation of a variety of transition-metal acetylacetonates was published [16]. The study examined 14 transition-metal complexes including almost all third-row metals. Signal assignments for all complexes were based on expected relative signal intensities

of methyl and methine functional-group signals. These groups have a ^{1}H intensity ratio of 6:1 in a symmetric environment of acetylacetonate ligands. This assumption was likely to have validity in the solution state, where rapid tumbling motions were present and would average out any minor structural distortions. This was not a valid approach for a solid sample, where crystal packing results in a more fixed structure. This subject will be discussed in a greater detail later in the thesis. Eaton[16] provided a more in-depth analysis of MO interactions that could lead to observed ^{1}H shifts, in line with the theoretical principles of the work of McConnell [11]. Another important contribution of this paper was the unambiguous correlation between observability of NMR and EPR spectra of the same complex. Eaton concluded that if a sharp NMR signal was observed for a paramagnetic sample, that same sample should have a broad or unobservable EPR resonance, and *vice versa*. Thus paramagnetic NMR and EPR can be thought to probe the same effects of unpaired electrons on the system but from different points of view. This observation is in agreement with the point-dipole model published by Solomon a decade earlier.

Research on metal acetylacetonates has continued throughout the development of paramagnetic NMR. A recent detailed study on a variety of coordination complexes, including some metal acetylacetonates in the solution phase, was done by Rastrelli and Bagno [17]. The authors used modern computational resources and high NMR fields to probe ^{1}H and ^{13}C environments. They pointed out some errors in earlier assignments which became apparent with modern advances in NMR technology. However there was no new development in their theory of paramagnetic interactions in NMR.

In the 1970s, the field of paramagnetic NMR saw a major advance in experimental work followed by refinements to the theory. This growth is correlated with technological advances in instrumentation over that period. By 1973, there had been enough experimental and theoretical

work done solely on paramagnetic NMR that La Mar *et al* published "NMR of Paramagnetic Molecules: Principles and Applications" [5]. This work listed all major discoveries in the field over the two previous decades and provided additional background to spectroscopists for the interpretation of paramagnetic spectra.

As interest in paramagnetic NMR bloomed and greater magnetic field strengths were becoming available, there was a rise in misguided spectral interpretation that led to wrong conclusions. These mistakes arose from the inappropriate use of theory to interpret observed paramagnetic shifts and the absence of additional experimental evidence that could justify assignments. Additional sources of confusion came from misused notations and unit conversions between cgs and SI unit systems. These errors were addressed in detail by La Mar *et al* Chapter 3.3 [5]. In 1979, Golding and Stubbs published "NMR shifts in paramagnetic systems: a nonmultipole-expansion method" [18]. Their conclusion was a warning signal to NMR spectroscopists to take extreme care in the interpretation of their NMR results. Golding and Stubbs pointed out that both molecular-orbital interactions and electron-nuclear dipolar contributions could lead to significant shifts in experimental NMR signals. Thus spectral interpretation had to have a comprehensive account of both interactions. Golding and Stubbs introduced approximated molecular orbitals and provided their mathematical formulation, based on a d^1 transition metal in an octahedrally coordinated environment. This was the first account of an approximated molecular-orbital contour-plot diagram that illustrated the relation between orbital occupancies and expected paramagnetic NMR shift. This brought into focus another potential problem with the interpretation of paramagnetic NMR spectra, which was the importance of an appropriate structure for modelling. This issue had not been previously tackled as geometries from x-ray diffraction (XRD) experiments were used. However, XRD structures

corresponded to molecular geometries in a solid state, whereas paramagnetic research up to that point had been done on solution NMR.

The development of paramagnetic NMR research to the solid state was constrained until the late 1980s by a few obstacles. The major obstacle was the difference in the sample state: molecules in a liquid undergo rapid tumbling motion which averages inhomogeneous magnetic interactions with respect to the stationary observer; in contrast, in the solid state all molecules have a more defined location, thus anisotropic interactions dominate the observed spectrum of a static solid sample, resulting in a variety of broad and often featureless spectral shapes. More information about these interactions can be found in the Theory section. The presence of unpaired electron density with its large unquenched magnetic moment creates a significant perturbation to the field of the nucleus, whereas this perturbation is successfully averaged in solution NMR. To avoid this detrimental signal broadening in the solid state, magic-angle spinning (MAS) was developed [19, 20]. This technique will be addressed in greater detail in the Theory section. In short, MAS averages anisotropic interactions with respect to a stationary observer by rotating a powdered sample about a specific angle with respect to the magnetic field. Improvements in technical aspects of MAS by 1988 allowed measurement and publication of the spectra of copper (II) chloride dehydrate [21], and the analysis set the fundamental ground for interpretation of anisotropic signals in solid-state paramagnetic NMR. The authors were able to estimate the degree of electronic delocalization through modeling of the anisotropic nuclear signal when affected by paramagnetic coupling.

Since the development of fast MAS, paramagnetic NMR has seen a dramatic increase in application to different areas of materials research. There have been many review articles that focus on applications of paramagnetic NMR to specific systems. In the 1960s, there were not

enough experimental results available to provide a comprehensive interpretation of all effects. A more comprehensive account of paramagnetic coupling in NMR of solutions was given in 1973 by La Mar *et al.* [5]. Greater attention was given to paramagnetic relaxation in solutions by Kowalewski *et al.* [22] in 1985. The next major reviews in the field followed 25 years later with the development of specific areas of interest in paramagnetic NMR, including the solid state. Clore *et al.* [23] in 2009 described the applicability of paramagnetic relaxation to biological macromolecules. Throughout 2010 to 2013, many reviews were published regarding the applicability of paramagnetic NMR to porous materials [24], protein structures [25], electronic properties in molecules [26] and for use as crystallographic restraints [27].

1.2 Application of paramagnetic solid-state NMR

Here are presented some recently developed areas of interest in the field of paramagnetic solid-state NMR.

1.2.1 Method development

McDermott *et al.* introduced ^{2}H MAS NMR of paramagnetic compounds [28]. The authors presented the capabilities of anisotropic electron-nuclear interaction in paramagnetic solid-state NMR to determine local environments. For demonstration, the authors used $V(acac)_3$ and $Mn(acac)_3$; however at that time, not all polymorphs of these structures were known [29]. The local geometries of paramagnetic environments were assessed through the spinning sideband manifolds of the ^{2}H NMR signal. Their result showed that the structure could be confirmed to within ±0.5 Å distance and ±20°angle with respect to the paramagnetic center and its magnetic tensor. Although this is a significant result achieved with an approximate point-dipole model, it

would fail to distinguish between existing polymorphs of these complexes (see below). The authors gave a promising conclusion regarding the potential application of this approach to large biomolecular systems, including local structure and dynamics at active site [30].

An important contribution to the methodology of experimental approaches to solid-state paramagnetic NMR was introduced by Ishii *et al.* from 2003 to 2008. His work focused primarily on ways to optimize experimental conditions to maximize the time efficiency in natural-abundance samples and introduce correlation experiments for signal enhancement and structural assignment [31-33]. These principles were tested on $V(acac)_3$ and $Mn(acac)_3$ as well-characterized model compounds. The authors relied on fast nuclear relaxation due to paramagnetic coupling to speed up ^{13}C and ^{1}H MAS NMR experiments by orders of magnitude, thus boosting their effective sensitivity. The improvement in experimental sensitivity, together with successes in cross polarization and dipolar Insensitive Nuclei Enhanced by Polarization Transfer (INEPT) $^{13}C\{^{1}H\}$ correlations, allowed two-dimensional heteronuclear correlation experiments at natural abundance in a relatively short timeframe.

Another notable contribution to the experimental acquisition of paramagnetic solid-state NMR came from Kervern *et al.* [34] in 2007, who described in great detail how to create short, high-power adiabatic pulses for NMR experiments. These pulses provide a more uniform excitation over a large spectral range, which is usually a requirement for paramagnetic solid-state NMR. Conventional hard pulses may not be able to excite the entire spectrum uniformly, as will be shown later in the thesis. Thus, signal intensities in such spectra are less representative of relative spin counts.

In 2003, Carlier *et al.* [35] presented theoretical work on paramagnetic solid-state NMR shifts in transition-metal oxides. The authors relied on the previous success of Oldfield *et al.* [36]

in the application of density functional theory (DFT) to interpret paramagnetic NMR shifts in solution. They found a correlation between predicted and experimental shifts. Another important contribution of this work is a detailed account of spin-density transfer pathways in order to generalize observed shift trends. These pathways correlate strongly with the local environment of the paramagnetic center and with occupancies of molecular orbitals.

Electron-spin-transfer effects in paramagnetic solid-state NMR were also investigated by Michaelis *et al.* [37] The work was based on nuclear shifts of ^{137}Ba and ^{89}Y in double perovskites of the form Ba_2YMO_6 (M = Mo, Re, Ru). This study is especially noteworthy as it illustrates the advantages of paramagnetic interactions to study unconventional nuclei. ^{137}Ba NMR is traditionally known to be challenging due to low sensitivity, requiring long experimental delays, and has broad resonances due to quadrupolar interactions. ^{89}Y has even lower sensitivity and due to its low spin and resonance frequency, the experimental delay makes it impractical for routine NMR (Chapter 8.2.1 [1]). The presence of paramagnetic interactions in these double perovskite structures solved most of those issues with improved relaxation rates for both nuclei. Additionally, extremely large paramagnetic shifts were recorded for the series. These shifts not only greatly enhanced the spectral resolution of ^{89}Y and ^{137}Ba NMR that could be used to identify impurities or multiple phases, but also provide a sensitive benchmark for distribution of unpaired electron spin density in the complex. A double perovskite of the same series with M = Os was later studied, where ^{89}Y MAS NMR was successfully applied to indicate possible site mixing [38].

1.2.2 Paramagnetic Tags

Brough *et al.* [39] showed that heavy paramagnetic ions, such as lanthanides, can be used for distance measurements in the solid state. These ions can be introduced to a substrate via chemical synthesis and provide a paramagnetic center. Their approach relied on measurements of nuclear-relaxation time with solid-state MAS NMR. With the use of the point-dipole model, the authors were able to extract distances to the paramagnetic site based on these measurements. To avoid the issue of ambiguous signal assignments, they applied selective isotopic enrichment and used the methods of Nayeem and Yesinowski [21] to experimentally verify the observed envelope of spinning sidebands from MAS. Agreement between all three identification methods confirmed both assignments and distances. Thus the authors demonstrated a working approach to the analysis of complicated paramagnetic ^{13}C spectra with signals spanning over 1000 ppm, whereas the conventional ^{13}C NMR of diamagnetic compounds is known to appear in the 0 - 200 ppm region with well-established assignments [40]. The analysis method used in this paper laid the ground for much subsequent work in solid-state paramagnetic NMR that is concerned with distance measurements from a known paramagnetic tag.

In 2012, Luchinat *et al.* [41] presented their work on structural determination in solid state paramagnetic NMR. They were able to characterize the structure of a protein bound to a paramagnetic Co^{2+} ion through shifts caused by the anisotropic magnetic moment of the ion. These shifts imposed distance restraints that together with pXRD data and dihedral angle restraints provided the necessary information to perform an ab-initio structure calculation of the protein. Their work showed the possibility of tackling protein-sized molecules with solid state NMR for structural analysis. Their results are in agreement with the single-crystal diffraction

data and could greatly simplify the process of structural elucidation of large molecules without the need to grow single crystals for diffraction.

An important application of paramagnetic tags is currently being applied successfully in magnetic-resonance imaging (MRI), a branch of NMR that focuses on imaging living tissue and organisms for medical purposes. Current applications focus on the use of gadolinium-containing paramagnetic tags in order to provide image contrast within the sample tissue. Here, researchers and medical professionals use the principles summarized in Solomon's point-dipole model on nuclear relaxation. Nuclei that are closer to the paramagnetic tag show fast relaxation and thus provide a contrast in the MRI image. These tags are currently being used successfully in hospitals. However, due to potential toxicity of degradation products, such as Gd^{3+} ion, the dosage has to be minimized and strictly regulated [42].

1.2.3 Battery materials

Interest in paramagnetic NMR includes materials with conducting properties for use in batteries. Kumar *et al.* [43] published a method to separate the quadrupolar coupling of ^{7}Li nuclei from the paramagnetic dipolar interaction. They showed how a two-dimensional experiment on a paramagnetic perovskite, $La_2Li_{0.5}Ni_{0.5}O_4$, can be used to measure quadrupolar couplings of ^{7}Li and clearly separate that contribution from paramagnetic dipolar coupling, which can then be used to describe the ionic mobility and proximity to the paramagnetic center. In principle, these parameters could be used to study conductivity in battery materials.

Grey's group [44] studied iron phosphate and its lithium derivatives for their promising application as cathode materials in lithium-ion batteries. Their ^{7}Li and ^{31}P MAS NMR spectra had been well-characterized and correlated with available XRD structures through calculations

with density functional theory and susceptibility measurements. Thus, the authors were able to establish a firm connection between the structure and observed experimental spectra, which could have potential application in further studies of battery materials, such as charge/discharge behavior. A recent publication from this group focuses on ^{25}Mg NMR of Mg-ion based batteries [45]. NMR of this nucleus is experimentally challenging; however, the paramagnetic interactions in these materials allow reasonably efficient acquisition and interpretation of local environments of Mg.

1.2.4 Glasses

Solid-state paramagnetic NMR has also been attempted in glass samples. Mortuza *et al.* showed the effect of paramagnetic impurities on sodium disilicate glasses at impurity levels of MnO reaching 0.8 mol%. This was one of the first studies of paramagnetic influences on the NMR spectra of glasses [46]. Their study indicated the systematic broadening of glass resonances and a slight shift to lower frequency. Resonance broadening is to be expected in the presence of paramagnetic interactions according to the Solomon's point dipole model; however, the origin of the shift remains unknown as there are multiple possible contributions that could result in slight shift changes. Their work was one of the first to show the general effects of paramagnetic impurities on glass spectra, apart from the reduction in ^{29}Si nuclear relaxation time, which allowed faster NMR experimental time.

1.2.5 Metal-organic frameworks (MOFs)

Aguiar *et al.* [47] studied cyanide coordination polymers containing transition metals by NMR. This work capitalized on enhanced nuclear relaxation from paramagnetic interactions to boost the sensitivity of natural abundance ^{13}C and ^{15}N MAS NMR experiments. The study

presented the capabilities of paramagnetic solid-state NMR to discover local connectivities and extract relevant distances to the paramagnetic center using the point-dipole model. Coordination polymers of this type bear a close resemblance to metal-organic frameworks (MOFs), three-dimensional porous solids composed of periodic organic linkers bound by metal ions at nodal intersections. These structures are currently studied for a variety of applications ranging from catalytic and biological to inert gas capture and materials for battery electrolyte [48, 49].

^{13}C MAS NMR of MOFs with paramagnetic centers was reported for the first time by Dawson *et al.* [50]. The authors were able to use the ability of NMR to study local nuclear environments in detail and determine potential structural variations that can occur in the extended MOF structure. The presence of structural variations can have an important role on MOF properties. The authors found that the assignment of NMR spectra in these extended structures was ambiguous and required selective isotopic enrichment to validate the signal assignments.

1.3 Metal acetylacetonate compounds

This thesis focuses on the interpretation of experimental NMR spectra in relation to electronic spin density distribution and the structure of transition-metal complexes involving the acetylacetonate ligand. In particular, the series includes tris-ligand complexes with titanium, vanadium, chromium, manganese and iron; bis-ligand complexes with nickel and copper metals and a vanadyl group. Additionally, a copper acetate dihydrate molecule will be presented as an example of a spin-coupled system. First-row transition metals are selected with d^1 (Ti^{3+}, V^{4+}), d^2(V^{3+}), d^3(Cr^{3+}), d^4(Mn^{3+}), d^5(Fe^{3+}), d^7(Co^{2+}), d^8(Ni^{2+}) and d^9(Cu^{2+}) electronic configurations.

The gradual increase in the *d*-orbital occupancy enables a systematic approach to the investigation of paramagnetic contributions to the ^{13}C and ^{1}H NMR signal of the ligands.

2,4 – pentanedione, also referred to as acetylacetone or acac, is illustrated in Figure 1.1 (top) in its two tautomeric forms. The enolate can form a bidentate ligand with medium- and small-sized cations, and is used as a metal sieve in ore processing [51]. Upon complexation with the metal, a six-membered ring is formed with the aromatic character, as illustrated in Figure 1.1 (bottom) with the extended π-bonding. The oxygen atoms chelate to the metal center via σ-bonding and π-donor interactions with the two lone pairs, one of which is found as a part of the pseudoaromatic system, while another is in the plane of the ligand. The term "pseudoaromatic" has been coined by Seko [52], as the metal is not considered to participate in the aromatic

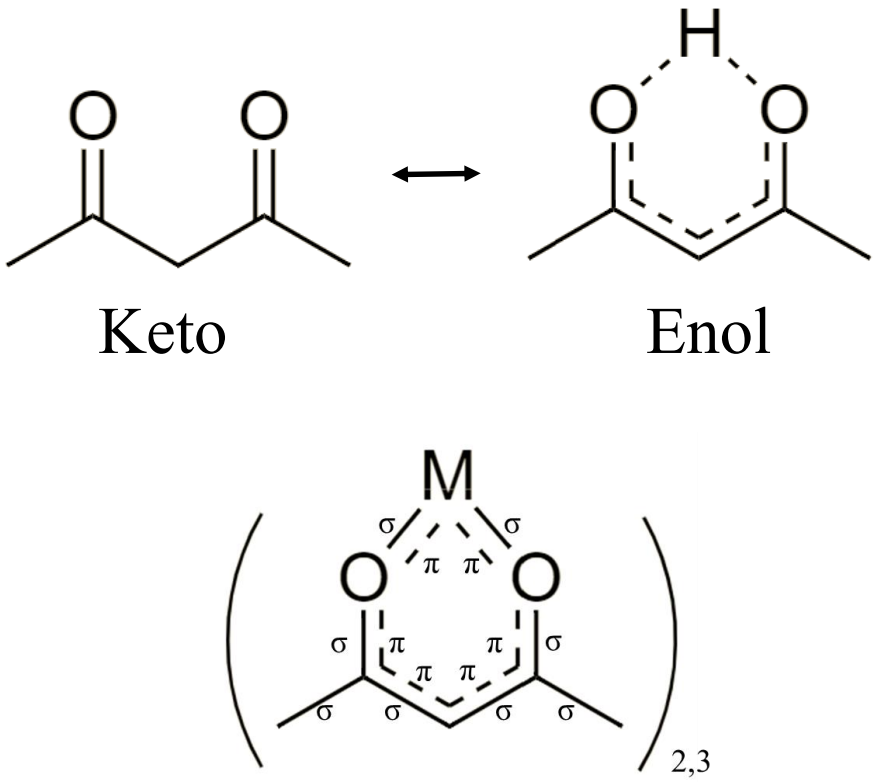

FIGURE 1.1: Molecular structures of 2,4 – pentanedione (top) and its complex with a metal (bottom) illustrating major diatomic orbital interactions.

stabilization. The complexation of three bidentate acac ligands provides a near-octahedral coordination of oxygen atoms around the metal center, while a complex with two ligands produces a near-square planar geometry. Bis-ligand complexes of Ni^{2+} and Co^{2+} are known to contain additional water molecules that complete the pseudo-octahedral geometry. Each complex has its own individual structural distortion due to crystal packing of molecular units and the Jahn-Teller distortion, where present.

Acetylacetonate complexes are used as catalysts and a starting material for nanoparticle synthesis [51, 53, 54]. Their general ease of synthesis, coupled with the ability to host nearly any metal, makes them a perfect target for theoretical investigation of electronic properties [55-58].

1.3.1 $Ti(acac)_3$

Tris(acetylacetonato)titanium(III), or $Ti(acac)_3$, consists of three acetylacetonate ligands chelating to the titanium metal having a single unpaired electron shared among its *d*-orbitals. The splitting of *d*-orbital energy levels can be approximated with that of the octahedral field in Figure 1.2. This electronic configuration is subjected to Jahn-Teller distortion that lifts the degeneracy of individual orbitals, as shown in Figure 1.2.

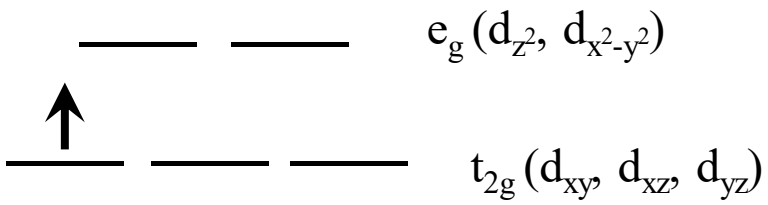

FIGURE 1.2: Crystal-field splitting of $Ti(acac)_3$ approximated by an octahedral field.

Our group has refined the crystal structure of a freshly made sample of $Ti(acac)_3$ at 55°C, which is in agreement with previously published results to within 3 standard deviations. The crystal structure contains two symmetry-equivalent stereoisomers with a space group $P2_1/n$. The complex undergoes a rapid oxidation upon exposure to the ambient environment that converts the deep blue powder to the dark brown diamagnetic form of $TiO(acac)_2$ [59].

1.3.2 $V(acac)_3$

Tris(acetylacetonato)vanadium(III), or $V(acac)_3$, with three bidentate ligands of acetylacetonate creates a near-octahedral coordination of the oxygen surrounding the vanadium center. Vanadium metal in its 3+ oxidation state contains two unpaired electrons that are shared among the three low-lying *d*-orbitals in the octahedral field, Figure 1.3. The complex is significantly more air stable than its titanium analog. Only upon prolonged exposure to the atmosphere, on the order of days, does the oxidation of V^{3+} to V^{4+} take place, with a characteristic color change: $V(acac)_3$ is dark-brown, which changes to lustrous green upon oxidation to $VO(acac)_2$ [60].

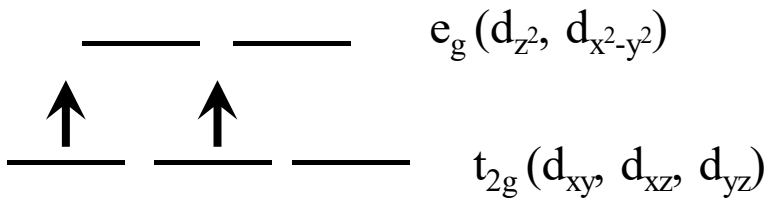

FIGURE 1.3: Crystal-field splitting of $V(acac)_3$ approximated by an octahedral field.

The electronic configuration of the metal in $V(acac)_3$ allows Jahn-Teller distortion. This effect is more pronounced than in $Ti(acac)_3$ as the vanadium complex has at least two packing

arrangements in the solid state [29]. The α-form of $V(acac)_3$ crystallizes in the *Pbca* space group, whereas the β-form crystallizes in the $P2_1/c$ group. A recent publication in 2017 reveals more crystal structures that retain the above group identities, yet they contain split crystallographic occupancies of one of the ligands [29]. Partly occupied ligands possess different degrees of distortion from the idealized D_3 symmetry of the molecule.

1.3.3 $Cr(acac)_3$

Tris(acetylacetonato)chromium(III), or $Cr(acac)_3$, has a stable oxidation state and coordination of the chromium ion. The crystal form of the complex at room temperature has a single unique molecular unit in a unit cell of $P2_1/c$ symmetry [61]. Chromium in this complex

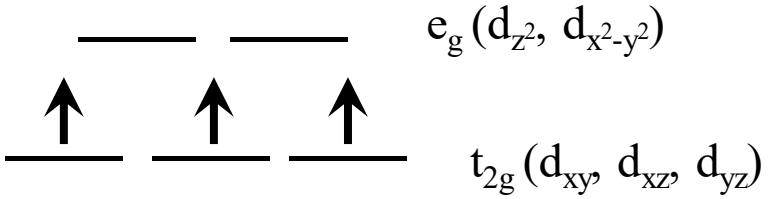

FIGURE 1.4: Crystal-field splitting of $Cr(acac)_3$ approximated by an octahedral field.

has three unpaired electrons in a near-octahedral field, Figure 1.4, therefore there is no Jahn-Teller distortion. There is another polymorph of the structure below 100 K, which retains the same symmetry as the high temperature form, but the unit cell is expanded to contain six unique molecules of $Cr(acac)_3$ [61]. Compared the titanium and vanadium analogs the chromium complex is the most stable and does not need to be stored in an oxygen-free environment. $Cr(acac)_3$ is commonly used in solution NMR as a relaxation agent due to its non-reactive nature and large magnetic moment.

1.3.4 $Mn(acac)_3$

Tris(acetylacetonato)manganese(III), or $Mn(acac)_3$, has several room-temperature polymorphs, which has caused some confusion in the literature [62, 63]. The ligand arrangement in the complex creates a near-octahedral environment around the Mn^{3+}ion, which bears four unpaired electrons. The electronic configuration of an idealized octahedral geometry is shown in Figure 1.5. Orbital occupancies in Figure 1.5 indicate the condition for the Jahn-Teller distortion, which is apparent in its various polymorphs.

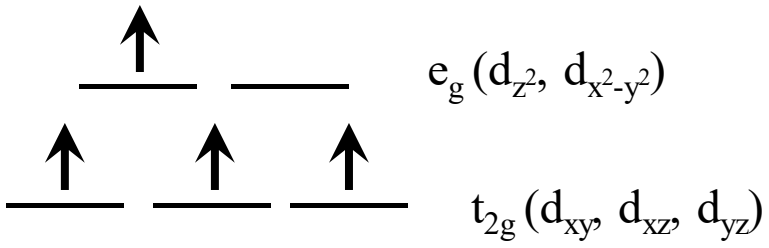

FIGURE 1.5: Crystal-field splitting of $Mn(acac)_3$ approximated by an octahedral field.

The α- $Mn(acac)_3$ adopts an orthorhombic unit-cell with the *Pbca* space group. This form can be obtained by crystallization at 100 K [29]. The unit cell contains a single molecule with a clear Jahn-Teller elongation of axial metal-oxygen bonds with the average length of 2.14(1) Å, while the average equatorial metal-oxygen bond distance is 1.93(1) Å, Figure 1.6.

The β-$Mn(acac)_3$ form crystallizes in a monoclinic unit-cell with the $P2_1/c$ space group. At least two crystal structures have been reported and labeled as β-$Mn(acac)_3$. The original publication [62] reported molecular dimensions correspond to a Jahn-Teller compressed form with the average axial metal-oxygen distance of 1.94(1) Å and an equatorial distance of 2.00(2) Å. A more recent structure of this form reveals a structural distortion with partial occupancy of

one of the ligands [29]. While average equatorial bond lengths are the same as in the 1974 publication, one of the oxygen atoms in the axial plane is displaced between 1.83(1) Å and 2.10(1) Å. This illustrates the potential variability of the crystal structure in the same packing arrangement with different methods of sample preparation. A presence of the site distortion should be well-resolved using NMR as there will be a significant difference in the Fermi coupling between the disordered positions.

The γ-Mn(acac)$_3$ form has a monoclinic unit-cell with the space group $P2_1/n$ [64]. This form is prepared at room temperature and is the most common structure of Mn(acac)$_3$ that is available commercially [65]. The structure has distinct Jahn-Teller elongation with the long bonds averaging 2.111(4) Å and equatorial bonds of 1.935(3) Å [64].

The δ-and ε-Mn(acac)$_3$ crystal structures contain multiple non-equivalent molecules of Mn(acac)$_3$ with different degrees of distortion [29, 66]. There has been a report of an irreversible structural change from δ to ε form upon slow cooling of the solid past 190 K [66].

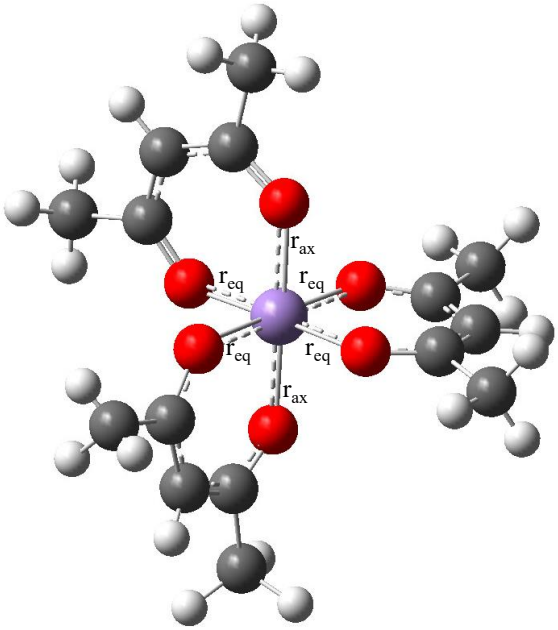

Figure 1.6: Model structure of Mn(acac)$_3$ illustrating different types of Jahn-Teller (JT) distortion. Structure is JT-elongated for $r_{ax} > r_{eq}$ and JT-contracted for $r_{ax} < r_{eq}$.

The sample purchased from Alpha Aesar was found to contain predominantly γ - $Mn(acac)_3$, as confirmed by our powder x-ray diffraction. The unit cell possesses a single unique molecule with a clear Jahn-Teller elongation along the octahedral z-axis (axial bonds in Figure 1.6).

1.3.5 $Fe(acac)_3$

Tris(2,4-pentanedionato)iron(III), or $Fe(acac)_3$, is a product of a well-known test [67] for the presence of β-diketone. In the reaction of ferric chloride with the ligand, a bright-red product is formed in an oxygen environment. The electronic configuration of Fe^{3+} in the pseudo-octahedral complex is approximated in Figure 1.7, where no Jahn-Teller distortion is expected to cause any significant variation to the local oxygen environment around the metal. The crystal forms in a $P2_1/n$ symmetry. The unit cell contains a single molecule of $Fe(acac)_3$ [68].

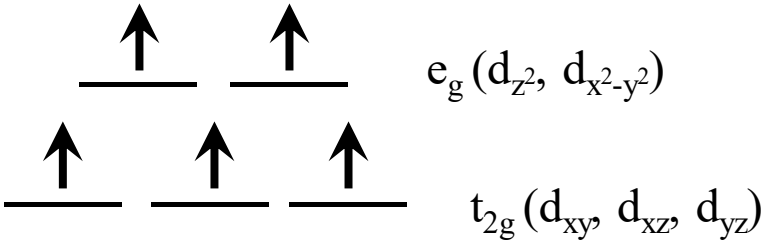

FIGURE 1.7: Crystal-field splitting of $Fe(acac)_3$ approximated by an octahedral field.

1.3.6 $Cu(acac)_2$

Unlike previous complexes with three bound ligands, bis(2,4-pentanedionato)copper(II), or $Cu(acac)_2$, adopts a near-square-planar oxygen coordination around the transition metal, which is a center of inversion symmetry [69]. The inversion symmetry leaves a single crystallographically unique acetylacetonate ligand per molecular unit. The packing arrangement

of individual molecules in the solid suggests no interaction between adjacent metal centers, as each metal is separated by the neighboring acac group, Figure 1.8.

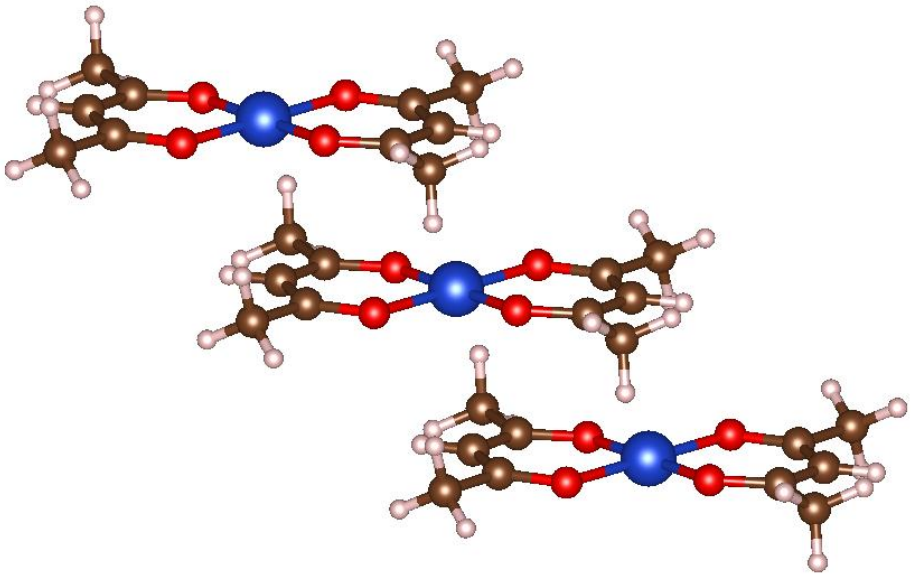

FIGURE 1.8: Three $Cu(acac)_2$ molecules illustrating the packing arrangement in a solid [69].

The copper ion has a d^9 configuration, which in a square-planar field leaves the unpaired electron in the highest energy *d*-orbital [55]. Figure 1.9 illustrates the idealized electronic configuration for the d^9 complex in a square planar field (D_{4h} point group).

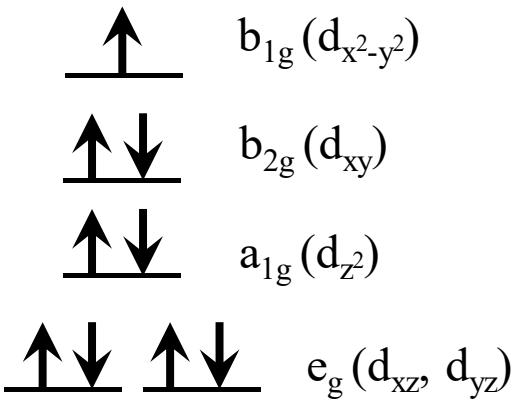

FIGURE 1.9: Crystal-field splitting of $Cu(acac)_2$ approximated by a square-planar field.

1.3.7 $Co(acac)_2 \cdot 2H_2O$ and $Ni(acac)_2 \cdot 2H_2O$

The presence of two water molecules that coordinate to the metal center along the perpendicular axis creates a distorted octahedral field around the transition metal, as seen in $Co(acac)_2 \cdot 2H_2O$ and $Ni(acac)_2 \cdot 2H_2O$, Figure 1.10. The structure of hydrated bis(acetylacetonato)cobalt(II) has been determined in 1959 by Bullen [70]. The molecule has a center of inversion at the cobalt atom, therefore there is a single water molecule and acetylacetonate ligand. The oxidation state of cobalt in this complex is +2, therefore it has seven *d*-electrons in its outer shell, surrounded by oxygen atoms in a distorted octahedral coordination with a characteristic elongation along the z-axis. The ground state electronic configuration in this coordination is $t_{2g}^5 e_g^2$, which is the high-spin state with net three unpaired electrons [71].

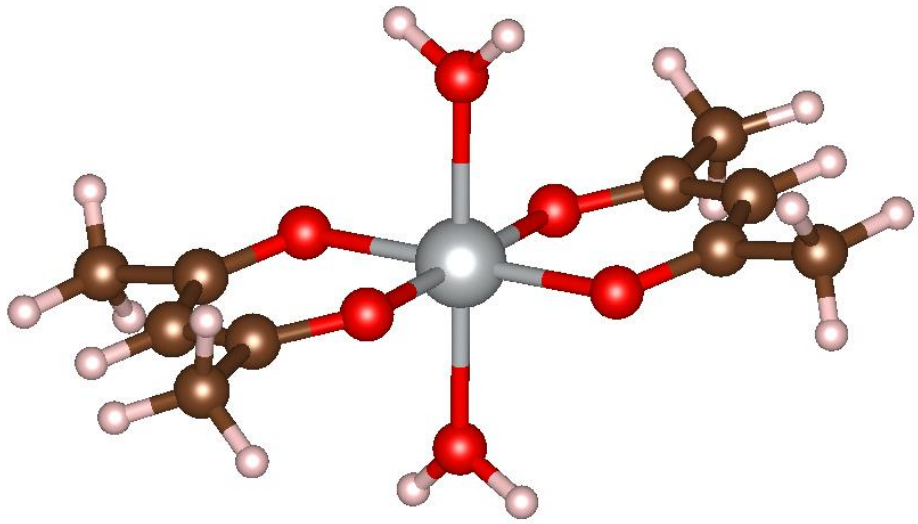

FIGURE 1.10: Molecular structure of $Co(acac)_2 \cdot 2H_2O$ and $Ni(acac)_2 \cdot 2H_2O$ [70, 72].

The structure of bis(2,4-pentanedionato)nickel(II) dihydrate has been known since 1965 [72]. The oxygen environment around the nickel creates a distorted octahedral shape in a similar manner to cobalt analog. The nickel complex, like cobalt and copper, possesses inversion symmetry at the metal, making the two ligands equivalent. The ground-state electronic configuration in $Ni(acac)_2 \cdot 2H_2O$ with a near-octahedral field symmetry is $t_{2g}^6 e_g^2$. Another hydrated form of the nickel complex has an additional water molecule in outer coordination, not interacting with the metal center [73]. Instead, this additional water molecule affects the orientation of hydrogen bonds of the metal-coordinated water.

1.3.8 $VO(acac)_2$

The structure of oxobis(2,4-pentanedionato)vanadium(IV) differs from previous complexes as it adopts a square pyramidal coordination of oxygen atoms around the vanadium center [74]. Molecular geometry and the crystal-packing arrangement are illustrated in Figure 1.11. The pentagonal oxygen coordination leads to a clear axis of distortion along the vanadyl bond. Both ligands no longer share the same plane and are now tilted at an angle with respect to each other.

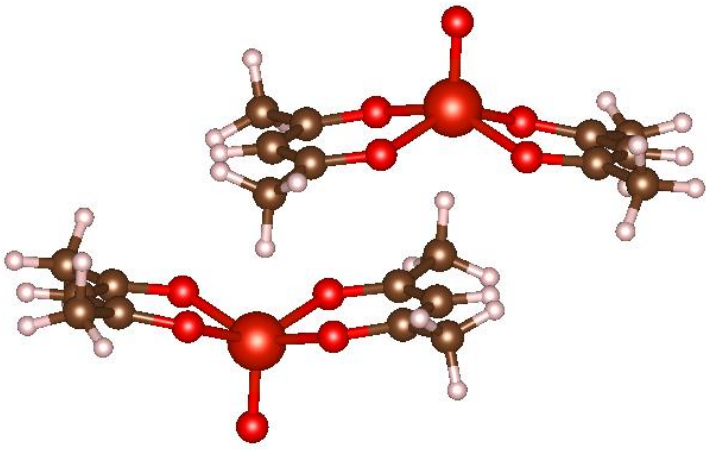

FIGURE 1.11: Crystal packing arrangement of $VO(acac)_2$ [74].

1.3.9 $[Cu(CH_3COO)_2]_2(H_2O)_2$

The structure of tetra-μ^2-acetatodiaquadicopper(II)was determined in 1952 [75]. It is composed of two copper metals coordinated to four shared acetate ligands with two coordinated water molecules creating a square pyramidal coordination of oxygen atoms around each copper center, Figure 1.12. This molecule is included in the series as it is a simple example of a related structure which can provide additional insight into the general applicability of the MO-based approach to NMR signal assignments. The complex is the simplest case of a system with two coupled magnetically active centers as both copper atoms have an antiferromagnetic interaction [75]. In such interaction, the unpaired spins in d-orbitals of the two copper centers are anti-parallel, and thus they quench the total magnetic moment of the molecule. However, in the case of copper acetate, the anti-ferromagnetic coupling allows a weak magnetic moment above 90K [76].

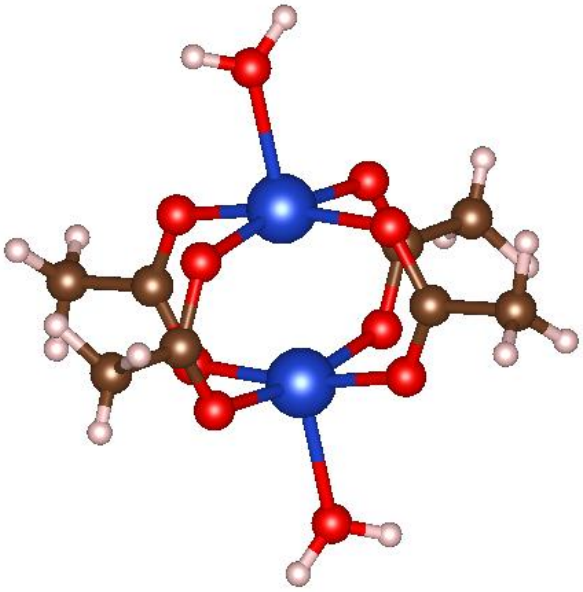

FIGURE 1.12: Molecule of $[Cu(CH_3COO)_2]_2(H_2O)_2$ [77].

1.4 Purpose

The objective of this thesis is to provide chemists with necessary tools to acquire and interpret paramagnetic NMR spectra in the solid state. We hope to achieve this through a series of well-studied coordination compounds presented above and establish a firm connection between the local environment of the paramagnetic center, the electronic configuration and the observed NMR signals in the solid state. A comprehensive account of NMR resonance shift and a method to explain undetectable signal is provided in relation to the physical properties of a complex and experimental conditions. An extension to Solomon's model of paramagnetic nuclear relaxation is proposed in an attempt to improve the modeling of paramagnetic relaxation in solids. To supplement our detailed structural assignments of crystallographic sites, computational modeling of electron-spin distribution through efficient hybrid-DFT calculation is used. Using these spin-density calculations a general model of the spin-density distribution is proposed in regard to specific electronic configurations, making this approach applicable to other paramagnetic systems. Anisotropic interactions are not considered in this work as they are under active investigation by Grandinetti [78] and Kervern [79] for solid-state systems. Upon investigation of the above paramagnetic contributions, a set of desirable physical qualities of the sample is proposed that would ensure the best quality NMR data. Together, these contributions provide spectroscopists with an essential set of tools to acquire and interpret solid-state MAS NMR spectra of paramagnetic compounds.

Chapter 2: Theory of NMR for crystalline diamagnetic and paramagnetic solids

2.1 Introduction to NMR

2.1.1 Origin of the NMR signal

An NMR signal originates from the magnetic moment of the nucleus in the applied magnetic field, B_0, of the instrument (Chapter 1 [80]). The nuclear moment, $\vec{\mu}$, is related to the quantum property of the nucleus called **spin**, denoted **I**, by the following relation:

$$\vec{\mu} = \gamma \hbar \vec{I} \qquad \textbf{(2.1)}$$

where ħ is the reduced Planck's constant and γ is the nuclear magnetogyric ratio. The nuclear spin is quantized and possesses a **spin quantum number** of the form *n/2*, where *n* is an integer number between 0 and 9. The total spin quantum number originates from spin contributions of unpaired protons and neutrons that occupy specific quantum energy states in an isotope [81, 82].

In the absence of an applied magnetic field, individual nuclear moments have random orientations, thus there is no net magnetic moment and all nuclear spins are in a degenerate energy state. In the presence of an applied field, a small excess of nuclear moments align themselves with the field axis, which is conventionally chosen as the z-direction in the laboratory frame, and precess about this axis at the **Larmor frequency**. This frequency, υ_l, is described with the following relation (Chapter 2 [1]):

$$\omega_{\boldsymbol{l}} = \gamma B_0 \quad \textbf{(2.2)}$$

where the magnetogyric ratio is measured in rad/(T·s). Its value is specific to a particular isotope and can be regarded as the sensitivity of the nuclear magnetic moment to an applied magnetic field. Conventional field strengths of modern NMR spectrometers range between 3 and 21 Tesla, with a few notable spectrometers operating at fields of up to 45 Tesla and recently up to 300 Tesla with pulsed magnets at LANL (Los Alamos National Laboratory) [83]. These fields generate specific Larmor precession frequencies in MHz up to the GHz range at higher fields for some nuclides.

Once the sample is placed into a strong magnetic field, its nuclear spins lose their energy degeneracy and split into 2I+1 states. This interaction of nuclear spins with the applied magnetic field is also known as the **Zeeman** interaction. The splitting of energy levels and the presence of the field direction creates a net magnetization in the z-direction, M_z, which is expressed in the high-temperature approximation as (Chapter 2 [1]):

$$M_z = \frac{N\gamma^2 B_0 \hbar^2 I(I+1)}{3kT} \quad \textbf{(2.3)}$$

where N is the number of nuclear spins, k is the Boltzmann constant, T is the sample temperature in Kelvin. The net magnetization in equation 2.3 is described by the Boltzmann distribution of nuclear magnetic moments that occupy the 2I+1 avaliable energy states. The magnitude of M_z is proportional to the signal intensity that can be achieved for a given sample at specific experimental conditions.

Equation 2.3 outlines the dependecies of the signal sensitivity on experimental aspects that are routinely used by NMR spectroscopists. Lower experimental temperature (T), greater sample size (N) and applied field strength (B_0) improve the signal intensity. These factors

encourage the use of greater sample mass and field strength in NMR. The largest amount of sample can be achieved in the most condensed phase of matter, the solid state. Therefore, it is commonly accepted that solid-state NMR gives more signal than solution NMR, as the latter contains less sample due to dilution by solvent.

2.1.2 Observation of an NMR signal

In order to observe an NMR signal, the sample in the magnetic field must be perturbed with a radiofrequency pulse near the Larmor frequency of the nucleus. An appropriate pulse disrupts the Boltzmann distribution of energy states, resulting in a non-equilibrium state. An electromagnetic pulse at the Larmor frequency is applied via a copper coil surrounding the sample. The effect on the net magnetization vector $\overrightarrow{M_z}$ can be seen in Figure 2.1. The pulse power and duration cause a change in direction of $\overrightarrow{M_z}$. The angle at which $\overrightarrow{M_z}$ inclines to the z-axis is termed the **tip angle**. The NMR signal can be detected in the xy-plane, and thus the projection of the magnetization onto the xy-plane, $\overrightarrow{M_{xy}}$, can be observed by the same copper coil. The precession of $\overrightarrow{M_{xy}}$ induces an electric current in the coil, which is then amplified and detected as a **free induction decay** signal (**FID**). As is apparent from Figure 2.1, the maximum signal can be obtained when the tip angle is 90˚, that is when magnetization M_z is converted into M_{xy} (Chapter 2 [1]).

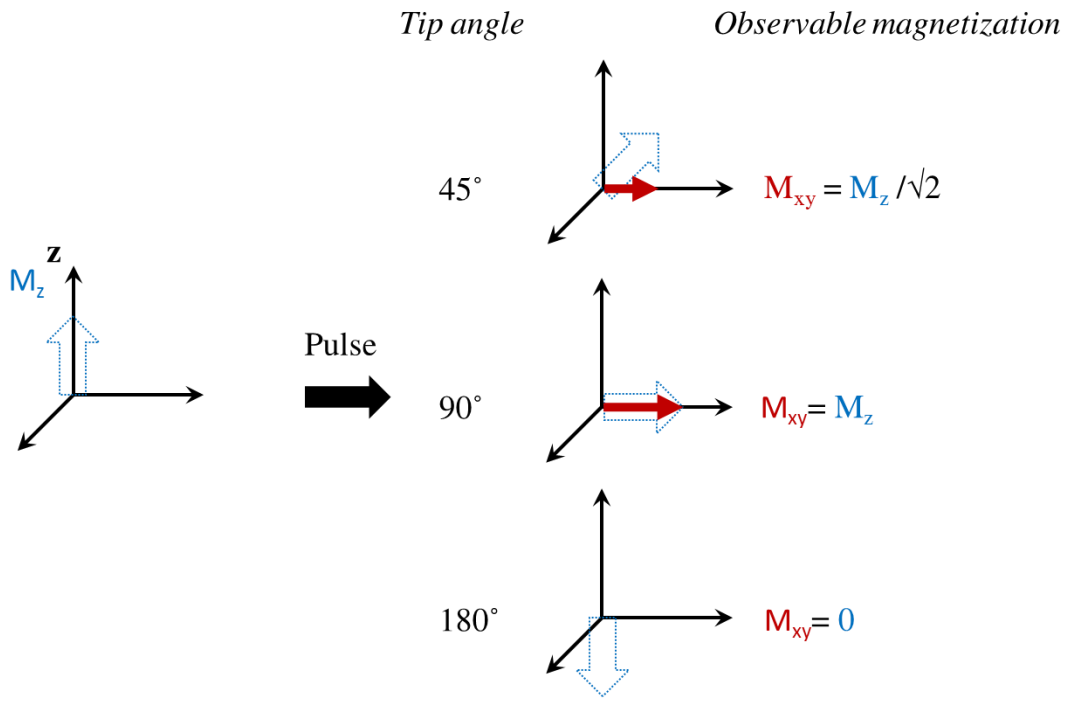

FIGURE 2.1: Illustration of magnetization transformation under pulses with various tip angles.

2.1.3 Relaxation of the NMR signal in single-pulse experiments

Shortly after the excitation, $\overrightarrow{M}_{xy}$ starts to lose coherence and precesses to its original state, $\overrightarrow{M}_z$, due to local inhomogeneities of the magnetic field around the nucleus. The rate at which $\overrightarrow{M}_{xy}$ loses coherence is defined as the transverse nuclear relaxation, T_2^{-1}, in units of Hz. A general formula for this type of relaxaion is given as:

$$M_{xy}(t) = M_{xy}(0)\, e^{-\frac{t}{T_2}} \qquad \textbf{(2.4)}$$

where *t* is the time dependence of M_{xy} magnetization. This relaxation mechanism is illustrated in Figure 2.2(a). The decay of transverse magnetization during the acquisition period, Figure 2.3, is detected by the copper coil as a function of time through induced electric currents. Fourier transformation of this FID signal converts the data to the frequency domain that is commonly used by spectroscopists for spectral interpretation. Equation 2.4 describes the decay of the NMR

signal in the time domain during the experiment. In order to acquire the majority of the signal, this relation is used to estimate the required length of acquisition time. For example, to record 95% of the signal, the acquisition time needs to be $3 \cdot T_2$.

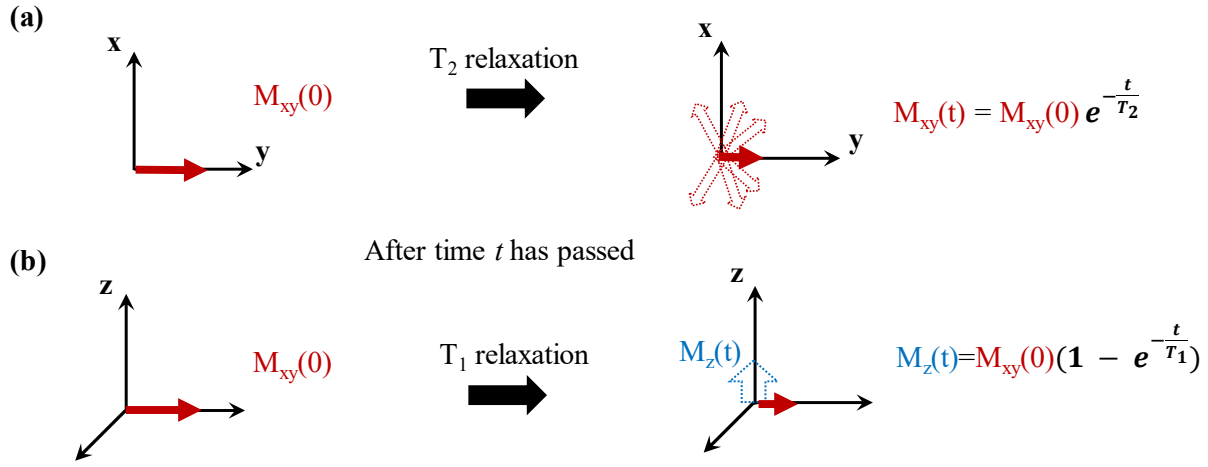

FIGURE 2.2: Relaxation processes: a) transverse (T_2) relaxation; b) longitudinal (T_1) relaxation.

The rate at which M_{xy} converts back to M_z is termed the longitudinal nuclear relaxation, T_1^{-1}, in units of Hz. This relaxation is described by the following general formula:

$$M_z(t) = M_{xy}(0)\,(1 - e^{-\frac{t}{T_1}}) \qquad \textbf{(2.5)}$$

Equations 2.4 and 2.5 are derived from the Bloch equations [84] for an ensemble of spins in a magnetic field (Chapter 2.8 [1]). The longitudinal relaxation of the system is important for acquisition of subsequent transients for signal averaging. In order to collect all of the signal in the next transient, the spin system needs to undergo full relaxation. The most common practice is to use a delay between the experiments equal to $5 \cdot T_1$, which would be equivalent to 99% of the M_z magnetization being restored according to equation 2.5. An illustration of the longitudinal relaxation process is given in Figure 2.2b.

A diagram of the simplest NMR experiment (Figure 2.3) outlines the three main stages of an NMR experiment: sample relaxation (*recycle delay*), pulse and signal acquisition. Respective delays are modified to account for spin relaxation rates, both transverse and longitudinal. These delays play a crucial role in NMR sensitivity as they define the repetition rate of signal acquisition.

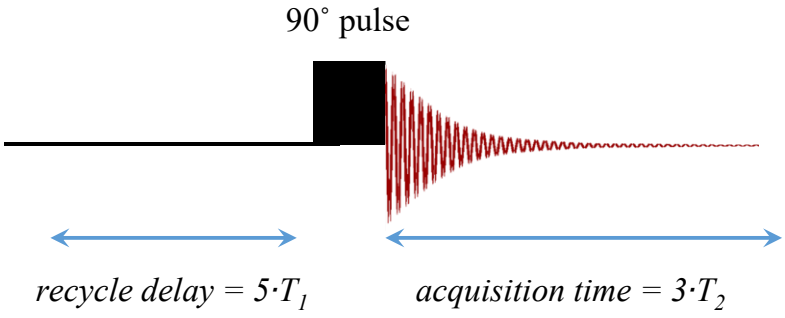

FIGURE 2.3: Single pulse NMR experiment.

The presence of an unpaired electron spin with unquenched net magnetization has a strong effect on nuclear-relaxation rates. Both transverse and longitudinal relaxation rates increase for all nearby nuclei [3]. Contributions to these rates will be outlined in section 2.2; here, I present the consequences of these effects on the observed NMR signal.

According to equation 2.5, an increase in the longitudinal relaxation rate leads to faster restoration of nuclear magnetization to the M_z state, and hence transients can be collected at a faster rate. Typical relaxation-rate enhancement from paramagnetic interactions are on the order of 100-1000 times that of diamagnetic analogs; thus NMR experiments can be done much faster, boosting the signal sensitivity per unit time [32]. This effect of paramagnetic interaction on relaxation rate is routinely used by spectroscopists to improve signal sensitivity through averaging of a greater number of transients per unit of time. The enhancement is achieved by

adding a small amount of a paramagnetic substance (e.g. $Cr(acac)_3$) directly to the sample solution in the case of solution NMR [1, 80].

Equation 2.4 indicates that an increase in transverse relaxation rate causes a rapid decay of the observable M_{xy} magnetization. This short FID signal in the time domain translates into broad spectral lines in the frequency domain after Fourier transformation. The relation between the full width at half maximum (FWHM) of the signal in the frequency domain has the following form:

$$\text{FWHM} = \frac{1}{\pi T_2^*} \qquad \textbf{(2.6)}$$

$$\frac{1}{T_2^*} = \frac{1}{T_2} + \frac{1}{T_2'}$$

where T_2^* represents composite transverse relaxation of a signal that determines the width of NMR signal. T_2' denotes relaxation caused by field inhomogeneity during the experiment. The effect of this relaxation mechanism can be minimized with an appropriate calibration of the field homogeneity throughout the sample. The effect of T_2' on experimental spectra will be ignored in this thesis as both these criteria have been met to minimize the effect of inhomogeneous broadening, hence $T_2^* \approx T_2$.

Contributions to the T_2 relaxation are numerous and well-studied and will be outlined in detail in section 2.2. In the presence of paramagnetic species, the T_2 relaxation time is dominated by electron-nuclear interactions, which significantly shorten the T_2 of the nucleus. Thus, according to equation 2.6, these interactions broaden the observed NMR peaks and lower spectral resolution.

The extremely short T_2 values imposed by paramagnetic interactions with nuclear spins lower the total signal intensity due to delays present in the pulse sequence. Electronics that

produce an electromagnetic pulse and detect the NMR signal require a finite time delay to switch their modes of action from transmitting to receiving. This time delay is also known as the **dead time** and is shown in Figure 2.4 for a single-pulse experiment. This delay is small relative to timescale of relaxation in conventional diamagnetic systems. However, if the signal decays rapidly, it could lead to a significant loss of signal. The example of a rapid signal decay is illustrated in Figure 2.4a for short T_2, which is commonly found in a paramagnetic sample.

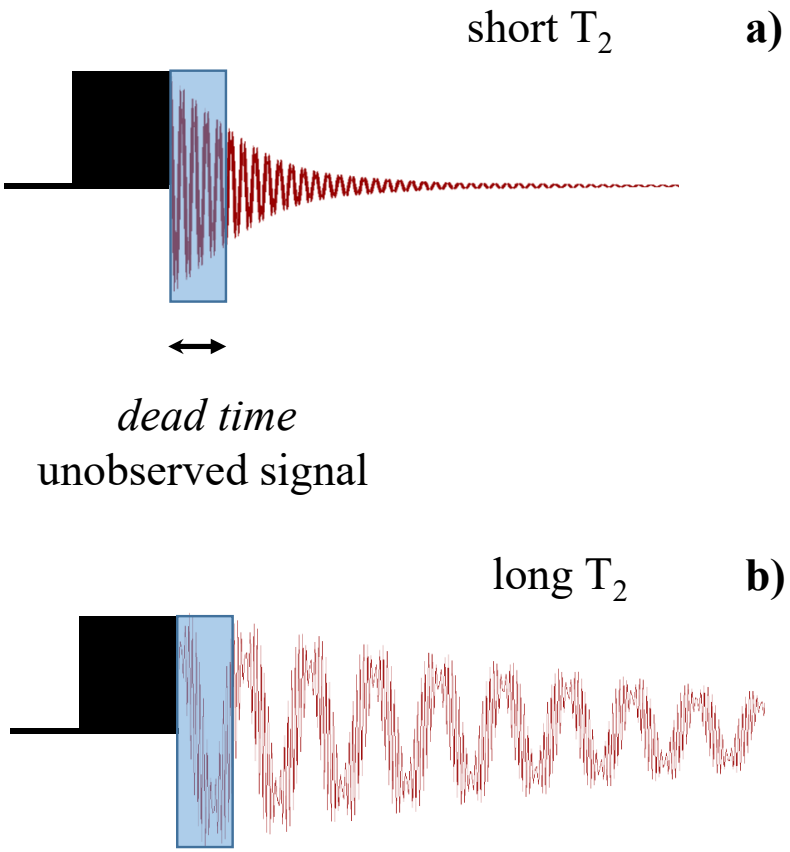

FIGURE 2.4: Effect of dead time on NMR signal with short and long T_2, corresponding to a) paramagnetic and b) diamagnetic samples, respectively.

Figure 2.5 shows the percentage of observable signal due to transverse relaxation before signal acquisition. In this example, single-pulse experiment is considered with no field inhomogeneity. The delay for the dead time has been set to the minimum allowed value by

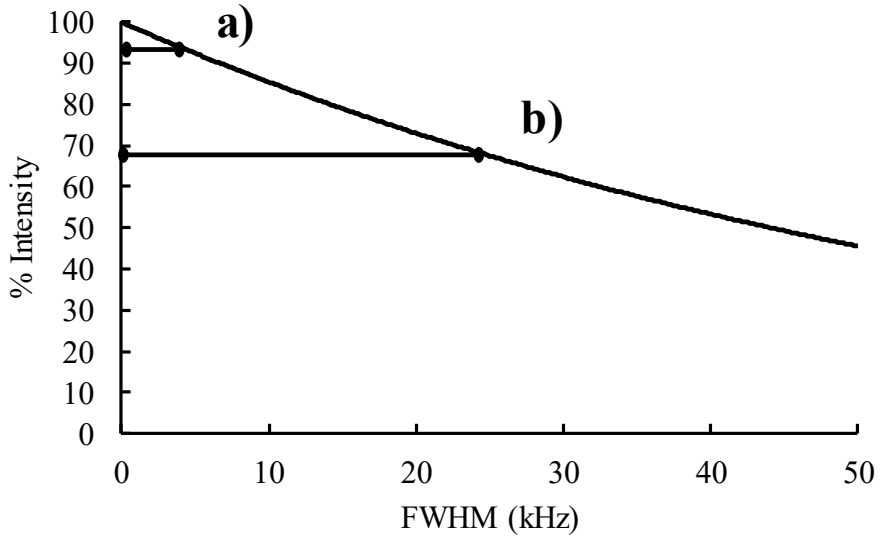

FIGURE 2.5: Effect of dead time delay of 5 μs on NMR signal intensity for resonances with different intrinsic width. Range of signal widths are typical of a) paramagnetic and b) diamagnetic systems.

Bruker spectrometers of 5 μs. The figure shows the monoexponential decay of magnetization that is characteristic of systems with substantial paramagnetic coupling (Chapter 2.3 [5]). This relation is described by equations 2.4 and 2.6 and shows the detrimental effect of paramagnetic coupling on both signal intensity and width. Figure 2.5 shows that for a typical signal width of a diamagnetic system, (b), the loss of signal intensity is not significant and could easily be neglected. If two signals are observed with widths of 1 and 5 kHz, their relative intensities resemble the stoichiometric ratios to within 5% error. Whereas if the contribution to T_2 relaxation is significant enough to cause broadening up to 40 kHz, Figure 2.5a, then the signal would have nearly half of the expected intensity with respect to a narrow 1 kHz resonance. Signal intensities in a single-pulse experiment are the best-case scenario where there is only a single short delay due to instrumental limitation.

2.2 Nuclear magnetic interactions

NMR-signal shapes are manifestations of interactions of the nuclear magnetic moment with its surroundings. A theoretical understanding of these processes is key to interpretation of observed NMR resonances in the frequency domain. An NMR spectrum reflects the net perturbation from all internal interactions that affect the total energy of the nucleus. These interactions can be summarized by the following Hamiltonian (Chapter 2 [1]):

$$\hat{H} = \hat{H}_Z + \hat{H}_{cs} + \hat{H}_{dip} + \hat{H}_p + \hat{H}_J + \hat{H}_Q + \ldots$$

where $\hat{H}_Z$ represents the Zeeman interaction of nuclear spins in a magnetic field, which was described in Section 2.1.1. Below are presented some of the well-known interactions that are studied with NMR.

2.2.1 Nuclear shielding interaction

$\hat{H}_{cs}$ is the Hamiltonian for nuclear shielding that originates from the magnetic effects of surrounding electron clouds. The sensitivity to electron density in the vicinity of the nucleus makes it possible to probe the chemical-bonding environment. Nuclear shielding due to chemical environments is also known as **chemical shielding** and is used to discriminate between different functional groups. The Hamiltonian has the following form (Chapter 2 [1]):

$$\hat{\mathrm{H}}_{CS} = \gamma_l h \vec{I}_z \bar{\boldsymbol{\sigma}} \vec{\mathrm{B}}_0 \qquad \textbf{(2.7)}$$

Shielding can be expressed as a minor deviation from the nuclear Larmor frequency as:

$$\sigma = \frac{\nu_l - \nu_{sample}}{\nu_l} \cdot 10^6 \qquad \textbf{(2.8)}$$

Equation 2.8 provides a normalization of the shielding, making it independent of the magnetic field. The experimental frequency of a nuclear resonance, ν_{sample}, is often close to the Larmor frequency. Thus the fraction in equation 2.8 is multiplied by 10^6, which converts shielding "units" into parts per million (ppm). Shielding values are specific to the nuclear environment in a particular molecule and can be compared directly using an appropriate reference. The chemical shift is defined with respect to the shielding of a standard (Chapter 2 [1]):

$$\delta = \frac{\sigma_{ref} - \sigma}{1 - \sigma} \cdot 10^6 \qquad \textbf{(2.9)}$$

As shielding is a second-rank tensor, it is represented by a 3 x 3 matrix and has three orthogonal components in its principal-axis system. According to the standard definition,[85] the resonance shifts of these components are labeled δ_{11}, δ_{22} and δ_{33}, where $\delta_{11} \geq \delta_{22} \geq \delta_{33}$ and $\delta_{iso} = (\delta_{11} + \delta_{22} + \delta_{33}) / 3$ is their isotropic value. The total variation between the shielding components, or span (Ω under Herzfeld-Berger notation) is defined as $\delta_{11} - \delta_{33}$. This value is also known as **span**, which signifies the amount of variation of the local magnetic environment of the nucleus with its orientation in the magnetic field. Thus, structures with low symmetry typically have greater shielding anisotropies. Anisotropy can be measured directly for a powdered sample, where all possible crystalline orientations outline the overall signal shape as in Figure 2.6. In these examples, δ_{iso} and Ω are kept constant while the relative magnitudes of the three components are changed. As can be seen from Figure 2.6, the anisotropic signal can adopt various shapes that reflect the magnitudes of the three shielding components. These components in turn outline the symmetry of the local atomic environment. The symmetry of the overall shape can be expressed through a parameter $\kappa = 3(\delta_{22} - \delta_{iso}) / \Omega$. The three examples of such

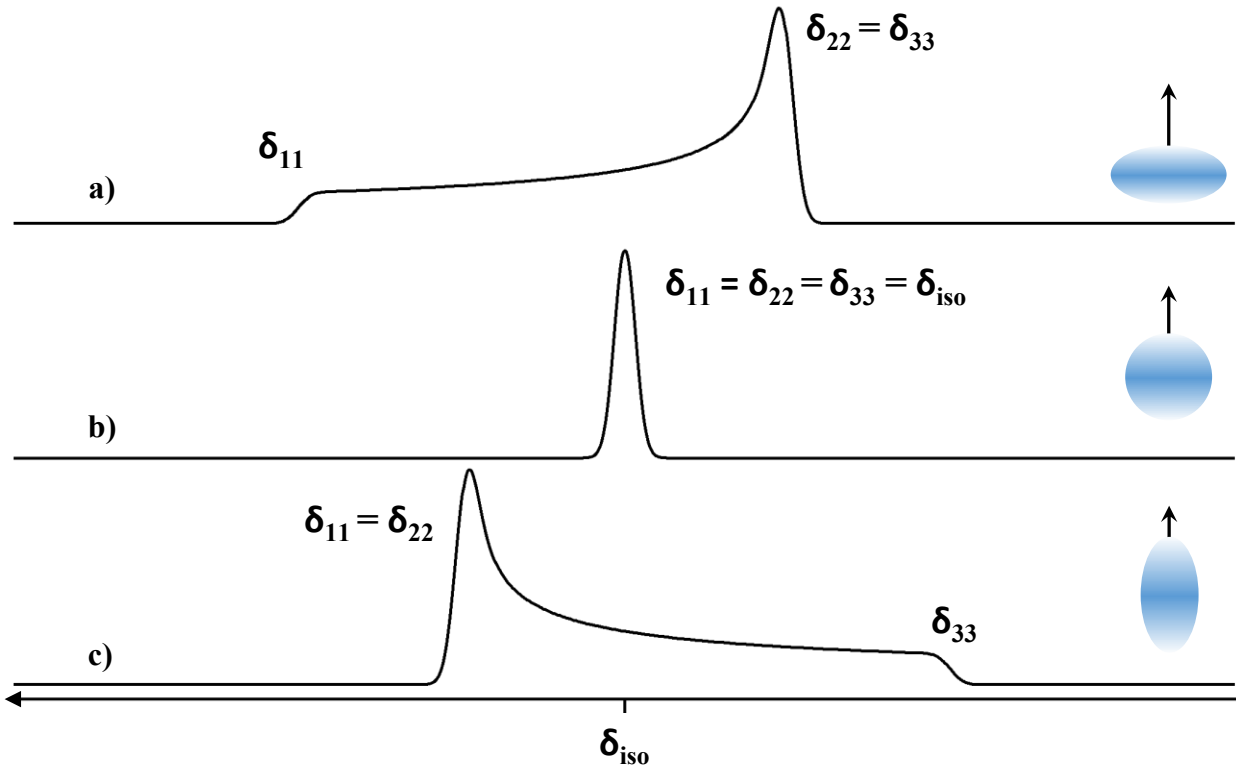

FIGURE 2.6: Examples of NMR chemical shift anisotropy of solid powdered samples. Anisotropies follow a) oblate; b) spherical and c) prolate symmetries.

environments are shown in Figure 2.6 and include oblate (κ = -1), spherical (κ = 0) and prolate (κ = 1) symmetries (Chapter 2 [1]).

2.2.2 Nuclear dipolar interaction

$\hat{H}_J$ represents the J-coupling interaction. This dipolar interaction is **indirect** as it is mediated via a pair of electrons in a chemical bond, and results in a characteristic splitting of resonances, with signal intensities following a binomial distribution. This characteristic splitting encodes the number of coupled nuclei, their spin and the magnitude of coupling. This interaction

occurs through a bond, and J-coupling is used to explore patterns of chemical bonding (Chapter 2 [1]).

$\hat{H}_{\text{dip}}$ symbolizes a direct dipolar interaction between two nuclear spins. This interaction occurs through space, thus it is considered to be a **direct coupling** between two nuclear magnetic moments. There are two categories of dipolar coupling, a heteronuclear coupling between different isotopes, and homonuclear coupling between identical isotopes. The time-independent Hamiltonian for a two-spin system has the following form (Chapter 2 [1]):

$$\hat{\mathrm{H}}_{homo} = \frac{\mu_o}{8\pi}\frac{\gamma_1\gamma_2\hbar^2}{r^3}(2\hat{I}_{1z}\hat{I}_{2z} - \frac{1}{2}(\hat{I}_{1+}\hat{I}_{2-} + \hat{I}_{1-}\hat{I}_{2+}))(3cos^2\theta - 1) \quad \textbf{(2.10)}$$

$$\hat{\mathrm{H}}_{hetero} = \frac{\mu_o}{8\pi}\frac{\gamma_I\gamma_S\hbar^2}{r^3}2\hat{I}_z\hat{S}_z(3cos^2\theta - 1) \quad \textbf{(2.11)}$$

Both cases depend on the distance between spins, r^{-3}, and the magnitude of their nuclear magnetogyric ratios, γ_I and γ_S. Thus a smaller distance between spins produces greater dipolar coupling, which can also occur if nuclei have high γ. Dipolar interactions become increasingly complicated as more spins participate in coupling, which is expected to occur in the solid state. The above relations outline an angular dependence (θ) of the interaction with respect to the magnetic-field axis.

2.2.3 Quadrupolar coupling ($\hat{H}_{\text{Q}}$)

The quadrupolar interaction, $\hat{H}_{\text{Q}}$, represents the effect of the nuclear electric-field gradient on the nuclear moment due to a non-spherical charge distribution for isotopes with I > ½. This interaction is readily observed in the solid state with characteristic signal lineshapes specific to the symmetry of the tensor and local atomic environment (Chapter 2 [1]). This interaction will not be further considered in this work as I focus on NMR of spin ½ nuclei.

2.2.4 Magic angle spinning

The spectra in Figure 2.6 are readily obtainable from an NMR experiment of a powdered sample. As one can anticipate, the anisotropic interaction has a detrimental effect on signal resolution where multiple distinct nuclear environments are present. As the anisotropic interaction depends on the sample orientation in the magnetic field, rapid molecular motion in a liquid sample provides an isotropically averaged signal, δ_{iso}. In order to eliminate this anisotropic broadening in powdered samples and mimic the isotropic averaging of a liquid sample, **magic-angle spinning** (MAS) was developed [20]. Thus the δ_{iso} values can be obtained in NMR of both solid and solution samples, which allow chemists to use NMR for structural determination of complex molecules on the basis of their local chemical environments.

NMR of powdered solids suffers from poor signal resolution due to anisotropic effects from dipolar coupling, quadrupolar coupling and magnetic-shielding interactions. To minimize anisotropic broadening from these interactions that arise from random orientation of crystallites in powdered samples, an instrumental technique was developed in 1980's [19, 20]. The method involved a mechanism for physical rotation of a sample container in the NMR magnet during the experiment, about the specific angle of 54.74° (Chapter 2 [1]). This angular dependence is present in the Hamiltonians of chemical shielding and dipolar coupling, equations 2.7, 2.10 and 2.11. According to these equations, the anisotropic component of these interactions can be nullified through a rapid averaging of crystallite positions in the magnetic field about an angle which satisfies the relation $3cos^2\theta - 1 = 0$, where θ is the angle of the crystallite orientation with respect to $\vec{B}_0$. The effect of this technique on a signal with an anisotropic contribution can be seen in Figure 2.7. In the absence of spinning, a powder pattern emerges, Figure 2.7a, which in

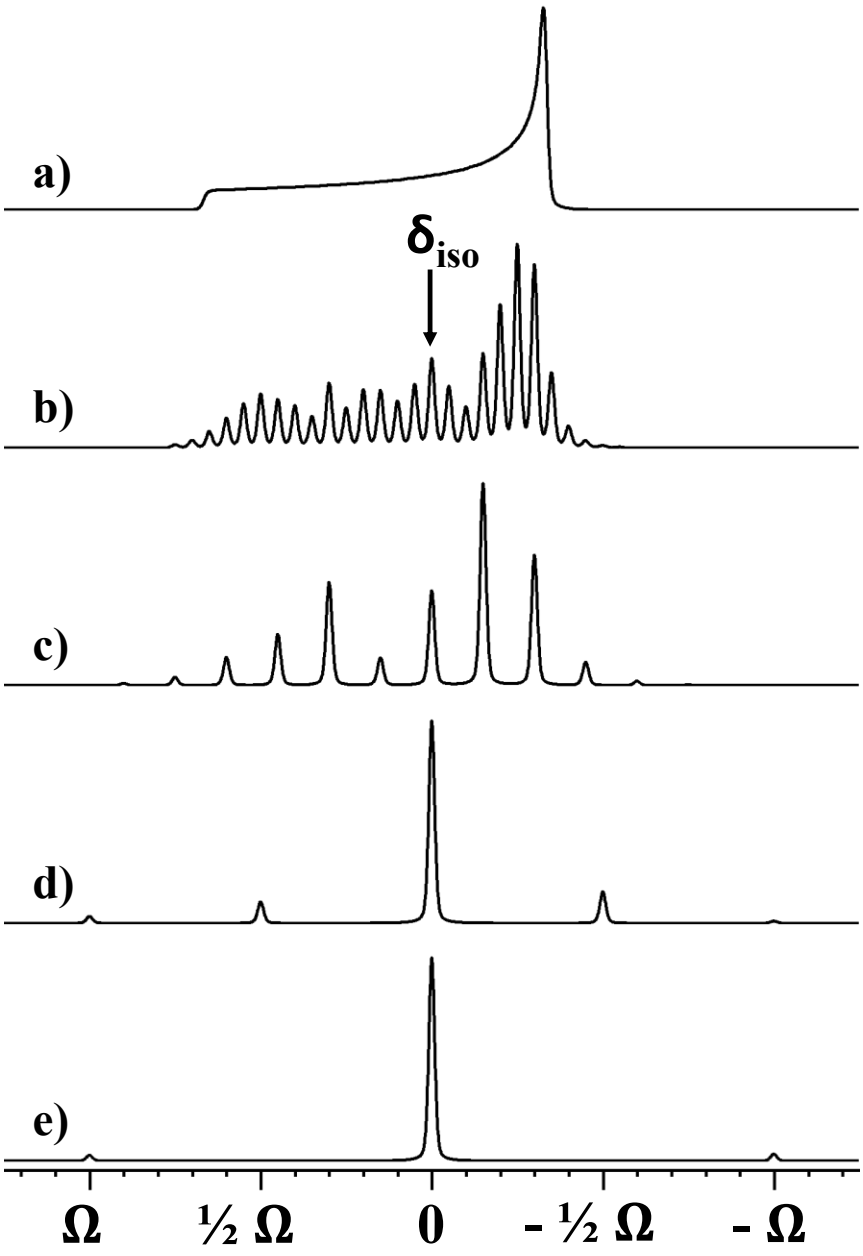

FIGURE 2.7: Effects of different MAS rates on a solid-state NMR spectrum with anisotropic broadening. Ω is the span of the signal. MAS rates are equivalent to a) static; b) $^{1}/_{20}$ Ω; c) $^{3}/_{20}$ Ω; d) $^{1}/_{2}$ Ω and e) Ω. All simulations are vertically scaled to match intensities of the most prominent signal.

this example indicates anisotropic interaction with oblate symmetry, as in Figure 2.6. If the spinning is not sufficiently rapid, artifacts are observed at a spinning-frequency increment from the isotropic peak. These are termed **spinning sidebands** and can be used to establish the overall shape and extent of the anisotropy (Figure 2.7b, c) as the pattern of artifacts outlines the static lineshape depicted in Figure 2.7a. As seen from this simulation, magic-angle spinning concentrates the signal in fewer, sharper resonances and thus significantly improves the signal resolution. Very fast spinning produces a spectrum which resembles the effect of random tumbling in solution where only the isotropic value of the shift is observed. However, as can be seen from Figure 2.7, in solid-state NMR one has control over this averaging process and can potentially obtain more information about the system through measurements of anisotropic shielding at lower spinning rates. Signal averaging and accumulation in fewer sharp resonances has the effect of increased effective sensitivity. Figure 2.8 shows the effect of MAS rates on the most intense feature of the spectrum that has appreciable anisotropy. As can be seen from the plot, the signal intensity has a convex dependence on the spinning rate with most of the intensity acquired at the point where the MAS matches the anisotropy, which is equivalent to the simulation in Figure 2.7e.

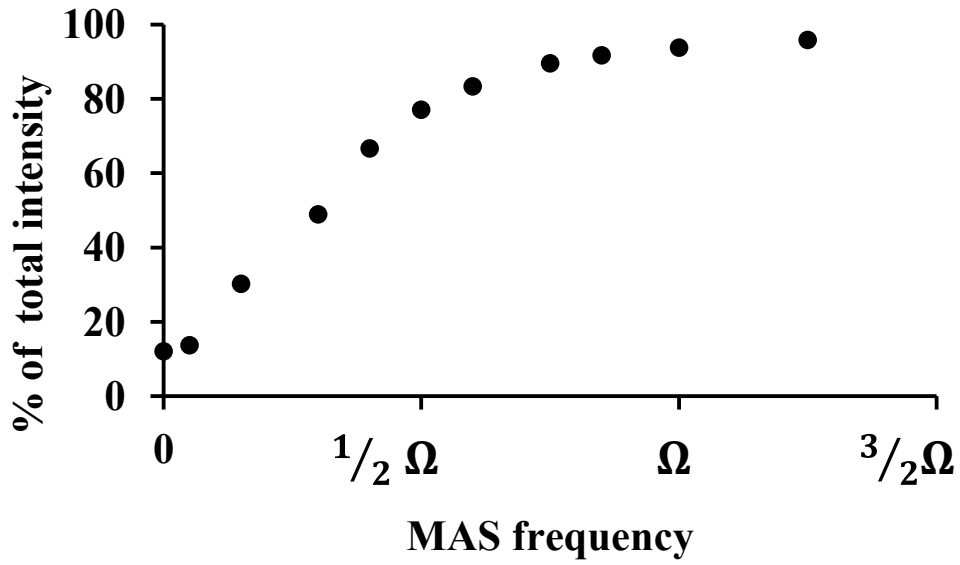

FIGURE 2.8: Effect of various MAS speeds on intensity of the most prominent signal with a span of Ω.

2.3 Hyperfine coupling in NMR ($\hat{H}_P$)

An unpaired electron has a strong magnetic moment, which can be expressed by the following equation (Chapter 1.3 [86]):

$$\vec{\mu} = g_e \mu_B \vec{S} \qquad \textbf{(2.13)}$$

where g_e is the electron g-factor, which is approximately equal to 2.0032 for a free electron, μ_B is the Bohr magneton, and S is the electron spin number. This formula is identical to that of the spin-active nucleus, equation 2.1, as $\gamma_e \hbar = g_e \mu_B$, where γ_e is the magnetogyric ratio of a free electron. The moment is 2-3 orders of magnitude greater than to any spin-active nucleus. Like the nuclear spins, electron-spin energy-levels are split under the influence of the magnetic field by the Zeeman interaction (Figure 2.9a) where the energy of the interaction is directly proportional to the strength of the applied magnetic field. Just as for nuclear spins, the Zeeman interaction leads to a precession of electron spins with the Larmor frequency, described by

equation 2.2. The population of energy states for electronic Zeeman splitting is governed by the Boltzmann distribution, and the splitting energy is outlined in Figure 2.9a.

Figure 2.9b illustrates energy levels of uncoupled nuclear spins in a system with a characteristic Zeeman splitting. An NMR experiment involves an observed transition between two I_z states $|+ ½ >$ and $| - ½ >$. As both depicted NMR transitions at S_z states $|+ ½ >$ and $| - ½ >$ have identical energy differences, the spectrum would carry no information regarding the unpaired electron. Figure 2.9c illustrates the effect of a coupling interaction between electron and nuclear spins. These perturbed energy levels carry the information on spin-spin interactions between the unpaired electron and the nucleus. This information is of most interest to spectroscopists as it provides a probe of interatomic interactions, local chemical environment and electronic states of the molecule. As this coupling energy perturbs both electron and nuclear energy levels, both EPR and NMR measurements can measure these effects (see section 2.5).

The Hamiltonian of the paramagnetic interaction may be expressed as (Chapter 1.5 [5]):

$$\hat{H} = \gamma_e \hbar B_0 S_z - \gamma_n \hbar B_0 I_z + \vec{S} \cdot A \cdot \vec{I} \qquad \textbf{(2.14)}$$

where individual contributions to energy splitting originate from the electron spin ($\hat{S}$), the nuclear spin ($\hat{I}$), and their coupling (A). Figure 2.9 shows the effects of these contributions on Zeeman-level splitting. NMR transitions may occur between $I_z = ½$ and $I_z = - ½$ states, thus the spectrum with paramagnetic coupling is expected to have two transitions, which are separated by a **hyperfine** coupling, Figure 2.9c.

This interaction has a close parallel with J-coupling, where electrons act as mediators of nuclear moments to produce an observable resonance splitting (Figure 2.10a). Coupling of the unpaired electron spin directly to the nuclear spin leads to a greater perturbation of the nuclear signal as the electron has a magnetic moment that exceeds any nuclear moment by several orders of magnitude. As the energy levels of electron spin under the Zeeman effect have a large

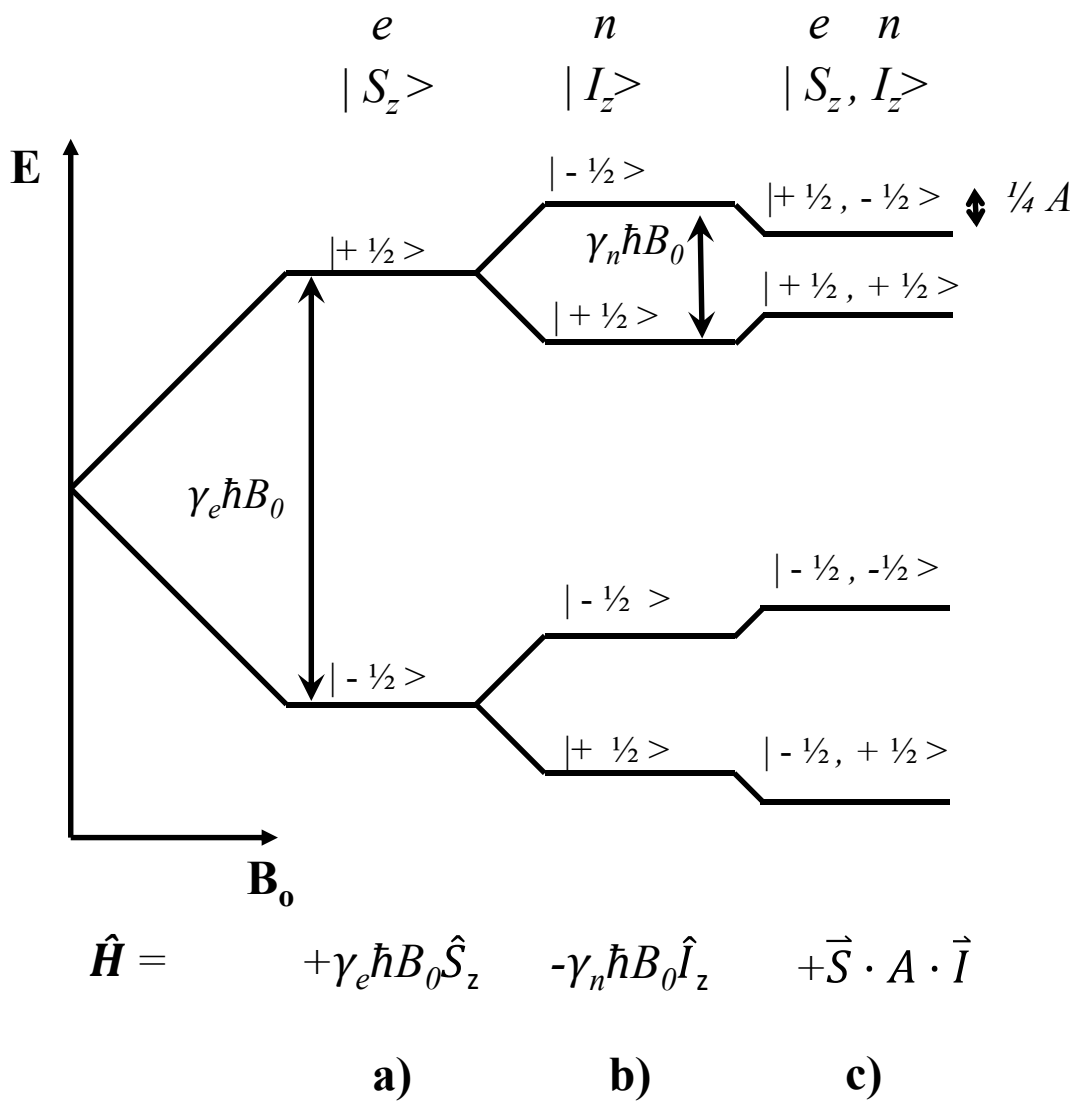

FIGURE 2.9: Zeeman energy splitting of a) electron spin, and b) nuclear spin c) with hyperfine interaction for a system of a spin-½ electron and a spin-½ nucleus.

splitting, they are subject to a strong Boltzmann distribution of populations. Such distributions, for example as shown in Figure 2.9a, can be expressed as (Chapter 1.4 [5]):

$$f\,|+\,1/2\,>=\,(1+\mathrm{e}^{\gamma_e \hbar B_0/\mathrm{kT}})^{-1} \qquad \textbf{(2.15)}$$

$$f\,|-\,1/2\,>=\,(1+\mathrm{e}^{-\gamma_e \hbar B_0/\mathrm{kT}})^{-1}$$

where $f\,|\,S_z>$ represents the Boltzmann population of the S_z state in Figure 2.9. These populations define the relative intensities of two resonances in an NMR spectrum that arise due to spin-spin coupling and could be attributed to both J and hyperfine coupling mechanisms. As the magnetogyric ratio of a nucleus is relatively small compared to that of an unpaired electron, the difference in occupancies of two resonances in a J-coupled doublet is usually neglected. The large magnetogyric ratio of the unpaired electron results in a greater Boltzmann separation in populations of states (equation 2.15). As a consequence, the doublet arising from the hyperfine interaction is asymmetric, reflecting their respective Boltzmann populations (Figure 2.10b).

In practice, splitting due to hyperfine coupling is never observed via NMR because of fast relaxation of electron spins. Such a process can be thought of as a rapid interconversion of | + ½ > and | - ½ > states of S_z in Figure 2.9. This relaxation process occurs in the nanosecond to picosecond time-scale in most paramagnetic systems, including those with transition metals [3, 17]. Thus the relaxation rate of electron spins far exceeds that of nuclear spins and it is generally greater than the hyperfine coupling. The effect of such relaxation on an NMR spectrum can be interpreted within Figure 2.9c, whereupon mixing of | + ½, - ½ > with | - ½, - ½ > states, and | + ½, + ½ > with | - ½, + ½ > states, the transitions located at + ½A and - ½A from the diamagnetic position become averaged. An observable hyperfine shift stems from a difference in population of these transitions as described by the Boltzmann distribution (equation 2.15) and

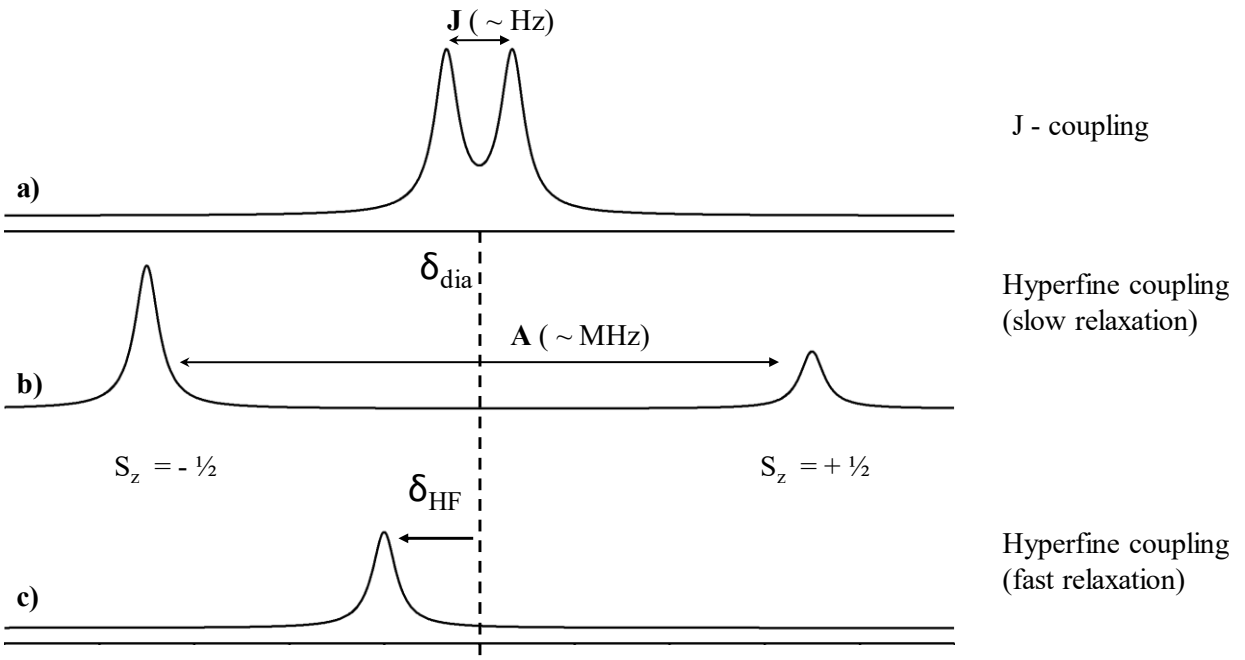

FIGURE 2.10: Theoretical NMR spectra of a) J-coupled system of two spins, b) hyperfine coupling according to Figure 2.9c) assuming slow electronic relaxation, and c) fast electronic relaxation.

depicted in Figure 2.10c. Thus, the observed center-of-gravity shift between unequally populated S_z states is not centered at the diamagnetic position and has a characteristic temperature dependence.

This center-of-gravity shift can be expressed as the weighted sum of the two extremes following the transition energy expression from Figure 2.9 and the Boltzmann factor from equation 2.15 for S = ½ [57]:

$$\delta_{HF} = \bar{\boldsymbol{A}}\bar{\mathbf{g}}\frac{\mu_B}{4\gamma_n kT} \tag{2.16}$$

This expression can be generalized for the S > 1/2 system, which has the following form [57]:

$$\delta_{HF} = \bar{\boldsymbol{A}}\bar{\mathbf{g}}\frac{\mu_B S(S+1)}{3\gamma_n kT} \quad \textbf{(2.17)}$$

Special attention will be devoted to the isotropic part of the hyperfine interaction, also known as the **Fermi** coupling. The expression for the Fermi shift can be readily deduced from equation 2.17 and has the following form:

$$\delta_{Fermi} = \mathrm{A}_{iso}\mathrm{g}_{iso}\frac{\mu_B S(S+1)}{3\gamma_n kT} \quad \textbf{(2.18)}$$

where A_{iso} is the isotropic value of the hyperfine tensor, $\bar{A}$. Another way to express this relation is through the molar magnetic susceptibility, χ_m. Susceptibility incorporates the effective magnetic moment, $\mu_{eff} = g_{iso}\sqrt{S(S+1)}$ and has the following general form [87]:

$$\chi_m = \frac{N_A \mu_0 \mu_B^2 \mu_{eff}^2}{3kT} \quad \textbf{(2.19)}$$

Substituting equation 2.19 into 2.18, the following relation for the Fermi shift is obtained [44]:

$$\delta_{Fermi} = \frac{\mathrm{A}_{iso}\chi_m}{N_A \mu_0 \gamma_n \gamma_e} \quad \textbf{(2.20)}$$

where χ_m incorporates the temperature dependence of the Boltzmann distribution of electronic states with any possible perturbations to the electronic environment, such as spin-orbit coupling, spin-spin coupling or zero-field splitting. Molar susceptibility can be determined experimentally using SQUID, Gouy balance or solution ^{1}H NMR measurements at a given temperature [88, 89]. A potential fundamental limitation of the first two techniques with regard to the interpretation of solid-state NMR shifts is its inability to reproduce the possible influence of the high magnetic field on the susceptibility of the sample, whereas a solution NMR experiment is not affected by possible effects of solid packing.

2.3.1 The origin of Fermi coupling

Fermi coupling is present where there is a finite probability density of an electron spin to tunnel into the nucleus. This concept of quantum tunneling originates from the particle/wave duality of elementary particles. In a system with a single unpaired electron residing in an *s*-type atomic orbital, the amount of spin density at the nucleus can be expressed with by following relation (derived by Fermi [90]):

$$A_{Fermi}^{max} = 4/3\gamma_n g_{iso}\mu_B|\Psi_s(0)|^2 \quad \textbf{(2.21)}$$

where $|\Psi_s(0)|^2$ represents the maximum possible value of the spin density at the nucleus where the Ψ_s orbital is singly occupied. As Fermi coupling occurs in the presence of unpaired spin density at the nucleus, the only atomic orbital that matches this criterion is the *s*-type orbital; all other orbitals with higher angular momentum (*p*, *d*, *f*, etc) have a probability density node at the nucleus. This is a good approximation for light elements where the size of the nucleus is small enough to be treated as negligible, which would forbid a partial overlap of the nucleus with higher-moment orbitals. However, for heavier elements, especially those that require a relativistic treatment of atomic orbitals near the nucleus (Z > 40), this mixing can occur and further complicate signal analysis [37, 91]. The most exact value for the maximum Fermi coupling is for the hydrogen atom (~1420 MHz), which was measured to five-decimal precision [92].

Molecular-orbital interactions provide pathways for electron-density distribution in which atomic orbitals share their unpaired electron density. Therefore, a more appropriate definition of Fermi coupling as observed in molecules follows the equation [5, 86]:

$$A_{Fermi} = 4/3\gamma_n g_{iso}\mu_B \sum |\Psi_S(0)|^2 \quad \textbf{(2.22)}$$

where the sum represents the net spin density at the nucleus. This summation can be replaced by the term $\rho_{\alpha\beta}(0)$, which signifies the net spin density at the nucleus. As unpaired electron spin can occupy two states of opposite sign, α and β, the net spin density is given by:

$$\rho_{\alpha\beta}(0) = \rho_{\alpha}(0) - \rho_{\beta}(0) \quad \textbf{(2.23)}$$

This means that molecular-orbital interactions and electronic configuration define the sign and magnitude of the spin density, and hence of the Fermi coupling. The observed Fermi shift can be expressed as a function of the spin density at the nucleus by combining equations 2.20 and 2.22:

$$\delta_{Fermi} = \frac{4}{3}\frac{\chi_m \rho_{\alpha\beta}(0)}{N_A} \quad \textbf{(2.24)}$$

From this relation, it is readily seen that the sign of the spin density dictates the direction of the resonance shift. Thus NMR is capable of providing a sensitive probe of both the electronic environment of the molecule (χ_m) and the specific nuclear site ($\rho_{\alpha\beta}$). A knowledge of molecular orbital interactions and electronic states can be used to estimate the sign and magnitude of the observed Fermi contact shift in NMR and provide the structural origin for the observed signal.

2.3.2 Key molecular-orbital interactions

Our understanding of the chemical properties of matter is based upon the knowledge of the atomic structure, where a nuclear core is surrounded by electrons in particular energy states with probability densities. This fundamental understanding can then be extended to molecules. Exact mathematical solutions for electron probability densities and interatomic interactions may be derived if all the information about the position and velocity of all elementary particles is available. Due to the wave/particle nature of electrons and the Heisenberg uncertainty principle,

the solution of the Schrödinger equation for a system with more than one electron is not possible, thus chemists are restricted to use the exact solution to the hydrogen atom as a model for electron probabilities [93].

The energy levels and probability densities of electrons in an atom are quantized, and in order to describe a particular atomic orbital, quantum numbers are used. The **principal quantum number** ($1 \leq n \leq \infty$) represents the size of the electronic orbital. The **angular-momentum quantum number** ($0 \leq l \leq n\text{-}1$) defines a number of orbitals as $2l + 1$ that have the same angular momentum. The **magnetic quantum number** ($-l \leq m_l \leq +l$) labels all possible variations in spatial density and orientation for orbitals of the same l number. The fourth number is the **spin quantum number**, m_s ($+ \frac{1}{2}$ or $- \frac{1}{2}$) that corresponds to the spin of the electron that occupies a particular orbital. This thesis will focus on complexes with 3rd row transition-metal centers; thus to a good approximation, only the first three angular-momentum quantum numbers will be considered, Figure 2.11.

Interactions between valence atomic orbitals may be represented by linear combinations of atomic orbitals (LCAO). This principle is the basis for molecular-orbital and valence-bond theories. For the purpose of describing interactions that lead to unpaired electron spin density at nuclei of the ligand, the principle of a **two-center molecular orbitals** will be used. In this model, only interactions between two atoms in a molecule are taken into account. This model will be propagated further through the molecule via the bonding-connectivity pattern to account for interactions between bonded atoms.

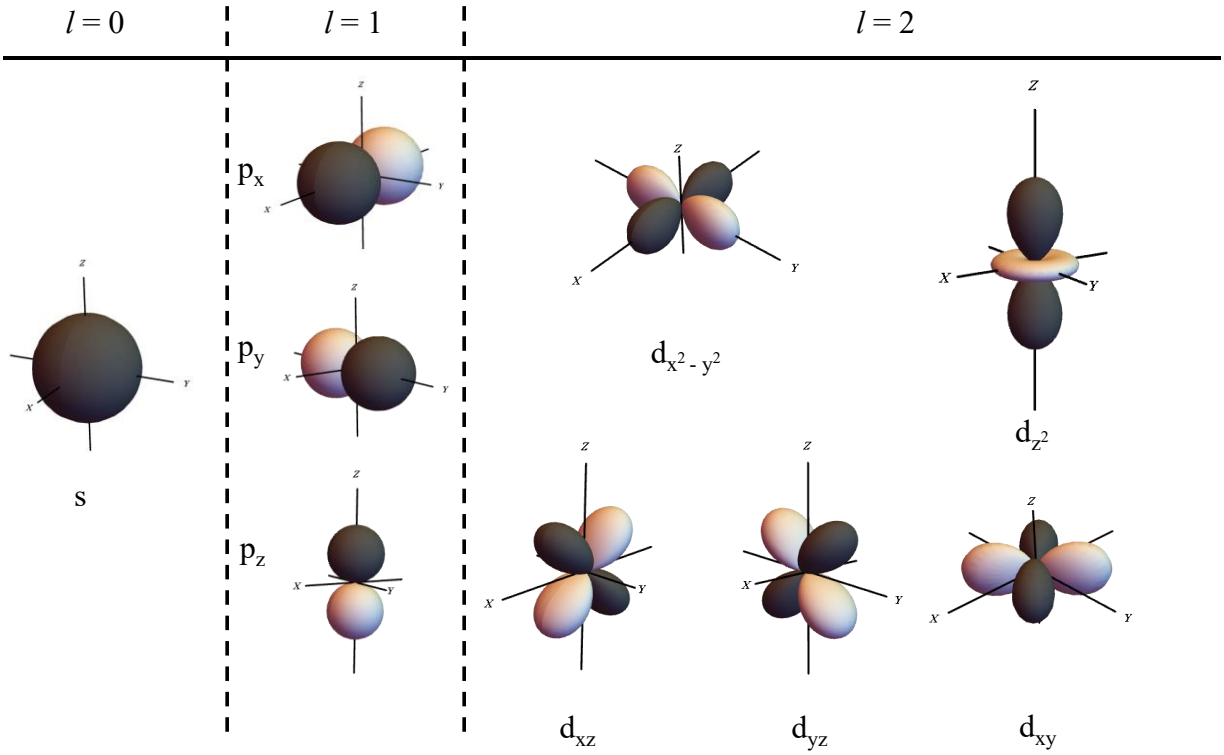

FIGURE 2.11: m_l orbitals that correspond to l = 0, 1 and 2. [94]

Interactions between two atomic orbitals can be constructive, destructive or symmetry forbidden. If the interaction is allowed by symmetry, then it is governed by the relative phases of the interacting orbitals and their symmetries, as illustrated in Figure 2.12 for the two-center

molecular-orbital approach. These interactions are important for understanding the distribution of unpaired electron density in the molecule, as they dictate which orbitals can serve as electron hosts through a **delocalization** process (Chapter 3.4 [5]). In Figure 2.12, a pair of interacting orbitals, either bonding or antibonding, can provide a pathway for delocalization of electron density between two atoms, provided that the host orbital is not fully occupied. In a stable molecule in its ground state, such free orbitals are usually high-energy antibonding orbitals, which have a characteristic shape due to their destructive interference (Figure 2.12).

The extent and orbital population of delocalized unpaired electron density can be explained by considering pairs of interacting atomic orbitals and extending the propagation of these interactions from the paramagnetic center to all ligand atoms. Figure 2.13 shows a simplified example of such a propagation for a system of two interacting orbitals. In this example, ψ_A contains a single unpaired electron and ψ_B has a pair of electrons. In the ground-state configuration, the resulting two-atom orbital contains a single electron in Ψ_{AB}* and paired electrons in Ψ_{AB}. The examples in Figure 2.13 shows possible scenarios for the relative energies of interacting atomic orbitals. The antibonding orbital Ψ_{AB}* hosts the unpaired electron, and thus its interactions will dictate further delocalization of the unpaired spin density. The proximity of energy levels determines the extent of orbital mixing and thus the shape and extent of electron delocalization. In Figure 2.13a, the energy of the ψ_A orbital is greater than that of the ψ_B orbital, and therefore most of the unpaired spin density will reside at the atom A. This case is common for coordination complexes with transition metals where the metal is atom A that interacts with the ligand atom B. As exact values of such energies are not experimentally accessible for large systems, computational simulation will be used to assess all molecular-orbital interactions and give the predicted Fermi-coupling constants.

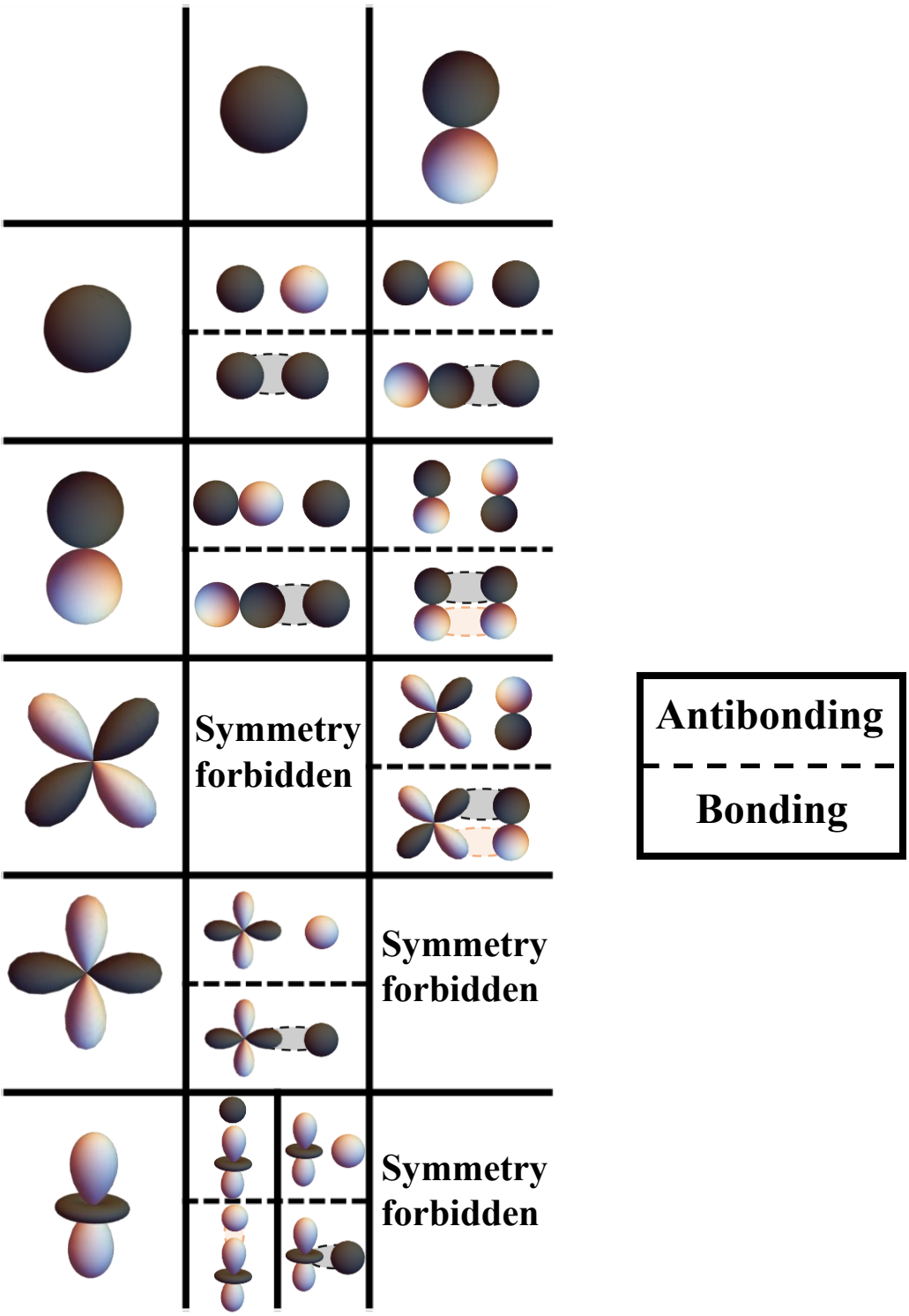

FIGURE 2.12: Two-center molecular-orbital interactions for a transition-metal coordination complex in octahedral coordination. Metal orbitals of *s*-, *p*- and *d*-symmetry are interacting with *s*- and *p*-orbitals of the ligand.

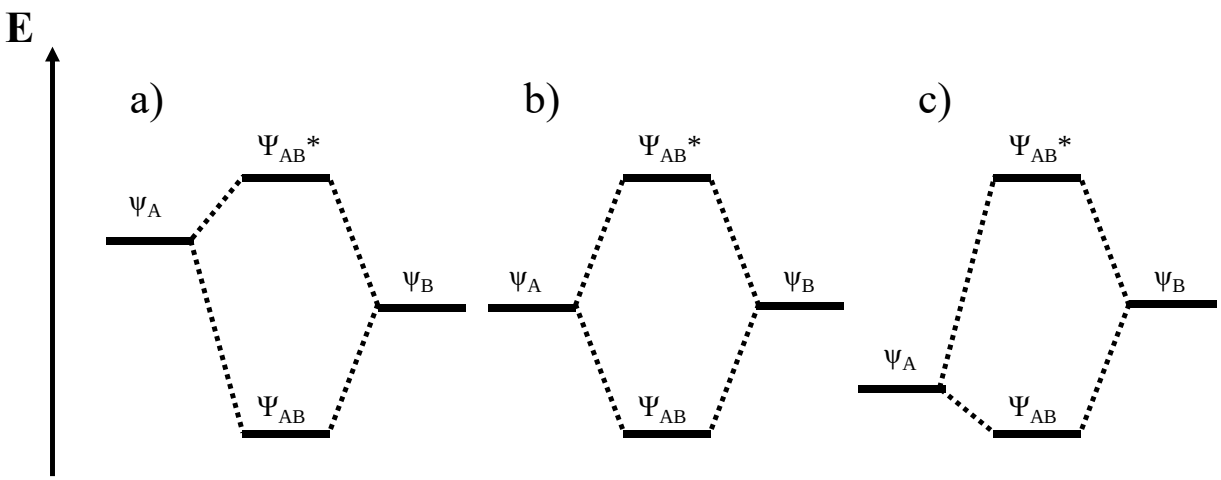

FIGURE 2.13: Two-center molecular-orbital energy diagrams with different relative energies of atomic orbitals: a) $E(\psi_A) > E(\psi_B)$; b) $E(\psi_A) = E(\psi_B)$; c) $E(\psi_A) < E(\psi_B)$.

Delocalization of spin density on its own does not account for the presence of net negative spin density ($\rho_{\alpha\beta} < 0$ in equation 2.23) as the paramagnetic center has a net positive spin density in the ground-state configuration under an applied magnetic field[5]. Regions of negative spin density in the electronic ground-state can arise from interactions of electron spins that occupy different orbitals via a mechanism involving **spin polarization** (Chapter 3.4 [5]). Figure 2.14 illustrates the polarization mechanism. In this example, a singly occupied orbital, $\Psi_{\uparrow}$, overlaps with a paired orbital, $\Psi_{\uparrow\downarrow}$, which results in a spatial separation of spins in a chemical bond. This interaction between like spins of overlapping orbitals stems from a favorable electron-exchange energy, which is the basis of Hund's rule for maximum multiplicity. The spin polarization described in Figure 2.14 results in nucleus A interacting with positive spin density, whereas nucleus B interacts with negative density.

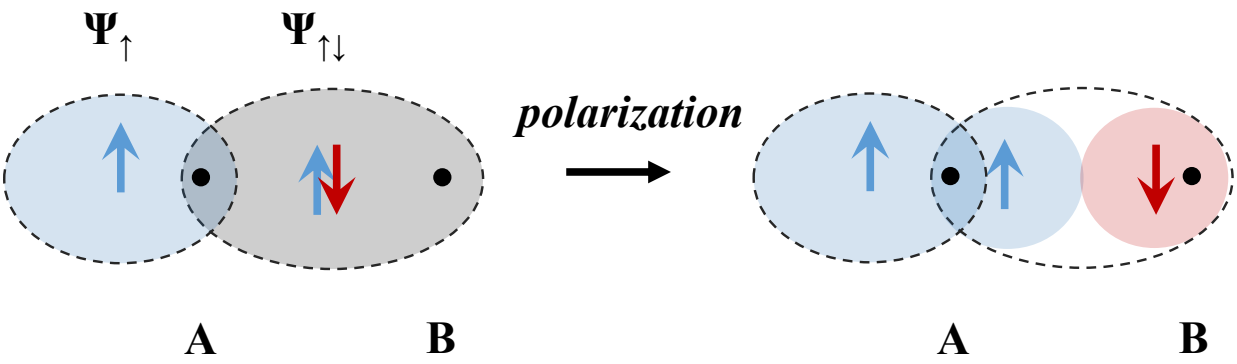

FIGURE 2.14: Polarization of a σ bond ($\Psi_{\uparrow\downarrow}$) with another orbital containing positive spin density ($\Psi_{\uparrow}$). Black dots indicate nuclear positions, arrows and colors indicate unpaired electron spins.

The spin delocalization and polarization mechanisms together form the complex pattern of unpaired electron-spin density distribution in paramagnetic complexes. These mechanisms can have either competing or cooperative contributions to the overall spin density at the nucleus. Whereas MO theory alone may not be sufficiently accurate to predict the absolute magnitudes of these interactions, it may be used to provide initial expectations on the direction of the Fermi shift. Computational software will provide more reliable information regarding the relative contributions of these mechanisms with regard to the model structure. More information regarding these quantum calculations is provided in the Materials and Methods section of the thesis.

2.4 Paramagnetic relaxation

2.4.1 Fermi coupling

The magnitude of Fermi coupling in NMR governs the frequency difference, which is proportional to the strength of electron-nuclear spin-spin interaction, Figure 2.9, which coalesce into a center-of-gravity resonance by fast electronic relaxation. This situation is conceptually identical to a model of fast motion, where the nuclear spin experiences multiple distinct environments with a fast rate of exchange. Thus, for the spin system in Figure 2.9c, the contribution to the nuclear spin-spin relaxation can be determined on the basis of this model as (Chapter 2.4 [5]):

$$\frac{1}{T_{2F}} = \frac{(A\pi)^2}{2T_{1e}} \tag{2.25}$$

where T_{1e} is the electronic spin – lattice relaxation time that determines the rate of exchange between spin states in Figure 2.9. Equation 2.25 is valid for a system with the total electron spin quantum number S = ½; however, it can be generalized to various spin states as follows (Chapter 2.4 [5]):

$$\frac{1}{T_{2F}} = \frac{4\pi^2 \mathrm{S}(\mathrm{S}+1)A^2}{3}\left(\tau_{1e} + \frac{\tau_{2e}}{1+\tau_{2e}^2(\omega_I - \omega_S)^2}\right) \tag{2.26}$$

where S(S+1) represents the averaged magnetic moment, ω_I and ω_S are nuclear and electron spin-resonance frequencies, respectively, and $\tau_{e1,2}$ are related to electronic relaxation as follows (Chapter 2.4 [5]):

$$\frac{1}{\tau_{1e}} = \frac{1}{T_{1e}} + \frac{1}{\tau_{e-ex}} + \frac{1}{\tau_{n-ex}} + \frac{1}{\tau_{int}} \tag{2.27}$$

$$\frac{1}{\tau_{2e}} = \frac{1}{T_{2e}} + \frac{1}{\tau_{e-ex}} + \frac{1}{\tau_{n-ex}} + \frac{1}{\tau_{int}} \tag{2.28}$$

where T_{1e} and T_{2e} are electronic spin-lattice and spin-spin relaxation times, respectively, $\tau_{e\text{-}ex}$ is the rate of electron exchange, $\tau_{n\text{-}ex}$ is the rate of nuclear site exchange, and τ_{int} is the rate of internal rearrangement. For a solid system with no (or slow) electronic coupling equations 2.27 and 2.28 can be further simplified. At low magnetic fields, it is reasonable to assume that $T_{1e} \approx T_{2e} = T_e$ [95]. As the electron Larmor frequency is much greater than that of the nucleus, equation 2.26 can be simplified to (Chapter 2.4 [5]):

$$\frac{1}{T_{2F}} = \frac{4\pi^2 S(S+1)A^2}{3}\left(T_e + \frac{T_e}{1+T_e^2{\omega_S}^2}\right) \quad \textbf{(2.29)}$$

From equation 2.29, it is clear that larger Fermi coupling will lead to a greater nuclear transverse-relaxation rate, thus broadening the signal. The same interaction is responsible for a Fermi shift; thus it is reasonable to expect signals with appreciable paramagnetic shifts to be systematically broader (Chapter 2.3 in [5]).

2.4.2 Electron – nuclear dipolar coupling

Another major paramagnetic relaxation mechanism of the nuclear spin includes the contribution from the direct dipolar coupling between the nucleus and the unpaired electron. The interaction between nuclear and electron spins follows the generalized equation according to the Solomon point-dipole model [8]:

$$\frac{1}{T_{2D}} = \frac{S(S+1)\gamma_I^2\mu_B^2 g_{iso}^2}{15r^6}\left(4\tau_{1c} + \frac{\tau_{2c}}{1+\tau_{2c}^2(\omega_I-\omega_S)^2} + \frac{3\tau_{1c}}{1+\tau_{1c}^2{\omega_I}^2} + \frac{6\tau_{2c}}{1+\tau_{2c}^2{\omega_S}^2} + \frac{6\,\tau_{2c}}{1+\tau_{2c}^2(\omega_I+\omega_S)^2}\right) \quad \textbf{(2.30)}$$

where r is the distance between electron and nuclear spins, which is conventionally taken as the distance between the paramagnetic center and the atom of interest. τ_{1c} and τ_{2c} are rate constants for the reorientation of electronic magnetic moments, which can be expressed as:

$$\frac{1}{\tau_{1c}} = \frac{1}{T_{1e}} + \frac{1}{\tau_{e-ex}} + \frac{1}{\tau_{n-ex}} + \frac{1}{\tau_r} \quad \textbf{(2.31)}$$

$$\frac{1}{\tau_{2c}} = \frac{1}{T_{2e}} + \frac{1}{\tau_{e-ex}} + \frac{1}{\tau_{n-ex}} + \frac{1}{\tau_r} \quad \textbf{(2.32)}$$

where τ_r is the rate of rotational motion between the coupling species. Equivalent arguments apply regarding the limitation of these correlation rates in a solid uncoupled system (see section 2.4.1) and relative resonance frequencies of electron and nuclear spins. A simplified form of 2.30 then becomes (Chapter 2.4 [5]):

$$\frac{1}{T_{2D}} = \frac{S(S+1)\gamma_I^2 \mu_B^2 g_{iso}^2}{15r^6}\left(7T_e + \frac{13T_e}{1 + T_e^2 {\omega_S}^2}\right) \quad \textbf{(2.33)}$$

This relation assumes a finite location for an unpaired electron at a certain distance r, which is a crude approximation as the electron is delocalized within molecular orbitals close to the paramagnetic center. The strength of such delocalization can be evaluated by measuring the Fermi shift in an NMR experiment. The point-dipole model fails at short distances to the paramagnet, below 7Å, due to failure to account for this delocalization [39]. My proposed modification to the point-dipole model attempts to account for this electron-spin delocalization onto the ligand and includes spin densities from nearby molecules in the solid structure. More detailed discussion is provided in Chapter 8.

2.5 NMR and EPR of paramagnetic molecules

Electron paramagnetic resonance (EPR) can provide the greatest level of detail on the electronic properties of a system. This method has identical theoretical and working principles as NMR spectroscopy; however, the major distinction is in the type of observed particles. EPR traces the information on the electronic environment via observable changes to the resonance frequency of the electron under an applied magnetic field. Both EPR and NMR take advantage of

paramagnetic particles, such as unpaired electrons and spin-active nuclei. NMR of paramagnetic molecules probes the same electron-nuclear interactions that influence EPR spectra, but from the point of view of a nucleus. Here I discuss some key features of EPR spectroscopy in relation to coupling with spin-active nuclei that can provide a better understanding of the interaction between these particles and its experimental manifestation between the two types of spectroscopy.

2.5.1 Measures of electronic environment

One of the most prominent differences between nuclear and electronic magnetic signals is the mechanism behind the change in resonance frequency under a magnetic field. The Zeeman-splitting Hamiltonian for the observed EPR has a similar form to that of the nuclear shielding (equation 2.7). Changes in local bonding, interactions between unpaired electrons, spin-orbit coupling and orbital-energy splittings all contribute to changes in the g_e of the unpaired electron and the observed resonance frequency (Chapter 5 [96]). Electronic interactions that change g_e can have anisotropic character and thus create an anisotropic g-tensor, which leads to orientational dependence of resonances on molecular axes with respect to the applied field. Such an interaction is analogous to the shielding anisotropy observed in NMR. However, unlike solid-state NMR, anisotropic EPR signals have dramatically greater magnitude, with g-tensor components spanning the range of approximately -2 to +10, whereas $g_e = 2.0023$. Such a spread of resonance signal is observed on a megahertz scale rather than kilohertz scale as in the case for nuclear resonance. An overall anisotropic powder pattern in EPR experiments is similar to the chemical shielding anisotropy in solid-state NMR (Figure 2.6) and thus results in familiar lineshapes but on a much greater frequency-scale. Because of such significant anisotropy, any attempts at signal averaging through MAS would fail, as current spinning rates cannot exceed

110 kHz. This MAS rate would be on the order of 1/10Ω of the typical electron signal span, and according to Figure 2.8 would not provide any noticeable signal-to-noise enhancement compared to a non-spinning experiment.

In NMR, each nucleus couples to electron spin via hyperfine coupling to produce a distinct shift that is directly linked to the unpaired spin density (equation 2.24). In contrast, in EPR the electron signal is affected by hyperfine couplings to all nuclei simultaneously. Each additional nuclear coupling introduces a new energy splitting (Figure 2.9c) and results in 2^n EPR lines where *n* is the number of coupled nuclei with spin ½ [5, 86]. Coupling occurs only with the spin-active nuclei, thus low abundant nuclei, such as ^{13}C, remain effectively invisible. In addition to the complexity of resolving all hyperfine interactions, these couplings bear no information on the sign of the spin density. Thus NMR is a unique technique for identification of hyperfine couplings that can be linked directly to structure and molecular-orbital interactions.

2.5.2 Experimental conditions for EPR and NMR

Magnetic field strengths in NMR and EPR instruments are significantly different. As the electronic magnetic signal is a few orders of magnitude greater than any nuclear magnetic signal, there is little justification for the application of high magnetic fields to improve the sensitivity. Typical magnetic field strengths in EPR experiments range from 0.3 to 1 T. If an interaction between unpaired electrons that is greater than the Zeeman splitting is present, it will not be observed, and thus a greater field may be required. In contrast, NMR benefits from high magnetic fields as they boost both resolution and much-needed sensitivity for low-resonance and/or low-abundant nuclei such as ^{13}C and ^{15}N. There are seldom perturbations to the nuclear

energy levels that exceed the Larmor energy splitting at conventionally used magnetic field strengths of 7 - 21 T.

EPR experiments are usually done at extremely low temperature to increase the relaxation times of electronic magnetization. This enhances signal resolution and provides additional signal sensitivity by maximizing the difference in Boltzmann populations between Zeeman energy states. There are cases where the electronic relaxation is sufficiently long, such as for long-lived excited states, organic radicals and highly ordered systems with few interaction pathways, where EPR can be done at higher temperature, including room-temperature conditions. In contrast, solid-state NMR is routinely done at room temperature, with the exception of cryo-NMR where experiments are done in the temperature range of liquid nitrogen. However, such experiments cannot benefit from fast MAS rates or sophisticated pulse sequences due to mechanical limitations of working at such low temperature.

2.5.3 Electron-spin relaxation

Electron-spin relaxation in EPR has the same significance as nuclear-spin relaxation in NMR. Both processes are described by Bloch equations using transverse, T_2, and longitudinal, T_1, parameters [96]. The width of the spectral line relates to T_2 according to equation 2.6, where a longer relaxation time is favorable as it leads to narrower signals on the frequency scale.

There are two main mechanisms responsible for electronic-spin relaxation. A **direct process** is a result of lattice vibrations, where the associated phonon energy is equal to the energy difference of the two states of the paramagnet between which an electronic transition occurs. Such a transition can have the change in spin states of $\Delta M_s = \pm 1, \pm 2\ldots$, which signifies flips of electron spin(s). An important consequence of such a process is the dependence of the

relaxation rate on the square of the applied field, meaning that at greater magnetic fields, the width of the EPR signal is expected to increase quadratically. Another well-known mechanism of electronic relaxation is the **Raman process**, in which a phonon is scattered inelastically, with the energy equal to the difference in energies of the two electronic states. This process has a more intricate dependence on the field and temperature [96]. Other effects that could change the electronic-relaxation time include electronic transitions, molecular motion and spin exchange.

The significance of electronic relaxation in paramagnetic NMR can be understood from a detailed analysis of nuclear-relaxation contributions from the Fermi-contact coupling and dipolar coupling as approximated by the point-dipole model (equations 2.26 and 2.30). These relations indicate that long electronic-relaxation times (T_{2e} and/or T_{1e}) increase the nuclear-relaxation rate, which would result in broader NMR lines, whereas the same electronic-relaxation times would produce narrow EPR spectra, as has been pointed out by Eaton [16]. Thus, mechanisms that reduce the electronic-relaxation time are valuable for paramagnetic NMR as these would improve both signal sensitivity and spectral resolution. As paramagnetic solid-state NMR is predominantly done near room temperature, certain mechanisms of electronic relaxation, such as direct and Raman processes, are already in effect. Further relaxation can occur if the paramagnetic complex possesses low-lying excited states which could be accessible through thermal and vibrational coupling [96].

Chapter 3: Materials and Methods

3.1 Samples

3.1.1 $Al(acac)_3$

A solution of $Al(NO_3)_3$ was prepared by dissolving 6.74 g of the solid in 200 ml of water. A 20% solution of NaOH was slowly added, with stirring, to initiate precipitation. The freshly made white solid was filtered and washed with water and transferred to another beaker. 10.8 ml of acetylacetone was added dropwise with stirring. The mixture was heated to 50°C for 15 minutes with stirring [63]. Product purity was confirmed with powder x-ray diffraction.

3.1.2 $Zn(acac)_2 \cdot 2H_2O$

A solution was prepared with 2 ml of acetylacetone and 0.8 g of NaOH in 10 ml of water. To this solution another solution (2.9 g of zinc sulfate heptahydrate in 10 ml of water) was added slowly with stirring. The resulting white precipitate was filtered and washed with water. The melting point was determined to be 138°C, which matches the literature value [97].

3.1.3 $Ti(acac)_3$

The sample was synthesized by Mr. Naser Rahimi from Dr. Budzelaar's group at the University of Manitoba. A 50-mL Schlenk tube was charged with 0.124 mL (1.214 mmol) of acetylacetone, 0.169 mL (1.214 mmol) trimethylamine, 15 mL of toluene, and a stirrer bar. The mixture was stirred for 3 h at room temperature. Solid $(THF)_3TiCl_3$ (0.150 g, 0.405 mmol) was added, the solution quickly turned dark violet, and the reaction mixture was stirred overnight.

The solution was passed through celite, and the solvent was removed under vacuum. The solid residue was dissolved in a few milliliters of toluene and separated with hexane. Crystallization at -35 °C gave dark violet crystals [59]. The structure was determined at 55°C with a single crystal XRD (details below).

3.1.4 $V(acac)_3$

The procedure was adapted from Dilli *et al.* [60] Reagent-grade oxovanadium (IV) sulfate trihydrate (1 gram) in 10 mL of warm water was added, with stirring, to a sodium dithionate water solution (2.5 grams in 10mL) to produce a dark-brown solution. Upon addition of 2.5 mL of acetylacetone solution with methanol (1:1 v/v, 15 mL) to the above mixture, a brown crystalline product formed. The solid was recovered, washed with water and dried under vacuum. Purity was confirmed by powder x-ray diffraction and the structure was found to be α-$V(acac)_3$. Additionally, the structure was refined at 55°C with single crystal XRD (details below).

3.1.5 $Mn(acac)_3$

The procedure was adapted from Manabendra *et al.* [98] 3.6 mL of acetylacetone was added, with stirring, to a solution of $MnCl_2 \cdot 4H_2O$ (0.9 grams) and sodium acetate (2.4 grams) in 35 mL of water. Then 0.2 grams of $KMnO_4$ in 9 mL of water were added slowly, with stirring. After the addition of a solution of 2.4 grams of sodium acetate in 9 mL of water, the mixture was heated for 10 minutes without boiling. The solution was then cooled and filtered to obtain the final product, which was then recrystallized under toluene and petroleum ether. The purity was confirmed with powder XRD and the phase was identified as δ-$Mn(acac)_3$ [66].

3.1.6 $Fe(acac)_3$

The synthesis was done as described by Fackler [67]. The procedure involved a mixture of 1 gram of $FeCl_3 \cdot 6H_2O$ with 1.5 mL of acetylacetone in 30 mL of water. Reaction proceeded rapidly with the formation of a bright red product, which was then filtered and dried under vacuum [67, 99]. The purity was confirmed by powder XRD.

3.1.7 $Co(acac)_2 \cdot 2H_2O$

The procedure was adapted from Ellern *et al.* [100]. A solution of 0.8 grams of NaOH in 7.5 mL of water was prepared and 2 mL of acetylacetone was added slowly with stirring. The solution was kept at 40°C. The resulting yellow solution was added dropwise to a mixture of 2.4 grams of cobalt (II) chloride hexahydrate in 12 mL of water. The resulting precipitate was extracted with vacuum filtration and washed with water. The solid was re-dissolved in a hot mixture of 20 mL of 95% ethanol and 13 mL of chloroform. After a short period of evaporation, the solution was cooled to induce precipitation and the final product was filtered and washed with 95% ethanol. The purity was confirmed by powder XRD.

3.1.8 $Cu(acac)_2$

The preparation of $Cu(acac)_2$ was described by Peacock [101]. The purity of the final product was confirmed by powder x-ray diffraction.

3.1.9 $VO(acac)_2$, $V(acac)_3$, $Cr(acac)_3$, $Mn(acac)_3$, $[Cu(Ac)_2H_2O]_2$, $Ni(acac)_2 \cdot 2H_2O$

The above complexes were purchased from Alpha Aesar and Sigma Aldrich at 97+% purity and used "as is", without any additional chemical processing, with the exception of $Mn(acac)_3$ which was only available as technical grade and used without any additional chemical processing. Powder x-ray diffraction was done on all complexes to assess purity. It identified the presence of exclusively β-$V(acac)_3$ phase in the commercial $V(acac)_3$ and a dominant γ-$Mn(acac)_3$ phase in the technical grade sample, along with impurities.

3.2 Powder X-ray diffraction

The sample purity and phase identity of all complexes were confirmed by powder x-ray diffraction, except $Ti(acac)_3$ due to its high reactivity in oxygen environment. Powdered samples were mounted on a diffraction plate. Data were collected on a Siemens D5000 powder diffractometer with Cu-*K*α radiation source. Experiments were done with the 2θ angle ranging from 5º to 50º degrees and a step size of 0.02º per s.

3.3 Single Crystal X-ray diffraction

Single crystal diffraction experiments were done by Dr. David Herbert at the University of Manitoba.

3.3.1 $Ti(acac)_3$

A black, multi-faceted crystal of suitable size (0.200 x 0.170 x 0.100 mm) and quality was selected from a representative sample of crystals of the same habit using an optical microscope and mounted onto a MiTiGen loop. X-ray data were obtained on a Bruker D8 QUEST ECO CMOS diffractometer (Mo sealed X-ray tube, K_α = 0.71073 Å) at 328 K. All diffractometer measurements, including data collection, integration and scaling were carried out using the Bruker APEX3 software suite [102]. An absorption correction was applied using SADABS [102]. The space group was determined on the basis of systematic absences and intensity statistics and the structure was solved by direct methods and refined by full-matrix least squares on F^2. The structure was solved in the monoclinic space group *P*21/*n* using XS [103] (incorporated in SHELXTL). No obvious missed symmetry was reported by PLATON [104]; despite finding all unit-cell angles close to 90°, no acceptable solution could be found in an orthorhombic space group. All non-hydrogen atoms were refined with anisotropic-displacement parameters. Hydrogen atoms were placed in idealized positions and refined using a riding model. The structure was refined to convergence (weighted least-squares refinement on F^2) and the final R_1 = 0.0399 ($I > 2\sigma(I)$, 4065 data) and wR_2 = 0.1174 (F^2, 65316 data points, 205 parameters).

3.3.2 $V(acac)_3$

A pale-orange, multi-faceted plate of suitable size (0.150 x 0.120 x 0.030 mm) and quality was selected from a representative sample of crystals of the same habit using an optical microscope and mounted onto a MiTiGen loop. X-ray data were obtained on a Bruker D8 QUEST ECO CMOS diffractometer (Mo sealed X-ray tube, K_α = 0.71073 Å) at 328 K. All diffractometer measurements, including data collection, integration and scaling were done using

the Bruker APEX3 software suite [102]. An absorption correction was applied using SADABS [102]. The space group was determined on the basis of systematic absences and intensity statistics and the structure was solved by direct methods and refined by full-matrix least squares on F^2. The structure was solved in the orthorhombic space group *Pbca* using XS [103] (incorporated in SHELXTL). No obvious missed symmetry was reported by PLATON [104]. All non-hydrogen atoms were refined with anisotropic-displacement parameters. Hydrogen atoms were placed in ideal positions and refined using a riding model. The structure was refined (weighted least-squares refinement on F^2) and converged to $R_1 = 0.0827$ ($I > 2\sigma(I)$, 3062 data points) and $wR_2 = 0.1561$ (F^2, 57830 data points, 205 parameters).

3.4 NMR methods

3.4.1 NMR Experimental conditions

Solid-state NMR experiments were done on a Bruker 500 (B_0 = 11.7 T) AVANCE III spectrometer. ^{13}C and ^{1}H MAS NMR spectra were collected with a 1.3 mm double-resonance MAS probe at a spinning rate of 60 kHz with an average sample size of 2 mg. Delays between pulses include both recycle delay and acquisition time; together they were on the order of a few milliseconds, at the limit of the probe duty cycle or 3 times the visible FID decay. ^{1}H and ^{13}C Hahn-Echo and $^{13}C\{^{1}H\}$ REDOR were done at 60 kHz MAS with matching 90˚ pulse lengths for ^{13}C and ^{1}H of 1.8 μs. The use of small NMR rotors is favorable for the study of paramagnetic complexes, as it minimizes the effect of anisotropic bulk magnetic susceptibility in addition to reducing the temperature gradient across the sample [105]. Paramagnetic resonance shifts are highly temperature-sensitive (see equation 2.18); therefore, it is necessary to do NMR experiments in a controlled environment. These experiments were acquired at a controlled

sample temperature of 55 ± 2 ˚C, unless specified otherwise. The temperature controller was calibrated using the ^{207}Pb chemical shift of the solid $Pb(NO_3)_2$ [106]. ^{13}C chemical shifts were referenced with the secondary standard, adamantane at 37.4 and 29.5 ppm; ^{1}H shifts were referenced with distilled water at room temperature at 4.75 ppm (Chapter 9.2 [1]).

Samples were packed in air except $Ti(acac)_3$, which is air sensitive. $Ti(acac)_3$ was loaded into a rotor in the inert atmosphere of a glove box. NMR spectra of $Ti(acac)_3$ were acquired shortly after the transfer of the sample rotor from the glove box to the spectrometer. The flow of dry nitrogen gas used to spin the sample is assumed to protect it from the oxygen-rich ambient environment.

3.4.2 Hahn-Echo experiment

A Hahn-Echo MAS NMR experiment is used preferentially in place of a simple single-pulse experiment, presented in Chapter 2.1, in order to reduce possible background irregularities that can obscure the signal from broad resonances. This experiment is also known to reduce the effect of field inhomogeneity, which would additionally broaden the isotropic signal [107, 108]. The schematic representation of the pulse sequence is presented in Figure 3.1. In a Hahn-Echo sequence, the initial excitation tips the magnetization into the x-y plane, after which the magnetization is allowed to lose coherence for a fixed period of time. This time period is synchronized with a single rotor period, $\tau_r = 1/\nu_{MAS}$. An inversion pulse is applied after the delay, which leads to refocusing of the coherence after an identical delay has passed. At this point, NMR acquisition starts, which eliminates the need for any major background phase processing as the acquired FID is an echo with the ideal starting point.

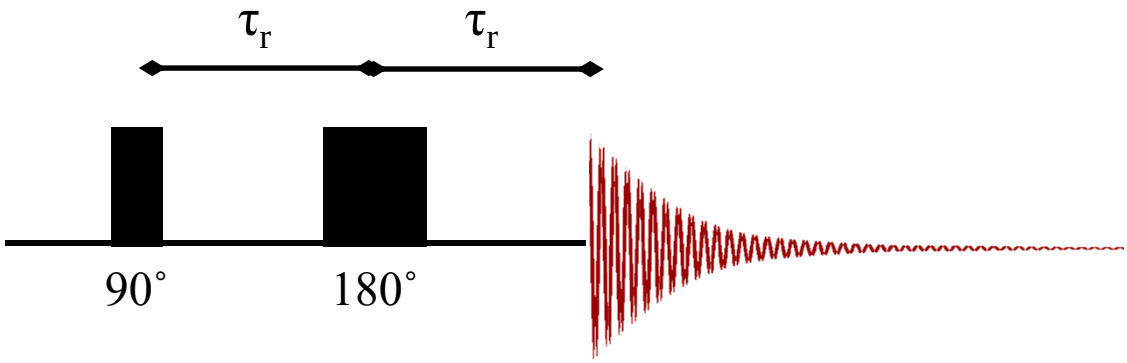

FIGURE 3.1: Schematic representation of the Hahn-Echo MAS pulse sequence [107].

3.4.3 Adiabatic Double-Echo experiment

The adiabatic double-echo pulse sequence is a valuable modification of the Hahn-Echo sequence that replaces hard inversion pulses with adiabatic inversion pulses capable of exciting a much greater frequency range [34]. This additional inversion excitation ensures that broad NMR spectra that span the range of up to 2000 ppm are observed with near-quantitative intensities. The effect of the pulse sequence on the magnetization is similar to that of the Hahn-Echo experiment seen in 3.4.2 with an additional refocusing block applied after the first inversion, Figure 3.2.

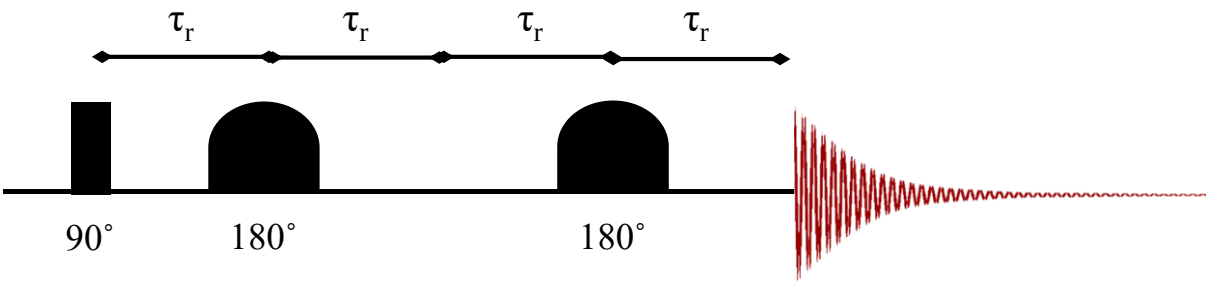

FIGURE 3.2: Schematic representation of the adiabatic double-echo MAS pulse sequence [34].

The adiabatic pulse in Figure 3.2 is created according to instructions provided by Kervern *et. al.* [34] where the pulse-excitation bandwidth for ^{13}C NMR was set to 1850 ppm for a spinning rate of 60 kHz, as was described in the publication [34].

3.4.4 $^{13}C\{^{1}H\}$ REDOR

$^{13}C\{^{1}H\}$ Rotational Echo Double Resonance (REDOR) is done with two separate experiments [109]. The first experiment serves as a standard to account for signal loss during the pulse sequence, and is equivalent to the rotor-synchronized ^{13}C Hahn-Echo sequence 3.4.2. The second experiment is done with an inversion pulse on the ^{1}H nucleus at an interval of half of the rotor period, as illustrated in Figure 3.3. This inversion pulse reintroduces the dipolar coupling between the two coupled nuclear spins that is otherwise partially averaged by MAS. The effect of the refocused dipolar coupling results in a characteristic decrease in signal intensity of the site closest to the coupled species. The most common application of these experiments is in the measurement of the distance between coupled nuclei. The distance is fitted to the relation of intensity modulation to the number of recoupling periods, which are denoted as **n** in Figure 3.3.

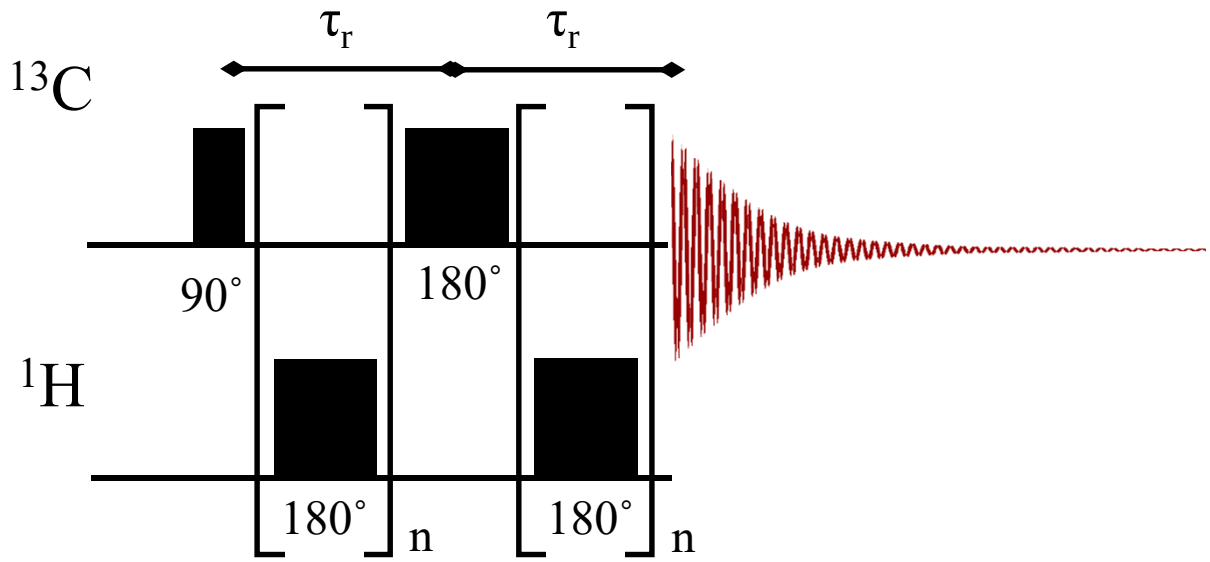

FIGURE 3.3: Schematic representation of the $^{13}C\{^{1}H\}$ REDOR pulse sequence.

In the current application, we keep n = 1 as we are only concerned with the distinction of the ^{13}C signal belonging to one of the three functional groups: methyl, methine or carbonyl. The signal from the carbonyl group is not expected to have dephasing upon ^{1}H recoupling as the carbon nucleus is far from any hydrogen atoms. The ^{13}C signal of the methine group is expected to lose intensity as the proton and carbon are directly bonded, and thus are in close proximity. The signal from the methyl group is also expected to lose intensity, but is a special case due to rotational motion. Despite there being three hydrogen atoms bound to the carbon, the signal reduction is smaller compared to the methine group. The single carbon-carbon bond of the methyl allows free rotational motion of the methyl group, which modulates the dipolar interaction between the three ^{1}H spins and the ^{13}C. The modulation is significant such that the signal reduction is actually smaller than that of the methine group, but still appreciable for a clear distinction from the carbonyl signal [33, 110].

3.4.5 $^{13}C\{^{1}H\}$ CP MAS NMR

Cross polarization (CP) is a common technique in NMR and is used to transfer magnetization between different types of nuclei, which boosts sensitivity of the least sensitive nucleus and permits heteronuclear correlation. Figure 3.4 shows the pulse sequence, where ^{13}C-channel pulses mimic that of a Hahn-Echo experiment, with the exception of the first pulse in CP being a **spin-lock** pulse. During this pulse, the ^{1}H channel is also irradiated with a continuous pulse that uses a ramped power level to achieve a coherent spin state between ^{13}C and ^{1}H nuclei. Coherence is best achieved through nearest-neighbor atoms, thus the hydrogen magnetization is transferred onto the bound carbon [111].

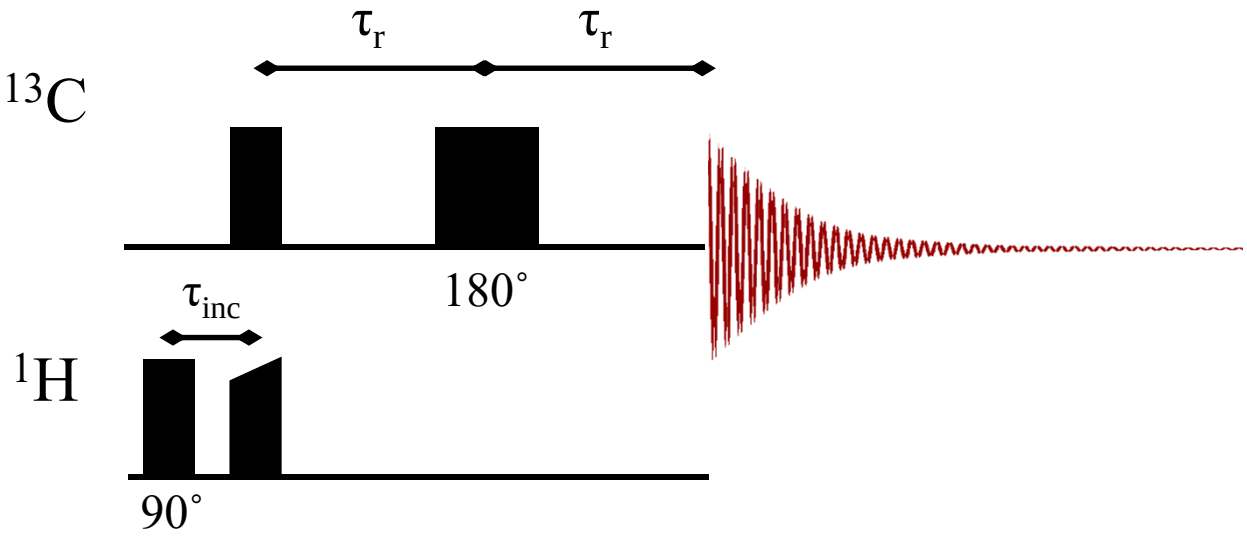

FIGURE 3.4: Schematic representation of the $^{13}C\{^{1}H\}$ CP MAS pulse sequence. τ_{inc} is the delay used for the second dimension in the ^{13}C-^{1}H 2D correlation experiment.

A two-dimensional version of this experiment is shown in Figure 3.4, where τ_{inc} is the delay that modulates the ^{1}H magnetization prior to mixing. This modulation produces a ^{13}C spectrum as a function of that magnetization, which appears as a correlated projection of a ^{1}H spectrum in the second dimension. The pulse sequence has been adapted from Ishii *et al.*[31]

2D $^{13}C\{^{1}H\}$ CP experiments were done at 9.4 and 11.7 T fields spinning at 14 kHz and 28 kHz, respectively. Experiments at 9.4 T were done with 4096 transients per slice, for a total of 64 slices, using a rotor-synchronized spectral width in the second dimension. The total delay between pulses was set to 30 ms. The experiment at 11.7 T was done with 16000 transients per slice with 96 slices in the second dimension, using the same waiting period of 30 ms.

3.5 Software

3.5.1 Gaussian 09

Quantum-chemical calculations of electronic properties were done using the commercially available software, Gaussian 09. This program is widely used by researchers focused on interactions of small-to-medium-scale molecules. Its availability made it an obvious choice to be used as the computational software for this work.

Energy calculations were done on all molecules in this study with a fixed basis set, def2TZVP, on the metal, and EPR-II on oxygen, carbon and hydrogen atoms. The def2TZVP basis set has proved capable of predicting the electronic configuration for 3^{rd} row transition metals [112, 113]. The EPR-II basis set is a modified version of the 6-31(d,p) basis set with an added set of contracted functions near the nuclear core in order to better approximate the spin density at the nucleus [114]. This modification makes this basis set theoretically more accurate at calculating the spin density at the nucleus. The model structures were taken directly from the crystal structures without any additional geometry optimization, so as to preserve the site degeneracy. A series of hybrid functionals were used with a variable degree of Hartree-Fock (HF) mixing. Results from all functionals used are consistent, and thus a functional mPW1PW91 was used throughout the thesis to illustrate the level of accuracy achievable by a single functional for multiple systems. This functional has been cited to be reliable in predicting metal-π charge transfer interactions [115, 116]. Calculations were done with unrestricted conditions to separate electrons of opposite spin into separate orbitals. This modification is important in achieving an accurate account of inter-orbital interactions with unpaired spin density [93]. All calculations showed negligible spin contamination, with $<S^2>$ value deviating by as much as 2%

in the worst cases. Natural population analysis (NPA) and natural bond order (NBO) calculations were done at the same level of theory. NPA summarizes the occupancy of individual atomic orbitals in the provided coordinate system [117]. The method of calculation uses the electron-spin density-distribution within the system, which is provided by the NBO calculation. The distribution of the spin density is visualized using an isosurface with a given value (usually $4 \cdot 10^{-4}$ e/au^3) and with a spin-density contour map. The map outlines the contours of multiple isosurfaces ($5 \cdot 10^{-5}$, $1 \cdot 10^{-4}$, $2 \cdot 10^{-4}$, $5 \cdot 10^{-4}$, $1 \cdot 10^{-3}$, $2 \cdot 10^{-3}$, $5 \cdot 10^{-3}$, $1 \cdot 10^{-2}$ e/au^3) and illustrates the changes in spin density in a chosen plane. The choice of the plane is important for a meaningful visualization of the spin density. The contour plane was selected to pass through carbonyl and methine carbons throughout the thesis, unless indicated otherwise.

3.5.2 Mathematica. SpinDynamica

Wolfram Mathematica [118] is a language environment used to process large amounts of data. “SpinDynamica” [119] was used within Mathematica to simulate the relaxation-induced decay of signal intensity during an NMR pulse sequence. An additional program, tentatively called “pNMRem” (paramagnetic NMR emulator), was written within the Mathematica language environment to automate the data readout from the Gaussian output file and produce a summary of calculated parameters [120]. The software reads in the Gaussian output file with the modeled structure in the .log format and allows modification of initial and calculated parameters as a part of the fitting process. The software strictly follows the equations presented in the theory section, Chapter 2. An additional capability of pNMRem is the ability to model the long-range dipolar contribution to the nuclear relaxation within a solid structure. To achieve this, two files are provided as inputs, the Gaussian output file with the NPA analysis in .log format, and the .pdb

file with a selected solid crystal space that represents the active space for modeling. The .pdb file can be readily generated using the Vesta software.

3.5.3 Vesta

Vesta is a visualization program for crystal structures [121]. The program is used to generate molecular structures from crystallographic .cif files that are then used for the computational calculation. Another application of the software in this work is to generate .pdb files with a large number of unit cells for modeling the dipolar interaction through pNMRem.

3.5.4 DMfit

DMFit is used to model frequency-domain NMR spectra and extract physical parameters from the lineshape [122]. Its iterative fitting capability makes this software an attractive choice for fitting spectra with multiple resolved sites. The software is used to fit NMR spectra in the thesis to obtain chemical shifts, isotropic signal widths and shielding.

Chapter 4:

Tris(2,4-pentanedionato)metal (d^1 – d^3)

This chapter will focus on NMR studies of d^n (n = 1-3) metal trisacetylacetonates with occupancies of "t_{2g}" orbitals. See sections 1.3.1 – 1.3.3.

4.1 Tris(2,4-pentanedionato)titanium(III), d^1

Crystalline $Ti(acac)_3$ is subject to a mild Jahn-Teller distortion associated with a d^1 system in an octahedral symmetry field, thus each atom experiences a unique local environment. The presence of a single electron between the three orbitals (d_{xy}, d_{xz} and d_{yz}) is expected to cause a Jahn-Teller distortion that breaks the symmetry of the oxygen coordination. According to the structure from the single crystal XRD measurement, Figure 4.1, the molecule contains two similarly distorted acetylacetonate ligands: O3, O4 (ligand 1) and O5, O6 (ligand 2), and a distinct ligand 3 with elongated Ti-O bonds, O1 and O2. This distinction is expected to be observed in both ^{13}C and ^{1}H NMR spectra as it points toward variations in local environment.

Solution ^{1}H NMR was done for $Ti(acac)_3$ that produced a single broad resonance [16]. The solid-state ^{13}C NMR spectrum of this complex can have up to 15 resonances and ^{1}H spectrum can have up to 21 resonances. The latter is not expected as methyl groups undergo fast rotational motion about the carbon-carbon σ-bond even in the solid state [123]; therefore, of the 18 methyl protons we expect at most 6 signals ,and, together with the signals from three methine groups, only up to 9 ^{1}H resonances should be expected.

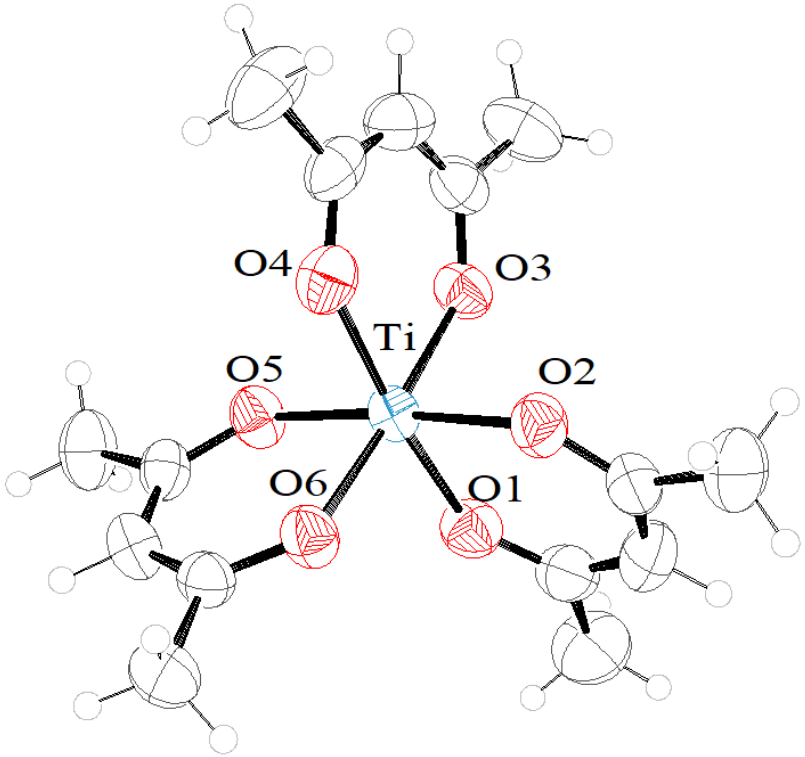

	Distance (Å)
Ti – O1	2.013(4)
Ti – O2	2.024(3)
Ti – O3	2.003(5)
Ti – O4	2.011(4)
Ti – O5	2.013(3)
Ti – O6	2.000(6)

FIGURE 4.1: ORTEP diagram of $Ti(acac)_3$ structure measured at 328 K and Ti - O bond lengths.

4.1.1 Molecular orbital formalism

Each oxygen of the acetylacetonate ligand chelates to the metal via σ-bonding, following the energy diagram according to the ligand field theory (Figure 4.2). The σ-bonding interaction between the oxygens and the metal in an octahedral field introduces the energy splitting of the metal *d*-orbitals into two distinct groups. This splitting is referred to as the **crystal-field splitting** (Figure 4.2). As the Ti^{3+} ion contains a single unpaired *d*-electron, that electron occupies the lower energy t_{2g} orbitals, which do not interact with the ligand orbitals due to their symmetry incompatibility (Figure 4.2). Oxygens chelating to the metal have two lone pairs of electrons in orbitals of *p* symmetry, where one is perpendicular to the plane of the ring and participates in the

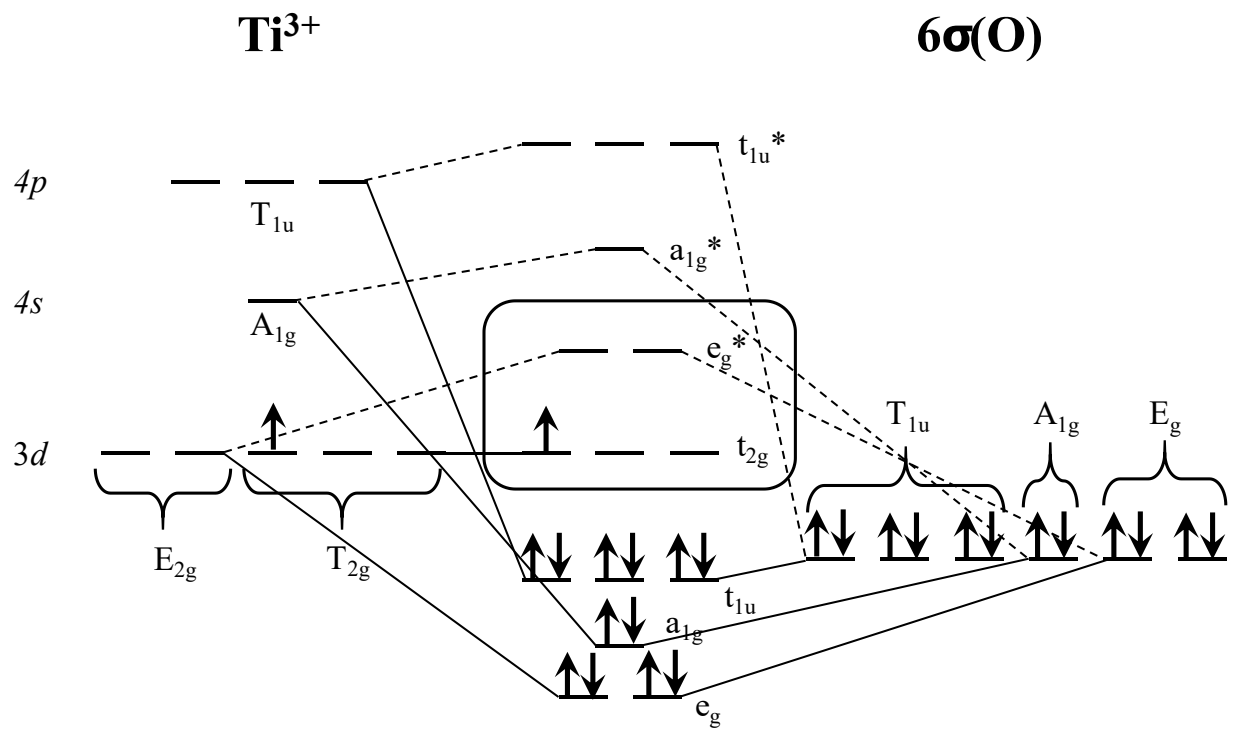

FIGURE 4.2: Ligand-field theory energy diagram for σ-bonded ligands coordinating to Ti^{3+} in an octahedral field. Encapsulated energy levels represent the crystal-field splitting.

pseudoaromatic bonding. The other lone pair occurs in the plane of the ring and completes the sp^2 hybridization of the oxygen orbitals. Both of these lone pairs have the correct symmetry for the $\pi(d - p)$ interaction with the metal. An illustration of one of the interacting metal *d*-orbitals with the oxygen *p*-orbitals is given in Figure 4.3. As all oxygen lone *p*-orbitals contain paired electrons, the only singly-occupied multi-atomic orbital has a characteristic anti-bonding character as shown in Figure 4.3. Within the two-center molecular-orbital formalism interactions between the metal *d*-orbital and the oxygen *p*-orbital are considered as π antibonding, or π*.

A unified axis reference frame in Figure 4.4a will be used throughout the thesis to provide a general framework for the description of molecular orbitals. The axis system is proposed such that each axis passes through the coordinated oxygen atom, which is labeled 1

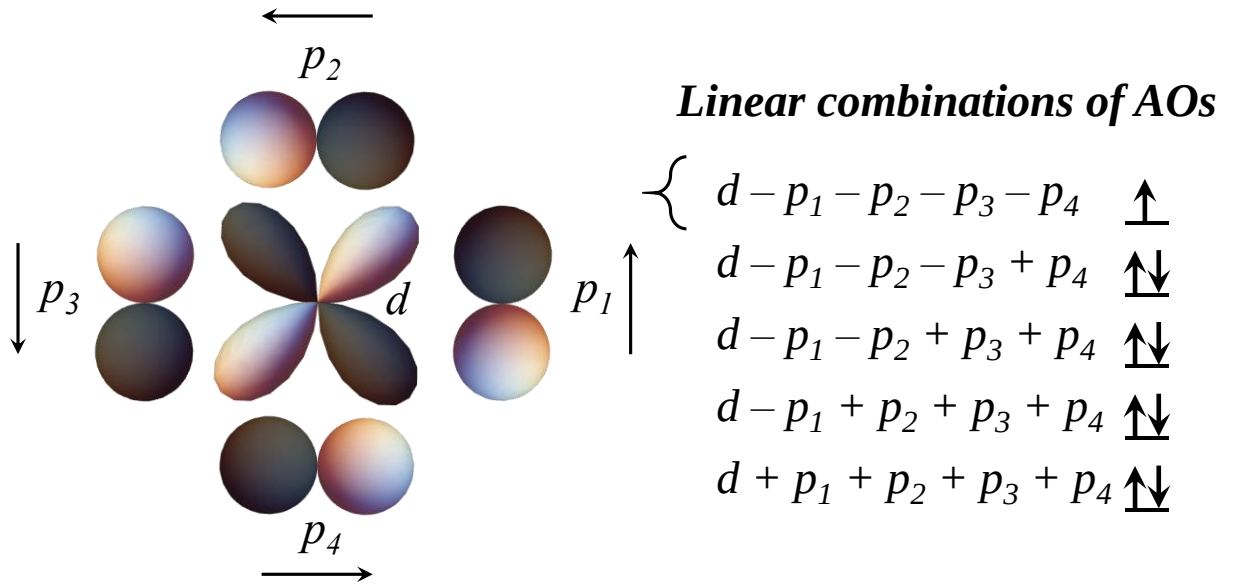

FIGURE 4.3: Linear combination of atomic orbitals with π-symmetry between one of the metal d_{xy}, d_{xz}, d_{yz} orbitals and the *p*-orbitals of ligands.

through 6 in Figure 4.4a. The coordination of oxygens around the metal is approximated as octahedral, where distinct distortions in metal-oxygen bond lengths point towards the presence of the mirror plane (Figure 4.4b). The axis normal to this pseudo-mirror plane is chosen as the z-axis of the molecule. These distortions can appear as the axial elongation and the equatorial compression or *vice versa*. As an example, $Ti(acac)_3$ in Figure 4.1 has the axial contraction within Ti - O3 and Ti - O6 bonds together with the equatorial elongation. This structure would be referred to as the Jahn-Teller compressed form. Individual oxygen atoms that coordinate to the metal have their own reference frames in Figure 4.4a, where the z-axis is fixed as normal to the plane of the ligand. This reference frame is chosen to preserve the identity of ligand p_z-orbitals as a part of the pseudoaromatic ring.

The highest-energy orbital interactions with π*-symmetry between metal (*d*)-oxygen (*p*) orbitals in an octahedral environment can be derived by analogy with Ballhausen's summary of the bonding π-interactions (page 158 in [124]). The author lists these as molecular-orbital

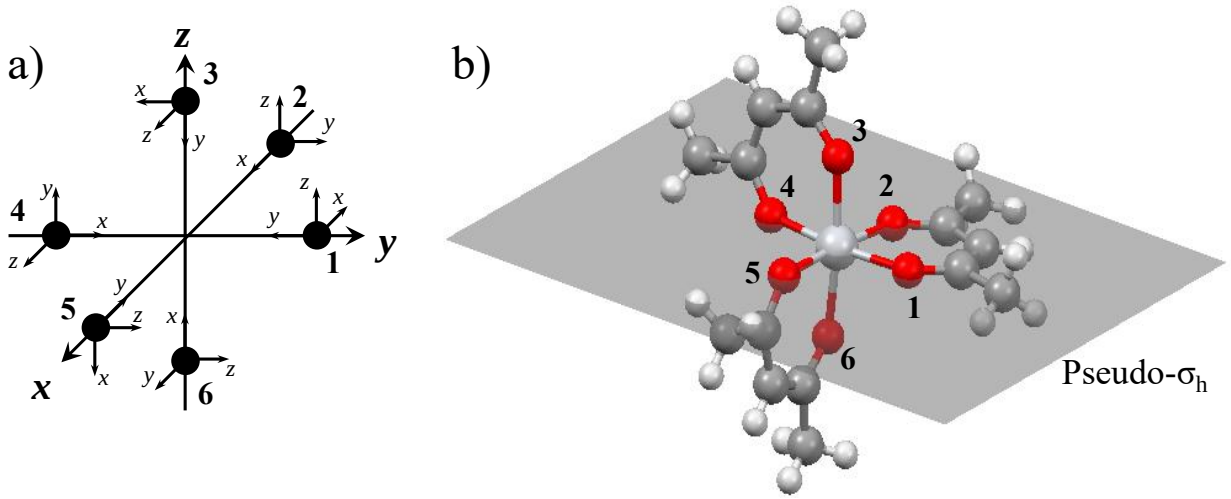

FIGURE 4.4: a) Reference-axis system for interpretation of MO diagrams, where z-axis of individual atoms is normal to the ligand plane; b) a molecule of $Ti(acac)_3$ in the reference system.

combinations with the t_{2g} band of metal orbitals. Table 4.1 provides a detailed summary of metal-oxygen interactions within the reference frame in Figure 4.4a, that include the delocalized unpaired-electron spin-density from metal t_{2g} as seen in Figure 4.3. The example in Figure 4.4b shows a possible arrangement of acetylacetonate groups, which determines the bonding nature of interacting *p*-oribtals. In this example according to Table 4.1, the d_{xy} orbital interacts with pseudoaromatic p_z-orbitals of oxygens 4 and 5 and with sp^2 hybrized *p*-orbitals of oxygens 1 and 2.

TABLE 4.1: $\pi^*(d - p)$ interactions in the octahedral field with the reference-axis system in Figure 4.4a.

t_{2g} orbital	Interacting oxygen *p*- orbitals
d_{xy}	½ (p_{x1} + p_{y2} + p_{z4} + p_{z5})
d_{xz}	½ (p_{z2} – p_{z3} + p_{x5} + p_{y6})
d_{yz}	½ (p_{z6} – p_{z1} + p_{x3} + p_{y4})

4.1.2 ^{13}C MAS NMR

The ^{13}C MAS NMR spectrum, Figure 4.5, of the crystalline compound features four main peaks, in addition to some small peaks indicating an impurity phase thought to be $TiO(acac)_2$ [59]. The peaks from the paramagnetic target compound are clearly shifted well outside the expected diamagnetic range defined by the diamagnetic compound (~20 - 200 ppm), reflecting significant contact coupling to unpaired spin density from the d^1 metal.

The three types of functional groups present in the ligand may be assigned to the groups of peaks according to DFT-calculation (see below): carbonyl carbon peaks between 620 – 780 ppm, methine carbon at -180 ppm, and methyl carbons at -300 ppm. Within each region, evidence of additional inequivalencies is seen in the multiplicity or asymmetry of peaks, reflecting the expected Jahn-Teller distortion. This is a result of the sensitivity of paramagnetic NMR, as the molecule contains two similarly distorted acetylacetonate ligands with Ti – O bond lengths of 2.011(4) Å, 2.003(5) Å (Ligand 1) and 2.013(3) Å and 2.000(6) Å (Ligand 2). The third ligand has larger bond distances of 2.013(4) Å, 2.024(3) Å (Ligand 3), Figure 4.1. This distinction in Fermi shifts between distorted ligands is also corroborated by the DFT calculations, Table 4.2. However, the spectral resolution does not permit a clear distinction of all 15 carbons present in $Ti(acac)_3$. The assignment of paramagnetically shifted peaks requires some degree of understanding of the MO and the unpaired spin density located near the nucleus of interest. For this, ab-initio or DFT calculations are used to create a map of the spin density and estimate the net spin density at the nuclear site.

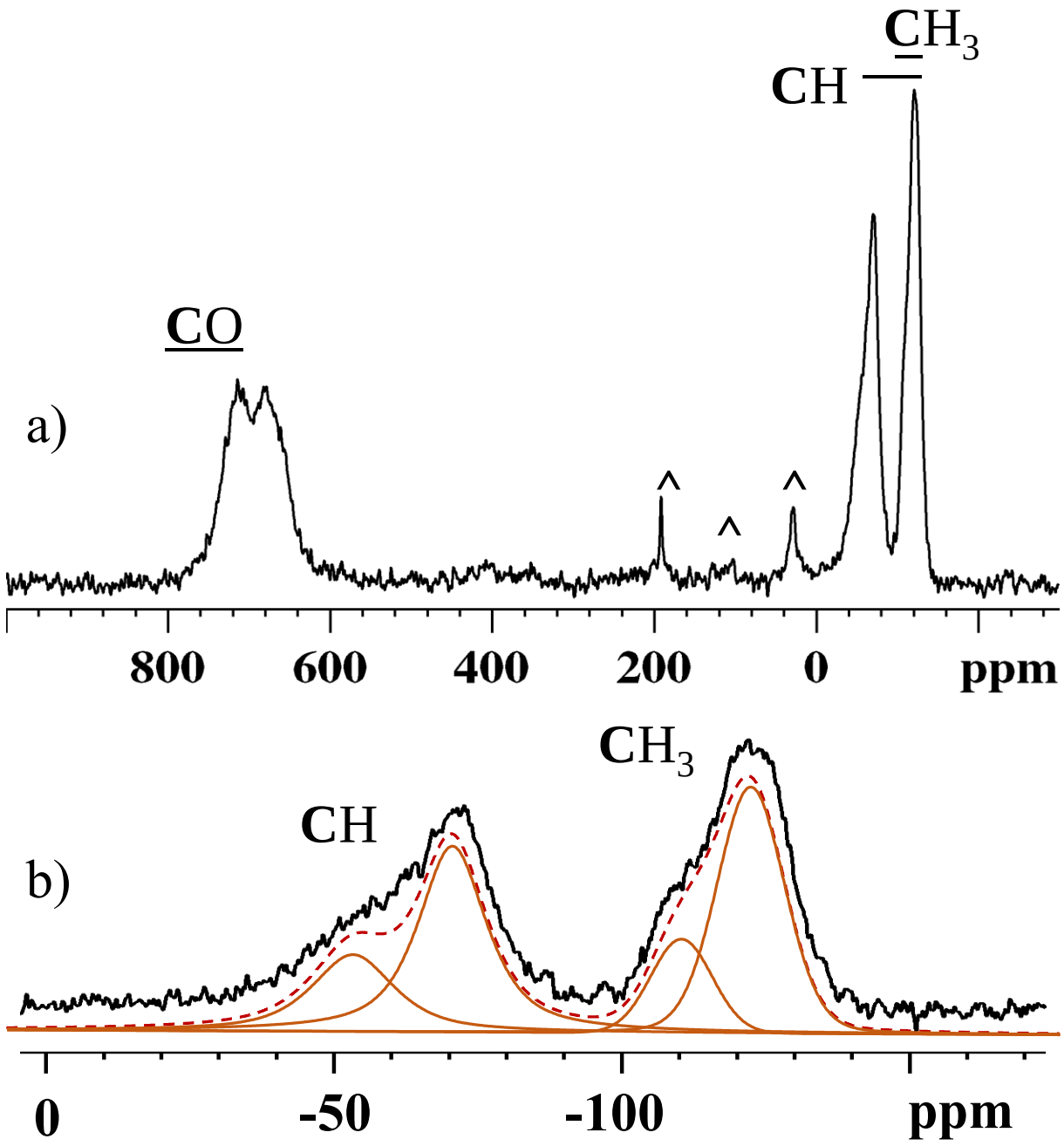

FIGURE 4.5: a) ^{13}C Hahn-Echo MAS NMR of $Ti(acac)_3$. Assignment of functional groups is based on DFT. "^" indicate a diamagnetic impurity thought to be $TiO(acac)_2$ [59]. Horizontal bars indicate calculated ranges for signal assignment. b) Signal fitting of CH_3 and CH groups in 2:1 ratio is depicted with solid lines. The dashed line presents the sum fit.

The distribution of the unpaired electron throughout the molecule is depicted in Figure 4.6a. There does seem to be an appreciable amount of spin-density propagation from the metal center to all three ligands of the molecule as evident from the spin-density isosurface. This surface encapsulates the net spin-density distribution, which is a sum of individual inter-orbital interactions. In order to study these interactions in detail, a slice of the spin density is taken along one of the ligands to form the contour plot in Figure 4.6b. The spin-density isosurface in Figure 4.6a shows that there is no significant difference in the spin-density distribution between the three acetylacetonate ligands, thus only one of the three ligands is presented for detailed analysis of the spin-density contour plot in Figure 4.6b.

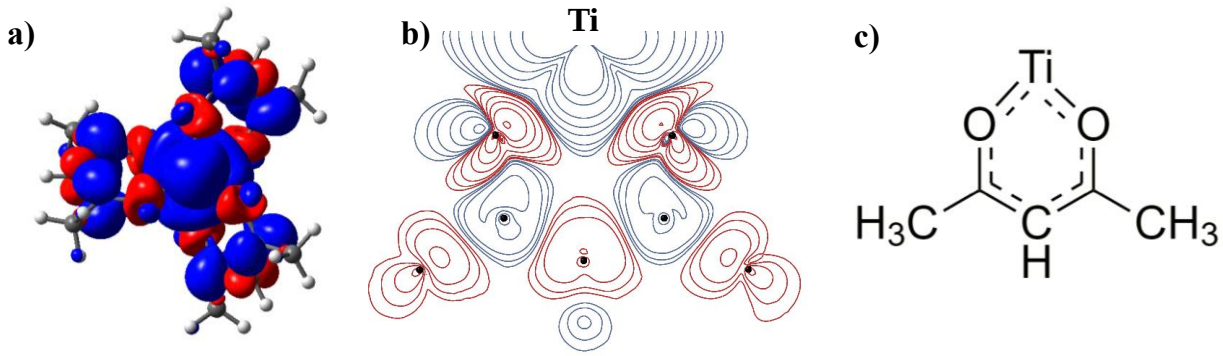

FIGURE 4.6: a) Spin-density distribution in $Ti(acac)_3$; spin-density isosurface, b) in-plane spin-density contour plot of one of the ligands, c) atomic labels of the contour plot. Blue regions represent positive spin-density, red are used for negative spin-density.

The spin-density distribution throughout the ligands originates from a favorable orbital symmetry of unpaired electrons at the titanium (III) metal with respect to the symmetry of the interacting ligand orbitals. The complex has a single unpaired electron in a pseudooctahedral field generated by six oxygen atoms surrounding the metal. Within the ground-state configuration the electron occupies the low-energy vacant d_{xy}, d_{yz} and d_{xz} orbitals. Thus, the

unpaired electron possesses the compatible symmetry for delocalization onto the ligand through $\pi^*(d - p)$ interactions according to Figure 4.3 and Table 4.1. As evident from the isosurface in Figure 4.6a, the unpaired-electron spin-density is distributed within the ligands with *p*-symmetry orbitals. This is an indication of the $\pi^*(d - p)$ overlap between the metal and the pseudoaromatic orbitals of the ligand. These are the lone-pair orbitals of oxygens marked as p_z on O1 and O2 in Figure 4.4, which interact with t_{2g}-type *d*-orbital according to Table 4.1. As pseudoaromatic *p*-orbitals are not hybridized with other orbitals of the same atom and they have a node at the nucleus, their effects on the Fermi coupling are minor.

The only mechanism by which the pseudoaromatic *p*-orbital can influence the Fermi spin-density of the host atom is through intra-atomic orbital polarization. Such a mechanism has been described by La Mar *et al.* (Chapter 5.1 [5]) and Bertini *et al.* (Chapter 2 [87]), where the orbital overlap between overlapping doubly-occupied *s*-orbital and a singly occupied *p*-orbital results in a spin-density polarization of the former. Thus the unpaired spin-density in the *p*-orbital forces the opposite sign of the Fermi spin-density on the same atom through the polarization of its doubly occupied *s*-orbital.

The spin-density contour-map in Figure 4.6b provides a cross-section of the acetylacetonate ligand and outlines contours of interacting orbitals in its plane. A detailed discussion of the contour map uses the ligand with O1 and O2 in the *xy*- plane of the reference frame in Figure 4.4. Figure 4.7a provides a detailed illustration of the interaction in the ligand plane between the hybridized oxygen *p*-orbital and the metal *d*-orbital. This is evident with the characteristic contour of the $\pi^*(d - p)$ symmetry, where the atomic orbitals are anti-bonding and possess the positive spin-density indicative of the delocalization mechanism. The in-plane oxygen *p*-orbital that participates in the π^* interaction with the metal is also a part of the oxygen

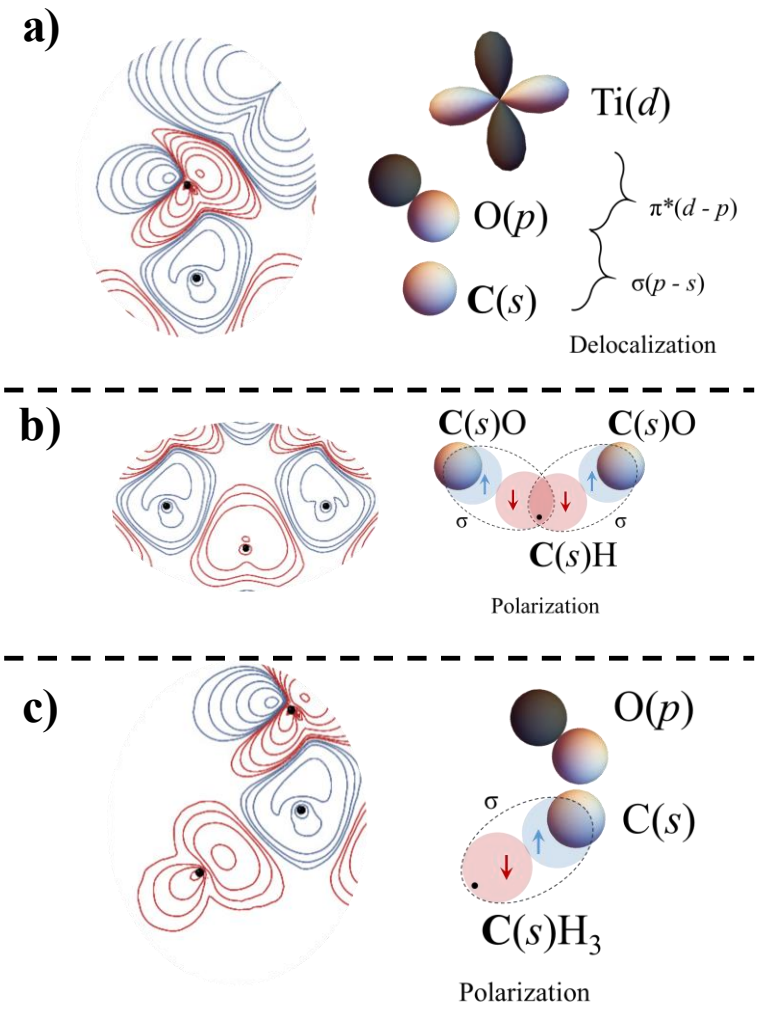

FIGURE 4.7: Spin-density contour-maps from Figure 4.6b showing the dominant contribution to the observed pattern. a) Spin density between the metal and the carbonyl group; b) spin density between carbonyls and a methine group; c) spin density between a carbonyl and a methyl group.

sp^2 hybridization. Thus the positive spin-density from this *p*-orbital is delocalized further onto the carbonyl carbon, where the spin density can be thought to occupy the high-energy vacant orbital of *s*-symmetry as evident from Figure 4.7a. The presence of positive spin-density at the carbonyl carbon nucleus is corraborated by the positive sign of the Fermi-coupling constant, which implies the presence of a positive spin-density at that ^{13}C site according to equation 2.21.

Tris(2,4-pentanedionato)metal (d^1 – d^3)

Another contribution to the positive spin density of the carbonyl carbon originates from the polarization of the metal-oxygen σ-bond, as seen in Figure 4.7a by the red contours at the oxygen atom. This net negative spin-density at the oxygen introduces spin-polarization of the carbonyl bond and adds positive spin-density at the carbonyl carbon.

The π*(*d* - *p*) interaction between oxygen atoms and the metal as well as the σ-bond polarization between them in Figure 4.7a and Table 4.1 has been deemed insignificant for spin-density transfer by Autschbach [57], where the idea of the ligand interaction exclusively with $d_{x^2-y^2}$ and d_{z^2} orbitals was used instead. The net spin-density contour outlines in Figure 4.7a the expected shape of the π* interaction of O(*p*) and Ti(*d*) with a characteristic polarization of the oxygen-metal σ-bond. I shall consider these mechanisms as primarily responsible for the spin-density distribution and will further focus on the delocalization pathway. As seen in Figure 4.7a, this delocalization extends to the carbonyl carbon via the oxygen *p*-orbital, making it the dominant contribution to the carbonyl Fermi shift and a probe of the electron density at the metal t_{2g} orbital in the plane of the ligand.

The access of the positive spin-density at the carbonyl carbon creates the condition for spin polarization of the carbon bonding orbitals in the presence of the overlap with that unpaired spin-density. According to Figure 2.14, this leads to a spacial separation of opposing electron spins within a doubly occupied bonding orbital and creates regions of negative spin-density at the other end of the carbonyl carbon bond. The effect of the spin polarization is expected to be present in all three bonds of the carbonyl carbon, and it is clearly visible in the bonding between carbonyl and methyl as well as carbonyl and methine groups, Figure 4.7b,c. The polarization of the carbon-oxygen bond is obscured by the overwhelming positive spin-density of the in-plane oxygen *p*-orbital; however, the effect of the polarization between oxygen and carbon can be

tracked with the spin density at the oxygen nucleus. The net positive polarization at the carbonyl carbon contributes negative Fermi spin-density to the oxygen. Additional polarization mechanisms that lead to the negative spin-density at the oxygen core include intra-atomic orbital interactions of O(*s*) with both O(*p*) orbitals that participate in π^*(*d*-*p*) interaction and the polarization of the σ bond between the metal and the oxygen, as shown in Figure 4.7a. DFT calculations indicate that all oxygen nuclei are dominated by the negative spin-density in agreement with our polarization-driven mechanisms.

The methyl ^{13}C signal is shifted to negative frequency from its diamagnetic position of around 27 ppm, which corresponds to the shift in the diamagnetic reference $Al(acac)_3$, Figure 4.5a. This negative Fermi shift is the result of the dominant spin-polarization mechanism that originates at the carbonyl group and affects the carbonyl-methyl σ bond. The methyl carbon is left with the net negative spin-density as a result of this inter-orbital interaction, Figure 4.7c. In addition to spin polarization, the unpaired electron-density on the carbonyl carbon is further delocalized through the ligand as it is present in a high-energy atomic orbital from the overlap of the in-plane O(*p*) orbital, Figure 4.7a. This electron density propagates further down the ligand through the high-energy anti-bonding C - C orbitals of σ* type. For the methyl group, this effect is minor and is dominated by the overall spin-polarization mechanism.

The ^{13}C signal of the methine group is shifted to negative frequency from the diamagnetic origin of around 101 ppm as found in $Al(acac)_3$, Figure 4.5a. This negative Fermi shift is even greater in magnitude than the shift of the methyl group. The dominant effect in this case is once again the spin polarization of the carbon-methine bond, Figure 4.7b; however, in this case, both carbonyl groups participate directly in polarizartion of the methine carbon. This polarization

from both sides of the group explains the greater negative contribution to the Fermi coupling of the methine carbon nucleus as compared to that of the methyl.

4.1.3 $^{13}C\{^1H\}$ REDOR

A $^{13}C\{^1H\}$ REDOR experiment was used to confirm the assignments of signals to functional groups, Figure 4.8. The signal at high frequency did not experience any loss upon recoupling of ^1H magnetization, therefore it is attributed to the carbonyl group. Resonances at negative shifts both experience a loss of signal intensity. The signal with the largest dephasing is assigned to the methine group, which leaves the signal at the lowest shift to the methyl group.

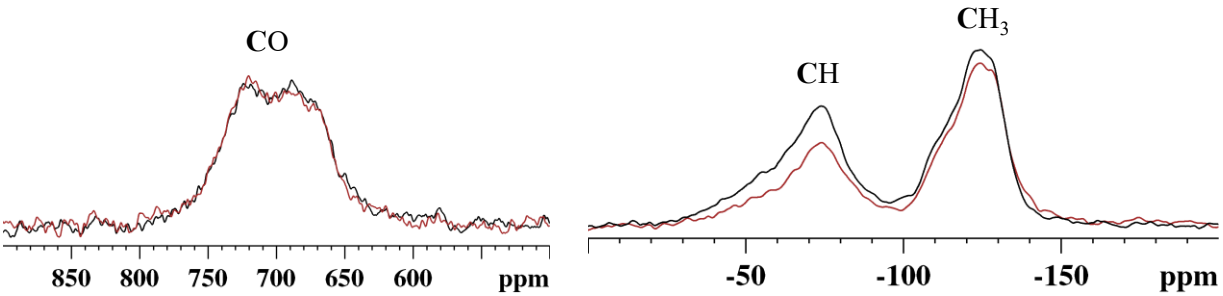

FIGURE 4.8: $^{13}C\{^1H\}$ REDOR MAS NMR of $Ti(acac)_3$. The black trace was acquired in the absence of dipolar recoupling, the red spectrum was acquired with dipolar recoupling.

4.1.4 ^1H MAS NMR

NMR can provide multiple approaches to probe the spin-density distribution in the system via signals from different types of nuclei. Figure 4.9 shows the ^1H MAS NMR spectrum of the paramagnetic titanium complex. Signals occur well outside the typical diamagnetic signal range of ^1H NMR (0 - 12 ppm), and the signal widths also appear broadened by paramagnetic and nuclear-dipolar interactions. The assignment of resonances is based on intensity and confirmed by DFT calculations (Table 4.2). The signals at the higher-frequency range of 50 – 60

ppm are attributed to methyl groups, whereas the two distinct low-intensity peaks in the lower frequency of 29 – 36 ppm represent the three methine groups.

Unlike the methyl groups, signals from the methine protons are not affected by averaging rotational motion and thus retain information about the rigid part of the molecule. As we have seen previously in ^{13}C NMR (Figure 4.5b), there is a subtle loss of degeneracy among the methine signal that splits the ^{13}C resonance in a 2:1 ratio. This variation in local environment of the methine groups is also observed in ^{1}H MAS NMR (Figure 4.9). The methine resonances appear well resolved at 35 and 30 ppm and retain the 2:1 intensity ratio (Table 4.2). ^{1}H NMR also indicates that the resonance at 35 ppm is composed of two signals with similar shifts, reflecting the fact that the three functional groups are not equivalent, as indicated by the crystal

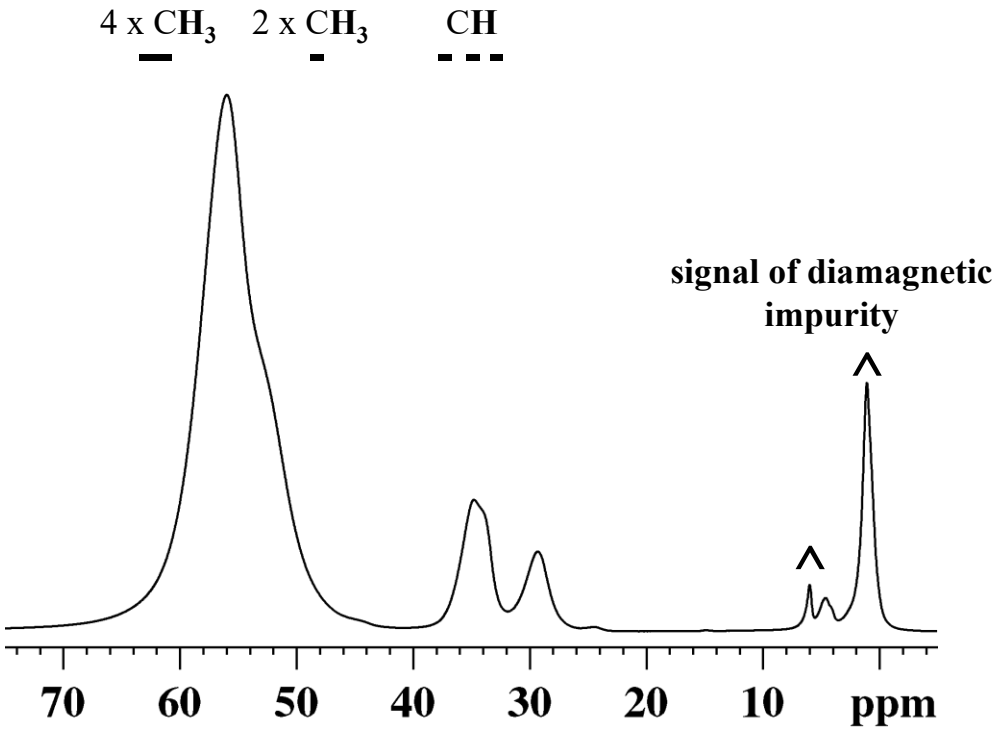

FIGURE 4.9: ^{1}H Hahn-Echo MAS NMR of $Ti(acac)_3$. Proposed signal positions are listed according to DFT calculation, where the expected signal regions are indicated.

structure. The positive Fermi-coupling constants of the methine groups can be attributed to the polarization of the methine CH bond as indicated in Figure 4.6b, where it must be opposite to that of the carbon polarization. An additional contribution arises from the occupancy of the

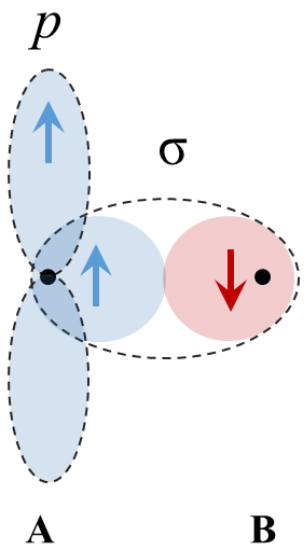

FIGURE 4.10: Polarization of the AB bond with unpaired electron in *p*-orbital of atom A.

methine p_z-orbital, perpendicular to the CH bond according to La Mar (Chapter 5.1 [5]), Figure 4.10. The driving force behind this effect is partial overlap of the p_z-orbital with the σ(CH) bond. The overlap causes polarization of the spin density of the latter. An empirical relation [5, 87] suggests that the spin density of the p_z-orbital on the carbon has proportionally opposite contribution to the hydrogen of the methine. In Figure 4.6a p_z-orbitals are occupied by the net negative spin-density, thus the contribution to the methine Fermi coupling and shift is positive. These orbital interactions, together with the electron delocalization, all contribute to the observed net positive-spin density of the methine hydrogen.

Calculated signal positions of methyl hydrogens have been averaged to simulate the fast rotational motion. Thus each of the methyl groups displays resonances with averaged hyperfine

interaction. The mechanism behind each of the individual hydrogen couplings within the group has been discussed in detail by Underwood and summarized by Luchinat [87, 125]. Where the methyl group is bonded to the sp^2 carbon, the p_z-orbital overlaps with the *s*-orbital of the hydrogen and thus causes a spin-density transfer via delocalization. Bertini *et al.* [87] provide an empirical expression for the magnitude of the coupling in relation to the torsion angle between the p_z-C-C and C-C-H planes. Thus in Figure 4.6a, the positive spin-density of the p_z-orbital of the carbonyl carbon extends onto the hydrogen atom of the methyl group if the CH bond is parallel to the orbital. Rapid rotation of the methyl group results in an averaged coupling between the hydrogen and p_z-orbitals over all torsion angles. Therefore, signals from three individual hydrogens of the methyl group become averaged and the atoms reach magnetic equivalency through the rapid exchange of environments.

4.1.5 Summary of computational assignments

Computational assignments rely on knowledge of the sample magnetic moment according to equation 2.22. EPR measurements have provided important information on the electronic environment of this paramagnetic titanium complex [59]. Among the most valuable parameters is the g-tensor. Unfortunately the experiment was done on a frozen solution of $Ti(acac)_3$ in CH_2Cl_2 at 77 K, which gave a broad featureless resonance with an isotropic g-value of 1.954 [59]. There is no published record of the g-value near room temperature. However, the value at low temperature does not differ significantly from the free electron g-value of 2.0023, which will be used as an approximation for the evaluation of Fermi contact shifts. This result implies the presence of a relatively low contribution of spin-orbit coupling in Ti^{3+}. Thus, with greater sample temperature, the electronic occupancy would bring the g-value closer to the free value through the Boltzmann factor [15].

TABLE 4.2: ^{13}C and ^{1}H NMR of $Ti(acac)_3$ and DFT calculation. Calculated and experimental shifts are in ppm at a sample temperature of 55 ˚C are presented along with the calculated Fermi coupling. ^{1}H and ^{13}C NMR shifts from the same functional groups are indicated and appear in the order listed.

Group [ligand]	^{13}C		^{1}H	
	A_{calc} (MHz) {A_{exp}}	δ_{calc} [a] {δ_{exp}}	A_{calc} (MHz) {A_{exp} [b]}	δ_{calc} [a] {δ_{exp}}
CO [2] CO [3] CO [1] CO [3] CO [1]	6.71, 6.22 5.98 {5.5(1)} 5.91, 5.72 5.59 {5.0(1)}	834, 787 764 {713(6)} 757,739 726 {680(6)}		
CH [3]	-1.73 {-1.63(5)}	-65 {-55(1)}	1.19 {0.99(3)}	34 {29(1)}
CH [2] CH [1]	-2.51 -2.73 {-1.81(5)}	-140 -160 {-71(2)}	1.24 {1.20(3)} 1.34 {1.24(3)}	35 {34(1)} 38 {35(1)}
CH_3 [3]	-1.36, -1.40 {-1.44(5)}	-103, -106 {-111(2)}	(1.90, 0.22, 3.68) {2.08, 0.23, 4.04} (3.93, 0.35, 1.50) {4.32, 0.39, 1.65}	48, 48 {53(1)}
CH_3 [1] CH_3 [2]	-1.60, -1.67 -1.67, -1.71 {-1.57(5)}	-125, -132 -132, -136 {-122(2)}	(3.84, -0.11, 3.57) {3.54, -0.10, 3.30} (0.79, 1.91, 4.74) {0.72, 1.73, 4.29} (2.81, 0.18, 4.63) {2.49, 0.16, 4.10} (2.98, 0.10, 4.53) {2.64, 0.09, 4.01}	61, 62 63, 63 {56(1)}

a) Shifts were calculated according to equation 2.18.

b) Couplings from individual hydrogens from the same methyl group are scaled to match the average experimental shift.

The diamagnetic reference shift for each of the functional groups in $Ti(acac)_3$ has been adopted from the $Al(acac)_3$ complex as these structures have similar local environments for each of the functional groups.

Table 4.2 provides numerical values for calculated and experimental ^{13}C and ^{1}H NMR shifts in $Ti(acac)_3$. The overall quality of signal assignment is satisfactory for a general assignment of functional-group regions as seen previously in Figures 4.5 and 4.9. The detailed crystallographic assignment of individual resolved resonances still suffers from the quality of the modeling. As an example, the ^{13}C signal of the carbonyl group has two distinct signals of equal intensity; however the calculation indicates that both signals should be asymmetric, Table 4.2. However, the quality of the calculation is sufficient to predict the distinct CH and CH_3 groups in both ^{13}C and ^{1}H spectra with a sufficient level of accuracy, Figures 4.5 and 4.9, Table 4.2.

4.1.6 Effect of structural variation with temperature on Fermi coupling

Another common method of structural assignment in paramagnetic NMR is the use of variable-temperature experiments and subsequent estimation of the diamagnetic shift through extrapolation to infinite temperature [37]. This method ignores the possibility of the change in hyperfine coupling constant with temperature through small changes in chemical bonding. As an example, the computational results in Figure 4.5 are produced using a crystal structure of $Ti(acac)_3$ that was determined at 55ºC in order to closely match the experimental condition of MAS NMR. There is [29] another closely related crystal structure of this complex at -173 ºC, which captures the thermal variation of mean atomic positions with respect to the structure at 55 ºC. The difference in the computed hyperfine coupling for the two structures is not uniform for every crystallographic site. Figure 4.11 presents a computed change in the Fermi coupling for

each crystallographic site that occurs on cooling the solid from 55 ºC to -173 ºC. The Fermi coupling between the two temperatures can vary as little as a fraction of a percent or as much as

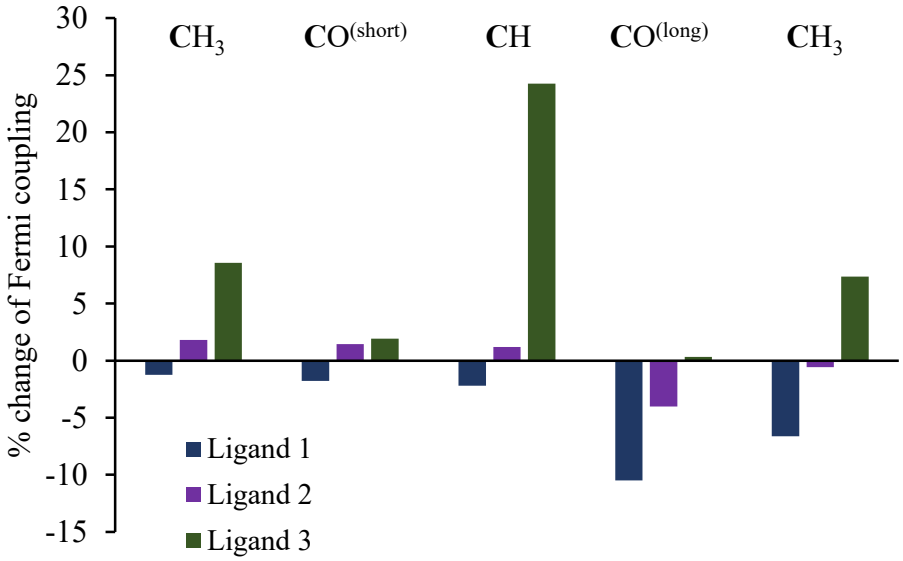

FIGURE 4.11: Change in computed ^{13}C Fermi coupling constants between the -173 ºC and 55 ºC structures of $Ti(acac)_3$. The change is calculated as $(A^{-173\ ºC} – A^{55\ ºC})/A^{55\ ºC}$

25% of the coupling without complete structural rearrangement or a change in packing. The structure at lower temperature displays an anisotropic variation to the spin density, where ligand 3 experiences an overall greater positive spin-density contribution and ligands 1 and 2 experience minor negative and neutral contributions. These variations in the Fermi coupling influence the temperature dependence of the resonance shift according to equation 2.19, which can lead to erroneous extrapolation of the diamagnetic position at the limit of infinite temperature and cause misassignment.

4.2 Tris(2,4-pentanedionato)vanadium(III), d^2

Among multiple reported crystal-structures of $V(acac)_3$, there are two distinct packing arrangements [29]. In each case, individual molecules do not have high molecular symmetry and therefore, as in the case of $Ti(acac)_3$, all 15 ^{13}C resonances and 9 ^{1}H resonances are expected to have distinct local environments and different NMR shifts.

Both forms of $V(acac)_3$ have a unique structural distortion that separates the three ligands into two groups. Detailed structural examination shows the presence of two ligands with common V-O bond lengths that differ from the third ligand. α-$V(acac)_3$ has two ligands with one short V-O bonds of 1.970(4) Å as compared to the remaining bonds of 1.983(4) Å. In β-$V(acac)_3$, one bond is elongated of to 2.001(6) Å compared to 1.981(6) Å for the remaining bonds. The two similar ligands are labeled 1 and 2, whereas the distinct ligand is labeled 3 in Tables 4.3 and 4.4.

4.2.1 ^{13}C MAS NMR

Upon the addition of one more unpaired electrons to the t_{2g} shell of the paramagnetic metal, the overall path of the electronic distribution does not change significantly. As a result, the ^{13}C NMR in Figure 4.12 for the two types of tris(2,4-pentanedionato)vanadium(III) ($V(acac)_3$) shows the same relative ordering of functional groups on the frequency scale. Carbonyl has the highest frequency shift, followed by the methine and methyl groups with smaller values. This assignment is again confirmed by the $^{13}C\{^{1}H\}$ REDOR experiment in Figure 4.13. A cluster of carbonyl signals occurs at the highest frequency shift with no observed dephasing, Figure 4.13a, followed by a set of sharp methine signals with the largest dephasing, Figure 4.13b, and a group of overlapping methyl signals at negative frequency range, Figure 4.13c. The overall order of

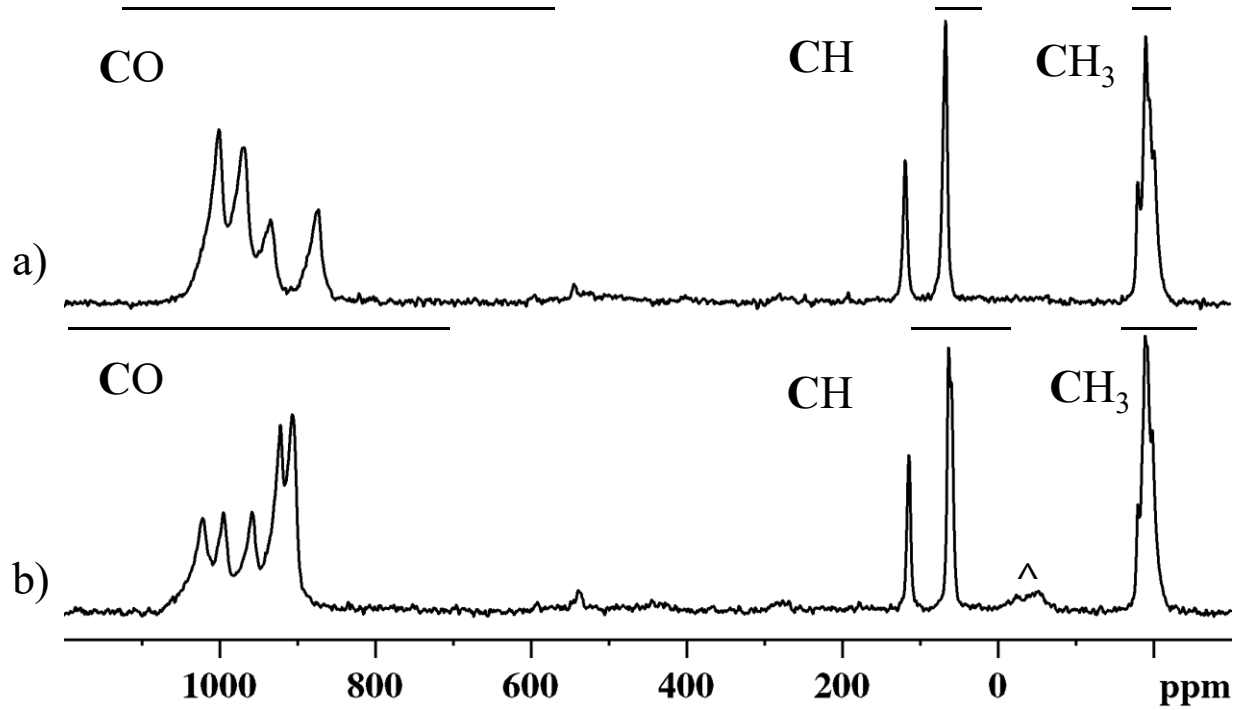

FIGURE 4.12: ^{13}C Hahn-Echo MAS NMR spectra of a) α- $V(acac)_3$ and b) β- $V(acac)_3$. Horizontal bars indicate calculated chemical shift regions of functional groups. "^" indicates the impurity signal of $VO(acac)_2$.

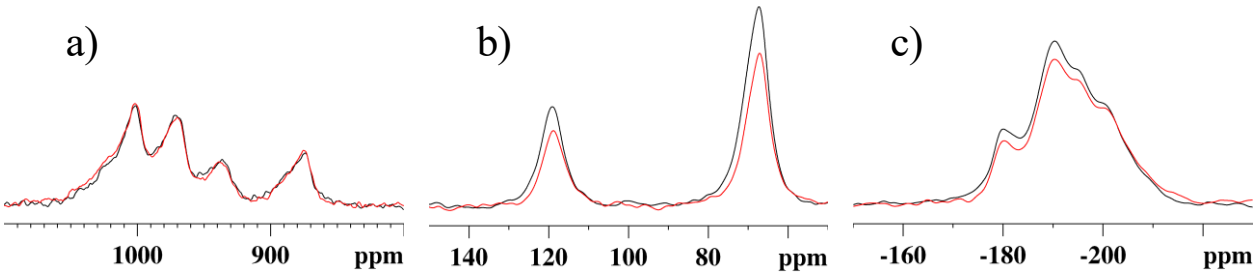

FIGURE 4.13: $^{13}C\{^1H\}$ REDOR MAS NMR of α- $V(acac)_3$. The black spectrum was acquired without dipolar recoupling; the red spectrum was acquired with dipolar recoupling.

appearances of functional groups is retained in the titanium and vanadium complexes, suggesting a similarity in spin-distribution mechanism.

A clear distinction between the two forms of $V(acac)_3$ can be seen from the pattern of carbonyl signals. Similarly to titanium, both forms of the vanadium complex show structural

distortion from D_3 symmetry, and as a result, ^{13}C NMR shows a slight difference in Fermi shifts among the same functional groups, Figure 4.12.

The calculated electron-spin density distribution in both forms of $V(acac)_3$, Figure 4.14, does not differ significantly from that of $Ti(acac)_3$, Figure 4.6. This is to be expected as the addition of another unpaired electron with t_{2g} symmetry retains the overall symmetry of the molecular-orbital interactions and leads to a similar spin-density distribution. As a consequence, the Fermi spin-density at the oxygen remains negative for both complexes, Figures 4.6 and 4.14. The negative spin-density at the oxygen nucleus of $V(acac)_3$ has been confirmed experimentally with ^{17}O NMR studies by Kong *et al.* [126], who report a large negative shift in all ^{17}O resonances. As that report does not specify which polymorph was used, I indicate the range of calculated Fermi coupling constants for all ^{17}O sites between the two forms as ranging from 2 to 5 MHz, according to our calculations. This would imply a Fermi shift in ^{17}O NMR on the order of -600 to -2300 ppm, which includes the observed experimental shifts in the above publication.

As the spin-distribution mechanism did not change between $Ti(acac)_3$ and $V(acac)_3$, the order of the ^{13}C signals between different functional groups remains the same, Figures 4.5 and 4.12. A subtle difference between contours in $Ti(acac)_3$ and $V(acac)_3$ can be observed at the methine position. The vanadium complex has a greater positive spin-density at that site as is apparent from the fewer contour lines of negative density, especially at the third ligand of β-$V(acac)_3$. This distinction can be attributed to an enhanced influence of the electron-delocalization path that accounts for the positive spin-density at the methine carbon.

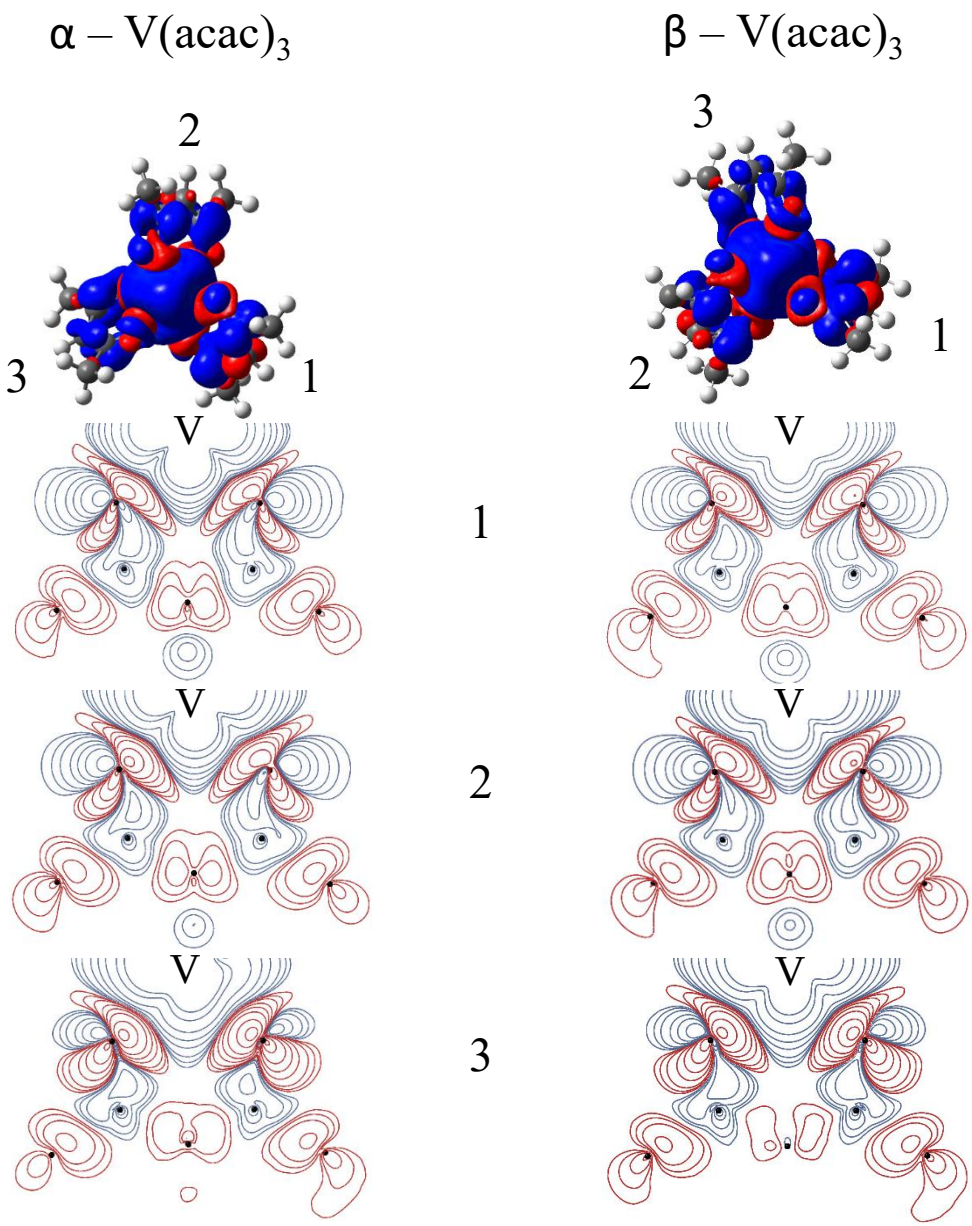

FIGURE 4.14: Spin-density isosurface and contour plots of the ligands of α-$V(acac)_3$ and β-$V(acac)_3$. Ligand 1 is in the xy-plane, ligand 2 is in the yz-plane, and ligand 3 is in the xz-plane.

The difference between spin-density distributions of individual ligands in either the α or β form of $V(acac)_3$ is subtle, Figure 4.14, and is reflected in the observed ^{13}C spectra, Figure 4.12. The most prominent distinction between ligands involves spin density around the methine

carbon. Ligands 1 and 2 in both forms of $V(acac)_3$ show a similar spin density at that position, which implies a similar Fermi-contact shift for methine groups with a distinct Fermi shift of the third ligand at a greater frequency. This distinction is used in further detailed assignment of the spectra.

4.2.2 ^{1}H MAS NMR

Despite similarities in ^{13}C NMR between the two vanadium complexes in Figure 4.12, the ^{1}H NMR in Figure 4.15 shows a significant variation between the two forms. The ^{1}H assignments based on DFT calculations cannot be used unambiguously for either form of $V(acac)_3$ due to a significant overestimation of the magnitudes of paramagnetic coupling. Nevertheless, the ^{1}H NMR spectra of these complexes are unique and can be used as a sensitive fingerprint of the structure. In both spectra the presence of a small amount of impurity, $VO(acac)_2$, is detected, which is a product of oxidation of $V(acac)_3$ [60]. This product is analogous to the $TiO(acac)_2$ seen previously in Figure 4.5. The difference in reactivity of the titanium and vanadium complexes in air is shown with the ^{1}H spectra: the titanium complex shows a significant diamagnetic impurity after minimal exposure to air (see Materials and Methods for sample handling). Both vanadium complexes have been exposed to atmospheric conditions on the order of hours and show minor oxidation, on the order of 5% for the commercial (β-form) and 2% for the synthesized samples (α-form).

The similarity in spin-density distribution pathways between both forms of vanadium and titanium complexes can be observed through the general direction of the ^{1}H shift. Neither of these structures show proton signals that would result from negative spin-density; instead, all resonances have a significant shift to high frequency, Figures 4.9 and 4.15. The relative ordering

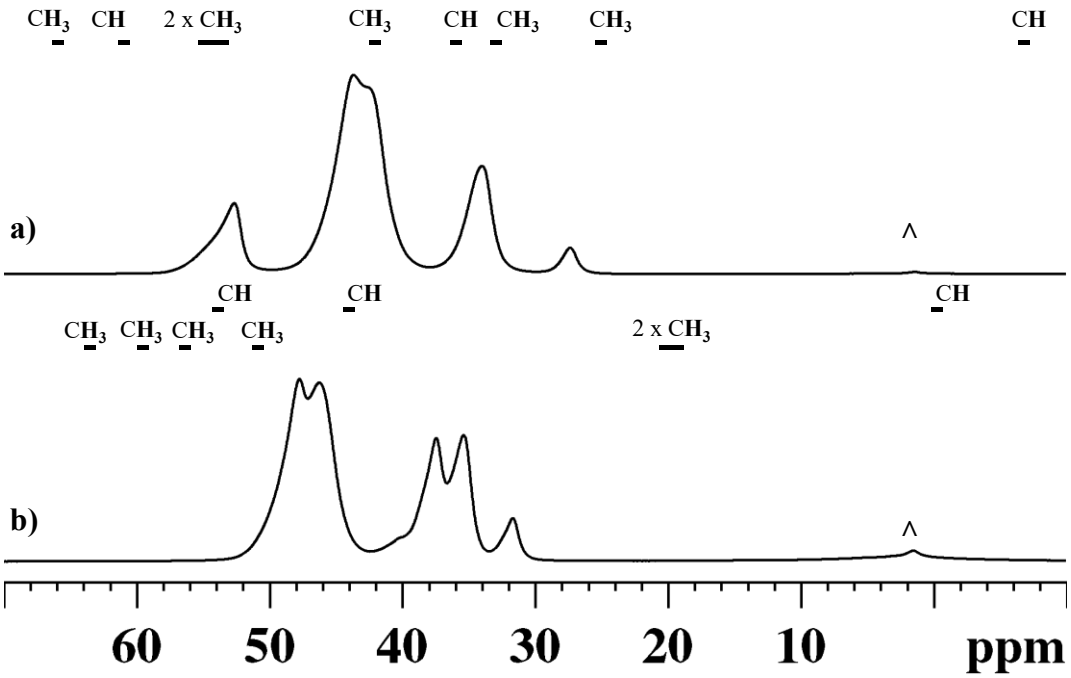

FIGURE 4.15: ^{1}H Hahn-Echo MAS NMR of (a) α- $V(acac)_3$ and (b) β- $V(acac)_3$. Proposed signal positions are listed according to the DFT calculation as used in Figure 4.10. "^"indicates the impurity signal of $VO(acac)_2$ (This complex is discussed in Chapter 7 of the thesis).

of ^{1}H signals from different functional groups, however, varies between all complexes, which signifies the presence of the structural distinction that creates a unique spin-density distribution in each case.

4.2.3 ^{1}H - ^{13}C 2D CP MAS NMR

The ^{13}C NMR resonances in Figure 4.12 appear well-resolved due to favourable nuclear relaxation that gives narrow signals and Fermi coupling that spreads these signals further apart. The advantageous transverse relaxation [32] of carbon nuclei in these complexes makes them good candidates for a 2D ^{13}C{^{1}H} CP MAS NMR experiment, which correlates the observed ^{1}H and ^{13}C MAS NMR spectra and is used as a sensitive method for structural assignment. The 2D

CP of $V(acac)_3$ has previously been reported by Ishii *et al* with the MAS spin rate of 23 kHz on a 9.39 T magnet [31]. Their spectra match our result for the α-$V(acac)_3$ phase. Here I show that the 2D - CP experiment can be done at a slower spinning rate, Figure 4.16, which allows a greater sample mass and less strict Hartmann-Hahn match condition (the detailed mechanism of this pulse sequence is outlined in Materials and Methods section). The 2D CP experiment on α - $V(acac)_3$, Figure 4.16a, not only clearly assigns the methine carbon resonances to the specific hydrogen signals, but manages to clearly resolve all six methyl signals. The β -$V(acac)_3$ at a lower magnetic field of 9.39 T did not show the desired signal resolution in the direct dimension, Figure 4.16. The spectrum suffered from the incomplete Hartmann-Hahn match condition, which could not be optimized for one of the methine carbon groups, as is evident by a weak cross peak

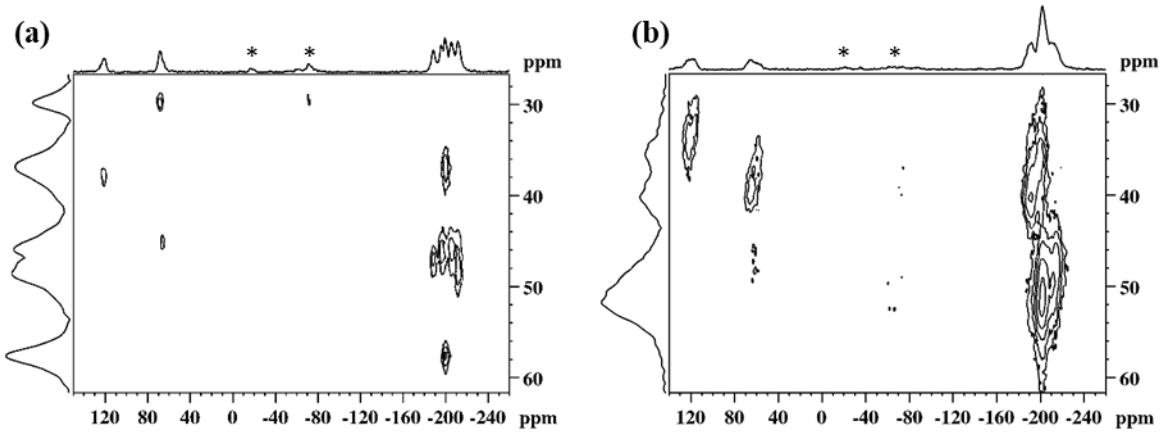

FIGURE 4.16: $^{1}H - ^{13}C$ 2D CP MAS NMR of (a) α- $V(acac)_3$ and (b) β- $V(acac)_3$ at 9.39 T field and MAS of 14 kHz. Asterisks represent MAS spinning sidebands.

on Figure 4.16b. A higher magnetic field together with faster MAS rate did not improve the match condition for the second methine group. However, both spectra contributed to a desirable level of resolution for the direct dimension and enabled a clear distinction of most methyl resonances, Figure 4.17.

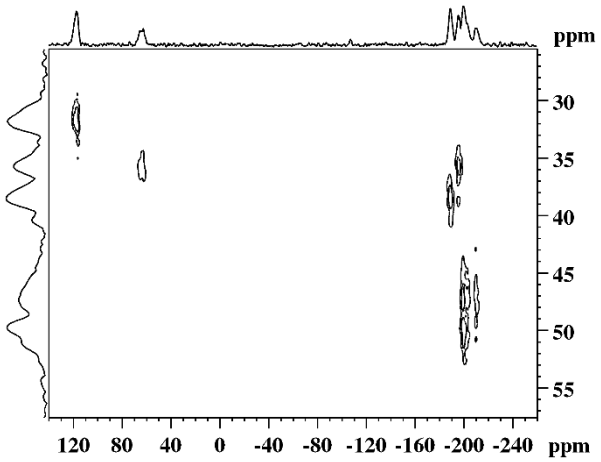

FIGURE 4.17: ^{1}H – ^{13}C 2D - CP of β- $V(acac)_3$ at 11.74 T field with MAS of 28 kHz.

These correlation experiments provide assignments for ^{1}H resonances as the quality of the computational predictions is insufficient for a detailed assignment of all resolved resonances.

4.2.4 Crystallographic assignment with NMR

A detailed NMR signal assignment of crystallographic sites in both $V(acac)_3$ forms is proposed on the basis of the qualitative distribution of predicted resonances together with the relative intensity fitting and ^{1}H – ^{13}C 2D – CP experiments, Tables 4.3 and 4.4. A detailed assignment of the carbonyl signal in both forms of the vanadium complex is ambiguous due to the low accuracy of the calculation, Figure 4.10. The proposed assignment patterns in Tables 4.3 and 4.4 are plausible, but not conclusive.

The magnetic properties of $V(acac)_3$ have been studied since 1967 when Machin [127] reported a series of susceptibility measurements at various temperatures. The effective magnetic moment at 31°C is 2.87 μ_B, which is close to the spin-only value of 2.83 μ_B. The spin-only value implies that the electron g-value is identical to that of the free unpaired electron. This is slightly greater than that determined from the EPR study of Krystek *et al* [128] for a solid sample at 5 K, which was found to have g_{iso} of 1.86. Unfortunately, the crystal structure of their sample was not

TABLE 4.3: ^{13}C and ^{1}H NMR of α - $V(acac)_3$ and DFT calculation.[a)] Calculated and experimental shifts are in ppm at a sample temperature of 55 ˚C. ^{1}H and ^{13}C shifts from the same functional groups are indicated and appear in the order as listed.

Group [ligand]	^{13}C			
	A_{calc} (MHz) {A_{exp}}	δ_{calc}[d)] {δ_{exp}}	A_{calc} (MHz) {A_{exp}[e)]}	δ_{calc} {δ_{exp}[b), c)]}
CO [1]	3.70, 3.53 {3.2(2)}	1135, 1093 {1001(8)}		
CO [2]	3.22, 2.89 {3.1(2)}	1012, 929 {970(8)}		
CO [3]	2.46 {2.9(2)}	820 {935(8)}		
CO [3]	1.56 {2.6(2)}	589 {875(7)}		
CH [3]	-0.33 {0.06(2)}	16 {119.0(5)}	-0.21 {0.46(5)}	-8 {34}
CH [2]	-0.15 {-0.14(2)}	64 {69.5(5)}	0.52 {0.40(4)}	33 {27}
CH [1]	-0.08 {-0.14(2)}	80 {67.0(5)}	0.94 {0.58(6)}	66 {43}
CH_3 [3]	-0.85 {-0.81(5)}	-189 {-180(2)}	(0.85, -0.23, 0.57) {1.39, -0.38, 0.94}	27 {43}
CH_3 [2]	-0.90	-202	(0.21, 0.77, 1.62) {0.16, 0.57, 1.22}	58 {44}
CH_3 [2]	-0.91	-205	(0.75, 0.33, 2.13) {0.35, 0.15, 0.98}	71 {34}
CH_3 [1]	-0.93 {-0.85(5)}	-211 {-190(2)}	(1.05, 1.65, -0.01) {0.92, 1.46, -0.008}	60 {53}
CH_3 [2]	-0.95 {-0.87(5)}	-215 {-195(2)}	(1.28, -0.06, 0.81) {1.25, -0.06, 0.79}	45 {44}
CH_3 [3]	-0.95 {-0.89(5)}	-215 {-201(2)}	(-0.01, 0.86, 0.71) {-0.02, 1.09, 0.94}	35 {44}

a) Occupancies at the metal t_{2g} orbitals: $d_{xy}^{0.66}$, $d_{xz}^{0.46}$, $d_{yz}^{0.65}$
b) Experimental error is ±1 ppm due to temperature variations
c) Signal assignments are based on $^{1}H - {}^{13}C$ 2D - CP NMR in Figure 4.16a
d) Shifts were calculated according to equation 2.18.
e) Couplings from individual hydrogens from the same methyl group are scaled to match the average experimental shift.

TABLE 4.4: ^{13}C and ^{1}H NMR of β - $V(acac)_3$ and DFT calculation.[a)] Calculated and experimental shifts are in ppm at a sample temperature of 55 ˚C. ^{1}H and ^{13}C shifts from the same functional groups are indicated and appear in the order as listed.

Group [ligand]	^{13}C		^{1}H	
	A_{calc} (MHz) {A_{exp}}	δ_{calc}[d)] {δ_{exp}}	A_{calc} (MHz) {A_{exp}[e)]}	δ_{calc} {δ_{exp}[b), c)]}
CO [1]	4.16 {3.3(2)}	1253 {1022}		
CO [1]	3.70 {3.1(2)}	1135 {995}		
CO [2]	3.33 {3.0(2)}	1041 {959}		
CO [2]	2.84 {2.9(2)}	915 {922}		
CO [3]	2.07, 2.03 {2.8(2)}	719, 710 {906}		
CH [3]	-0.01 {0.050(4)}	97 {114}	-0.11 {0.42(4)}	-1 {32}
CH [2] CH [1]	-0.28 {-0.15(1)} -0.42 {-0.16(1)}	29 {63.5} -5 {60}	0.65 {0.46(4)} 0.82 {0.63(4)}	47 {35} 68 {46}
CH_3 [3]	-0.84 {-0.82(6)}	-186 {-180}	(-0.06, 0.77, 0.23) {-0.11, 1.39, 0.41}	22 {38}
CH_3 [3]	-0.85 {-0.84(6)}	-190 {-187}	(0.65, -0.19, 0.37) {1.21, -0.36, 0.69}	20 {35}
CH_3 [2]	-0.88, -0.96 {-0.86(6)}	-196, -217 {-189}	(1.08, -0.06, 1.75) {0.81, -0.04, 1.30} (1.76, 0.42, 0.30) {1.20, 0.29, 0.21}	61 {46} 55 {38}
CH_3 [1]	-0.97 {-0.86(6)}	-220 {-192}	(1.78, -0.06, 1.37) {1.24, -0.04, 0.95}	68 {48}
CH_3 [1]	-1.04 {-0.88(6)}	-238 {-198}	(1.72, -0.13, 1.33) {1.26, -0.10, 0.98}	64 {48}

a) Occupancies at the metal t_{2g} orbitals: $d_{xy}^{0.81}$, $d_{xz}^{0.34}$, $d_{yz}^{0.61}$
b) Experimental error is ±1 ppm due to temperature variations
c) Signal assignments are based on $^{1}H – ^{13}C$ 2D - CP NMR in Figures 4.16b and 4.17
d) Shifts were calculated according to equation 2.18.
e) Couplings from individual hydrogens from the same methyl group are scaled to match the average experimental shift.

determined, and the authors assumed that they had both α and β forms of the complex present in their samples. As in the case of $Ti(acac)_3$, there will be no consideration of a spin-orbit coupling contribution to the electron moment, and a free electron g-value will be used to evaluate the Fermi shifts in Tables 4.3 and 4.4.

The methine group is bound to both carbonyl groups, and thus its hyperfine coupling is most affected by their electronic environments. The spin densities observed at the methine carbons reflect the effects of spin delocalization and polarization in these bonds. Individual methine resonances can be assigned on a structural basis with the knowledge of relative magnitudes of Fermi couplings within carbonyl carbons, Table 4.3 and 4.4. In both polymorphs, the methine signal splits into two regions with a 1:2 intensity ratio, which mimics the separation of the carbonyl groups. The order of the resonance shifts of the methine groups is reversed with respect to the bound carbonyl groups of the α - $V(acac)_3$, Table 4.3. The shift of methine groups to negative frequency signifies an excess of negative spin-density. The source of this spin is the polarization of the carbonyl - methine bond, as previously described in the spin-density contour-plot of the $Ti(acac)_3$ complex, Figure 4.7b. Therefore, polarization is the dominant mechanism, which determines the direction of the methine shift and provides a structural link between the methine and carbonyl groups in α - $V(acac)_3$. This assignment is consistent with our previous distinction between methine groups based on spin-density contour-plots, Figure 4.14. The computed Fermi coupling constant at the methine carbon of the 3rd ligand does not agree with either the established experimental signal assignment, Table 4.3, or the spin-density contour-map, Figure 4.14, as it is predicted to have a greater spin-density compared to ligands 1 and 2. The carbonyl groups of β - $V(acac)_3$ are also assigned with the third ligand having the lowest-Fermi coupling constants according to the computed model, Table 4.4. By analogy with α -

$V(acac)_3$, the distribution of methine signals mimics the assignments of carbonyl groups in reverse order, indicating that the polarization mechanism is preferred at the methine site. Unlike α - $V(acac)_3$, the computed Fermi coupling for the methine on ligand 3 of β - $V(acac)_3$ has the expected sign and magnitude relative to ligands 1 and 2 as visualized from the contour plots.

$V(acac)_3$ can have multiple crystal structures that depend on the method of sample preparation and crystallization [29]. As some of the reported structures contain sites with partial disorder, ^{13}C NMR can be used to discriminate between those structures. The partial occupancy in the absence of motion would appear as the presence of additional carbon resonances at stoichiometric intensities. As these signals are not observed in our sample, Figure 4.10, we can conclude that our samples do not contain partially disordered sites.

4.3 Tris(2,4-pentanedionato)chromium(III), d^3

A chromium ion in its 3+ oxidation state in an octahedral field of local oxygen coordination has three unpaired electrons that occupy the three low-lying *d*-orbitals, d_{xy}, d_{xz} and d_{yz}. The complex crystallizes in the $P2_1/c$ space group near room temperature. Despite the absence of conditions for the Jahn-Teller distortion, all atoms are in unique crystallographic sites. The distortion between chemically equivalent groups is minor, with all Cr-O bond lengths within the range of 1.95 – 1.97 Å, thus the distortion is attributed to weak intermolecular effects in the solid state. As all sites are crystallographically unique in the molecule of $Cr(acac)_3$, a total of 15 ^{13}C and 9 ^{1}H resonances are expected to be observed, as in the previously described titanium and vanadium complexes.

There is another crystal structure of $Cr(acac)_3$ at 110 K, which has the same space group as the structure at room temperature. However, the low temperature form has a large unit-cell

that contains 6 unique molecules of $Cr(acac)_3$. If solid-state NMR experiments were to be done on $Cr(acac)_3$ at 110 K, the ^{13}C spectrum should have 90 resonances and the ^{1}H should have 54 resonances. The effect of the structural variation with temperature has been previously analyzed in Section 4.1.6 for $Ti(acac)_3$.

4.3.1 ^{13}C MAS NMR

In contrast to previous paramagnetic complexes, the ^{13}C signal from $Cr(acac)_3$ appears broad and featureless, with characteristic Fermi shifts that place resonances far outside the diamagnetic region, Figure 4.18. The assignment of functional groups remains consistent with that in the previously discussed titanium and vanadium acac complexes, as only t_{2g} orbitals are singly occupied. The calculations predict the same assignment regions and places the carbonyl signal around 1300 ppm, which is experimentally unobserved (see Figure 4.18).

Figure 4.19 shows the spin-density distribution in the ligand. In comparison with the previous metal complexes that had fewer unpaired electrons, the distribution remains identical for the carbonyl and methyl groups. The spin distribution at the methine carbon experiences a significant effect of spin-density delocalization, seen in Figure 4.19 as the blue contour surrounding the carbon nucleus. This is consistent with our previous observations of increasing influence of delocalization with greater t_{2g} occupancy of unpaired spins, as per the titanium and vanadium complexes.

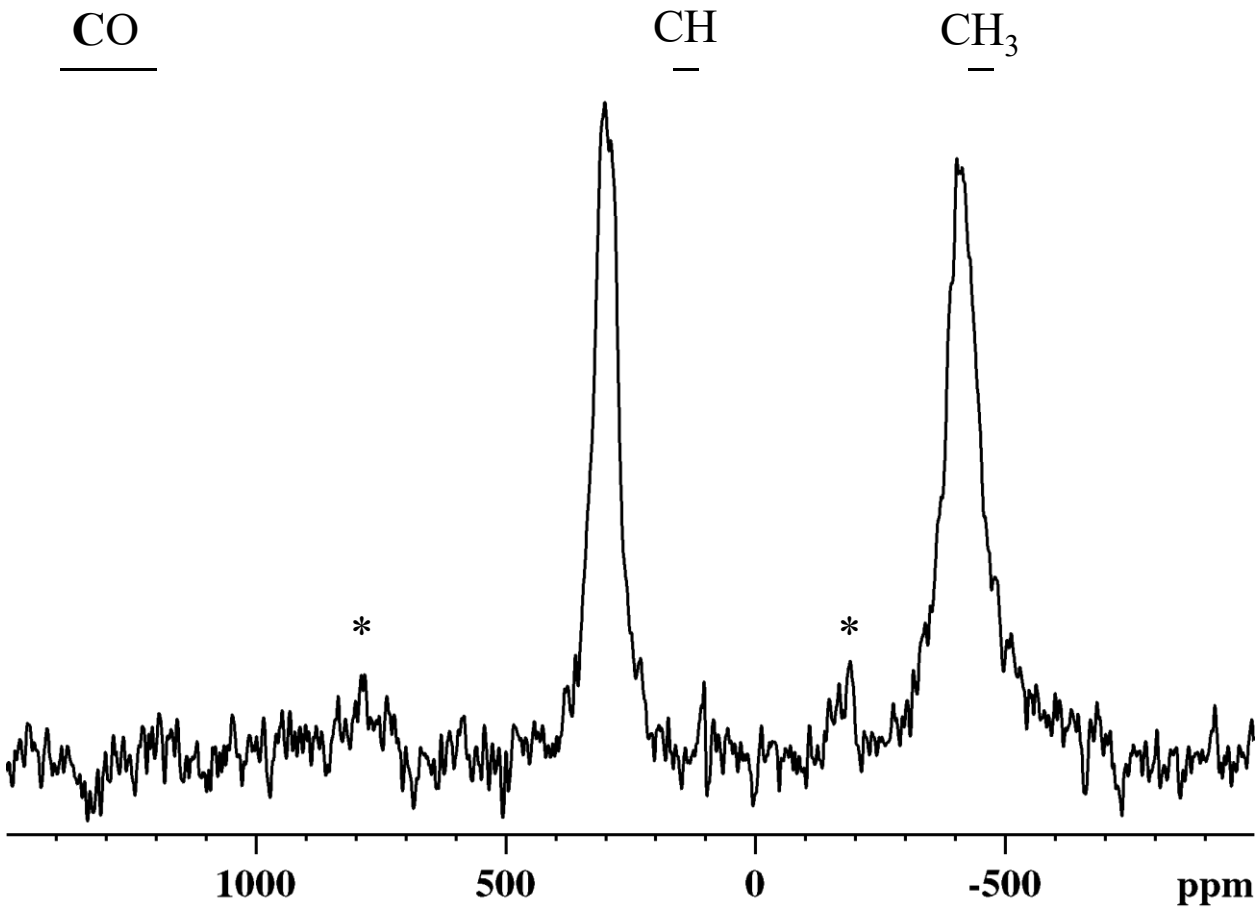

FIGURE 4.18: ^{13}C Hahn-Echo MAS NMR of $Cr(acac)_3$. Assignment of functional groups is based on the DFT calculation, Table 4.5. Asterisks indicate the spinning sidebands of MAS.

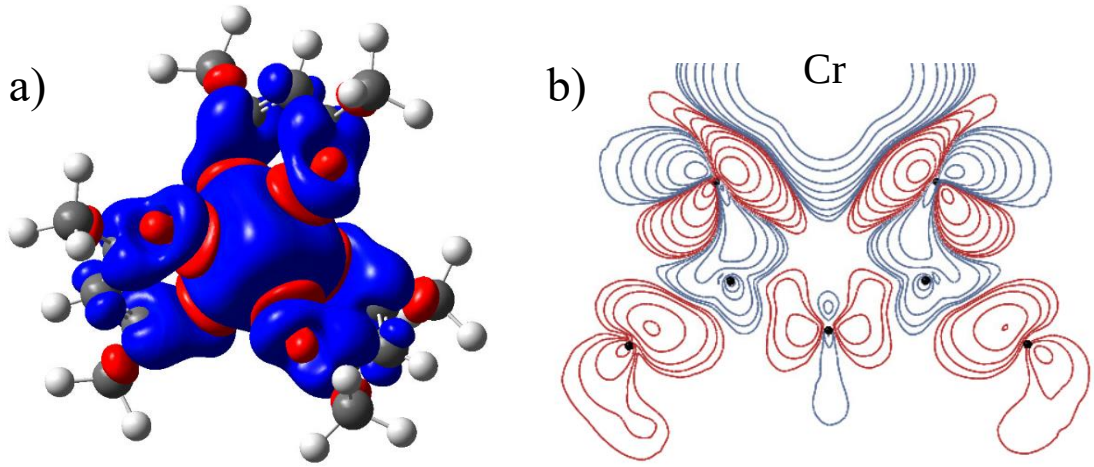

FIGURE 4.19: Spin-density a) isosurface and b) contour-plot of one of the ligands of $Cr(acac)_3$.

4.3.2 ^{1}H MAS NMR

Despite the strong overlap of the signal from functional groups in the ^{1}H NMR spectra of $Cr(acac)_3$, the general shift of the resonances remains to higher frequency, which indicates net positive spin-density at the hydrogen nuclei. This is consistent with the titanium and vanadium

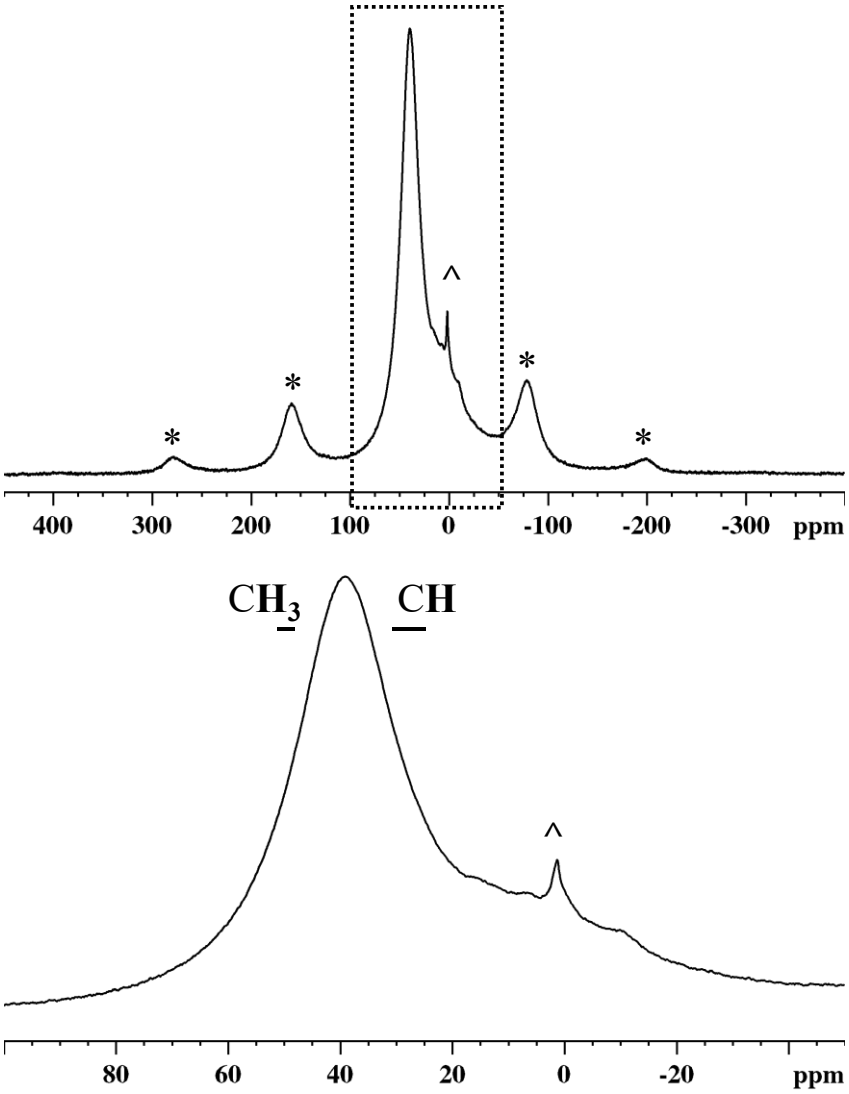

FIGURE 4.20: ^{1}H Hahn-Echo MAS NMR of $Cr(acac)_3$. Proposed signal positions are listed according to DFT calculation as used in Figure 4.18. Signals from methyl groups are averaged to simulate fast rotation. Asterisk indicate the artifacts of MAS. "^" indicates the signal from the rotor material.

complexes, and together with the assignment of the ^{13}C resonances, suggests a fundamental similarity in spin-density distributions among these complexes with occupied t_{2g} orbitals in a near-octahedral field. Computational predictions of ^{1}H shifts in Figure 4.20 suggest that all methyl groups should occur in a narrow shift region and that the methine is shifted to higher frequency from the diamagnetic position. Both assignments confirm the general position of the observed featureless resonances. Signal assignments for both ^{13}C and ^{1}H spectra are presented in Table 4.4.

4.3.3 Summary of computational assignment

The magnetic moment required for the calculation of the Fermi shift from the coupling constant according to equation 2.18, was estimated from EPR experiments [129]. EPR studies of this complex at low temperatures reveal only a small variation in the g-tensor components, between 1.985 and 1.997, which is not significantly different from the free-electron value. Hence, the free-electron g-value will be used to calculate the Fermi shift from the computed coupling constants in Table 4.5.

Table 4.5 provides a summary of the computed shifts for each of the functional groups in $Cr(acac)_3$. As all atomic positions are unique, each nucleus has a separate Fermi coupling-constant. However, the variation in Fermi couplings among the same functional groups is not significant but still provides the correct order of resonance assignments. The low variation in Fermi couplings is insufficient to provide site-specific resolution in either ^{1}H and ^{13}C NMR spectra, Figures 4.18 and 4.20, due to unfavorable nuclear transverse relaxation.

TABLE 4.5: ^{13}C and ^{1}H NMR of $Cr(acac)_3$ and DFT calculation.[a)] Calculated and experimental shifts are in ppm at a sample temperature of 55 ˚C. ^{1}H and ^{13}C shifts from the same functional groups are indicated and appear in the order as listed.

Group	^{13}C		^{1}H	
	A_{calc} (MHz) {A_{exp}}	δ_{calc}[b)] {δ_{exp}}	A_{calc} (MHz) {A_{exp}[c)]}	δ_{calc} {δ_{exp}}
CO	2.1, 2.2, 2.3, 2.3, 2.3, 2.5 {not observed}	1196, 1253, 1282, 1300, 1309, 1408 {not observed}		
CH	0.015, 0.03 0.11 {0.41(1)}	108, 117, 154 {300(5)}	0.17 – 0.22	25 - 32
CH_3	-0.95, -0.96, -0.97, -1.01, -1.03, -1.05 {-0.91(2)}	-427, -433, -438, -457, -467, -475 {-410(5)}	(-0.27 … 0.88) {-0.22 … 0.70}	48 – 52 {38(1)}

a) Occupancies at the metal t_{2g} orbitals: $d_{xy}^{0.89}$, $d_{xz}^{0.89}$, $d_{yz}^{0.8}$
b) Shifts were calculated according to equation 2.18.
c) Couplings from individual hydrogens from the same methyl group are scaled to match the average experimental shift.

4.4 Effect of t_{2g} orbitals on spin density in $M(acac)_3$ (M = Ti, V, Cr)

Figure 4.21 shows the relation between the calculated spin density of the in-plane t_{2g} orbital and the spin density at the ^{13}C nucleus that has been converted from the measured Fermi-coupling constant via equation 2.22 for all these $M(acac)_3$ complexes. An increase in spin population of the t_{2g} orbital leads to a rise of positive spin-density at the carbonyl nucleus. This is to be expected according to our previous interpretations of the spin-distribution mechanisms, where the spin density at the carbonyl is largely composed of the delocalization from the metal-oxygen π*interaction (see Section 4.1). The nuclear-spin density at the methine carbon originates

at negative values when the t_{2g} occupancy is low. This signifies the dominance of the polarization mechanism from the carbonyl group. In fact, both methyl and methine groups experience nearly identical degrees of polarization at those conditions, Figure 4.21. Upon increase of the t_{2g} population, we can observe a clear distinction in trends between the two functional groups. The methine group shows a larger degree of delocalization, whereas the methyl group remains dominated by the polarization. This difference stems from the relative ordering of high-energy antibonding orbitals of sp^2 and sp^3 carbon species. Delocalization between the sp^2 carbonyl and sp^2 methine is expected to be more energetically favorable than among the sp^2 carbonyl and sp^3 methyl groups.

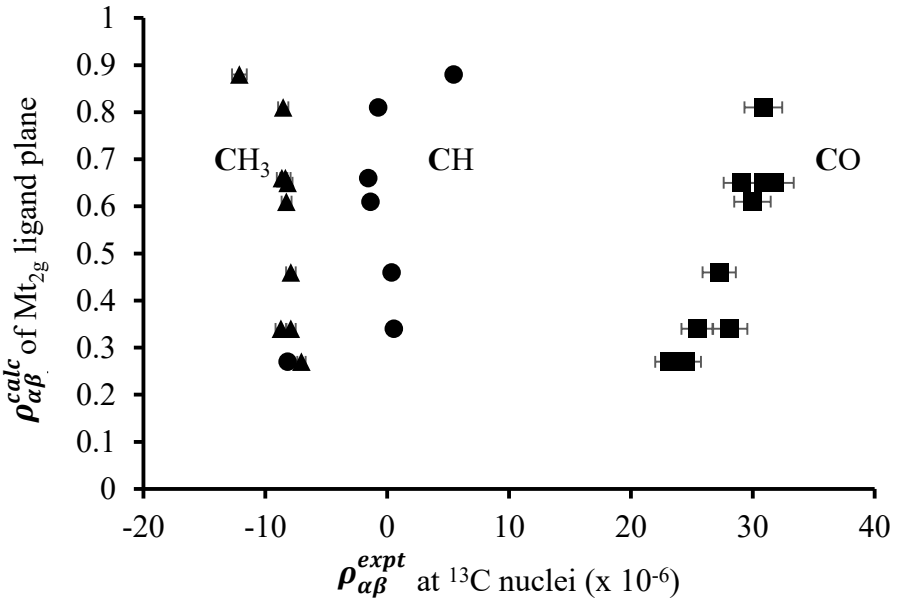

FIGURE 4.21: Relation between spin density in the t_{2g} orbital in the ligand plane and experimental spin density at the carbon nuclei of the ligand for $M(acac)_3$ (M = Ti, V, Cr). Squares denote the carbonyl group, circles denote the methine group, and triangles denote the methyl group.

4.5 Nuclear transverse relaxation in $M(acac)_3$ (M = Ti, V, Cr)

Between the three tris(acetylacetonato)metal(III) complexes we have seen so far, there has been significant variation in signal widths in both ^{13}C and ^{1}H spectra across the series. The width of the isotropic NMR signal is affected by the nuclear transverse relaxation, see equation 2.6. General formulations for paramagnetic contributions to the nuclear transverse relaxation are in equations 2.26 and 2.30, where both interactions are scaled by the same quantity, the electron-relaxation time, T_e. The electron-relaxation time is unique for the entire molecule and therefore it scales the NMR resonance widths of all nuclei. Electron-relaxation mechanisms were outlined in Section 2.5.3. The systematic variation between the three ligands in the molecules discussed in this section is the degree of occupancy of the unpaired electrons in the low-lying t_{2g} state, which gives different electronic relaxations across the series. The electron-relaxation time is significantly reduced in the presence of thermally accessible low-lying excited states [96], hence most EPR measurements are done at low temperatures. Both titanium and vanadium electronic configurations can have three distinct microstates. For example, in Ti^{3+}, the unpaired electron can occupy either one of the d_{xy}, d_{xz} and d_{yz} orbitals, which signifies the three electronic states. A calculation provides a superposition of these microstates with the account of probabilities of electron occupancies. The electronic relaxation time is reduced with variation in its environment; thus, the presence of accessible spin states reduces the electronic-relaxation time. The spin state of Cr^{3+} forbids fast electronic relaxation as its configuration in an octahedral field confines the electron environment to a single microstate in which all d_{xy}, d_{xz} and d_{yz} orbitals are singly occupied. As a result, the electronic relaxation in Cr^{3+} is long, estimated by low-field EPR to be on the order of nanoseconds at 123 K in $Cr(acac)_3$ [129]. The long electronic relaxation leads to broad NMR resonances in the solid state for both ^{13}C (Figure 4.18) and ^{1}H (Figure 4.20) spectra.

4.6 Conclusion

This series of transition-metal acacs demonstrates the relation between the occupancy of the metal orbital and the observed NMR signals. This relation has a deep connection to the underlying molecular-orbital interactions that produce a specific distribution of unpaired electron spin-density. This distribution enhances the overall signal span and can lead to enhancement in resolution along with a drastic increase in effective signal sensitivity. These systems show an intuitive pathway for an unambiguous signal-assignment process in paramagnetic NMR, which can be extended to other, more complicated cases.

Chapter 5: Exploring Jahn-Teller effects in tris(2,4-pentanedionato)manganese(III) with solid state NMR

$Mn(acac)_3$ has been investigated for decades, but only recently has there been a comprehensive account of variations in packing symmetry and molecular distortion [29]. In this complex, manganese contains four unpaired electrons in its 3+ oxidation state. The pseudo-octahedral coordination of oxygen atoms surrounding the metal is perturbed by the strong influence of a Jahn-Teller distortion that minimizes the total energy through the loss of electronic degeneracy. The structure can undergo a variety of distortions between extreme elongation and compression and includes intermediate forms that are stabilized in different crystal-packing symmetries through favorable intermolecular interactions [29, 64]. Figure 1.6 illustrates $Mn(acac)_3$ with outlined metal-oxygen bonds that undergo the characteristic Jahn-Teller elongation/contraction. The most recent comprehensive account of various $Mn(acac)_3$ structures includes five different crystal structures: α-, β-, γ-, δ- and ε- $Mn(acac)_3$ [29]. The detailed structural description of these polymorphs is in Section 1.3.4. In all reported crystal structures of $Mn(acac)_3$, the difference in metal-oxygen bond-lengths is more pronounced than in $Ti(acac)_3$ and $V(acac)_3$, therefore there should be a significant variation in the Fermi coupling between the ligands with similar Mn-O bond lengths *vs* the ligands with different bond lengths. The high magnetic moment of Mn^{3+} with S = 2 provides additional sensitivity to the resonance shift from the Fermi coupling according to equation 2.18. The greater magnetic moment increases the overall signal anisotropy through

electron-nuclear dipolar coupling, and fast MAS is even more crucial for the enhancement of resolution and signal sensitivity than for d^1 - d^3 systems [32].

5.1 ^{13}C MAS NMR

The purchased sample was identified by powder x-ray diffraction as γ - $Mn(acac)_3$ phase. The molecule of the γ - $Mn(acac)_3$ crystal has an elongation along the two axial Mn-O bonds that produces two types of acetylacetonate ligands, Figure 1.6. Two out of three ligands have a single elongated oxygen-metal bond of 2.11 Å along the z-axis, while the third ligand is in the plane perpendicular to the axis of elongation and has short metal-oxygen bonds of 1.93 Å. The ^{13}C MAS NMR spectrum is presented in Figure 5.1, showing the extent of the observable signal and sensitivity of the resonance shift to the local environment via the contribution of the Fermi coupling. The overall signal breadth and the isotropic-shift distribution are too large to be uniformly excited by the hard pulses of the Hahn-Echo sequence. Multiple experiments were collected with various transmitter offsets to excite the full spectrum, Figure 5.1a, b and c. Simultaneous excitation of a broad spectral range under fast MAS was achieved with an adiabatic double-echo pulse sequence, Figure 5.1d.[34] This image illustrates the scale of the paramagnetic coupling, which produces ^{13}C NMR resonances over a range spanning nearly 2000 ppm. This is approximately a factor of 10 increase with respect to the diamagnetic shift range of 0-200 ppm.

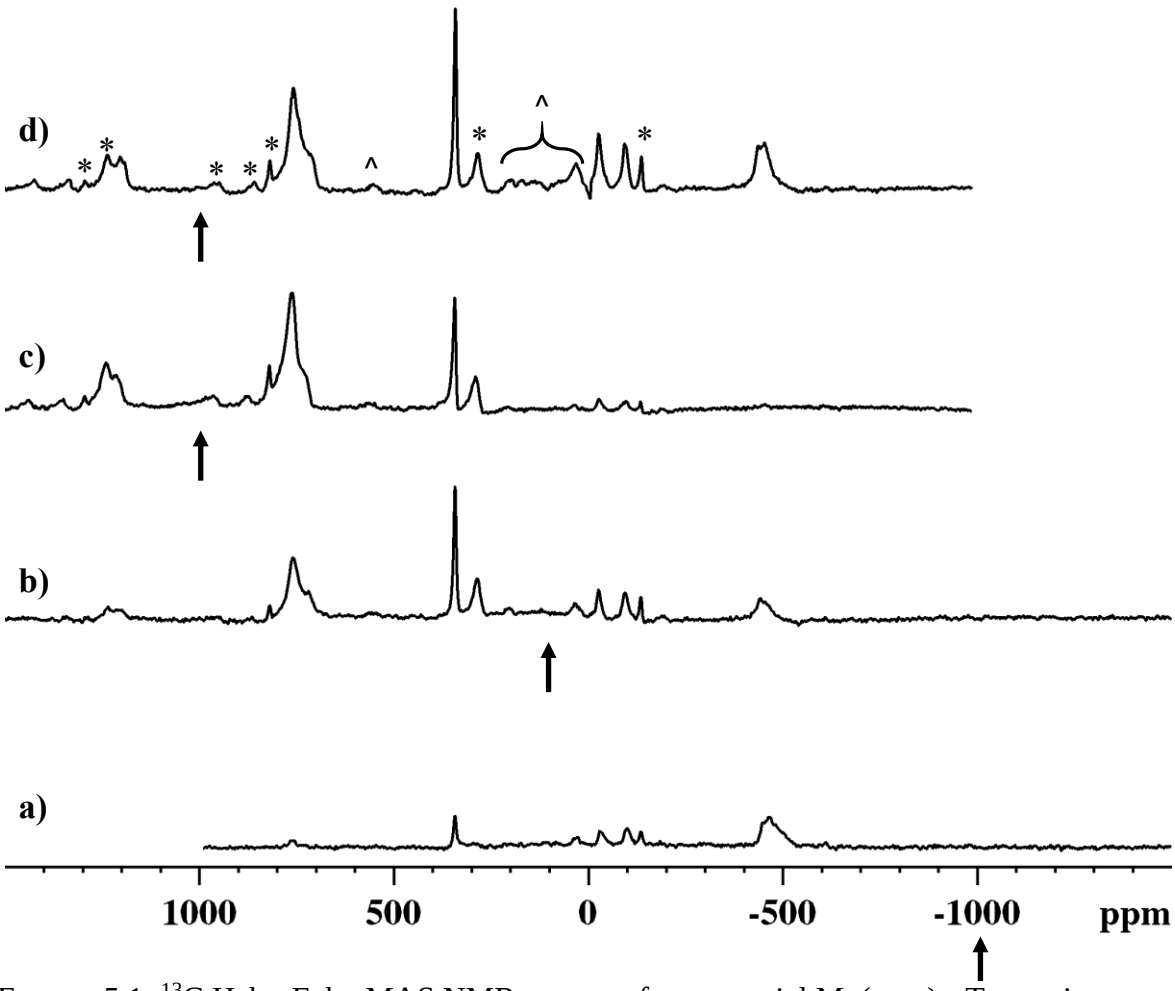

FIGURE 5.1: ^{13}C Hahn-Echo MAS NMR spectra of commercial $Mn(acac)_3$. Transmitter frequency at a) -1000 ppm, b) 100 ppm, c) 1000 ppm; d) ^{13}C Adiabatic Double-Echo MAS NMR of commercial $Mn(acac)_3$ with transmitter frequency at 1000 ppm. Asterisks indicate spinning sidebands, "^" indicates an impurity signal (see below).

The variation in temperature results in a change of the Fermi shift according to equation 2.18, where high temperature lowers the magnitude of the shift and brings it closer to the diamagnetic limit. This general pattern is shown in Figure 5.2, where both blue and red lines are directed toward the diamagnetic region of 0 to 200 ppm with increasing temperature. This dependence highlights yet another advantage of paramagnetic NMR, which is the ability to finely

control the resonance shift. As can be seen from Figure 5.2, the temperature change of only 20 K provides enough evidence to conclude that the intense signal at ~760 ppm is composed of multiple resonances with different Fermi-coupling constants. In the absence of the pseudocontact shift, overlapping signals with different Fermi shifts must also have different diamagnetic shifts. Thus this signal overlap is likely to occur between different functional groups. The small variation in temperature far from any phase transition is not expected to cause significant changes to the crystal structure, therefore Fermi couplings are expected to remain constant. Differences in Fermi couplings between distinct molecular sites are used to separate resonances, enhance spectral resolution, and provide structural assignments on the basis of the spin-density distribution model or experimental methods [32].

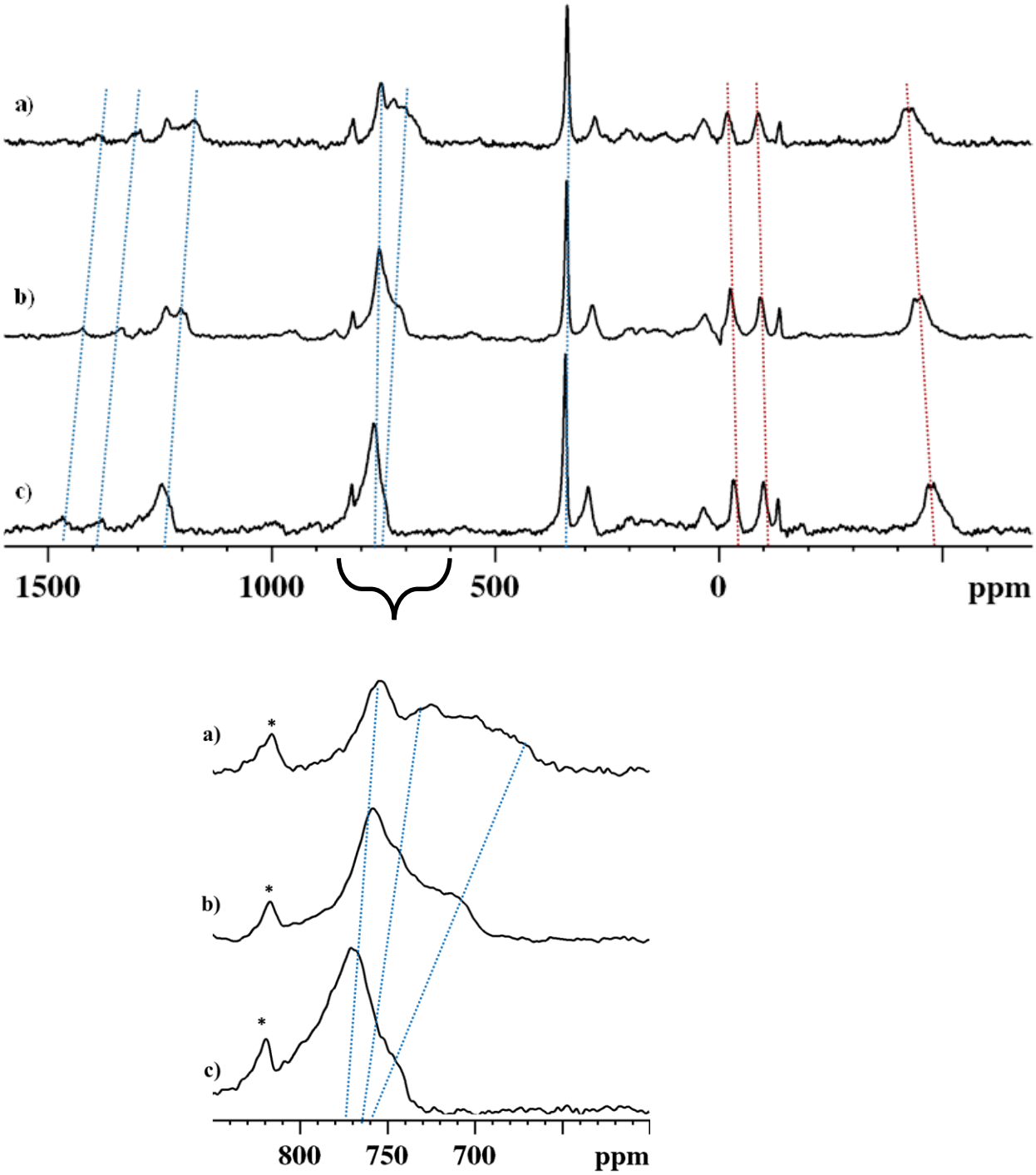

FIGURE 5.2: Variable temperature ^{13}C adiabatic double-echo MAS NMR of γ - $Mn(acac)_3$ at a) 65˚C, b) 55˚C and c) 45˚C. The red lines indicate isotropic signals with negative Fermi shifts, the blue lines indicate signals with positive shifts. Asterisks indicate spinning sidebands of MAS.

5.2 $^{13}C\{^{1}H\}$ REDOR

The signal assignment of the three functional groups is done with $^{13}C\{^{1}H\}$ REDOR. The strong signal overlap, large range of isotropic shifts and the significant signal anisotropy combined require the use of various transmitter offsets, MAS rates and temperatures (Figure 5.3). The shift of the transmitter offset was done to excite specific regions of the spectrum for detailed assignment with REDOR. Sharp resonances under 500 ppm undergo dephasing upon the introduction of 1H recoupling. These can be identified as methine and methyl groups. The results of the assignment are indicated on Figure 5.3 and correlate well with those obtained by Ishii *et al* [32, 33]. Their experimental spectra were influenced by the selective signal enhancement of $^{13}C\{^{1}H\}$ INEPT experiments, which together with the slow MAS rate were not able to show resonances beyond 500 ppm.

Resonances below 500 ppm appear as well-resolved signals that do not undergo any additional splitting at variable temperature, Figure 5.3, which suggests an absence of an overlapping signal from different functional groups. Above 500 ppm there are regions of signal overlap at specific temperatures and MAS rates. Variable temperature and variable spinning help resolve and identify overlapped signals, Figure 5.3. The composite peak at ~760 ppm undergoes only partial dephasing upon REDOR recoupling, which suggests strong signal overlap from different functional groups. As additional evidence of the overlap from different functional groups, this signal becomes more resolved at higher temperature, as was discussed above. Further details about this signal require analysis of the spin-density distribution.

The methyl group has a large negative shift, Figure 5.3a, which can only be caused by a dominant polarization mechanism induced at the carbonyl group. The methine group has a positive Fermi-shift, as it is strongly affected by the delocalization from the carbonyl group due to their equivalent hybridization. Carbonyl groups occur at even greater resonance shifts as they

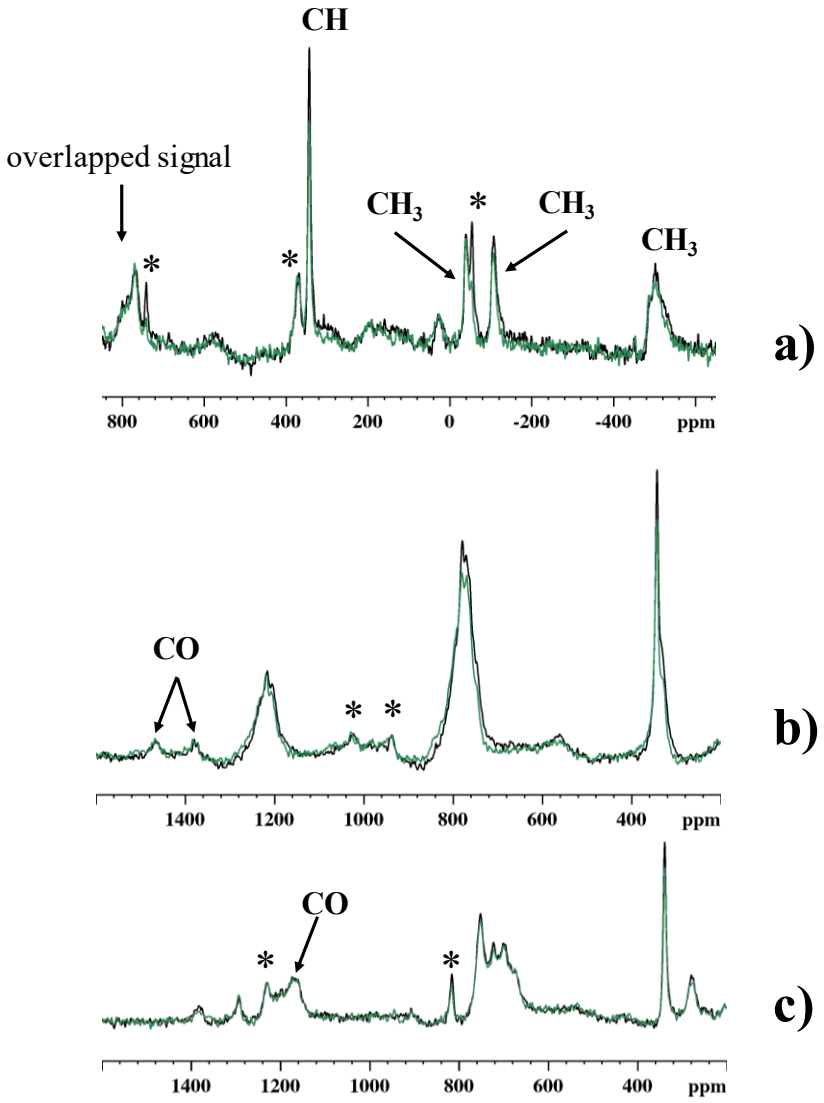

FIGURE 5.3: ^{13}C {^{1}H} REDOR NMR spectra at a) 50 kHz MAS, 100 ppm offset and 55°C sample temperature; b) 55 kHz MAS, 1000 ppm offset and 55°C sample temperature; c) 60 kHz MAS, 1000 ppm offset and 68°C sample temperature. Green spectra are acquired with ^{1}H recoupling pulse, black spectra are acquired without the ^{1}H recoupling. Asterisks indicate artifacts of MAS.

experience the greatest effect of the delocalization through the metal-oxygen orbital interaction. This indicates the dominance of the electron-spin distribution mechanism that is common to d^1-d^3 series of acetylacetonate complexes. This observation is anticipated as three of the four unpaired electrons are known to occupy the d_{xy}, d_{xz} and d_{yz} orbitals, whereas only a single electron occupies either one of the d_{z2} or d_{x2-y2} orbitals in $Mn(acac)_3$. However, that additional electron in the higher-energy orbital is responsible for the distinct structural distortion and is expected to cause additional pathways of electron-density distribution in the acetylacetonate ligand in $Mn(acac)_3$.

5.3 Spin-density maps

Jahn-Teller distortion of the octahedral field in the presence of four unpaired *d*-electrons is clearly visible from the calculated electron-spin-density contour-plot in Figure 5.4. The model structure is γ-$Mn(acac)_3$, which has a Jahn-Teller elongation, therefore the d_{z2} orbital is expected to be occupied instead of the d_{x2-y2}. This distortion is visible in the spin-density contour-maps within the axial ligands, Figures 5.4b and c, while it is absent from the equatorial ligand, Figure 5.4a.

The spin density of the equatorial ligand retains local C_2 symmetry which passes through the methine group. This symmetry leads to three distinct paramagnetic shifts of ^{13}C resonances, one for each functional group as depicted in Figure 5.4a. Axial ligands experience the distortion and symmetry-breaking of the spin-density distribution. This loss of symmetry leads to the prediction that each of the five carbon resonances in the axial ligands must have distinct Fermi shifts. Notably, the shifts of methyl groups in these ligands are expected to appear in both negative and positive ranges, depending on their proximity to the z-axis of the distortion, Figure

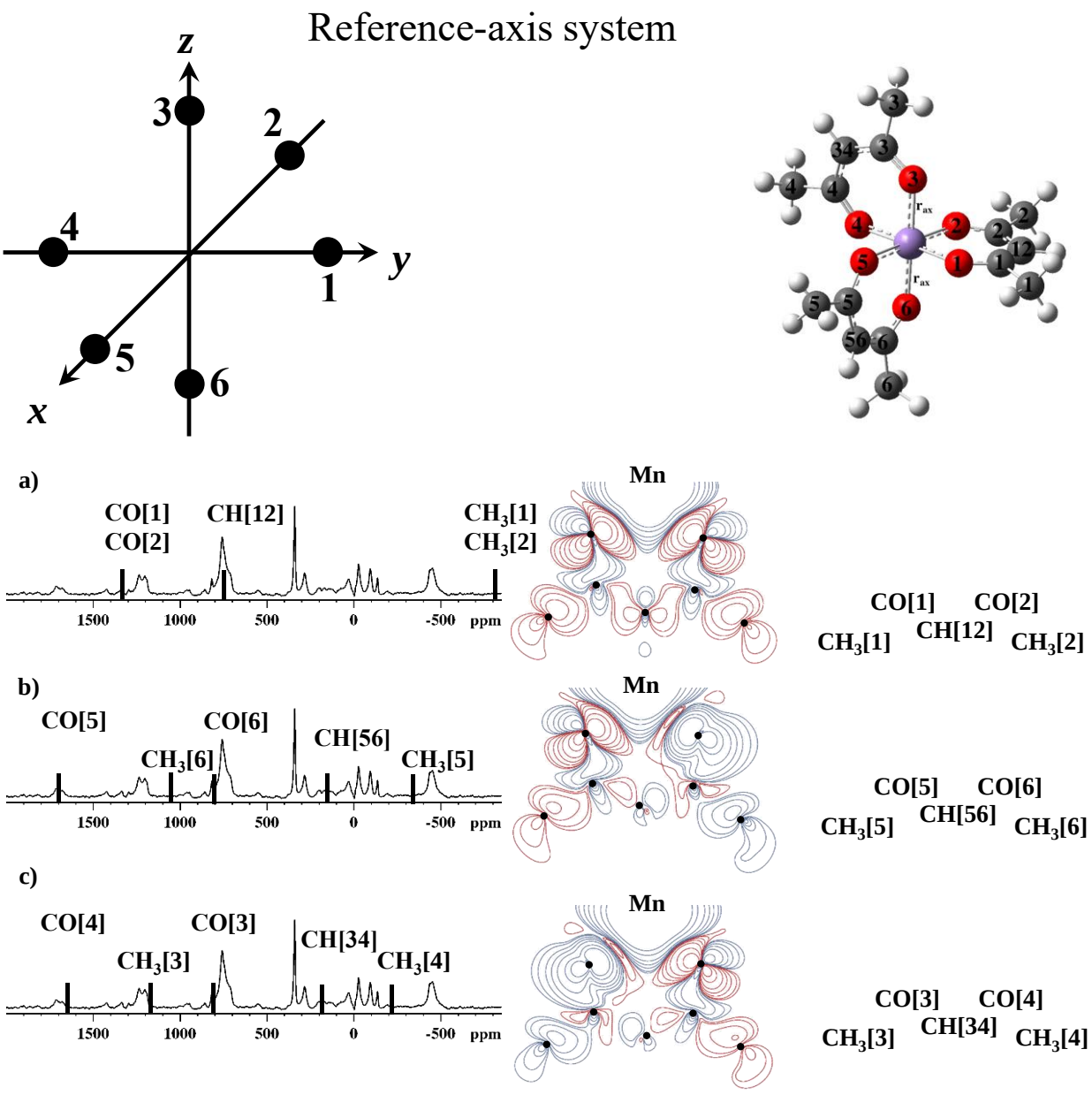

FIGURE 5.4: Detailed crystallographic assignment of ^{13}C NMR of γ-Mn(acac)$_3$ with equatorial elongation (r_{eq}) as illustrated in the reference diagram (top right). Contour plots (middle) and calculated resonance shifts (left, black bars) are presented for each of the three ligands in the reference-axis system, where a) is the xy-plane ligand, b) is the xz-plane ligand and c) is the yz-plane ligand. Red contours signify regions of negative spin density, blue contours signify regions of positive spin density.

5.4b and c. This difference in Fermi shifts stems from the nature of the MO interactions of the d_{z^2} orbital with the oxygen atoms. According to Table 5.1, this orbital has a stronger overlap with axial ligands than with equatorial ligands. This asymmetric interaction is the cause of the distorted spin-density in elongated ligands and additional positive-spin density at the methyl groups. The two distorted ligands in Figure 5.4b and c possess similar Fermi shifts, which reflect their comparable chemical environments.

TABLE 5.1. Selected molecular-orbital symmetries in O_h field.

Metal *d*-orbital	Metal - Ligand orbitals
$d_{x^2-y^2}$	$1/2\ (\sigma_1 + \sigma_2 - \sigma_4 - \sigma_5)$
d_{z^2}	$\sqrt{2}/6\ (2\sigma_3 + 2\sigma_6 - \sigma_1 - \sigma_2 - \sigma_4 - \sigma_5)$

The magnetic moment in $Mn(acac)_3$ has been approximated as spin-only with a free-electron g-value. EPR studies of $Mn(acac)_3$ have been done exclusively at 20 K and give broad resonances with g_{iso} of 1.99, which is near the free-electron g-value [65]. The assignment of the experimental spectrum with computational data is given in Table 5.2. Signal identification of functional groups agrees approximately with the assignments based on $^{13}C\{^1H\}$ REDOR spectra Figure 5.3. Table 5.2 provides information on the magnetic environments of distorted ligands. Signals from CH_3[4] and CH_3[5] groups are in the equatorial plane and both are predicted to have a negative shift. Carbonyl groups, CO[4] and CO[5], that are directly attached to these methyls are also magnetically inequivalent and possess a slight difference in their Fermi couplings. However, methine groups of the two axial ligands, CH[34] and CH[56], are observed

TABLE 5.2: ^{13}C and ^{1}H NMR of γ-$Mn(acac)_3$ and DFT calculation. Calculated and experimental shifts are in ppm at a sample temperature of 55 ˚C. ^{1}H and ^{13}C shifts from the same functional groups are indicated and appear in the order as listed.

Group	^{13}C		^{1}H	
	A_{calc} (MHz) {A_{exp}}	δ_{calc} [a] {δ_{exp}}	A_{calc} (MHz) {A_{exp} [b]}	δ_{calc} {δ_{exp}}
CO[5]	1.99 {1.61(3)}	1703 {1423}		
	1.94 {1.49(3)}	1639 {1334}		
CO[1]	1.51	1344		
CO[2]	1.50 {1.36(3)}	1335 {1234}		
CH_3[3]	1.48	1154	(0.16, 0.076, 0.041)	19.3
CH_3[6]	1.35 {0.91(2)}	1059 {720}	{0.28, 0.13, 0.072} (0.071, 0.270, 0.044) {0.09, 0.34, 0.06}	26.5 {32.8}
CO[6]	0.81	806		
CO[3]	0.80 {0.74(2)}	801 743		
CH[12]	0.84 {0.86(2)}	{758}	0.212 {0.22(1)}	45.2 {48.3}
CH[34]	0.11	183	-0.004 {0.040(2)}	3.6 {12.5}
CH[56]	0.08 {0.31(1)}	162 {340}	-0.011 {0.016(2)}	2.5 {8.4}
CH_3[4]	-0.33 {-0.07(1)}	-224 {-26.8}	(0.118, -0.355, 0.128) {-0.004, -0.005, 0.014}	-5.1 {2.2}
CH_3[5]	-0.50 {-0.16(1)}	-352 {-93.9}	(0.096, 0.116, -0.321) {-0.004, -0.005, 0.014}	-5.1 {2.2}
CH_3[2]	-1.09 {-0.61(2)}	-803 {-439}	(0.245, 0.566, -0.033) {0.15, 0.35, -0.021}	51.5 {32.8}
CH_3[1]	-1.10 {-0.63(2)}	-810 {-454}	(0.540, -0.103, 0.302) {0.35, -0.067, -0.20}	49.1 {32.8}

a) Shifts were calculated according to equation 2.18.
b) Couplings from individual hydrogens from the same methyl group are scaled to match the average experimental shift.

as a single resonance, whereas the prediction states that these should be separate signals according to the fixed molecular structure model. As these methine groups are not equivalent in the unit cell, their single magnetic resonance suggests a presence of a vibrational motion by which these two sites give indistinguishable resonances. Unfortunately, other carbonyl (CO[3] and CO[6]) and methyl (CH_3[3] and CH_3[6]) groups have Fermi coupling magnitudes that cause their resonances to overlap at our experimental conditions, Table 5.2. This coincidental overlap is caused by an unfortunate combination of different diamagnetic positions of these functional groups with the compensating difference of their Fermi shifts at a particular temperature. This "on-resonance" condition can be regulated by temperature variation, Figure 5.2.

With the knowledge of the expected shifts of the functional groups through spin-density maps, conclusions may be drawn that the overlapped signal in Figure 5.2 is composed of carbonyl (CO[3] and CO[6]) and methyl (CH_3[3] and CH_3[6]) groups of the two distorted ligands, and the methine group, CH[12], of the undistorted ligand, Figure 5.4. Higher sample temperature could further increase the resolution; however, the instrumentation is limited to 70˚C. A Hahn-Echo experiment at the sample temperature of 45˚C, Figure 5.2c, indicates that the carbonyl and methyl groups are nearly degenerate between the two distorted ligands. Both groups form a single sharp resonance at ~760 ppm with no sign of site-specific separation. In other words, there is a single temperature where resonances with different hyperfine couplings and different diamagnetic origins can produce a single featureless peak. ^{13}C NMR suggests that distorted ligands, with JT-elongated Mn-O bonds, undergo asymmetric vibrational motion where the ligand structure is relatively immobile near the xy-plane, but undergoes greater vibrational motion of functional groups the further they are from the xy-plane. This demonstrates the potential of solid-state NMR to evaluate local structural dynamics in bulk solid material.

5.4 ^{1}H NMR as a phase indicator

Figure 5.5 shows the ^{1}H NMR spectrum of γ-Mn(acac)$_3$ at the fast spinning-rate of 60 kHz. This spinning rate enables the observation of an additional resonance at 50 ppm that was not resolved in earlier works of Ishii that used slower MAS [32]. This resonance is attributed to the methine group in accord with computational predictions and relative signal intensities, Table 5.2. Signal fits and assignments for the ^{1}H NMR spectrum are presented in Figure 5.6. Parameters of the fit are outlined in Table 5.3. The signal assignment based on computational modeling, Table 5.2, agrees with the stoichiometric intensities of the fit in Figure 5.6 as well as the 2D INEPT experiments of Ishii *et al.* [32] Three distinct regions of methyl functional groups mimic the inequality in spin-density distribution at the ^{13}C sites. Methyl groups with ^{13}C nuclei with negative spin-density occur in the xy-plane of the molecule. Spin densities at these methyls are dominated by similar molecular orbital interactions as the d^1-d^3 metal complexes discussed in Chapter 4. The ligand that mimics the d^1-d^3 complexes the most is in the xy-plane of Mn(acac)$_3$. This similarity in spin-density distribution can be seen through the order of the ^{13}C assignments, as well as the net positive Fermi shift of the ^{1}H signal. Signals from the C**H** groups are indicative of the inequivalence between the xy-ligand and the two z-elongated ligands, as there is a characteristic separation in resonances, Figure 5.6. This scenario mimics the resonance distribution in the Ti^{3+} complex, where there is a clear separation between the two types of ligands in the ^{13}C and ^{1}H spectra (Chapter 4).

The strong signal sensitivity of the ^{1}H peaks finds applicability in paramagnetic NMR for the detection of impurities (Figure 5.5). This impurity signal in the 10-25 ppm range was previously detected by Ishii's group, but was attributed to a methine signal in their 2008 publication [33], where their spectrum in Figure 1d closely resembles our result in Figure 5.5. Their previous study of this complex in 2006 using $^{13}C\{^{1}H\}$ 2D INEPT correlation experiment [32] is missing the ^{1}H signal in the indirect dimension between 10 and 25 ppm, which we attribute to an impurity phase.

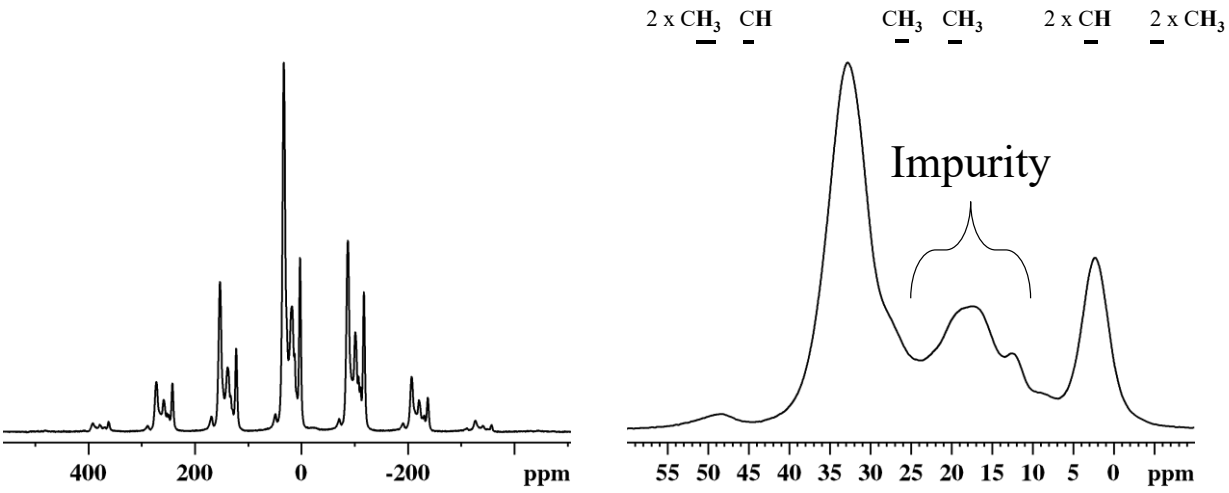

FIGURE 5.5: ^{1}H MAS NMR of γ - $Mn(acac)_3$ at 55˚C. Proposed signal assignment regions are indicated according to DFT calculation as used in Figure 5.4 and Table 5.2, where signals from individual methyl hydrogens are averaged to simulate fast rotation.

TABLE 5.3: ^{1}H NMR fit parameters from Figure 5.6. Fitting included the spinning sideband manifold, not shown in Figure 5.6. Assignments from Table 5.2, group labels from Figure 5.4.

Group	δ_{iso} (ppm)	FWHM(kHz)	I_{fit} (%)	$I_{stoichiometry}$(%)
CH[12]	50	2.5	3.6	4.8
CH_3[4, 6] CH_3[1,2]	34	2.7	56	57
CH[34]	12	1.3	6.3	4.8
CH[56]	8	1.2	2.6	4.8
CH_3[3,5]	1.7	1.7	31.4	28.6

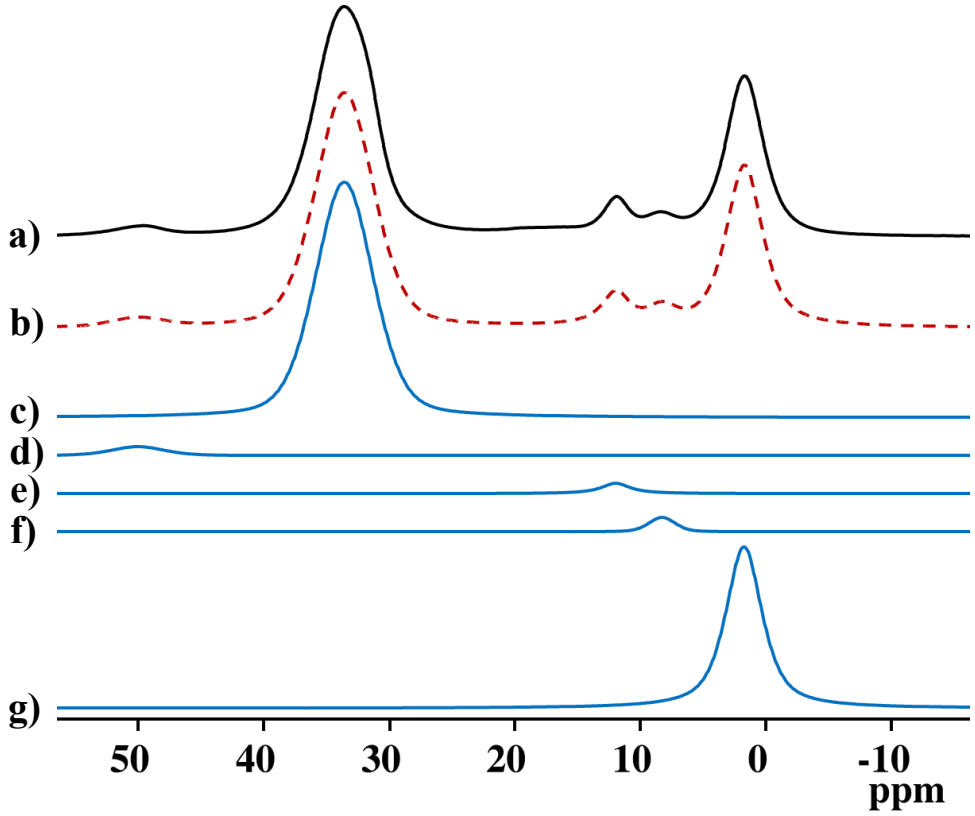

FIGURE 5.6: ^{1}H NMR of γ - $Mn(acac)_3$ at 55˚C of a) experimental spectrum, b) deconvolution fit, c) C**H**$_3$[4] + C**H**$_3$[6] + C**H**$_3$[1]+ C**H**$_3$[2], d) C**H**[12], e) C**H**[34], f) C**H**[56] and g) C**H**$_3$[3]+ C**H**$_3$[5]. (see Table 5.3)

The presence of the impurity can be explained by the fact that the sample quality of γ - $Mn(acac)_3$ can only be obtained as technical grade. Most studies do not attempt to purify the sample as the recrystallization step can lead to structural alteration.[29, 32, 62, 65] The additional crystalline phase was sensitive to an open-air environment. Figures 5.7d shows the ^1H spectrum of the sample as received from Alfa Aesar and spectrum e is the same sample after a prolonged exposure to air. Changes in intensity in the region of 12 - 30 ppm indicate conversion of the second phase to γ - $Mn(acac)_3$. There has been a previous report of phase changes in $Mn(acac)_3$ that were triggered by variations in temperature [66]. This change was reported to occur irreversibly from the δ to ε phase on slow cooling of δ - $Mn(acac)_3$ below 190 K [66]. A subsequent increase in temperature to ambient conditions did not reverse the transition. My hypothesis is that a similar phase-change might occur with the γ –phase upon heat treatment, but the new phase would not be stable at ambient conditions. I varied the temperature by submerging

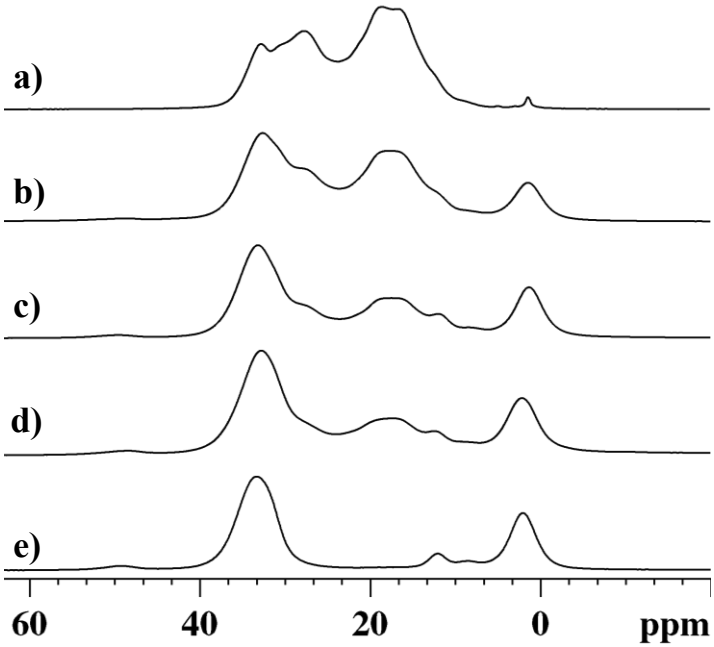

FIGURE 5.7: ^1H NMR of $Mn(acac)_3$ at 55˚C: a) as-made sample; b, c) two trials of $N_2(l)$ cooling of commercial sample; d) original sample from Alfa Aesar; e) Alfa Aesar sample after extended air exposure.

a sealed-glass NMR tube containing the powdered sample as obtained from Alfa Aesar in liquid nitrogen. The sample was brought to room temperature by slow nitrogen evaporation. Results of two evaporation trials are shown in Figure 5.7b and c, where the secondary phase gains intensity relative to the signal from γ - $Mn(acac)_3$. Figure 5.7a shows the ^1H spectrum of δ-$Mn(acac)_3$ that was synthesized by conventional methods [98]. The sample identity was confirmed using powder x-ray diffraction (see Appendix Figure 5.1) [66]. This signal matches the secondary phase in the region 12 - 30 ppm to the δ-$Mn(acac)_3$. Additional evidence for this identification can be drawn from the ^{13}C MAS NMR spectra in Figure 5.8, which are for selected samples from Figure 5.7. The impurity phase can be traced through these samples at different concentrations and matches the synthesized δ-$Mn(acac)_3$ like a fingerprint. The ^{13}C spectrum of δ-$Mn(acac)_3$, Figure 5.8a, is extremely complicated as the unit cell contains four unique molecules with different degrees of Jahn-Teller compression; therefore a detailed assignment was not done.

An interesting observation was made regarding the conditions of this phase change. A slow rate of heating, i.e., temperature increase through the slow nitrogen evaporation, seems to be essential for phase interconversion. When the sample was heated rapidly to room temperature, there was no observed change to the ^1H NMR spectrum. My hypothesis is that a slow rate of heating seems to allow enough energy and time for the phase change to occur through an increase in entropy and allows the system to crystallize into a more disordered, yet less thermodynamically stable Jahn-Teller compressed δ-phase. The thermodynamic instability of this phase is apparent in the phase reversal upon prolonged exposure to air. Thus, on the basis of the previous study and current findings, there seems to be a pathway for conversion of the γ-phase into the δ- and ε- phases via the thermal treatment alone [66].

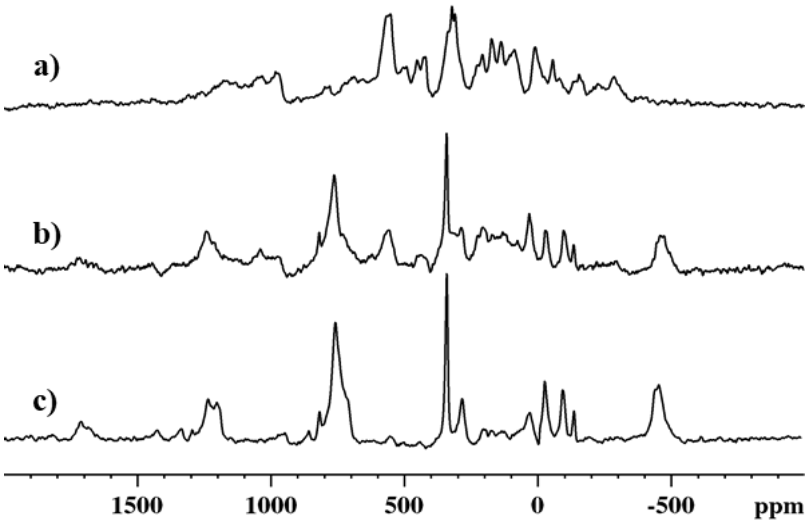

FIGURE 5.8: ^{13}C NMR of $Mn(acac)_3$ at 55˚C. a) Hahn-Echo of the synthesized sample corresponding to Figure 5.7a (transmitter at 300 ppm); b) adiabatic double-echo of the sample in Figure 5.7b; c) adiabatic double-echo of the original sample from Alfa Aesar, Figure 5.7d.

5.5 Effect of elongation vs compression in $Mn(acac)_3$

The large variation in atomic arrangements of $Mn(acac)_3$ stems from the ability of the molecular structure to adopt either a compressed or an elongated Jahn-Teller distortions. As paramagnetic NMR shifts are sensitive to orbital occupancies of unpaired electrons, one would expect to observe a clear spectroscopic distinction in signals between the two forms of distortion in any of the structures. This sensitivity to orbital occupancies can be seen in the calculated spin-density contour maps in Figure 5.9, which provides evidence of different occupancies of Jahn-Teller elongated and compressed molecules according to Table 5.1, where the positive spin-density traces antibonding orbitals between the metal and oxygen atoms. The unpaired-spin density in the metal-oxygen region of the equatorial ligand in the compressed structure shows the dominant σ* antibonding character, in contrast to the contour of the elongated molecule. Table

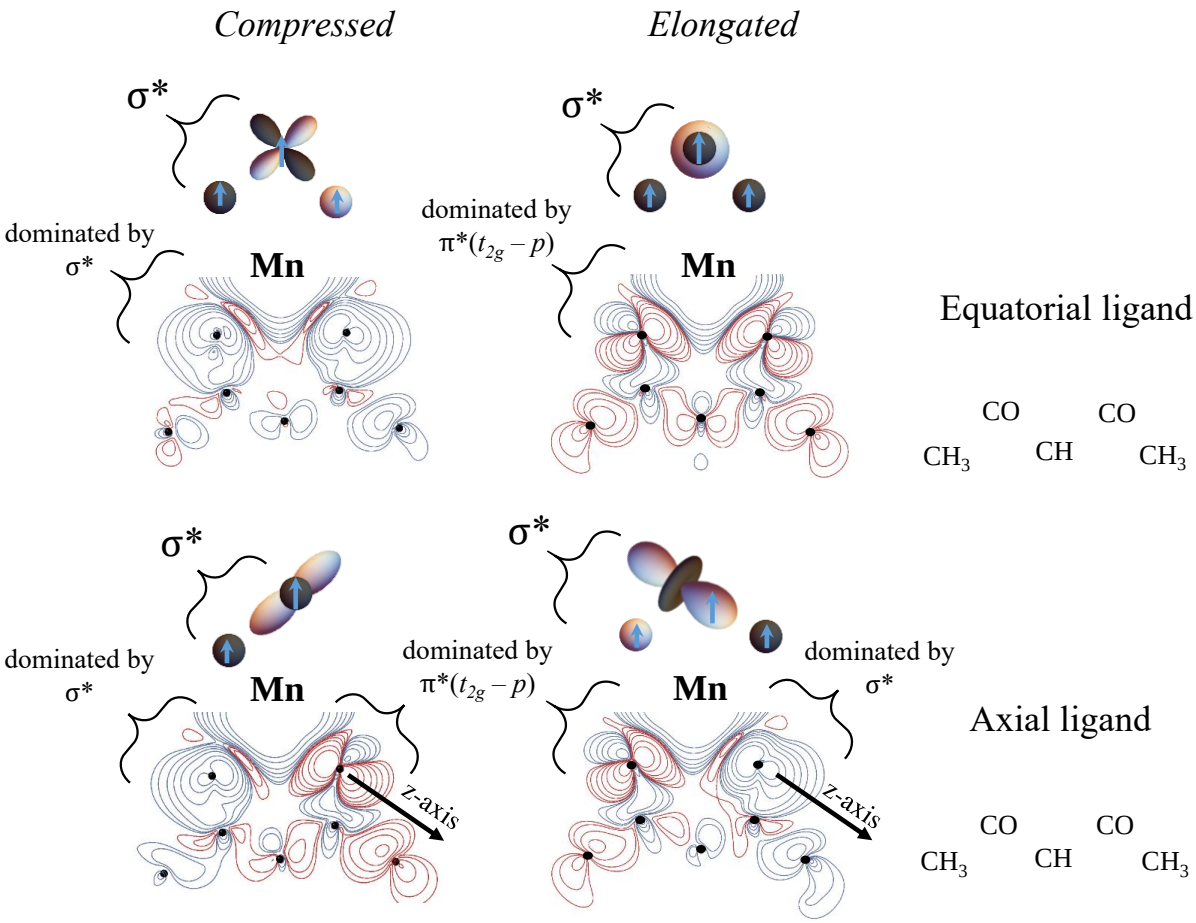

FIGURE 5.9: Representative spin-densities of Jahn-Teller elongated and compressed forms of $Mn(acac)_3$. Both axial ligands show similar spin-densities in either form of distortion, thus a single plot is provided for each case. The direction of the distortion is indicated with the z-axis.

5.1 suggests that metal-oxygen orbitals in the equatorial plane have a normalization coefficient of 0.5 upon an interaction with the d_{x2-y2} metal orbital. However, the same metal-oxygen orbitals only have the coefficient of about 0.236 when bonded with the d_{z2} orbital, which is occupied in the elongated structure. These coefficients represent the different degree of mixing of these orbitals and, thus, a difference in degree of delocalization of the unpaired-electron density. Therefore, it is expected that the spin-density contour-plot of the equatorial ligand in the compressed structure would show a greater degree of σ* character than its elongated counterpart, as observed in Figure 5.9. As a result of the low mixing coefficient of the d_{z2} orbital, the spin

density distribution of the equatorial ligand in the elongated structure is dominated by the $\pi^*(t_{2g} - p)$ interaction, Figure 5.9, as seen in the d^1 - d^3 complexes in Chapter 4. As a consequence, these different metal-orbital occupancies lead to distinctions in overall spin-density propagation in the equatorial ligand. The remaining two ligands are parallel to the z-axis of distortion and have similar spin-density distributions between elongated and compressed forms. However, their Fermi shifts should not lead to overlapped ^{13}C NMR signals as the magnitudes of their metal-oxygen orbital overlaps differ according to Table 5.1.

Figure 5.10 summarizes the calculated ^{13}C shifts of all individual molecules in the five known forms of $Mn(acac)_3$, with their respective shift ranges. These ranges include structural distortions (such as ligand asymetry, out-of-plane methyl groups, etc.) that have not been addressed in great detail due to their complex nature, but they introduce additional variation to the magnitude of the Fermi coupling. Nevertheless, general pattern of resonance shifts emerges that is consistent with our previous discussion on the main differences between elongated and compressed forms of $Mn(acac)_3$. This is an illustration of the sensitivity of paramagnetic NMR to site-specific magnetic environments, whereas distortions due to packing arrangements act as pertubations to the spin-density distribution model.

The predicted resonance-shift ranges in Figure 5.10 suggest the absence of a methyl signal in the negative range between -50 to -900 ppm for Jahn-Teller compressed molecules. This observation correlates with the experimental ^{13}C spectrum of the elongated molecule of the γ- phase, Figure 5.4, where three distinct signals are observed at -21 ppm, -96 ppm and -450 ppm, of which all correspond to methyl groups. The ^{13}C spectrum of the δ- phase shows the signal extending all the way to -200 ppm; however, due to severe signal overlap from the four

distinct Jahn-Teller compressed molecules and spinning sidebands, no definitive assignment can be made.

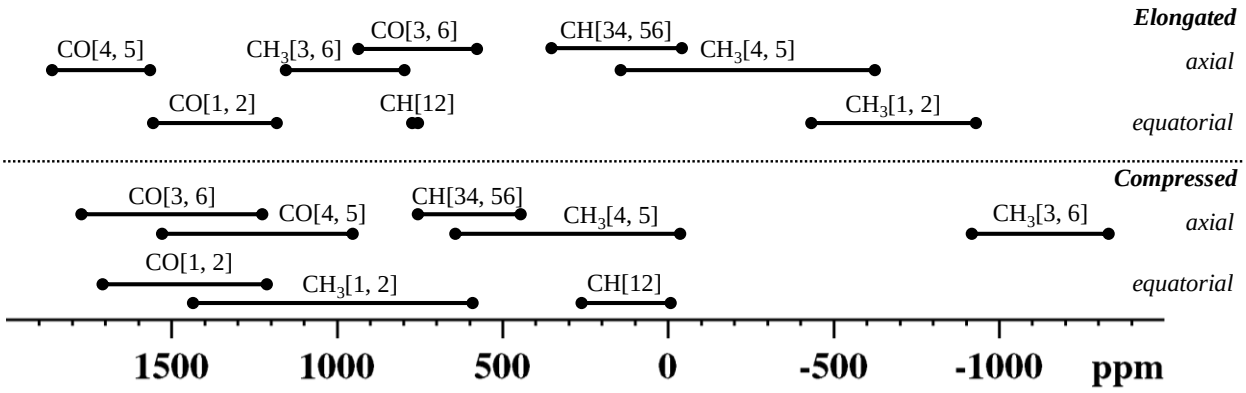

FIGURE 5.10: Ranges of calculated chemical shifts for individual functional groups from all molecules in five known crystal structures of $Mn(acac)_3$. Notation follows the reference system in Figure 5.4.

Figure 5.10 provides additional confidence in assignment of the region with signal overlap in the γ- phase, Figure 5.4. The narrow range of possible shifts of the methine group suggests that the signal overlaps with the two signals from carbonyl and two methyl groups, but unfortunately cannot be resolved within the 20 K temperature variation allowed by our instrumentation. A definitive assignment of the overlapped region could be provided by a correlation experiment with ^1H through cross polarization; however, attempts to achieve the Hartmann-Hann match were unsuccessful.

5.6 Effect of d_{z^2} orbital on spin density in equatorial ligand

The elongated molecule of $Mn(acac)_3$ has similarities in the spin-density distribution of the equatorial ligand with the d^1 - d^3 metal acacs. Distorted ligands, with the JT-elongated Mn-O bond, exhibit uneven contributions from the d_{z^2} orbital. The major difference between the

equatorial ligand in $Mn(acac)_3$ and the acac ligands in the Ti^{3+}, V^{3+} and Cr^{3+} complexes is the presence of an additional contribution from the d_{z^2} orbital, which interacts symmetrically with the oxygen atoms in the equatorial plane (Table 5.1). Thus, a direct comparison of spin densities at ^{13}C sites between the d^1 - d^3 systems and the d^4 system illustrates the contribution of the d_{z^2} orbital to the spin density of the equatorial ligand.

Additional data points for the equatorial ligand of $Mn(acac)_3$ are added to Figure 4.21 to obtain Figure 5.11. The carbonyl group exhibits a more negative contribution to its spin density with the introduction of the d_{z^2} orbital. This can be explained with the model of orbital interactions, Figure 5.12, where the additional contribution of σ* electron density to the oxygen produces polarization of oxygen-carbon bond. As a result, the **C**O is left with the negative spin-density contribution. This effect can be seen in Figure 5.11, where the carbonyl of $Mn(acac)_3$ shows more negative spin-density than the general trend would suggest. The overall reduction in positive spin-density at the carbonyl reduces the polarization of the carbonyl-methyl bond and thus, the methyl ^{13}C nucleus exhibits slightly more positive spin-density as compared to the Cr^{3+} analog, Figure 5.11. The reduction in polarization and enhanced delocalization from the carbonyl to the methine group produces the observed increase in spin density with respect to t_{2g}^3 $Cr(acac)_3$.

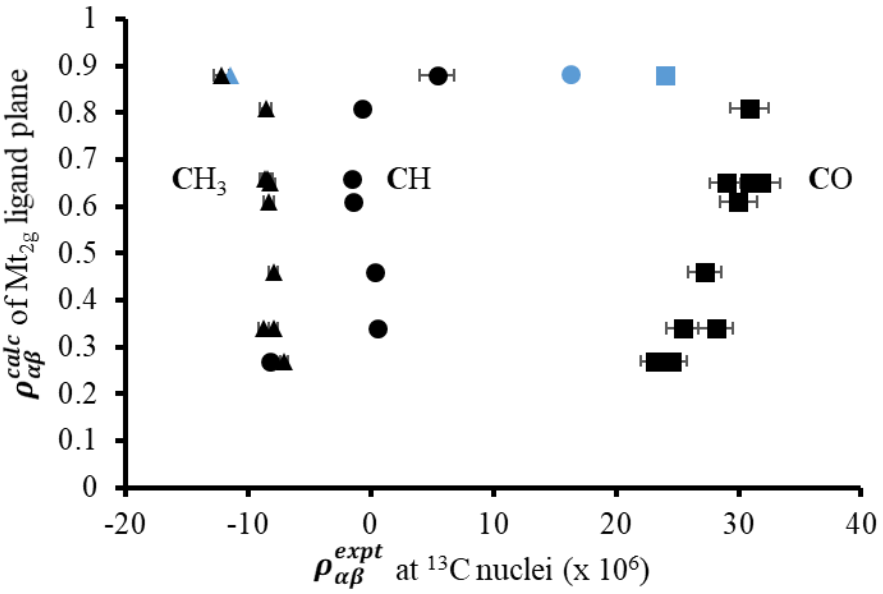

FIGURE 5.11: Relation between spin density in the t_{2g} orbital in the ligand plane and spin density at carbon nuclei of the ligand for $M(acac)_3$, where M = Ti, V, Cr in dark. Blue data points are added from the equatorial ligand of γ - $Mn(acac)_3$ that include the effect of the d_{z^2} orbital. Squares denotes the carbonyl group, circles denote the methine group and triangles denote the methyl group.

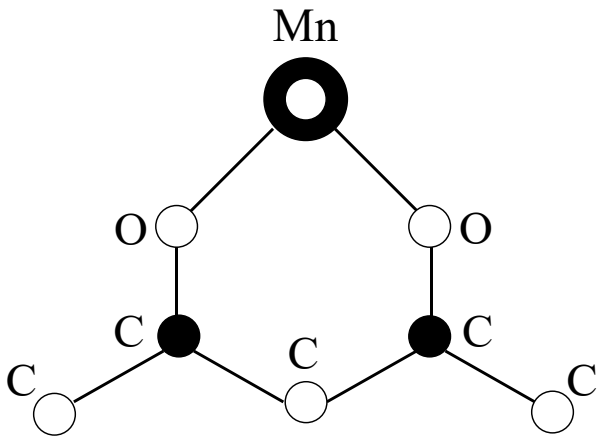

FIGURE 5.12: Delocalization of the unpaired electron spin density from the d_{z^2} orbital to the acac ligand in the equatorial plane. Dark and light colors indicate orbital phases. All orbital interactions are outlined as antibonding σ* - type.

5.8 Conclusion

Paramagnetic solid-state NMR can be used to assess reliably the local chemical environment near the paramagnetic center, even with many unpaired spins of S = 2. Spin-distribution pathways can successfully provide an intuitive interpretation of the Fermi-shift direction and magnitude. The Fermi shift together with the large magnetic moment introduces a significant increase in the sensitivity of the peak position to the local chemical environment. The structure of elongated $Mn(acac)_3$ follows the spin-density distribution pathway and is used as a model to study the effect of the occupied d_{z^2} orbital on the acetylacetonate ligand.

Chapter 6:

Bis(2,4-pentanedionato)metal ($d^9 – d^7$)

Bis(acetylacetonato)metal(II) compounds with d^n (n = 7-9) configurations were studied to assess the impact of occupied orbitals of e_g – type symmetry. These will be presented in order of increasing complexity, beginning with the S = ½ complex of $Cu(acac)_2$ (d^9) , proceeding with the S = 1 complex of $Ni(acac)_2 \cdot 2H_2O$ (d^8) and concluding with the S = 3/2 complex of $Co(acac)_2 \cdot 2H_2O$ (d^7).

6.1 $Cu(acac)_2$, d^9

Bis(acetylacetonato)copper(II) is an anhydrous paramagnetic complex with a square-planar geometry of oxygen coordination around the central copper(II) [69]. The molecule has inversion symmetry at the metal center that leads to a pair of equivalent ligands. Therefore, only up to five distinct resonances of ^{13}C can be expected in NMR spectra and up to three resonances in ^{1}H NMR spectra owing to the rotational averaging of the methyl groups.

6.1.1 ^{13}C MAS NMR

The ^{13}C MAS NMR spectrum of $Cu(acac)_2$ is shown in Figure 6.1. It has three resolved ^{13}C resonances near the diamagnetic region. The assignment of these resonances as indicated by DFT calculation is that the signal at the lowest frequency belonging to the methine carbon, and the two overlapping resonances belonging to carbonyl groups. The methyl signal is predicted to be at very high frequency, on the order of 1000 ppm, which is experimentally unobserved,

presumably due to broadening from its large Fermi-coupling constant (see Chapter 8). The observation of a single methine signal is consistent with the presence of a unique acetylacetonate ligand and the presence of an inversion center of symmetry in the molecule. This contrasts with the metal trisacetylacetonates (Chapters 4 and 5), where the ligands are not related by molecular symmetry.

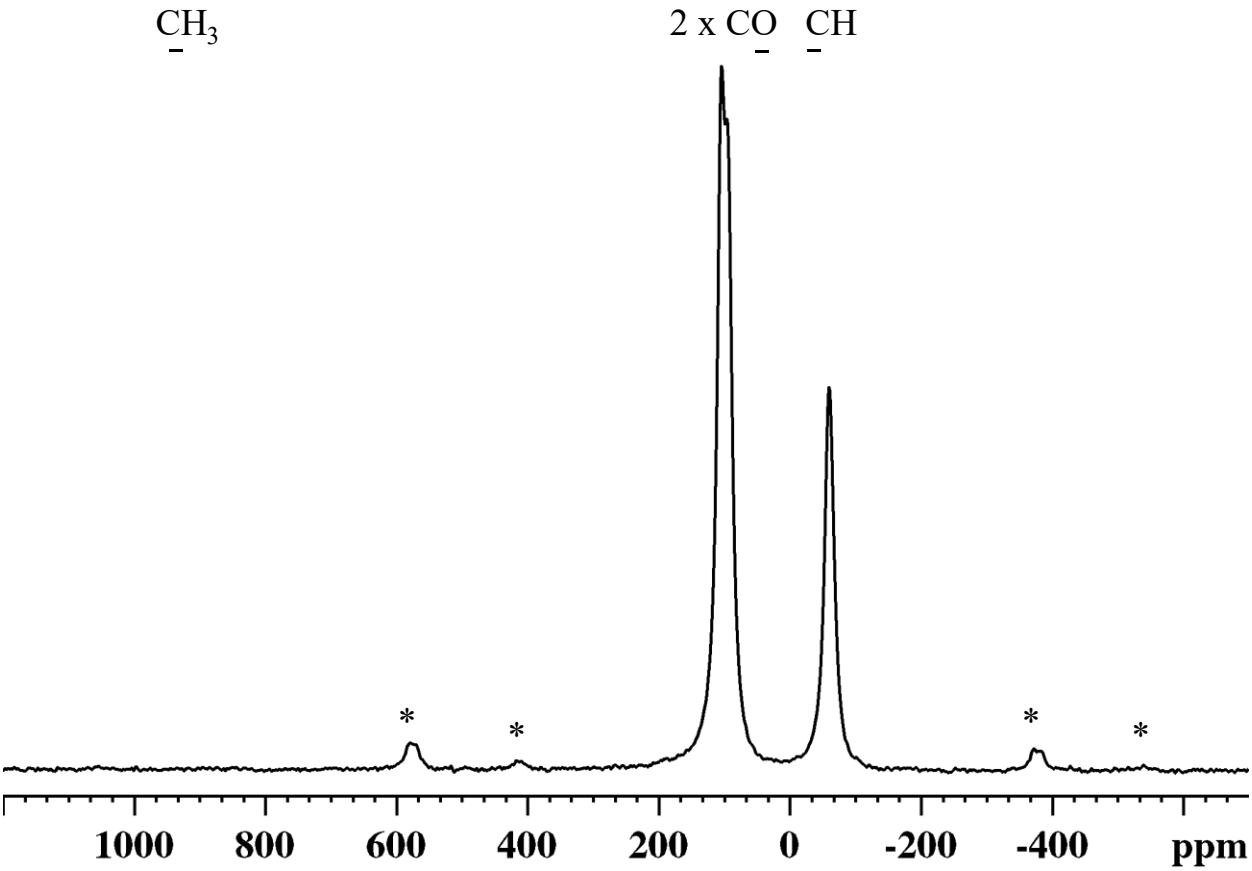

FIGURE 6.1: ^{13}C MAS Hahn-Echo spectrum of $Cu(acac)_2$ with bars indicating calculated shift regions. Asterisks indicate MAS spinning sidebands.

The assignment of the ^{13}C resonances was confirmed by $^{13}C\{^1H\}$ REDOR, Figure 6.2, where the largest dephasing is attributed to the methine signal at -60 ppm, and the two signals that show no intensity loss are confirmed as due to the carbonyl groups.

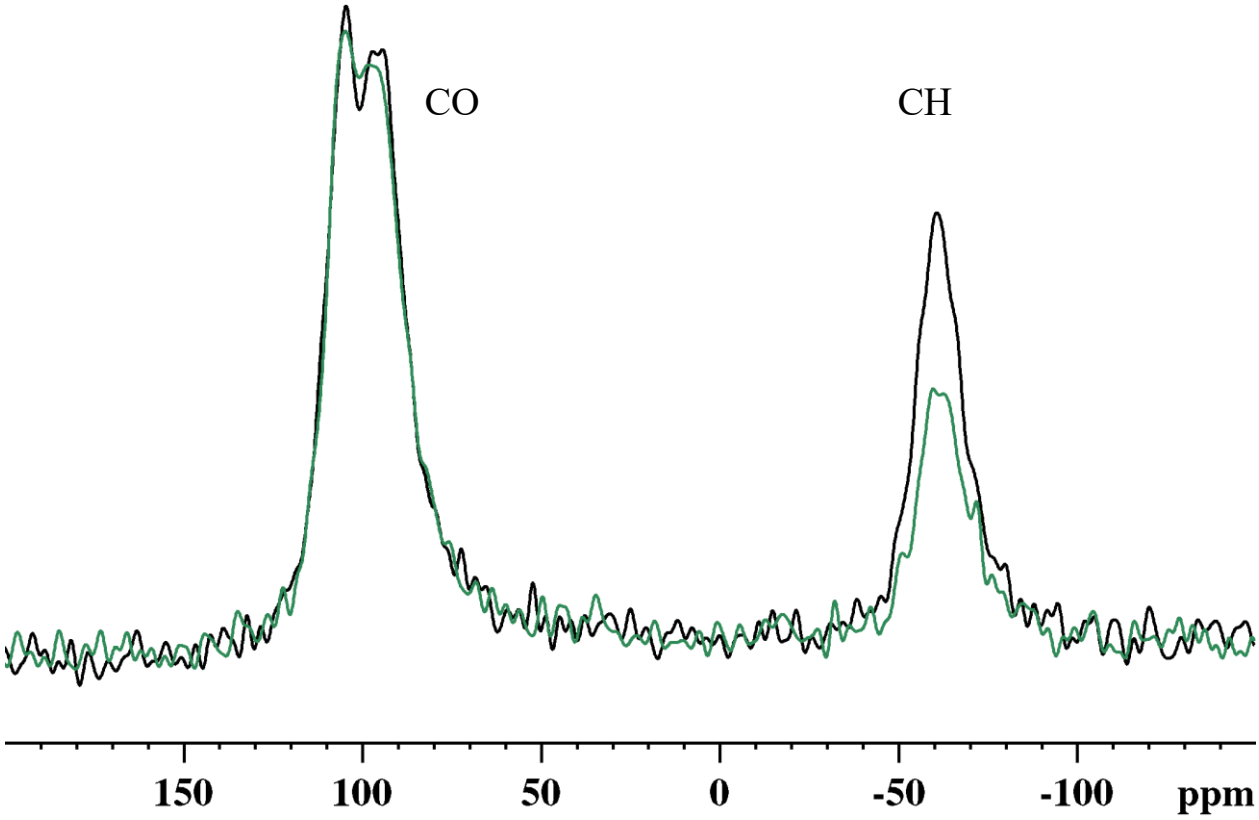

FIGURE 6.2: $^{13}C\{^1H\}$ REDOR of $Cu(acac)_2$. The spectrum in black indicates no dephasing, whereas the spectrum in green has introduced a ^1H recoupling pulse.

6.1.2 Spin-density distribution

The only metal orbital that is singly occupied in this complex has $d_{x^2-y^2}$ symmetry, which makes $Cu(acac)_2$ unique, as its unpaired spin-density distribution represents only interactions with the $d_{x^2-y^2}$ orbital. The contour plot is given in Figure 6.3, where a clear contour line illustrates the shape of the $d_{x^2-y^2}$ symmetry at the metal center that interacts with oxygen atoms exclusively through σ* symmetry. This is analogous to the interaction of the equatorial ligand in compressed $Mn(acac)_3$ structure only in the absence of interfering t_{2g} – symmetry orbitals, Figure 5.9. Thus, oxygen atoms are left with a significant amount of positive spin-density in the *s*-orbital, which

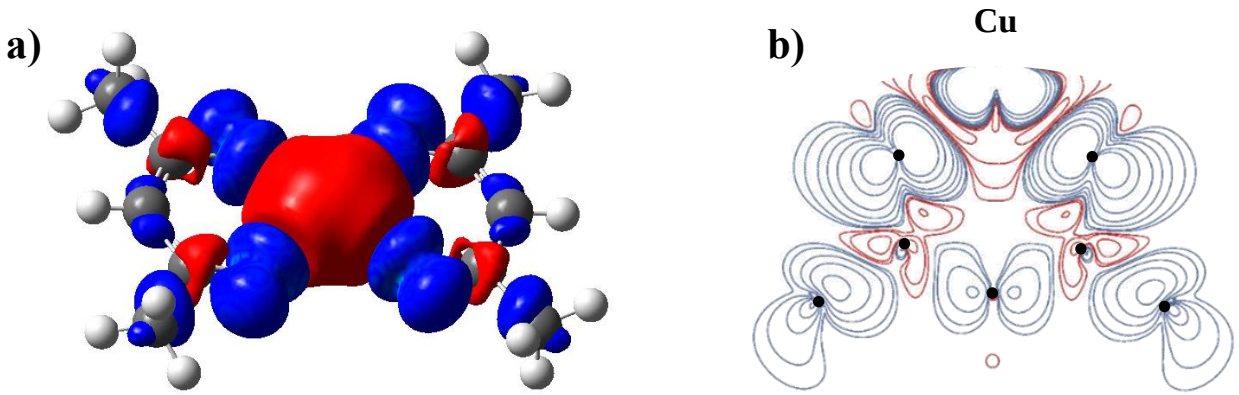

FIGURE 6.3: Spin-density of $Cu(acac)_2$: a) isosurface, b) contour-plot in the plane of the ligand.

would in turn polarize all bonds of the oxygen with other atoms, in this case with the carbonyl carbon. This polarization can be seen in the spin-density plot, Figure 6.3. The significant amount of positive spin-density at the oxygen *s*-orbitals leads to delocalization from the oxygen to carbon via σ* orbitals. This positive spin-density counteracts the negative contribution from the polarization and lowers the magnitude of the Fermi coupling for the carbonyl carbon.

The propagation of delocalization stops at the methine carbon as the phase symmetry of the $d_{x^2-y^2}$ orbital creates an orbital node at that location, Figure 6.4. Therefore, the spin density at **C**H cannot have any positive spin-density contribution from the delocalization mechanism. The excess of negative spin-density at **C**O creates polarization among its other bonds to **C**H_3 and **C**H groups which leaves the latter with a positive density contribution. In Figure 6.3, a large positive Fermi shift is expected at the methyl due to the polarization mechanism from the **C**O. The same mechanism can also be expected to cause positive spin-density at the methine group. The spin-density contour-plot does suggest that the positive density is concentrated near the methine nucleus; however, there is no overlap at the atomic core. This unique spin-density distribution

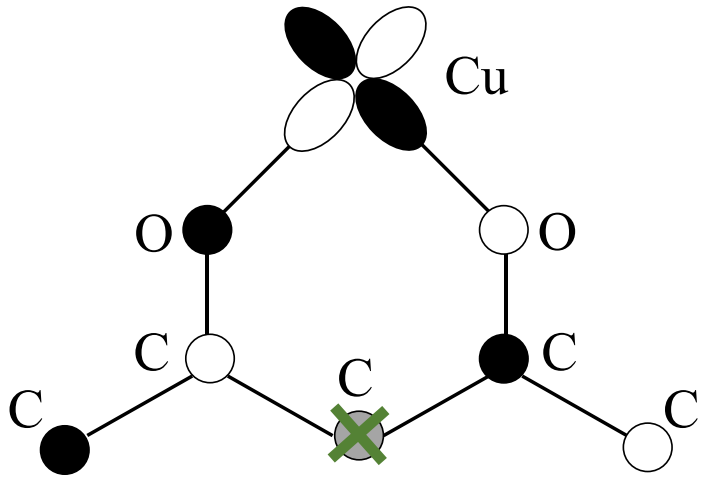

FIGURE 6.4: Delocalization of the unpaired electron spin-density from the d_{x2-y2} orbital. Dark and light colors indicate orbital phases. All orbital interactions are outlined as anti-bonding σ*. The green "X" indicates a node.

can be explained by a phase dependence of the polarization mechanism that has not yet been considered in the literature. The polarization mechanism stems from the ability of overlapping orbitals to exchange electrons with like spins that lowers the interaction energy between the two orbitals and causes the preferential spatial spin-distribution. In order for the two orbitals to overlap they must possess the same phase. In the case of $Cu(acac)_2$, the phases of the unpaired spin-density at the carbonyl carbons are opposite, thus the polarization of each methine-carbonyl bond has opposing phase signs that cancel at the nuclear core and create a node in which only the negative spin-density from delocalization can reside. Therefore, **C**H cannot have any positive spin-density contribution due to the symmetry restriction of the d_{x2-y2} orbital in this system.

6.1.3 Theoretical treatment of paramagnetic shifts

The axial and equatorial components of the g values for this complex are 2.254 and 2.075 respectively, for a single crystal [130], with the isotropic value being 2.135, which deviates by only about 6% from the free-electron value of 2.0023. This is a small deviation for the purpose of the signal assignment when shifts are dominated by strong Fermi coupling. The magnitude of this deviation will be presented with additional discussion during the evaluation of the calculated resonance shifts.

Spectral assignments for $Cu(acac)_2$ can be done with an approximate spin-only model, as shown in Table 6.1, where the diamagnetic shifts have been selected from the ^{13}C and ^{1}H spectra of $Zn(acac)_2 \cdot 2H_2O$ as a model diamagnetic analog of bis(acetylacetonato)metal(II) complexes. In Table 6.1, the anisotropic term of the electronic magnetic moment is neglected and the paramagnetic shift is assumed to be solely governed by the Fermi coupling. As we have the structural information and the measurement of the magnetic anisotropy[130] in $Cu(acac)_2$, it is possible to estimate the contribution of the dipolar or pseudocontact shift to the net resonance shift using to the following equation [87]:

$$\delta_{pc} = \frac{\mu_0 {\mu_B}^2 S(S+1)}{36\pi r^3 kT}(3\cos^2\theta - 1)(g_{\parallel}^2 - g_{\perp}^2) \qquad \textbf{(6.1)}$$

where the r is the distance from the metal center to the NMR nucleus and θ is the angle between the Z-axis and the metal - nucleus internuclear vector. For $Cu(acac)_2$, we shall apply the point-dipole model with the assumption that the structure can be considered as axially symmetric (Figure 6.5) and that $g_{\parallel}$ and $g_{\perp}$ can be used to describe the magnetic anisotropy. This relation, together with geometrical parameters of the molecule in the solid state and magnetic anisotropy values, provides the following shifts for each of the functional groups: -5 ppm for the carbonyl,

-3.5 ppm for the methine and -1.5 ppm for the methyl ^{13}C shifts. The pseudocontact shift of the methine hydrogen is on the order of -1.5 ppm and for the methyl group the averaged ^{1}H shift is around -1.2 ppm. The magnitudes of these values are small compared to the observed paramagnetic shifts, and thus it is safe to conclude that the observed shifts are caused predominantly by the Fermi coupling.

TABLE 6.1: ^{13}C and ^{1}H NMR of $Cu(acac)_2$ and DFT calculations. Calculated[a)] and experimental shifts are in ppm at a sample temperature of 55 ˚C. ^{1}H and ^{13}C shifts from the same functional groups are indicated and appear in the order as listed.

Group	^{13}C		^{1}H	
	A_{calc} (MHz) {A_{exp}}	δ_{calc}[b)] {δ_{exp}}	A_{calc} (MHz) {A_{exp}[c)]}	δ_{calc} {δ_{exp}}
CO	-1.54 {-1.0(1)} -1.46 {-0.9(1)}	34 {95} 42 {104}		
CH	-1.28	-30 {-60}	-0.83 {-0.71(5)}	-16.5 {-10.5}
CH_3	8.84	930 {not observed}	(-0.45, -1.06, 0.58) {-0.14, -0.35, 0.19} (-1.13, -0.51, 0.76) {-0.39, -0.17, 0.26}	-6.0 {1.6} -5.6 {1.6}

a) shifts are calculated with the $g_{iso} = 2.135$
b) Shifts were calculated according to equation 2.18.
c) Couplings from individual hydrogens from the same methyl group are scaled to match the average experimental shift.

These values cannot be considered as analytical solutions, but rather a first approximation to the pseudocontact shift, as the point-dipole model only accounts for a single source of highly localized electron-spin density. The close packing of a crystalline solid introduces additional contributions to the pseodocontact shift from other molecules in the vicinity. The point-dipole method is an appropriate approximation to study the structures of macromolecules, such as

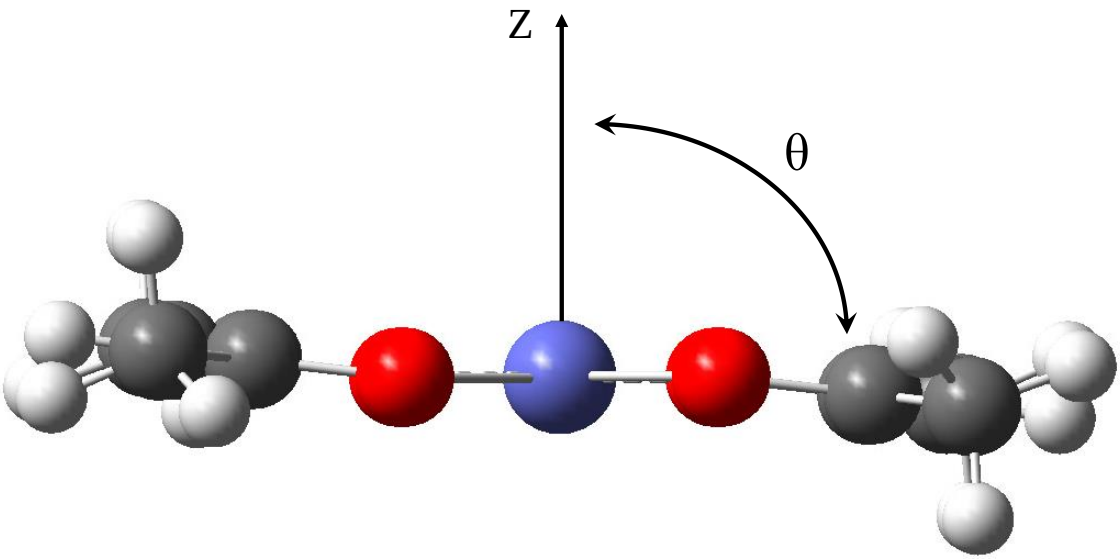

FIGURE 6.5: Illustration of pseudoaxial symmetry in $Cu(acac)_2$ with the relevant angle for the pseudocontact shift calculation.

proteins [41, 131]. There, the distance between paramagnetic centers is large and r distances are greater than 7 Å [87], which additionally lowers the contribution to the pseudocontact shift from spin delocalization.

Another way to estimate the pseudocontact shift is using the anisotropic part of the hyperfine-coupling tensor [132]. This method has the advantage of including the contribution from electron-spin delocalization from the metal center onto the ligand. However, this computational approach is heavily tied to the modeling system, i.e. the choice of theory level and model structure. In this scenario, I have done the modeling with the same level of theory as has been used throughout this thesis, mPW1PW91, and the structure is confined to a single molecule in the gas phase. The general equation for the pseudocontact shift for a doublet spin state has been given by Martin *et al* [132, 133] as:

$$\delta_{pc} = \frac{\Delta A \Delta g \mu_B}{2\gamma kT} \quad \textbf{(6.2)}$$

where Δg is the g-anisotropy defined as $1/3(g_{zz} - (g_{xx} + g_{yy})/2)$, and ΔA is the anisotropy of the hyperfine tensor defined as $1/3(A_{zz} - (A_{xx} + A_{yy})/2)$. The above relation is valid if both anisotropies are expressed in a common axis-system. The primary-axis system is generally chosen to be that of the g-tensor, which coincides with the molecular-axis of symmetry. Vector orientations and scalar magnitudes of both tensors are calculated or can be determined by EPR spectroscopy of a single crystal. Calculation at the mPW1PW91 level of theory indicates the following pseudocontact shifts: -0.2 ppm for the carbonyl, 0.9 ppm for the methine and -0.1 ppm for the methyl ^{13}C signals. The same calculation produced the following shifts for ^{1}H signals of the methine at -0.2 ppm and the averaged methyl shift of -0.2 ppm. All these shifts are negligible compared to the contribution of the Fermi coupling, as was previously concluded from the point-dipole calculation.

6.1.4 ^{1}H NMR interpretation

The ^{1}H MAS NMR spectrum of $Cu(acac)_2$ is shown in Figure 6.6 along with shift predictions from Table 6.1. In this case, the assignment is obvious due to the favorable signal resolution and characteristic integrated signal intensities. Unlike previous complexes considered in this thesis, the ^{1}H shift of $Cu(acac)_2$ tends to have overall negative spin-density. As the pseudoaromatic ring does not interact with a singly occupied metal orbital, there is no appreciable unpaired spin-density perpendicular to the ring plane that could interact with the protons. The majority of the unpaired spin-density is distributed within the ring plane, as indicated by the isosurface diagram in Figure 6.3. The carbon of the methyl group experiences significant positive spin-density from the polarization mechanism, which can extend onto the

proton in the plane of the ring. However, the out-of-plane protons do not experience the extended polarization from the carbonyl and are most affected by polarization originating at the carbon of the methyl group. Thus, the majority of CH_3 protons are predicted to have negative spin-density and a negative Fermi-shift.

Group	I_{fit} (%)	$I_{stoichiometry}$(%)
2 x CH_3	87	86
CH	13	14

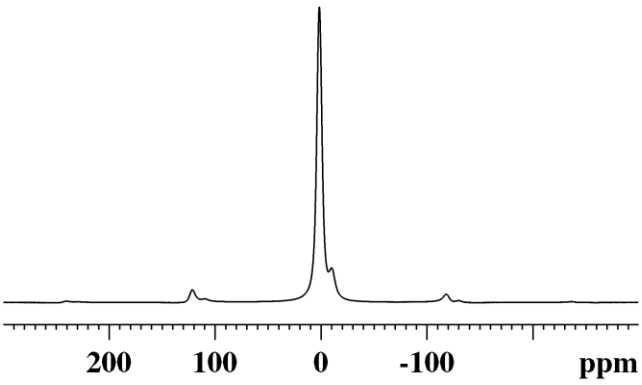

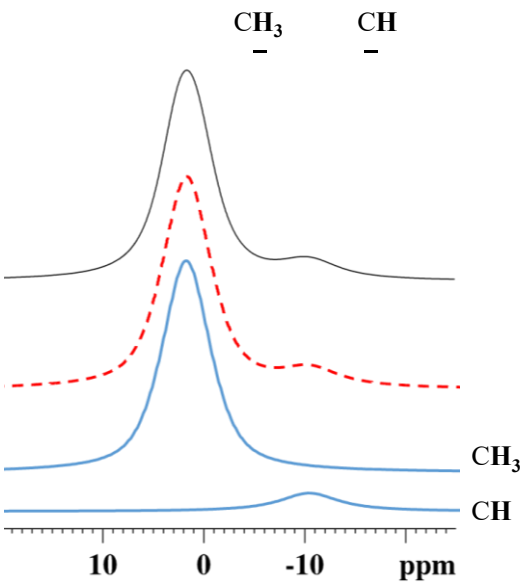

FIGURE 6.6: ^{1}H MAS Hahn-Echo of $Cu(acac)_2$ with intensity fitting. Detailed intensity fits (on the right) follow closely with the stoichiometric intensity from a single molecule (top-left table).

The methine proton experiences negative spin-density due to the specific symmetry restriction of the methine carbon that forbids any delocalization at that position. Figure 6.3 shows that the methine carbon is surrounded by regions with positive spin-density as a result of the polarization from both carbonyl groups. This positive spin-density can polarize the carbon-hydrogen bond, leaving the hydrogen with excess negative spin-density as there is no pathway for spin delocalization.

6.2 $Ni(acac)_2 \cdot 2H_2O$, d^8

The nickel(II) analog of bis(acetylacetonato)copper(II) has a hydrated form that brings the local coordination environment around the metal to a pseudo-octahedral arrangement. The structure also has the inversion center at the metal, and only up to five distinct resonances are expected from ^{13}C NMR and three resonances from ^{1}H NMR, excluding the water signal. Water molecules are coordinated directly to the metal and require additional attention as their dynamic behavior is not known. The water molecule can rotate around the Ni-O axis, in which case the NMR signals from the two hydrogen nuclei would average. There may be an additional long-range hydrogen-bonding interaction that restricts hydrogen reorientation, in which case each hydrogen will produce a distinct signal.

The magnetic properties of this complex have been studied extensively [71, 134, 135], and there is no appreciable magnetic anisotropy. Thus, the pseudocontact contribution to the shift will not be considered and the spin-only formulation will be used in the evaluation of the Fermi shifts. A recent solid-state NMR study of this complex proposed [135] incorrect assignments based simply on site proximity to the metal center. Only later did they correct their assignments to reflect the Fermi-contact coupling [136].

6.2.1 ^{13}C NMR and assignments

The spectrum in Figure 6.7 shows the NMR response from ^{13}C nuclei in paramagnetic $Ni(acac)_2 \cdot 2H_2O$. There are three distinct regions of signals that mimic the assignments for the copper complex, Figure 6.1. Signal assignments are confirmed through $^{13}C\{^{1}H\}$ REDOR where the largest dephasing is for the methine group and a negligible dephasing is at the carbonyl,

Figure 6.8. In this case, REDOR helps clarify the distinction between methine and carbonyl peak assignments, as the computational prediction suggests an overlap of the two signals, Figure 6.7.

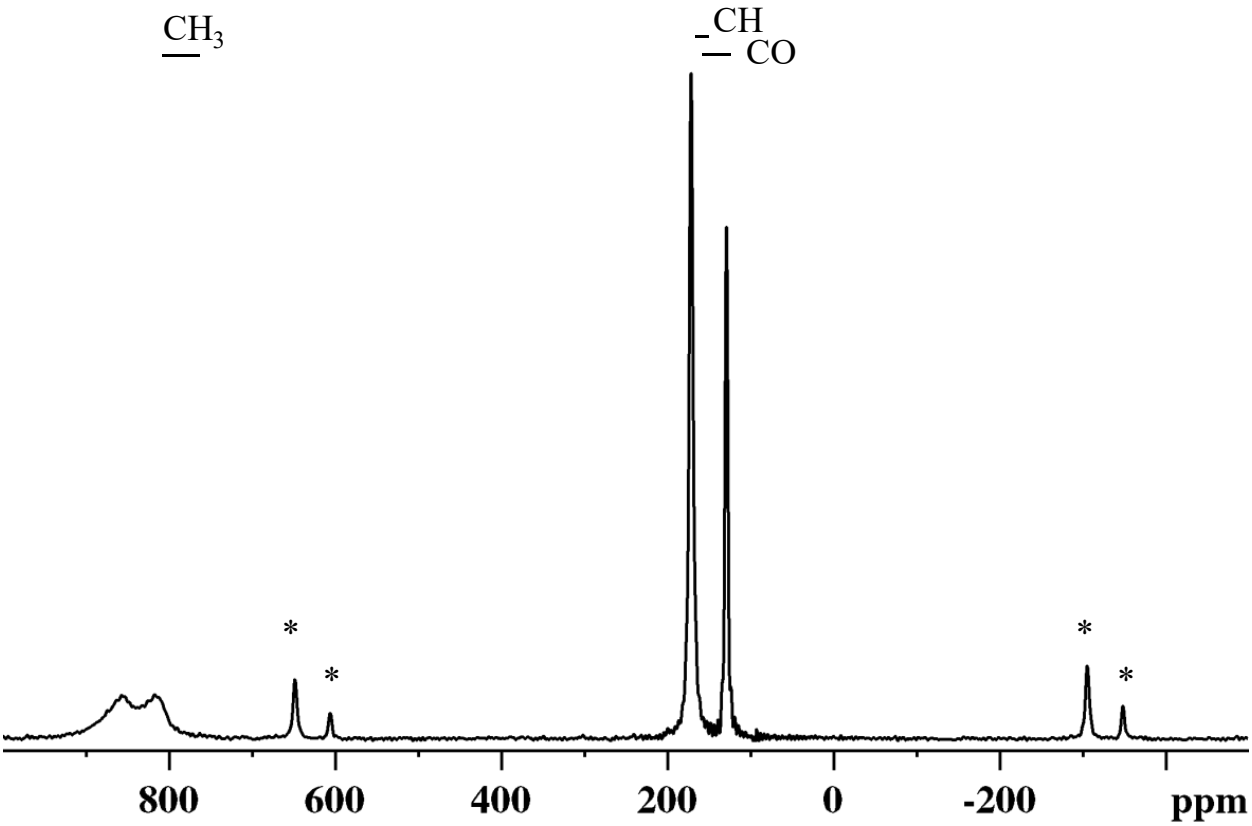

FIGURE 6.7: ^{13}C MAS Hahn-Echo of $Ni(acac)_2 \cdot 2H_2O$ with bars indicating the calculated chemical shift regions. Asterisks indicate artifacts of MAS.

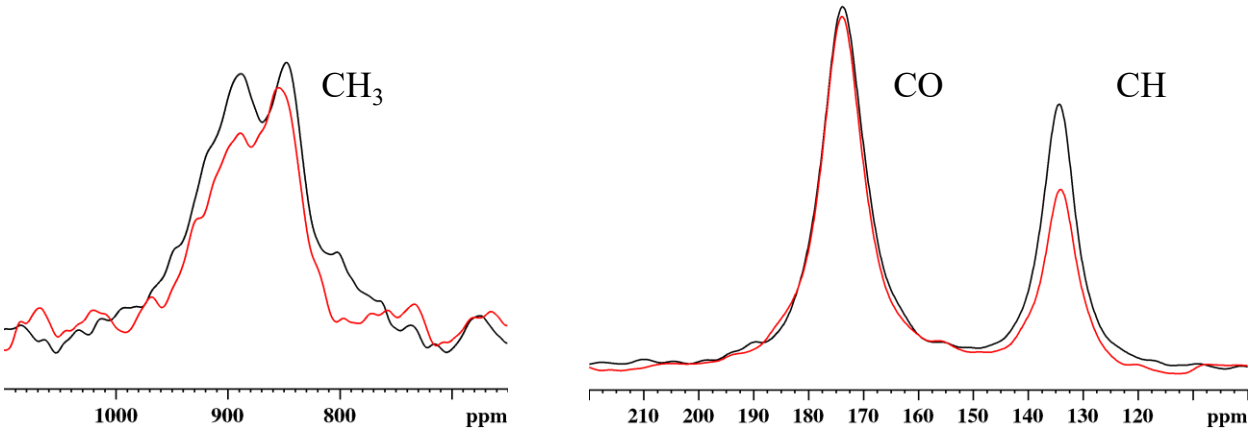

FIGURE 6.8: $^{13}C\{^1H\}$ REDOR of $Ni(acac)_2 \cdot 2H_2O$. The spectrum in black indicates no dephasing, whereas the spectrum in red results from an introduced ^1H recoupling pulse.

6.2.3 Spin-density distribution

According to crystal-field theory for an octahedral coordination environment, two unpaired electrons of a d^8 metal occupy high-energy e_g-orbitals. The interaction of the d_{z^2} orbital with ligands in the xy-plane is analogous to that in the undistorted ligand in the xy-plane of $Mn(acac)_3$. Whereas the effect of the $d_{x^2-y^2}$ on the spin-density distribution has been observed in $Cu(acac)_2$, both of these orbitals are given in Table 6.1 with the appropriate phases and symmetries of interacting oxygen orbitals interacting with the metal. The contour-plot in Figure 6.9 shows the effect of both metal orbitals on the spin density of the ligand. A detailed discussion of the individual contributions from each of these orbitals was given for $Mn(acac)_3$, Figure 5.4 for d_{z^2}, and for $Cu(acac)_2$, Figure 6.4 for $d_{x^2-y^2}$. Figure 6.9 shows the sum of these contributions applied to the molecular structure of $Ni(acac)_2 \cdot 2H_2O$. The contour-plot resembles that of $Cu(acac)_2$, Figure 6.3, where clear σ* symmetry is seen between the metal and the oxygens. This is in agreement with Table 5.1 where only a σ-type symmetry interaction is expected at the oxygen atoms.

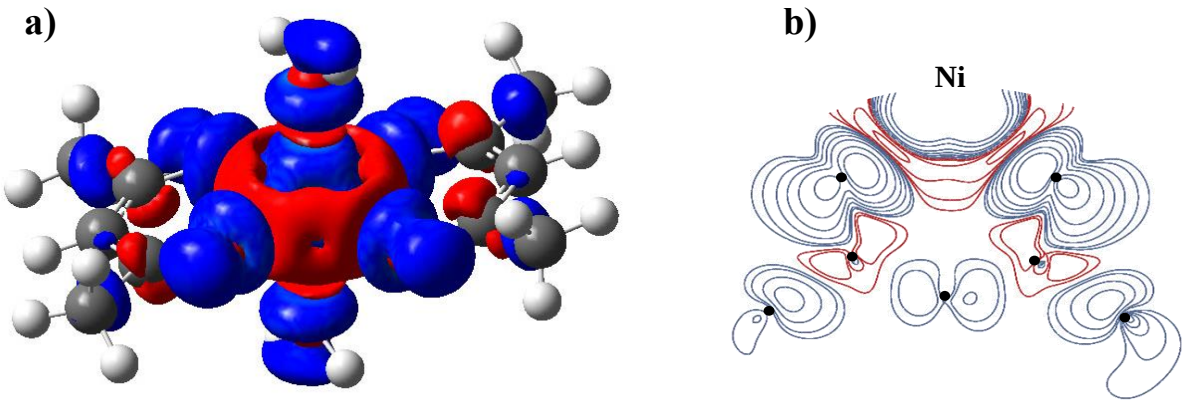

FIGURE 6.9: Spin-density distribution of $Ni(acac)_2 \cdot 2H_2O$: a) isosurface, b) contour plot in the plane of the ligand.

6.3.3 ^{1}H NMR interpretation

The ^{1}H MAS NMR spectrum of the nickel complex is given in Figure 6.10. The general pattern resembles that of $Cu(acac)_2$, where there is a clear distinction between C**H** at low frequency and a single methyl peak at higher frequency, indicative of an inversion center. In addition, there is a low-intensity broad resonance at a high shift of 70 ppm, which is attributed to a water signal according to Table 6.2. According to integrated intensities of each signal and the relative proximity of the shift to one of the predicted hydrogen signals from the water, I conclude that the broad resonance comes from a single proton of the water molecule, which suggests that the orientation of the water molecule is perpendicular to the pseudoaromatic ring (Figure 1.10) and is relatively fixed in space. The signal from the other hydrogen is expected to appear at much

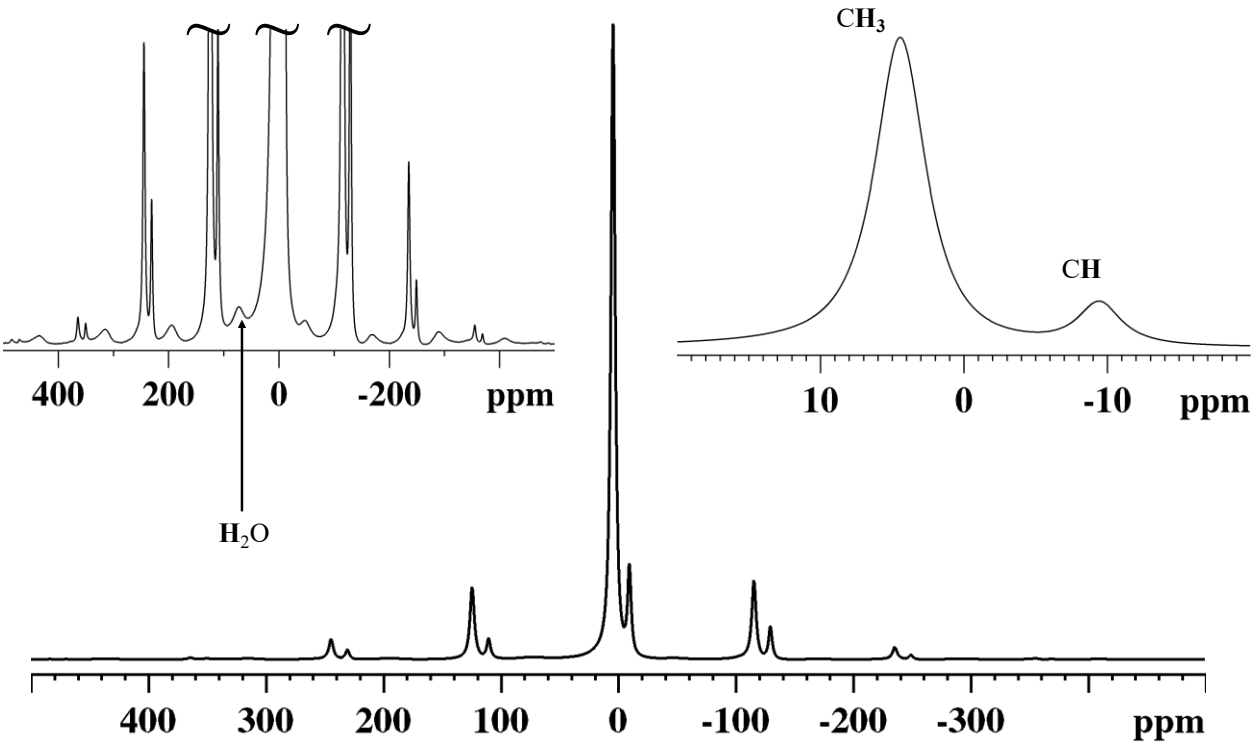

FIGURE 6.10: Regions of the ^{1}H MAS Hahn-Echo spectrum of $Ni(acac)_2 \cdot 2H_2O$.

TABLE 6.2**:** ^{13}C and ^{1}H NMR of $Ni(acac)_2 \cdot 2H_2O$ and DFT calculation. Calculated and experimental shifts are in ppm at a sample temperature of 55 ˚C. ^{1}H and ^{13}C chemical shifts from the same functional groups are indicated and appear in the order as listed.

Group	^{13}C		^{1}H	
	A_{calc} (MHz) {A_{exp}}	δ_{calc}[a] {δ_{exp}}	A_{calc} (MHz) {A_{exp}[b]}	δ_{calc} {δ_{exp}}
CO	-0.21, -0.12 {-0.089(1)}	139, 160 {171}		
CH	0.25 {0.11(1)}	166 {129}	-0.21 {0.22(1)}	-8.5 {-9.3}
CH_3	2.92, 3.05 {3.1(1), 3.3(1)}	774, 806 {818, 858}	(-0.37, -0.34, 0.57) {0.37, 0.34, 0.57} (-0.26, -0.39, 0.51) {0.24, 0.36, -0.46}	-0.9, -1.2 {4.5}
H_2O			3.73, 0.50 {0.98(3)}	244, 37 {70}

a) Shifts were calculated according to equation 2.18.
b) Couplings from individual hydrogens from the same methyl group are scaled to match the average experimental shift.

higher frequency, and due to the significant Fermi coupling, it is not expected to be observed (more discussion on the signal breadth will be given in Chapter 8).

There is another hydrated form of the complex with an additional water molecule, $[Ni(acac)_2 \cdot 2H_2O] \cdot H_2O$, where the additional water molecule participates in hydrogen bonding, breaking the inversion symmetry of the complex [73]. The two waters coordinating nickel are no longer related by inversion symmetry. Hydrogen atoms are in a near-parallel orientation with respect to the pseudoaromatic system, Figure 6.11. This breaking of symmetry results in distinct NMR resonances for individual crystallographic sites: the ^{13}C spectrum is predicted to have 10 resonances, and the ^{1}H spectrum should have up to 12 resonances if one assumes unique signals for individual water hydrogens and rapid methyl rotation. Table 6.3 summarizes these

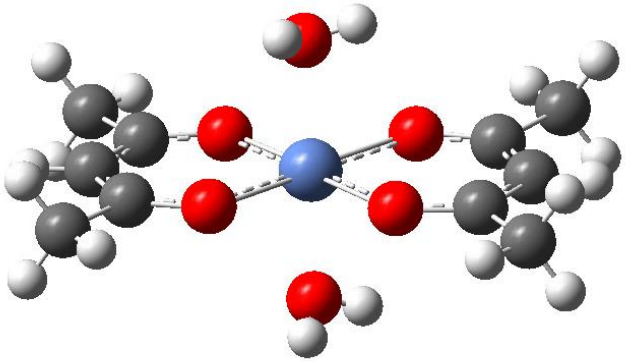

FIGURE 6.11: Molecular structure of $[Ni(acac)_2 \cdot 2H_2O] \cdot H_2O$. Image does not include the external water molecule.

TABLE 6.3**:** ^{13}C and ^{1}H NMR of $Ni(acac)_2 \cdot 2H_2O$ and DFT calculation of $[Ni(acac)_2 \cdot 2H_2O] \cdot H_2O$. Calculated and experimental shifts are in ppm at a sample temperature of 55 ˚C. ^{1}H and ^{13}C shifts from the same functional groups are indicated and appear in the order as listed.

Group	^{13}C		^{1}H	
	A_{calc} (MHz) {A_{exp}}	δ_{calc} [a] {δ_{exp}}	A_{calc} (MHz) {A_{exp} [b]}	δ_{calc} {δ_{exp}}
CO	-0.22, -0.21, 0.45, 0.18 {-0.089(1)}	135, 137, 306, 237 {171}		
CH	0.44, 0.34 {0.11(1)}	213, 187 {129}	-0.22, -0.18 {0.22(1)}	-9.6, -7.1 {-9.3}
CH_3	3.41, 3.47, 2.97, 2.97 {3.1(1), 3.3(1)}	897, 914, 786, 786 {818, 858}	(0.04, -0.27, -0.20) (0.06, -0.25, -0.21) {0.37, 0.34, 0.57} (0.07, -0.20, -0.24) (0.08, -0.26, -0.19) {0.24, 0.36, -0.46}	-7.2, -6.5, -6.0, -5.7 {4.5}
H_2O			-1.52, -1.24, -1.37, -1.73 {0.98(3)}	-92, -75, -83, -106 {70}

a) Shifts were calculated according to equation 2.18.
b) Couplings from individual hydrogens from the same methyl group are scaled to match the average experimental shift.

predictions and gives the experimental chemical shifts in $Ni(acac)_2 \cdot 2H_2O$ for comparison. The loss of symmetry should be easily apparent in ^{13}C NMR; however, our spectrum shows evidence of high molecular symmetry, confirming the structure as the dihydrate. Nielsen's group reported ^{13}C shifts of this extra hydrate form, and it shows a loss of site degeneracy as the structure no longer has inversion symmetry [136, 137].

Further distinction between the two hydrated forms of the nickel complex can be made with the ^1H Fermi shift from waters directly attached to the metal. The orientation of the hydrogen with respect to the pseudoaromatic ring determines the symmetry of molecular-orbital interaction. If the hydrogen atoms are parallel to the direction of the d_{z^2} orbital, there is strong overlap of the σ* from the oxygen that creates a significant positive spin-density at the hydrogen positions (Figure 6.12a). If the hydrogen is parallel to the plane of the pseudoaromatic ring, the overlap is symmetry forbidden and the hydrogen atom has strong polarization of the σ bonds with the oxygen; as a result, it is left with the net negative spin-density, Figure 6.12b. ^1H MAS NMR clearly shows the presence of a high-frequency shift for the water molecule, which

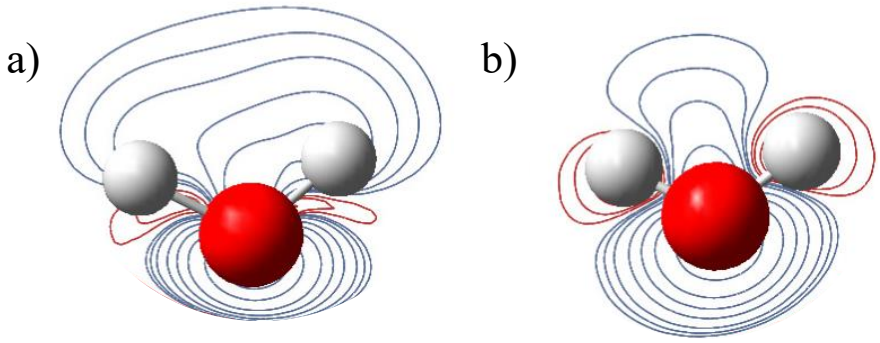

FIGURE 6.12: Spin-density contour-plots of the water molecule with direct coordination to the nickel metal for a) $Ni(acac)_2 \cdot 2H_2O$ where water is perpendicular to the ligand, and b) $[Ni(acac)_2 \cdot 2H_2O] \cdot H_2O$ where water is parallel to the ligand.

uggests a positive spin-density and confirms the assignment of the hydrated form to be $Ni(acac)_2{\cdot}2H_2O$ and not $[Ni(acac)_2{\cdot}2H_2O]{\cdot}H_2O$, Table 6.3.

6.3 $Co(acac)_2{\cdot}2H_2O$, d^7

The structure of $Co(acac)_2{\cdot}2H_2O$ contains two crystallographically equivalent ligands that are related by inversion symmetry [70]. Therefore, ^{13}C NMR gives a maximum of five resonances, and ^{1}H NMR has three resonances, accounting for the rotation of the methyl group, without accounting for the water signal.

Cobalt(II) complexes are known to possess notoriously large magnetic anisotropies and are used as paramagnetic tags for structural determination of complex molecules [41, 131]. The magnetic properties of $Co(acac)_2{\cdot}2H_2O$ were characterized by Lohr *et al* [71] who reported the dependance of magnetic susceptibility to temperature on the basis of Griffith's expressions [15]. These magnetic properties are essential to evaluating the observed hyperfine interactions in this cobalt complex.

6.3.1 ^{13}C MAS NMR

The ^{13}C MAS NMR spectrum in Figure 6.13 shows three distinct regions of signal that can be readily assigned with computational prediction. The signal with the highest chemical shift is attributed to the methyl group. The splitting of the methyl signal indicates a slight distortion between the two functional groups of the same ligand. The carbonyl signal is at a lower frequency than the methyl group. As it is closest to the metal center, the signal possesses the greatest dipolar anisotropy, as indicated by the intense spinning sideband manifold, that is appreciable even at the high MAS frequency of 60 kHz. The carbonyl signal also consists of two

closely spaced resonances, which suggests a slight distortion between the two carbonyl groups of the same ligand, as previously observed for the methyl groups. The methine signal can be recognized by its lower intensity and relative proximity to the carbonyl site, as predicted from

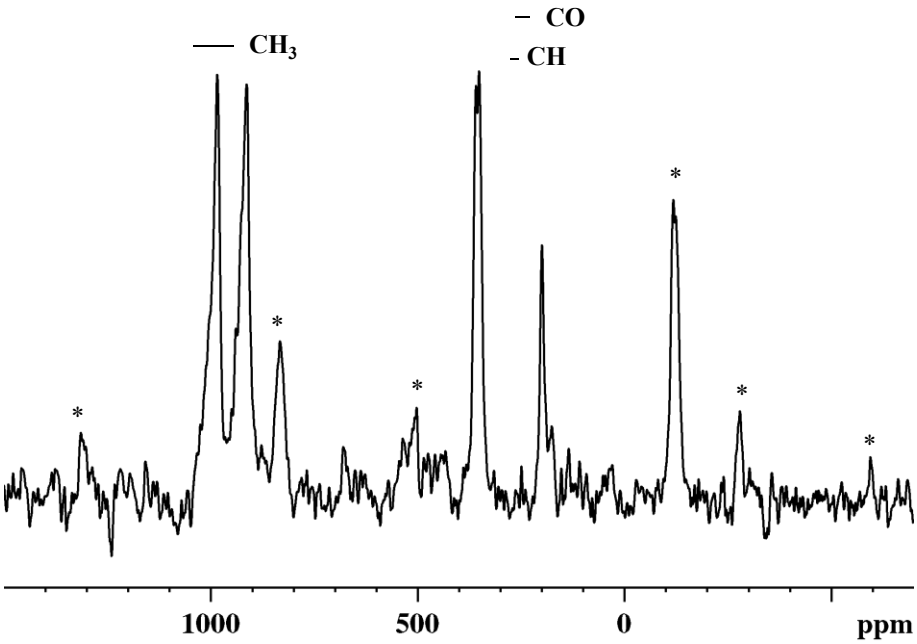

FIGURE 6.13: ^{13}C MAS Hahn-Echo NMR of $Co(acac)_2 \cdot 2H_2O$ at 60 kHz MAS rate with calculated-shift ranges. Asterisks indicate spinning sidebands.

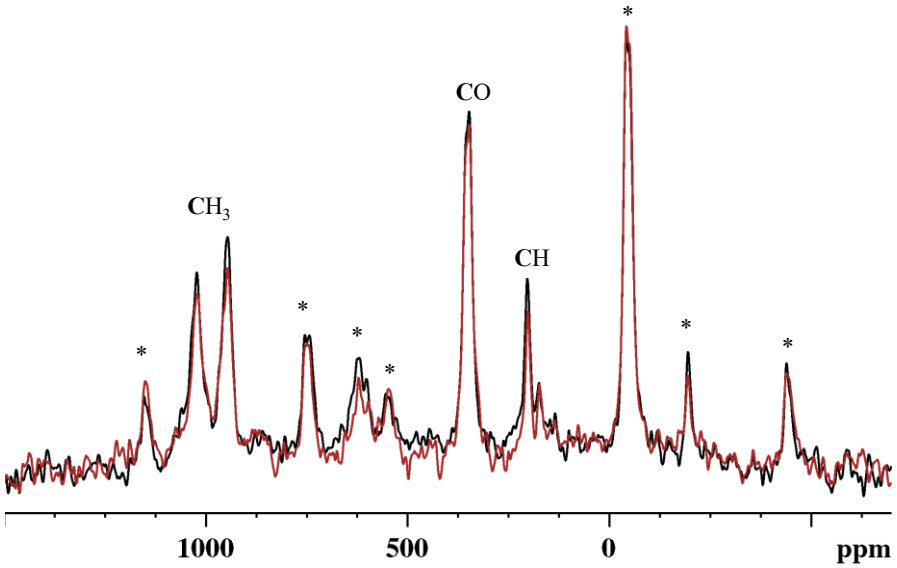

FIGURE 6.14: $^{13}C\{^1H\}$ REDOR NMR of $Co(acac)_2 \cdot 2H_2O$ at 50 kHz MAS rate. The spectrum in black has no dephasing, whereas the spectrum in red results from the introduced ^1H recoupling pulse.

the calculations, Figure 6.13. The signal consists of a single peak, which confirms the presence of a single unique methine group between the two ligands of the molecule as explained above.

The assignment of functional groups was confirmed using $^{13}C\{^1H\}$ REDOR, Figure 6.14. The signal with the largest dephasing at 199 ppm belongs to the methine group, with intermediate dephasing associated with **C**H_3. The **C**O group is at 355 ppm and shows no change with ^1H recoupling pulses. It is interesting to note that at 50 kHz, the intense spinning sidebands of the carbonyl group could lead to erroneous signal assignment, as the spinning sideband around -50 ppm in Figure 6.14 is the most intense signal, which can be erroneously attributed to the isotropic shift. Both spectra in Figure 6.14 were recorded at 50 kHz MAS to confirm the positions of the isotropic signals. A clear identification of the isotropic peak can be made based on Figures 6.13 and 6.14, as isotropic shifts are fixed with variable spinning.

6.3.2 Spin-density distribution

In $Co(acac)_2{\cdot}2H_2O$, Co(II) is a d^7 metal, where both high-energy d_{z^2} and $d_{x^2-y^2}$ orbitals are singly occupied and the third unpaired electron is unevenly delocalized among the lower-energy

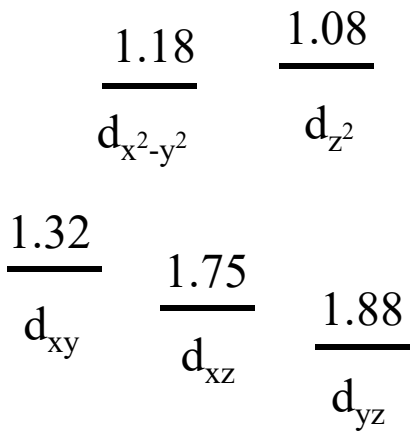

FIGURE 6.15: Electron-density distribution in the metal valence orbitals of $Co(acac)_2{\cdot}2H_2O$ calculated with the level of theory used in Figure 6.13.

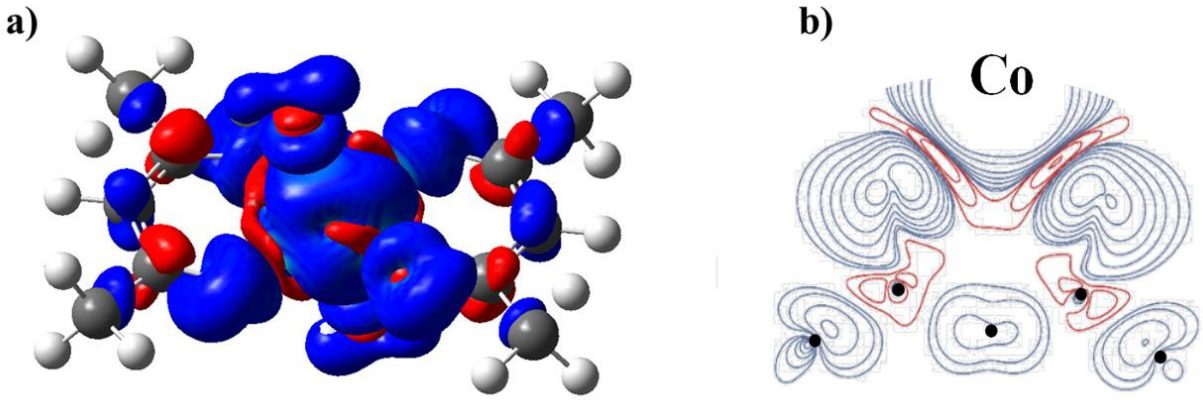

FIGURE 6.16: Unpaired spin-density distribution in $Co(acac)_2 \cdot 2H_2O$: a) isosurface, b) contour plot in the plane of the ligand.

orbitals, d_{xy}, d_{yz} and d_{xz} (Figure 6.15). The contour plot in Figure 6.16 shows a similar distribution to the nickel complex (Figure 6.9), as both structures have similar geometries and the occupancy at the metal differs only by a single unpaired electron delocalized over the three metal orbitals.

The interaction between the metal-t_{2g}-type and the oxygen orbitals follows the same pathway as outlined for the d^1-d^3 metal complexes in Chapter 4. This mechanism is responsible for the alteration of the contour shapes in Figure 6.16b with respect to the nickel complex in Figure 6.9, and can be considered as a perturbation to the spin-density distribution from the e_g orbitals. The pathway is the delocalization of the spin density from the metal t_{2g} orbital in the plane of the ligand via π* interactions with the oxygen and a subsequent overlap with the carbon σ* orbital. The strength of the overlap between the oxygen and the carbon orbitals is expected to be dictated by the planarity of the metal-ligand ensemble. The dihedral angle between the ligand and the xy-plane of the cobalt-oxygen coordination is approximately 15°, Figure 6.17. This tilt is expected to lower the degree of overlap between the carbonyl carbon and the π* between the oxygen and the metal, which would decrease the degree of spin-density delocalization onto the ligand.

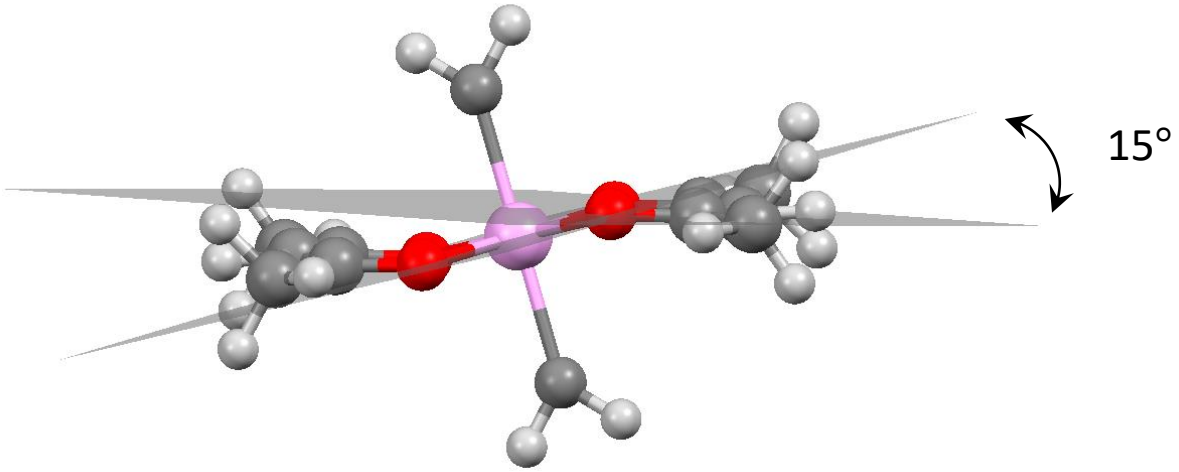

FIGURE 6.17: $Co(acac)_2 \cdot 2H_2O$ with the xy-plane and the tilted plane of the ligand.

6.3.3 Beyond the spin-only approximation

One of the major assumptions in our theoretical evaluation of Fermi coupling has been to ignore the contribution of the anisotropy of the magnetic susceptibility and any significant contribution from spin-orbit coupling. Thus, the formula of the Fermi shift is reduced to the spin-only formulation of equation 2.18, which gives the shifts for $Co(acac)_2 \cdot 2H_2O$, Figure 6.13, where the overall distribution of signal assignments is predicted with acceptable accuracy. A clear separation between signals from the methyl and those from other functional groups indicates that the spin distribution gives significant positive spin-density at the methyl groups. This contrasts with previously observed methyl shifts for d^1 - d^3 complexes where the methyl signals had a significant negative Fermi-shift (Figures 4.5, 4.12 and 4.18). Both carbonyl and methine groups are predicted to have an overall small positive Fermi-shift, which indicates the net positive spin-density at both sites. The order of appearance of these groups is reversed between prediction and experiment, which could be caused by such factors as an error in the Fermi-coupling calculation and neglect of the pseudocontact shift, which is expected to be significant in Co^{2+}. Nevertheless,

the assignment of these two groups is confirmed on the basis of both REDOR (Figure 6.14) and the relative signal intensity and multiple observed peaks.

In 1964, Golding introduced a formula for the Fermi shift that accounts for the spin-orbit interaction in octahedral and tetrahedral coordination environments [13]. The derivation was based on the earlier work of Griffith [15] that used the Russell-Saunders coupling scheme [138]. The spin-orbit coupling constant, ζ, in $Co(acac)_2 \cdot 2H_2O$ is significant, at 435 cm^{-1} [71], in comparison with the Boltzmann energy at room temperature, which is approximately 208 cm^{-1}. This spin-orbit splitting acts as an additional perturbation to the electronic-energy levels and affects the magnetic moments of the individual microstates. The Boltzmann-averaged magnetic moment leads to the following equation for the Fermi-contact shift in $Co(acac)_2 \cdot 2H_2O$ [13]:

$$\delta_{\mathrm{Fermi}} = A_{\mathrm{iso}} \frac{\mu_B}{3\gamma_n kT} \left(\frac{\left(\frac{65}{12} + \frac{140kT}{9\zeta}\right) e^{\frac{5\zeta}{4kT}} + 2\left(\frac{44}{15} - \frac{616kT}{225\zeta}\right) e^{\frac{\zeta}{2kT}} + 3\left(\frac{63}{20} - \frac{84kT}{20\zeta}\right) e^{\frac{-3\zeta}{4kT}}}{e^{\frac{5\zeta}{4kT}} + 2e^{\frac{\zeta}{2kT}} + 3e^{\frac{-3\zeta}{4kT}}} \right) \quad \textbf{(6.3)}$$

where the idealized model of the weak-field ligand has been used, which is in accord with findings of Lohr regarding the cobalt complex [71]. Formula 6.3 replaces the $g_{iso}S(S+1)$ term of the spin-only approximation, equation 2.18, and introduces an additional temperature-dependent perturbation due to the spin-orbit coupling. Application of Golding's formula to the calculated Fermi coupling yields no appreciable change to the CH and CO predictions, but shifts the CH_3 prediction by about +200 ppm, resulting in poorer agreement with the experimental data (Table 6.4).

More recently, Martin [132] formulated the dependence of the Fermi shift on the splitting of electronic-energy states, the **zero-field splitting**, D. This perturbation to energy levels occurs in systems with multiple unpaired spins or S > 1/2, where it represents the spin - spin dipolar interaction. This relation was derived for both the Fermi and pseudocontact parts of the hyperfine interaction. For Co^{2+} the analytical solution has the following form:

$$\delta_{\mathrm{Fermi}} = \mathrm{A_{iso}}\frac{\mu_{\mathrm{B}}}{3\mathrm{kT}\gamma_{\mathrm{n}}}\left(\frac{1+9\mathrm{e}^{-\frac{2D}{kT}}}{4\left(1+\mathrm{e}^{-\frac{2D}{kT}}\right)}(\mathrm{g_{iso}}+2\Delta\mathrm{g})+\frac{1+\frac{3\mathrm{kT}}{4D}(1-\mathrm{e}^{-\frac{2D}{kT}})}{1+\mathrm{e}^{-\frac{2D}{kT}}}(2\mathrm{g_{iso}}-2\Delta\mathrm{g})\right) \quad \textbf{(6.4)}$$

$$\delta_{\mathrm{PC}} = \Delta\mathrm{A}\frac{\mu_{\mathrm{B}}}{3\mathrm{kT}\gamma_{\mathrm{n}}}\left(\frac{1+9\mathrm{e}^{-\frac{2D}{kT}}}{4\left(1+\mathrm{e}^{-\frac{2D}{kT}}\right)}(\mathrm{g}+2\Delta\mathrm{g})+\frac{1+\frac{3\mathrm{kT}}{4D}(1-\mathrm{e}^{-\frac{2D}{kT}})}{1+\mathrm{e}^{-\frac{2D}{kT}}}(2\mathrm{g_{iso}}-2\Delta\mathrm{g})\right) \quad \textbf{(6.5)}$$

where g_{iso} is the isotropic g-tensor, a term that incorporates the effect of spin-orbit coupling according to the Golding's formulation, Δg is the anisotropy of the g-tensor, and ΔA is the anisotropy of the hyperfine tensor in the reference frame of the g-tensor. *D* represents the zero-field splitting.

Table 6.4 summarizes the different levels of theory used to determine the paramagnetic shift. The simplest level of theory was the spin-only approximation in the absence of a pseudocontact shift and is sufficient to distinguish methyl signals from other resonances. Introduction of the spin-orbit coupling contribution to the magnetic moment via Golding formulation (equation 6.3) systematically increases the magnitudes of Fermi shifts by ~24%. The addition of the zero-field splitting term by Martin-Autschbach (equation 6.4) slightly increases the magnitude of the Fermi shift by farther ~2-3%. Thus, overall the effect of the zero-field splitting on the Fermi shift is minor compared to that of the spin-orbit coupling correction and both are minor perturbations relative to the spin-only formulation (equation 2.18). Introduction

of the pseudocontact-shift contribution, Table 6.4, is meant to show a potential significance of such shift for a highly anisotropic Co^{2+} ion. The sensitivity of the pseudocontact shift to the magnetic anisotropy is amplified by the high magnetic moment of Co^{2+} compared with Cu^{2+}, which has a comparable Δg but overall much smaller pseudocontact shifts, Table 6.1. The presence of multiple unpaired electrons and the large magnitude of the zero-field splitting, which was determined for $Co(acac)_2 \cdot 2H_2O$ [71], introduces an additional large correction to the pseudocontact shift, Table 6.4. The variation between the point-dipole model and the anisotropic hyperfine-coupling model of Martin-Autschbach without the zero-field splitting term is not significant and remains within a factor of 2. Both models predict pseudocontact shifts on the order of the Fermi shifts or much smaller. The introduction of the zero-field splitting correction amplifies these pseudocontact shifts by an order of magnitude, making them dominant for carbonyl groups which are closest to the metal. Unfortunately, as for $Cu(acac)_2$, these pseudocontact shifts cannot be regarded as analytical solutions as the system used for these calculations does not include effects of a periodic solid structure with multiple paramagnetic

TABLE 6.4: ^{13}C MAS NMR of $Co(acac)_2 \cdot 2H_2O$ and DFT calculations. Calculated and experimental shifts are in ppm at a sample temperature of 55 ˚C. Values are presented at different levels of theoretical treatment. M-A stands for Martin-Autschbach formalism, equations 6.4, 6.5.

Functional group	$Zn(acac)_2 \cdot 2H_2O$ δ_{dia}	δ_{Fermi}			δ_{PC} (+SOC)				δ_{exp}
		Spin-only	Golding (+SOC)	M-A (+SOC+D)	No D PDM	With D PDM	No D M-A	With D M-A	$\delta_{dia}+\delta_{Fermi}+\delta_{PC}$
CO	194(5)	54	67	68	27	108	51	323	359(3)
CO	194(5)	41	51	52	26	104	48	305	351(3)
CH	101(1)	176	218	222	19	74	11	69	199(1)
CH_3	28(1)	1004	1243	1280	9	35	10	64	985(5)
CH_3	28(1)	915	1132	1166	7	33	16	100	913(5)

centers but the calculations were done on individual molecules in gas phase. Thus, these values are presented as a first approximation to the pseudocontact shift in a solid. However, Table 6.4 shows that the significance of the zero-field splitting term is much greater in the pseudocontact-shift formulation than in the Fermi shift formulation.

6.3.4 ^{1}H MAS NMR

The ^{1}H MAS NMR spectrum of $Co(acac)_2 \cdot 2H_2O$ is given in Figure 6.18 with proposed signal assignments based on computational predictions, Table 6.5. The spectrum has a large anisotropic component due to the strong electron-nuclear dipolar interaction. The anisotropy of the ^{1}H NMR signal is comparable to that of $Cr(acac)_3$, Figure 4.20, as both systems have the same number of unpaired electrons. The signal anisotropy of the cobalt complex is slightly greater as the complex has an additional magnetic-moment contribution through the spin-orbit interaction, which brings the g_{iso} to 2.55 near room temperature [71]. A general expression for the dipolar contribution to the nuclear anisotropic signal has the following form [33, 39]:

$$\Omega_{aniso} = \frac{3\mu_0 g_{iso}{}^2 \mu_B{}^2 S(S+1)}{4\pi r^3 3kT} \qquad (6.6)$$

where the anisotropic component is given in the notation of Herzfeld and Berger, [139] and r is the distance between the metal center and the observed nucleus in a point-dipole approximation. Whereas such an approximation provides limited accuracy, as was seen in the account of the pseudocontact shift in copper and cobalt complexes, its general principles can be applied to help

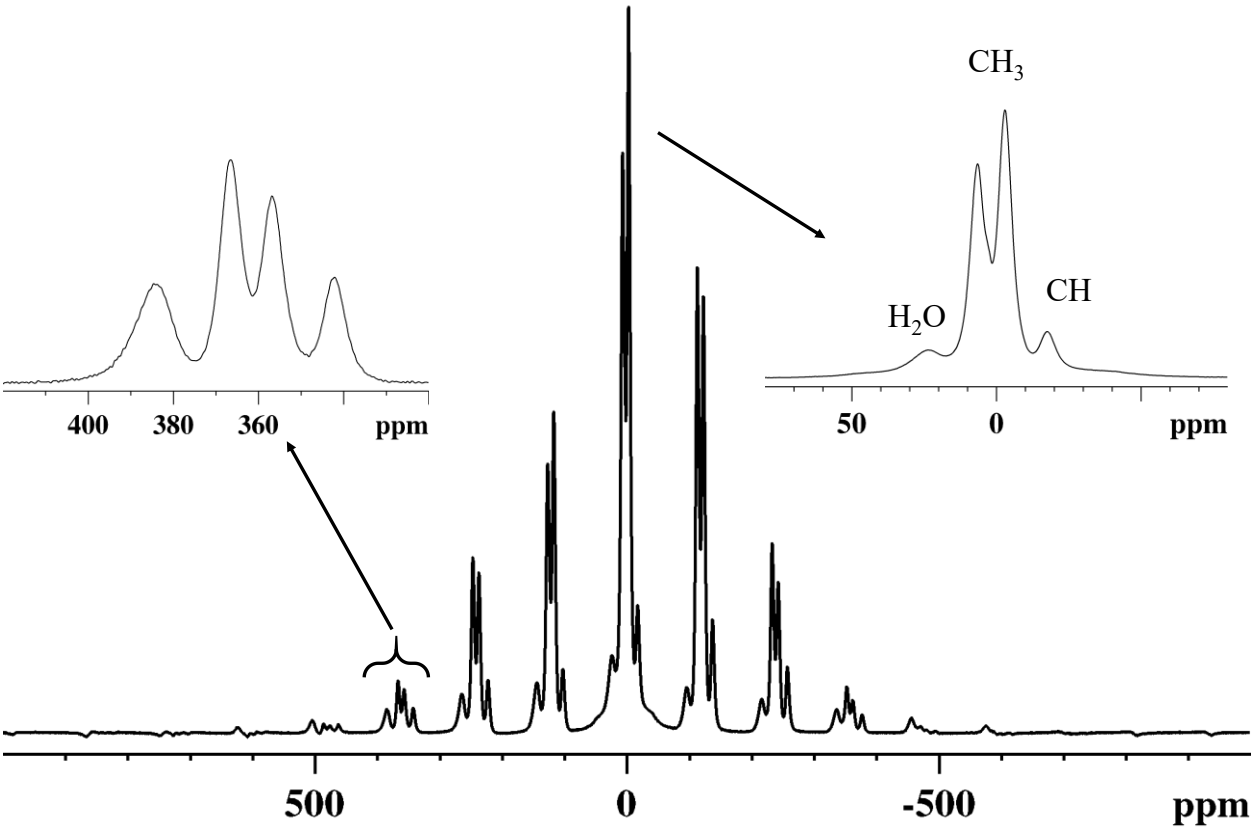

FIGURE 6.18: ^{1}H MAS Hahn-Echo NMR of $Co(acac)_2 \cdot 2H_2O$ with insets illustrating the differences in spinning-sideband intensity.

spectroscopic assignment. Equation 6.6 is equivalent to the point-dipole model that considers the SOC contribution but neglects the ZFS, which is one of the levels of theory given in Tables 6.4 and 6.5. Unlike the pseudocontact-shift formulation [5], the anisotropic contribution to the shift from the dipolar electron-nuclear coupling does not depend on the relative orientation of the two points with respect to $\bar{\boldsymbol{g}}$, but only on the distance between them. Thus, nuclei that are located closer to the paramagnetic center are expected to show a greater anisotropic component of their nuclear-resonance signal. Figure 6.18 provides two insets that show a rough ordering of magnitudes of the anisotropic interactions. The comparison can be made based on the relative intensities of the echo signals far from the isotropic position with respect to those of the isotropic

TABLE 6.5: ^{1}H of $Co(acac)_2 \cdot 2H_2O$ and DFT calculation. Calculated and experimental shifts are in ppm at a sample temperature of 55 ˚C. Values are presented at different levels of theoretical treatment. M-A stands for Martin-Autschbach formalism, equations 6.4, 6.5.

Functional group	$Zn(acac)_2 \cdot 2H_2O$ δ_{dia}	δ_{Fermi}			δ_{PC} (+SOC)				δ_{exp}
		Spin-only	Golding (+SOC)	M-A (+SOC+D)	No D PDM	With D PDM	No D M-A	With D M-A	δ_{dia}+ δ_{Fermi}+ δ_{PC}
CH	5(1)	-26	-32	-32	7	8	9	61	-17(2)
CH_3	1.6(3)	-15	-18	-18	5	6	8	49	-3(1)
CH_3	1.6(3)	-15	-18	-18	5	6	8	53	6(1)
H_2O	7(1)	284	351	351	-38	-46	-52	-334	20(2)
H_2O	7(1)	454	562	561	-39	-46	-51	-328	20(2)

resonance. The two signals in the middle of the spectrum with the highest intensities at isotropic positions -3 ppm and 6 ppm show the lowest anisotropy, followed by the signal at -17 ppm and the signal with the greatest anisotropy at 20 ppm. An approximate fit of these anisotropies can be found in Figure 6.1(Appendix). This relative ordering is in agreement with equation 6.6, where the distances to the metal center have the following order: $R(H_2O) < R(CH) < R(CH_3)$ and the anisotropic components of the dipolar coupling were estimated to follow $\Omega(H_2O) > \Omega(CH) > \Omega(CH_3)$.

Table 6.5 given corrections to the resonance shift of ^{1}H in $Co(acac)_2 \cdot 2H_2O$ that include the effects of g-anisotropy, spin-orbit coupling and zero-field splitting. As in Table 6.4, the contribution of the spin-orbit coupling correction to the Fermi shift is on the order of 24%, whereas the zero-field splitting contribution is negligible for the Fermi shift of the ^{1}H. The pseudocontact shift is smaller than the calculated Fermi-shift; however, it is not negligible in both point-dipole and Martin-Autschbach formulations. The effect of the zero-field splitting correction to the pseudocontact shift is more pronounced in the M-A formalism, where the shift increases in magnitude by approximately a factor of 6, whereas in the PDM the correction

influences the pseudocontact shift by about 10%. This shows the dramatic uncertainty in our ability to interpret NMR shifts in systems with appreciable magnetic anisotropy and zero-field splitting. To improve this situation there is a need to improve computational modeling and include accurate account of anisotropic hyperfine coupling in a periodic system.

Chapter 7:

Oxobis(2,4-pentanedionato)vanadium(IV) and tetra-μ²-acetatodiaquadicopper(II)

Oxobis(2,4-pentanedionato)vanadium(IV) ($VO(acac)_2$) with the d^1 configuration was studied to assess the impact of a distorted geometry in a bis(acetylacetonato)metal complex. Tetra-μ2-acetatodiaquadicopper(II) ($[Cu(Ac)_2H_2O]_2$) is an example of a coupled spin system, which was studied to represent the effects of the coupling on solid-state NMR spectra.

7.1 $VO(acac)_2$, d^1

The molecular structure of $VO(acac)_2$ consists of a distorted pentahedral coordination of oxygens around the vanadium, Figure 1.11. This arrangement has a significant effect on the overlap of the metal *d*-orbitals with the ligands, which changes the spin-density distribution. Unlike $V(acac)_3$, $VO(acac)_2$ is coordinated to five oxygens. As a result, the vanadium does not lay in the plane of the oxygen coordination between the two ligands, Figure 7.1. With the vanadyl oxygen chosen as the direction of the z-axis of symmetry of the local vanadium environment, the plane of the acetylacetonate ligands is tilted with respect to the xy- plane by approximately 15°, Figure 7.1. The unpaired electron is thought to occupy the d_{xy} orbital as $g_{\parallel} < g_{\perp}$, which are 1.943 and 1.983 respectively [140]. As g_{iso} differs from the free electron value by

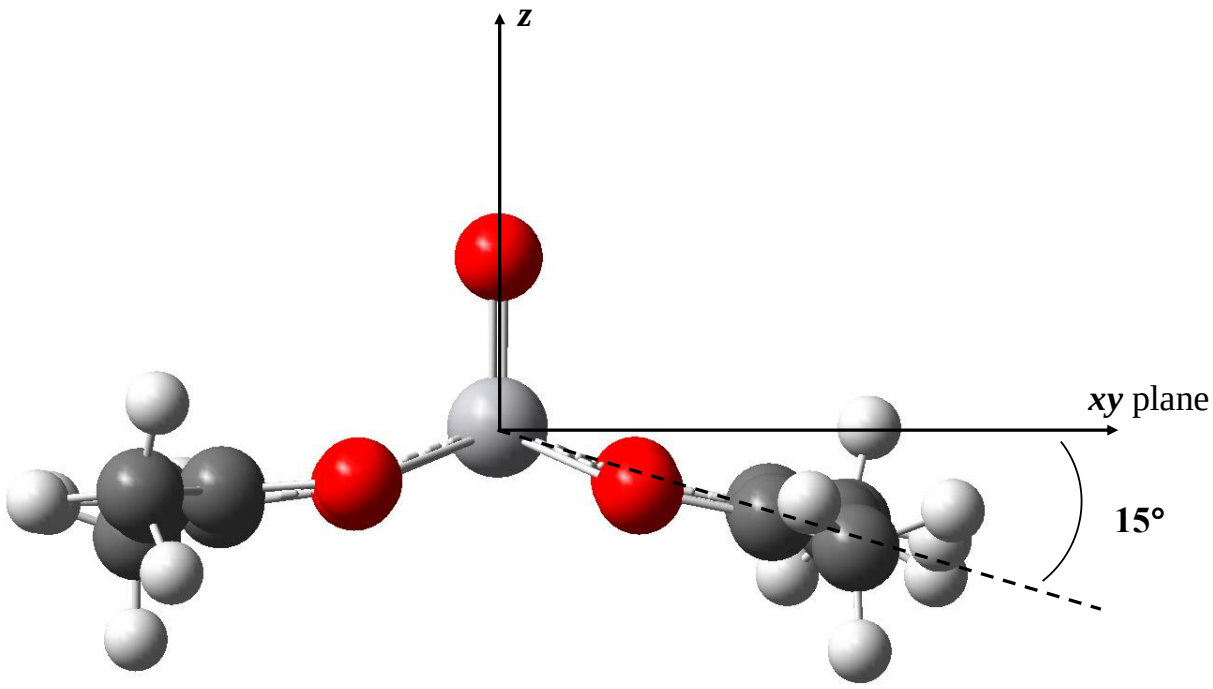

FIGURE 7.1: Illustration of the distortion of the ligand plane with respect to the plane normal to the z-axis.

merely 2%, a spin-only value will be used to estimate the magnitude of the Fermi shift near room temperature. The molecule does not have an axis of symmetry, therefore the ^{13}C spectrum is expected to give ten resonances. The ^{1}H can produce six resonances, taking into consideration the fast rotation of the methyl groups.

7.1.1 ^{13}C and ^{1}H MAS NMR spectra

The ^{13}C MAS NMR spectrum of $VO(acac)_2$ is significantly broadened by the paramagnetic interaction, Figure 7.2. Two broad peaks are observed above and below the diamagnetic-shift range. These shifts indicate positive and negative spin densities at those nuclear sites, respectively. The spectrum resembles those of the d^1-d^3 $M(acac)_3$ complexes, Chapter 4, where signals with negative Fermi-shift are attributed to the methyl groups, signals

with near-zero Fermi-coupling are assigned to methine, and the highest Fermi-shift belongs to the carbonyl group. Computational results predicts these three functional groups in the same order, which indicates a dominance of a similar spin-distribution mechanism as found in d^1-d^3 $M(acac)_3$ complexes. The carbonyl group is not observed in $VO(acac)_2$ and the methine shift has a small positive Fermi-shift. The ^{13}C MAS NMR spectrum bears a strong resemblance to that of $Cr(acac)_3$, where signals from only two out of three functional groups are detected and characteristic resonances are significantly broadened by paramagnetic coupling. $^{13}C\{^1H\}$ REDOR of $VO(acac)_2$ in Figure 7.3 confirms the assignment and confirms that signals from the

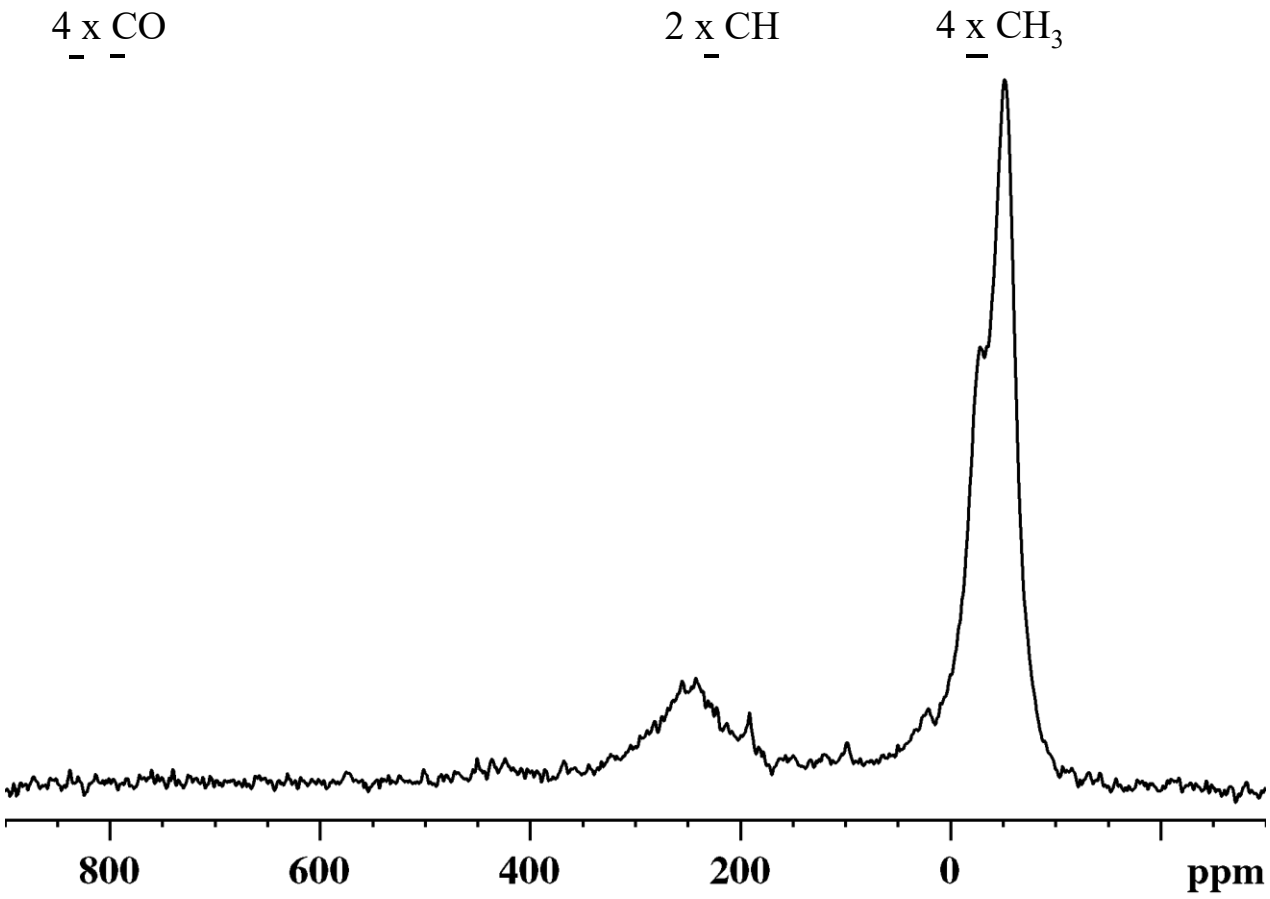

FIGURE 7.2: ^{13}C MAS Hahn-Echo of $VO(acac)_2$ with calculated assignment regions.

carbonyl groups are not observed experimentally due to unfavorable electron relaxation (for a more detailed discussion see Chapter 8).

There is a clear peak assignment observed for the methyl peaks, which signifies site inequivalence. The signal resolution is not sufficient to observe all four possible methyl resonances, but is sufficient to separate the signal from a single signal from the most distorted methyl group. Figure 7.4 shows the fit of the ^{13}C spectrum, where there is agreement with the expected stoichiometric intensities. The slightly lower methine signal-intensity may be explained by a signal loss of the broad resonance, Figure 7.4, during the echo-period delay (see Chapter 2, Figure 2.5). The fit confirms the separation of the signals from methyl groups in a 3:1 proportion as predicted from the calculation, Table 7.1. The exact nature of the distortion between the

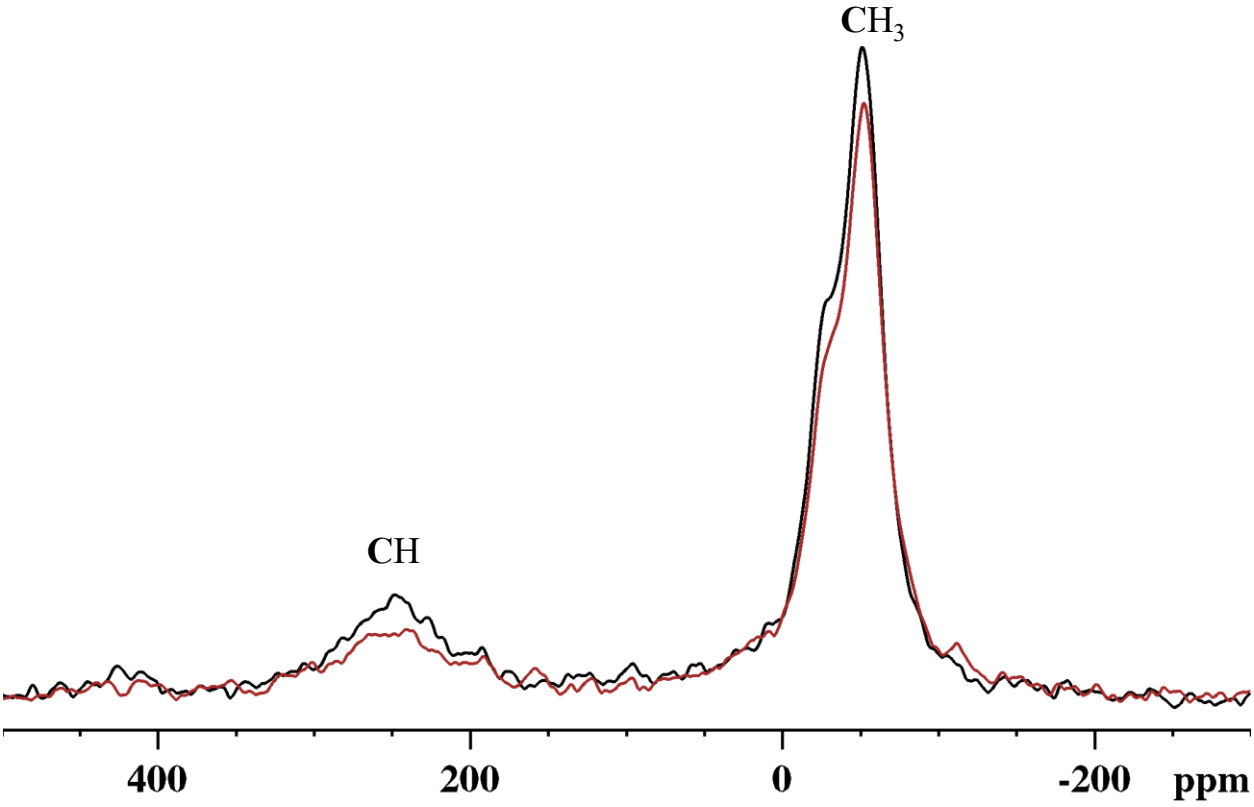

FIGURE 7.3: ^{13}C {^{1}H} REDOR of $VO(acac)_2$. The spectrum in black has no recoupling, whereas the spectrum in red is acquired with ^{1}H recoupling.

Group	δ_{iso} (ppm)	FWHM(kHz)	I_{fit} (%)	$I_{stoichiometry}$(%)
CH	246	10.3	24.4	33.3
CH_3	-27.2	2.9	19.6	16.7
3 x CH_3	-52.6	3.2	56	50

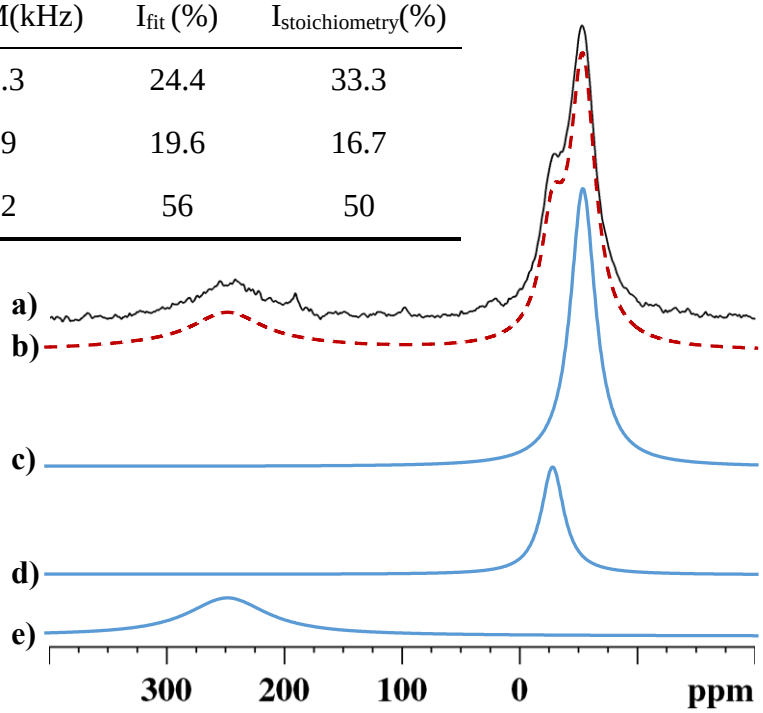

FIGURE 7.4: ^{13}C MAS Hahn-Echo spectra of $VO(acac)_2$, a) Experiment, b), with deconvolution fit that consists of, c), three methyl groups d), a single methyl group and, e), two methine groups.

methyl groups remains unidentified as the effect on the Fermi coupling is calculated to be relatively small based on the available x-ray crystal structure, on the order of 3%, Table 7.1, whereas the difference in coupling between the two methyl ^{13}C regions is estimated to be 30% according to the observed Fermi-shift, Table 7.2. This discrepancy indicates insufficient accuracy in our modeling method.

^{1}H MAS NMR, Figure 7.5 shows a single broad resonance with a net positive Fermi-shift, similar to the d^1-d^3 $M(acac)_3$ compounds, Chapter 4. The broad unresolved signal resembles that of $Cr(acac)_3$, where a single ^{1}H resonance is observed, Figure 4.20. Unlike Cr^{3+}, the V^{4+} compound contains a magnetic moment characteristic of a single unpaired electron

which produces a smaller anisotropic dipolar contribution to the ^{1}H signal and results in fewer spinning sidebands. The broad, intense ^{1}H resonance in Figure 7.5 is attributed to the rotationally averaged signal from the methyl groups, Table 7.1. The signal from the methine group is not expected to be detected due to the large broadening from paramagnetic interactions (see Chapter 8 for details). The sharp feature with low intensity at 1.5 ppm is attributed to an impurity.

^{1}H MAS NMR was presented as a sensitive probe of phase purity in Chapter 5 where multiple phases of $Mn(acac)_3$ were readily detected. Signals in the range 30-50 ppm in Figure 7.5 are attributed to β - $V(acac)_3$, which is the commercially available form. The impurity-signal pattern matches the ^{1}H MAS NMR of β - $V(acac)_3$ form like a fingerprint, Figure 4.15, which

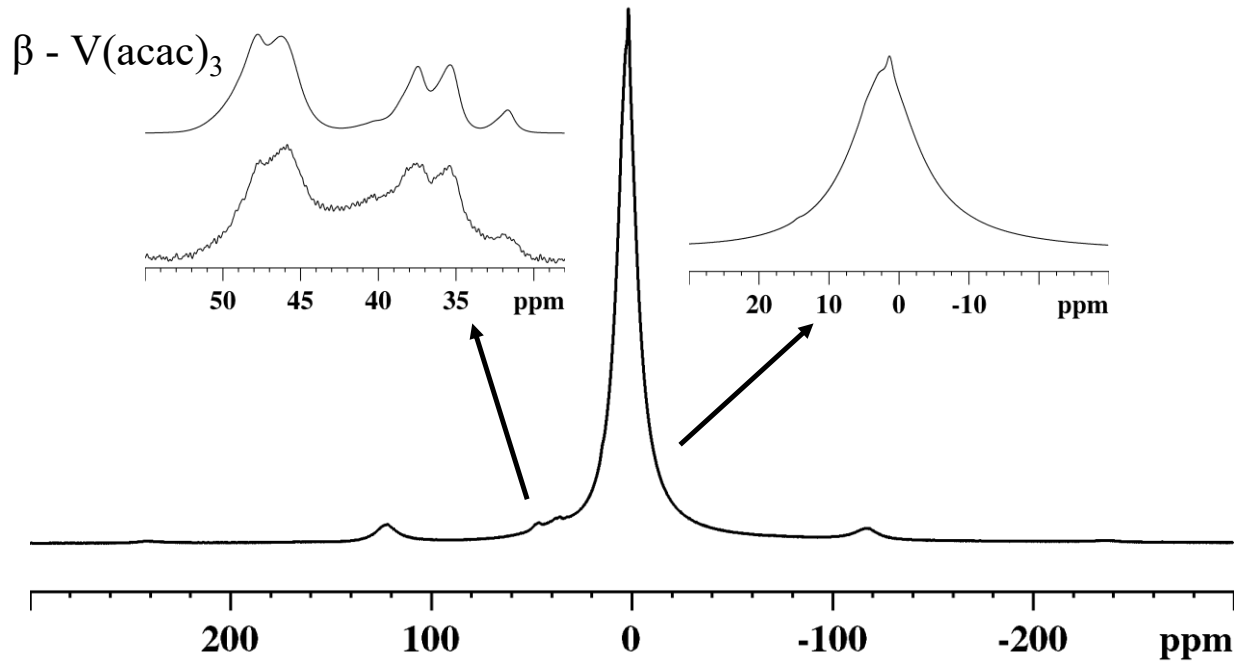

FIGURE 7.5: ^{1}H MAS Hahn-Echo of $VO(acac)_2$. Signals at 30-50 ppm are attributed to an impurity signal of β - $V(acac)_3$. A low-intensity signal at 1.5 ppm is attributed to an unknown impurity.

TABLE 7.1: ^{13}C and ^{1}H NMR of $VO(acac)_2$ and the results of the DFT calculation. Calculated and experimental shifts are in ppm at a sample temperature of 55 ˚C. ^{1}H and ^{13}C shifts from the same functional groups are indicated and appear in the order as listed.

Group	^{13}C		^{1}H	
	A_{calc} (MHz) {A_{exp}}	δ_{calc} [a] {δ_{exp}}	A_{calc} (MHz) {A_{exp} [b]}	δ_{calc} {δ_{exp}}
CO	6.81, 6.70 6.29, 6.22 {not observed}	843, 833 794, 786 {not observed}		
CH	1.22 1.26 {1.53(2)}	217 221 {246(5)}	1.29 1.36 {not observed}	36.1 37.7 {not observed}
CH_3	-0.901 {-0.58(2)}	-58.8 {-27(3)}	(0.21, -0.26, 0.23) {0.02, -0.06, 0.11}	3.5
CH_3	-0.918 -0.921 -0.922 {-0.84(3)}	-60.5 -60.7 -60.8 {-53(3)}	(0.08, -0.23, 0.34) {0.03, -0.08, 0.11} (0.05, -0.19, 0.34) {0.03, -0.05, 0.08} (0.10, -0.16, 0.28) {0.07, -0.09, 0.08}	3.5 3.6 3.8 {2.4(5)}

a) Shifts were calculated according to equation 2.18.
b) Couplings from individual hydrogens from the same methyl group are scaled to match the average experimental shift.

supports the ability of ^{1}H NMR to successfully detect low-concentration impurities in the solid state. In this case, the impurity level is estimated to be on the order of 3%.

Table 7.1 summarizes the assignments from modeling the ^{13}C and ^{1}H MAS NMR spectra of $VO(acac)_2$. The computed shifts are in a good agreement with experiments for both ^{13}C and ^{1}H. A small magnetic moment of the single unpaired electron in the system leads to low sensitivity of the Fermi shift to the coupling constant according to equation 2.18. This measured sensitivity allows a greater error tolerance in prediction of the hyperfine-coupling constant, thus good agreement is obtained with computational modeling.

7.1.2 Spin-density distribution

Figure 7.6 shows the spin-density contour-plot for $VO(acac)_2$ where a clear similarity is observed with the spin-density patterns for the d^1-d^3 $M(acac)_3$ complexes, Chapter 4. According to the calculation, the electron occupancy at the vanadium ion is limited to d_{xy} with less than 7% of unpaired electrons in other orbitals. The symmetry of the occupied orbital correlates with the proposed mechanism of spin distribution that is equivalent to those described in Chapter 4, where ligand orbitals interact with the *d*-orbital in the plane of the ligand. The structural distortion in $VO(acac)_2$ with respect to the orbital symmetry of the transition metal, Figure 7.1, affects the effectiveness of the overlap between the metal-oxygen π* orbital and the carbonyl carbon as seen from the contour plot, Figure 7.6. Therefore, the contours at the carbonyl group are clearly less pronounced than in the $M(acac)_3$ complexes, Figures 4.2, 4.12 and 4.17. The absence of significant overlap at the carbonyl significantly lowers its polarizing ability. As a result, the methyl and methine signals do not experience significant negative spin-densities, shown in Figure 7.6 as weak regions of negative spin-density.

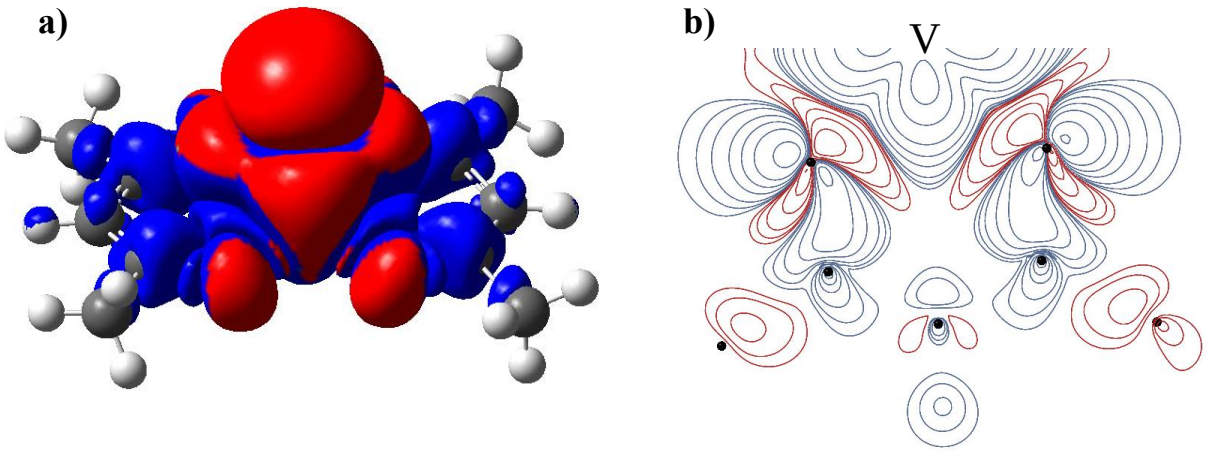

FIGURE 7.6: Spin-density isosurface, a), and a contour plot, b), of one of the acac ligands in $VO(acac)_2$.

The methine group experiences a net positive spin-density, in contrast to the observed signal of $Ti(acac)_3$, where polarization dominates to yield a net negative spin-density, Figure 4.7. The positive spin-density of the methine can be attributed to the high occupancy of the d_{xy} orbital, which is the major source of the unpaired spin-density in the vanadyl complex. This trend in metal-orbital occupancy and the spin density at the methine carbon is also observed in the d^1-d^3 $M(acac)_3$ systems, Figure 4.19. An additional contribution to the spin density at that site may be caused by the reduced strength of the spin polarization from the carbonyl groups. This is a direct consequence of the structural distortion that affects the spin-density distribution in the ligand while maintaining the overall spin-propagation mechanism. This is illustrated in Figure 7.7, where the spin density at the methine nucleus of the vanadyl complex is the greatest among all studied complexes despite the fact that the system has only a single unpaired electron.

Experimental methyl-carbon spin-densities in Figure 7.7 are the least negative among all other metal complexes. This confirms our previous argument of the reduced-polarization effect due to the ligand tilt of 15° with respect to the symmetry of the vanadium d_{xy} orbital. This reduction in polarized spin-density follows closely with the reduced delocalization as predicted for the carbonyl group, Figure 7.7. These predictions can be considered moderately reliable based on the overall sucess of the calculation as seen in Table 7.1.

In summary, $VO(acac)_2$ is unique among the metal acetylacetonates considered here as it provides additional variation to the local geometry around the metal center. ^{13}C MAS NMR of $VO(acac)_2$ shows a high sensitivity to the local structural distortion around the metal of the observed shifts, whereas ^{1}H MAS NMR provides additional signal receptivity that can be used to estimate sample purity through the characteristic fingerprint pattern.

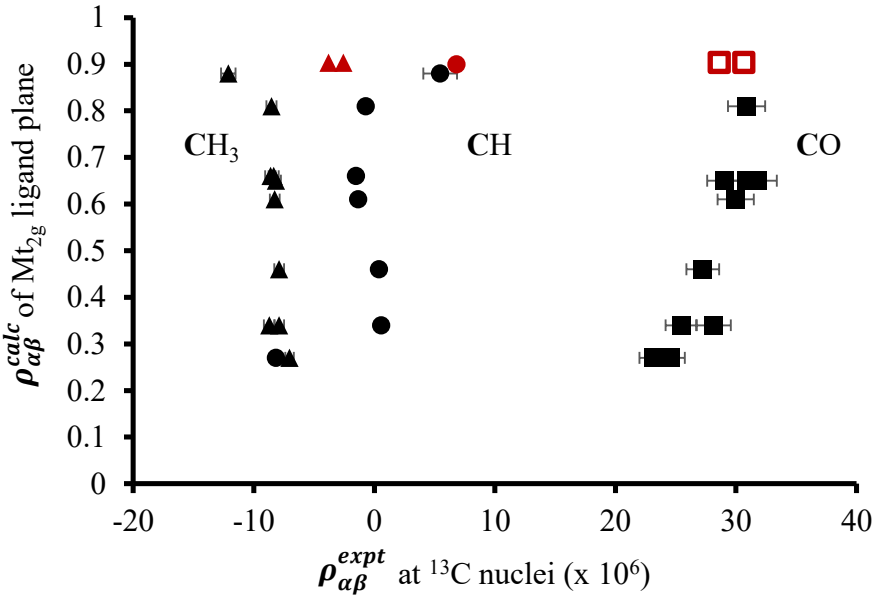

FIGURE 7.7: Relation between spin density in the t_{2g} orbital in the ligand plane and spin density at the carbon nuclei of the ligand for $M(acac)_3$, where M = Ti, V, Cr in black. Spin density with added vanadyl data points uses red marks. Hollow marks indicate calculated predictions that are not observed experimentally.

7.2 $[Cu(Ac)_2H_2O]_2$, $d^9 + d^9$

Copper acetate hydrate, $[Cu(CH_3COO)_2]_2(H_2O)_2$, is the simplest case of an anti-ferromagnetically coupled system with two spins. This binuclear complex is unique due to the proximity of the Cu(II) ions that are thought to form a δ-bond and complete each other's coordination to a distorted octahedron [77]. The distance between the two metals is 2.61 Å and the complex has an antiferromagnetic coupling constant of J = 315 cm^{-1} [75]. This is the energy difference between the two spin-states that differ by the relative electronic alignments at each of the copper atoms, Figure 7.8. This is one of the most basic examples of a coupled model where the spin-only treatment of the magnetization is no longer adequate. The low-energy state of the complex is a magnetically inactive singlet-state that represents antiparallel alignment, whereas

the higher-energy state is a triplet, which is expected to influence the NMR spectra of ^{13}C and ^{1}H at room temperature.

Powder EPR spectroscopy of this complex has been reported at 80 K with the following g-tensor principal components: g_{xx} = 2.0545(3), g_{yy} = 2.0792(2) and g_{zz} = 2.3637(2). The complex contains an inversion center in the middle of the di-copper bond. This inversion symmetry leads to signal degeneracy of equivalent functional groups. Therefore, a single molecule of the complex is expected to produce two carbonyl and two methyl ^{13}C signals with up to two methyl ^{1}H signals, in addition to the water resonances.

7.2.1 ^{13}C and ^{1}H MAS NMR spectra

The ^{13}C MAS NMR spectrum of $[Cu(CH_3COO)_2]_2(H_2O)_2$ is given in Figure 7.9 where all four carbon resonances are resolved, in agreement with our expectation based on the crystal structure. All resonances are paramagnetically broadened and are outside the diamagnetic region, which indicates a significant contribution from the Fermi coupling and the influence of the high-energy triplet state, Figure 7.8.

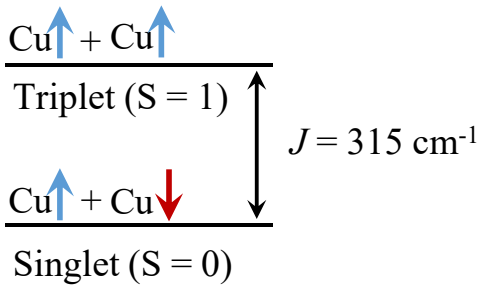

FIGURE 7.8: Schematic energy diagram showing the antiferromagnetism in $[Cu(CH_3COO)_2]_2(H_2O)_2$

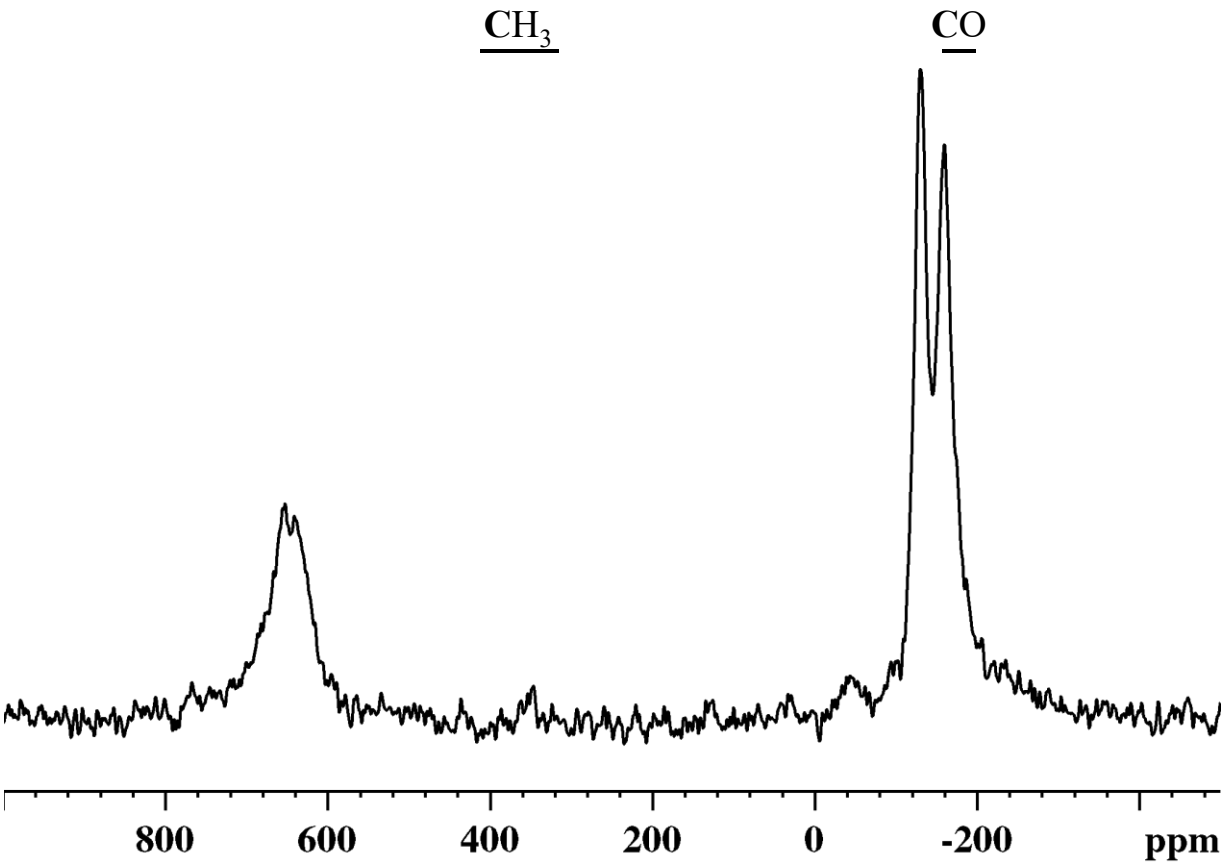

FIGURE 7.9: ^{13}C adiabatic double echo MAS NMR of $[Cu(CH_3COO)_2]_2(H_2O)_2$. Calculated regions are based on susceptibility,χ, formulation from equation 2.19.

The unpaired electron reside in the d_{x2-y2} orbitals of each copper ion with the z-axis passing through the copper centers [75, 77]. Oxygen coordination from the acetate ligands forms a local environment resembling that of bis(acetylacetonato)copper(II), Chapter 6, where four oxygen atoms interact with the d_{x2-y2} orbital of the copper. Oxygen orbital interactions with the d_{x2-y2} symmetry at the metal involve σ*symmetry, which is considered a primary pathway of electron delocalization in $Cu(acac)_2$. Further distribution of the spin density onto the carbon atoms can be interpreted as a close relation to the acetylacetonate analog, where the carbonyl group experiences competing delocalization/polarization effects, whereas the methyl is expected to experience their cooperative action, Figure 6.3. Thus, based on the preliminary arguments as

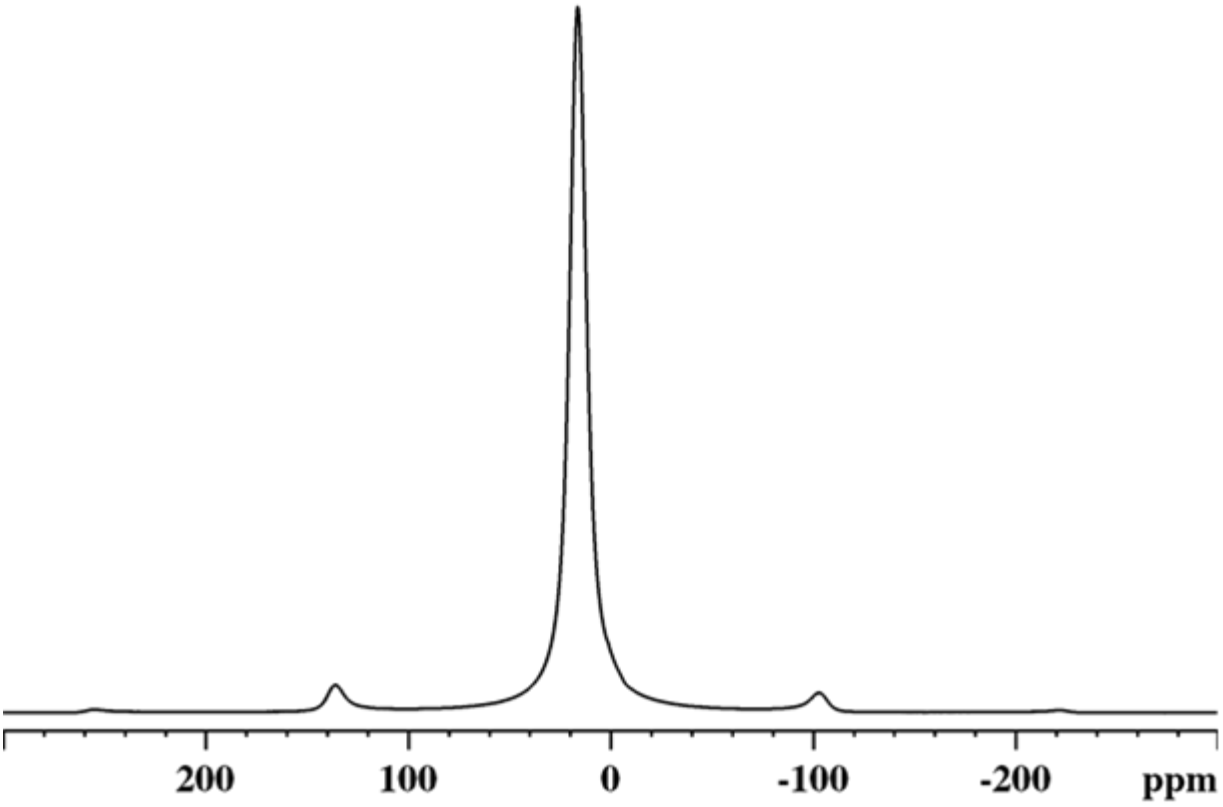

FIGURE 7.10: ^{1}H MAS Hahn-Echo spectrum of $[Cu(CH_3COO)_2]_2(H_2O)_2$.

learned from $Cu(acac)_2$, the ^{13}C signals at the negative Fermi-shift of **[**$Cu(CH_3COO)_2]_2(H_2O)_2$ are attributed to the carbonyl groups, while the resonances at the positive Fermi-shifts are assigned to the methyl groups.

The ^{1}H NMR spectrum of **[**$Cu(CH_3COO)_2]_2(H_2O)_2$ is shown in Figure 7.10, where a single broad resonance is observed with a substantial paramagnetic shift of 16 ppm, indicating appreciable Fermi coupling. The two methyl groups are unresolved, and individual hydrogens are averaged by a fast rotational motion.

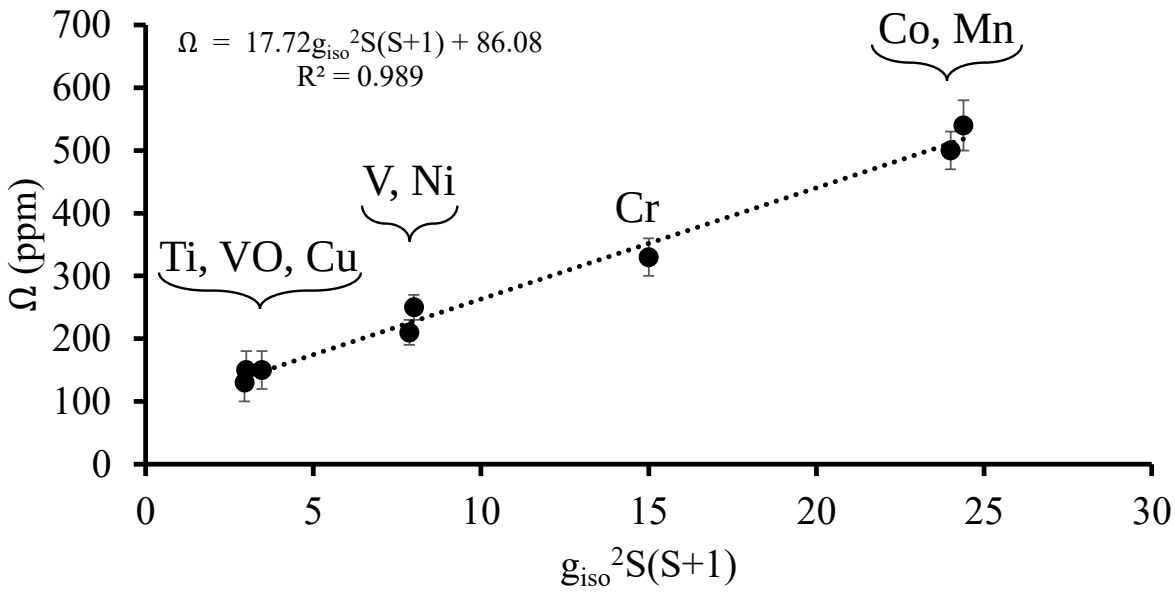

FIGURE 7.11: Anisotropic ^{1}H shift of M(acac)x where M = Ti, V, VO, Cr, Mn, Ni, Co, Cu under the Herzfeld-Berger convention as a function of the square of the effective magnetic moment.

The signal span of ^{1}H NMR provides the first insight into the spin state of the molecule. Figure 7.11 shows the experimental dependence of the anisotropic ^{1}H shift and the magnitude of the effective magnetic moment for various spin states of acetylacetonate complexes from S = ½ to S = 2. The span values in Figure 7.11 were obtained by analogy to the ^{1}H fit of $Co(acac)_2 \cdot 2H_2O$ in Figure 6.1(Appendix). The relation follows from the dipolar contribution to the nuclear anisotropic signal according to equation 6.6, where an intercept in Figure 7.11 constitutes diamagnetic contributions to the signal span, such as dipolar coupling, which is on the order of 60 ppm between two methyl protons [141], and chemical shielding, on the order of 5 ppm for ^{1}H signals in organic moeities [142, 143]. The comparison can be considered as reasonable within the point - dipole approximation as the metal-methyl distances are similar in all these structures and average at 4.67 ± 0.05 Å. The distance from the averaged methyl

hydrogens to the metal in copper acetate is 4.66 ± 0.06 Å, which is comparable to that of the other acetylacetonate complexes. The slope in Figure 7.11 indicates an average distance between methyl hydrogens and the metal center of 4.59 ± 0.17 Å, which agrees well with the distances from crystal structures. The relatively small signal anisotropy of the copper acetate ^{1}H NMR is indicative of the electron - nuclear dipolar contribution resembling that of the S = 0.4(2) ~ 1/2 spin-state according to the linear fit in Figure 7.11. This is an indication that the magnetic moment of the molecule is quenched by the presence of the populated antiferromangetic spin-state.

Measurements of the ^{1}H signal span below 200 ppm in Figure 7.11 is not reliable due to the small number of spinning sidebands that can be used for the fit as a result of the fast MAS rate. However, the general linear trend of the span with the magnetic moment is retained from measurements past 200 ppm, which suggests that lower-span values are not recorded with significant deviation. An experimental way to accurately determine the signal span of a lower magnitude is to reduce the MAS rate. This produces more spinning sidebands for a fit of the span, Figure 2.7. Unfortunately, such reduction in spinning frequency would lead to a significant change in sample temperature, on the order of 30°C, which would influence the dipolar contribution to the signal span according to equation 6.6.

7.2.2 Spin-density distribution

Figure 7.12 shows the spin density of the triplet state of the copper acetate dihydrate molecule. The spin-density distribution can be interpreted through a series of interacting valence orbitals. The interaction between the acetate oxygens and the copper d_{x2-y2} orbital is clearly traceable and leaves the oxygen atom with a net positive spin-density in the high-energy *s*-

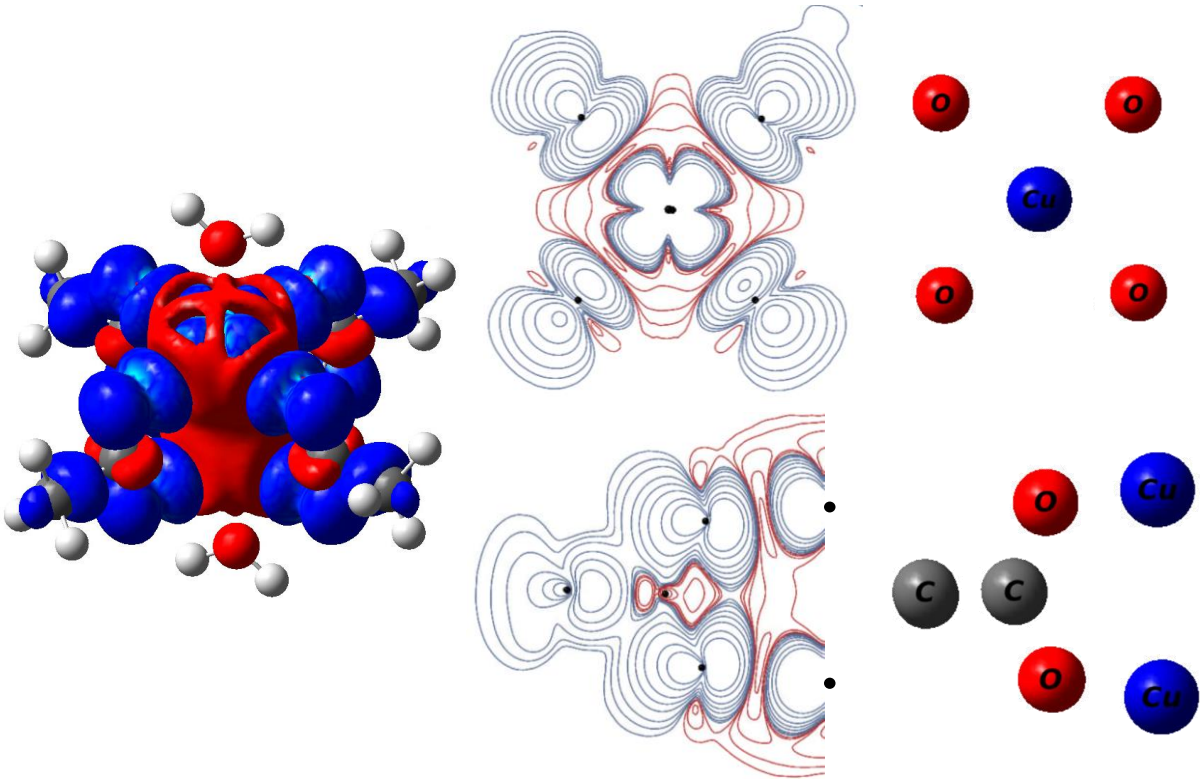

.

FIGURE 7.12: Spin-density map of $[Cu(CH_3COO)_2]_2(H_2O)_2$. Selected spin-density contours in the center; isosurface on the left.

orbital. This excess of positive spin-density then delocalizes further to the carbonyl carbon; meanwhile the polarization of the oxygen-carbon bond leaves the carbon site with a net negative spin-density. Both interactions compete and closely resemble the interactions in bis(acetylacetonato)copper(II), Figure 6.3. As a result, the carbonyl carbon of copper acetate has a net small negative spin-density, which confirms our previous assignment of the shift with the negative Fermi contribution. Polarization propagates further down the ligand to the methyl group and causes excess positive spin-density at the methyl, together with possible delocalization. Thus, the signal at positive Fermi-shift is attributed to the methyl group, Figure 7.9.

7.2.3 Description of the Fermi shift in a coupled spin-state

According to the equation 2.18, the Fermi shift has a scaling dependence on the magnetic moment of the sample. As we have seen previously, the magnetic moment can be altered by the spin-orbit coupling and zero-field splitting for systems with multiple unpaired spins, for example, $Co(acac)_2 \cdot 2H_2O$, Chapter 6. For the antiferromagnetically coupled copper acetate, the magnetic moment is quenched by thermal averaging of low-lying states with different magnetic moments, Figure 7.8.

Table 7.2 shows the results of calculations for the triplet state of the dicopper complex with various levels of theoretical treatment to show the effects of averaged spin-states on NMR shifts. The singlet spin-state is the low-energy state with no unpaired electrons, and thus its chemical shift contains only a diamagnetic component. The diamagnetic component of the triplet state differs slightly from that of the singlet as the two states lead to different electronic environments that influence the nuclear shielding. The Fermi coupling derived from the triplet state shows the ferromagnetic coupling where both spin-½ centers contribute to produce an S = 1

TABLE 7.2. ^{13}C NMR of $[Cu(CH_3COO)_2]_2(H_2O)_2$ and DFT calculation. Calculated and experimental shifts are in ppm at sample temperature of 55 ˚C.

Group	A_{calc} (MHz)	Singlet δ_{dia}	Triplet δ_{dia}	Triplet δ_{Fermi}	S = 0.4(2) δ_{Fermi}	χ δ_{Fermi}	δ_{exp}
CO	-3.29	171	183	-908	-254(160)	-195	-160
CO	-2.81	166	177	-777	-218(140)	-167	-130
CH_3	5.26	11.4	15.2	1452	406(260)	312	640
CH_3	6.85	2.60	5.10	1891	530(340)	407	654

state. The large magnetic-moment of this state leads to significant overestimation of the Fermi

coupling even with the calculated coupling constants. The effective spin-state derived from the anisotropic component of ^{1}H MAS NMR has a large error but provides a better scaling factor to the calculated Fermi coupling and agrees better with the experimental shifts.

Griffith[15] introduced a formulation for the magnetic susceptibility, χ, of a system with two coupled spin - ½ metal centers. His expression for the magnetic susceptibility is as follows:

$$\chi = \frac{g_{iso}{}^2 N_A \mu_0 \mu_B^2}{k_B T(3 + e^{\frac{-J}{k_B T}})} \quad \textbf{(7.1)}$$

where g_{iso} is the isotropic g-factor that is included in the expression to account for deviations from the spin-only value, N_A is Avogadro's constant and *J* is the electron spin-spin coupling constant. This equation can be substituted into equation 2.20 to give an expression for the Fermi shift:

$$\delta_{Fermi} = \frac{\mu_B A_{iso} g_{iso}}{k_B T(3 + e^{\frac{-J}{k_B T}})\gamma_n} \quad \textbf{(7.2)}$$

which is used to determine the theoretical shifts in Table 7.2. From equations 7.1 and 2.18 the effective spin-state of copper acetate can be derived from the relation:

$$S(S+1) = \frac{3}{(3 + e^{\frac{-J}{k_B T}})} \quad \textbf{(7.3)}$$

The solution gives S = 0.32, which is in agreement with the predicted S = 0.4(2) from the anisotropic component of the ^{1}H MAS NMR, which was measured over all $M(acac)_x$ complexes in this thesis (Figure 7.11).

Table 7.3 gives the hyperfine-coupling constants derived from the experimental shifts in Table 7.2, using equation 7.2. The calculated model underestimates the effect of spin

TABLE 7.3. Fermi-coupling constants of ^{13}C sites in $[Cu(CH_3COO)_2]_2(H_2O)_2$ as derived with equation 7.2.

Group	$^{13C}A_{calc}$ (MHz)	$^{13C}A_{exp}$ (MHz)
CO	-3.29	-5.7(2)
CO	-2.81	-5.2(2)
CH_3	5.26	10.5(3)
CH_3	6.85	10.8(3)

polarization as the carbonyl group has a more negative Fermi-coupling while the methyl has a greater positive coupling than predicted computationally.

In conclusion, the antiferromagnetically coupled tetra-μ²-acetatodiaquadicopper(II) complex shows the transferability of MO interaction principles to help in assignment of solid-state NMR resonances of paramagnetic systems. The ^{13}C NMR of the dicopper complex produces resonances and spin-density contour-maps, which are directly related to the previously studied $Cu(acac)_2$ complex. The electron-electron coupling in this complex can be taken into account by considering the Boltzmann distribution of states, equation 7.1, which describes the effect of the coupling on the magnetic susceptibility. This approach can be used for spectral interpretation of coupled and mixed-state systems.

Chapter 8: Understanding signal width in paramagnetic coordination compounds

8.1 Multiple-point-dipole model

Small paramagnetic molecules are closely packed in the solid state such that unpaired electron(s) on neighboring molecules have a non-negligible dipolar interaction with NMR-observed nuclei. In this scenario, a point-dipole approximation with a single paramagnetic center may no longer give an adequate description. An alternative approach was given in Chapter 6, where the pseudocontact shift is calculated using anisotropic hyperfine-coupling. This approach accounts for the effect of electronic distribution outside the metal center on the observed pseudocontact shift at a nucleus. To account for the effects of nearby molecules, they would need to be added to the calculation, at which point it becomes impractically time-restrictive even with efficient hybrid-DFT functionals. A tris(acac)metal complex contains 43 atoms, whereas if one such molecule is modeled with the surrounding molecules in crystal, the number of atoms to be modeled suddenly becomes on the order of 900, which is equivalent to months of computational time. This calculation was attempted with 64 processors and 100 GB hard-disk space, but failed after several weeks during the calculation of the hyperfine interaction, as the program ran out of disk space. Another alternative is to expand the point-dipole model from a single point to include multiple points in the crystal structure, where individual points are approximated from atomic positions. Each individual atom in the structure is treated as a source of some unpaired electron-density, which is calculated using Natural Population Analysis (NPA) [117]. The electron-

nuclear dipolar contribution is calculated separately from each atomic position with the point-dipole model and all contributions are summed to yield the net contribution to the nuclear relaxation. The modified expression may be referred to as the **multiple-point-dipole model** (MPDM), which I expressed by equation 8.1. The quantity of unpaired electrons is ρ = 2S, which is unique to individual atomic positions in the crystal as calculated by NPA. The new equation has the following simplified form based on equation 2.30:

$$\frac{1}{T_{2D}} = \sum_{i}^{n} \frac{\rho_{\alpha\beta}^{i}\left(\rho_{\alpha\beta}^{i}+2\right)}{60 r_i^6} \gamma_I^2 \mu_B^2 g_{iso}^2 \left(7T_e + \frac{13T_e}{1+T_e^2 {\omega_S}^2}\right) \qquad \textbf{(8.1)}$$

where $\rho_{\alpha\beta}{}^{i}$ = 2S is the density of unpaired electrons at a particular atom location *i* with the sign of the spin density retained, *n* is the number of atoms within a selected interaction sphere, and r_i is the distance from the observed nucleus to the atom position with the unpaired spin-density within the interaction sphere, g_{iso} is the isotropic g-value, and T_e is the electron-relaxation time. An appropriate choice of the cutoff for the sphere that surrounds a given nucleus in a solid can provide a realistic account of the paramagnetic dipolar contribution. An illustration of the sphere projection that includes the first molecular coordination in the solid is shown in Figure 8.1. Here, 20 entire molecules of $Cr(acac)_3$ are included, which constitute the full set of nearest-neighbor molecules to that for which the nuclear property is being calculated. In all complexes in this thesis, the interaction sphere has a radius of 20 Å, which meets the convergence criterion of < 1%, as shown in Figure 8.2 for $Cr(acac)_3$. In addition to probing long-range dipolar interactions with distant molecules, equation 8.1 attempts to account for close-range interactions with neighboring atoms that host non-negligible unpaired electron-spin density. In the limit of the absence of such long-range and short-range effects, equation 8.1 reduces to equation 2.33 where unpaired electrons are assumed to be located solely at the paramagnetic center.

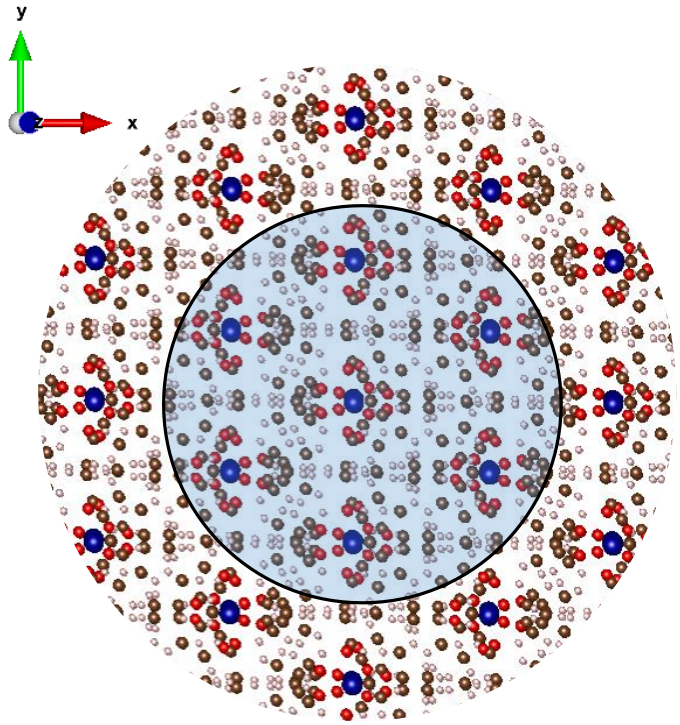

FIGURE 8.1: Interaction sphere in a $Cr(acac)_3$ crystal that includes the first molecular coordination sphere [61].

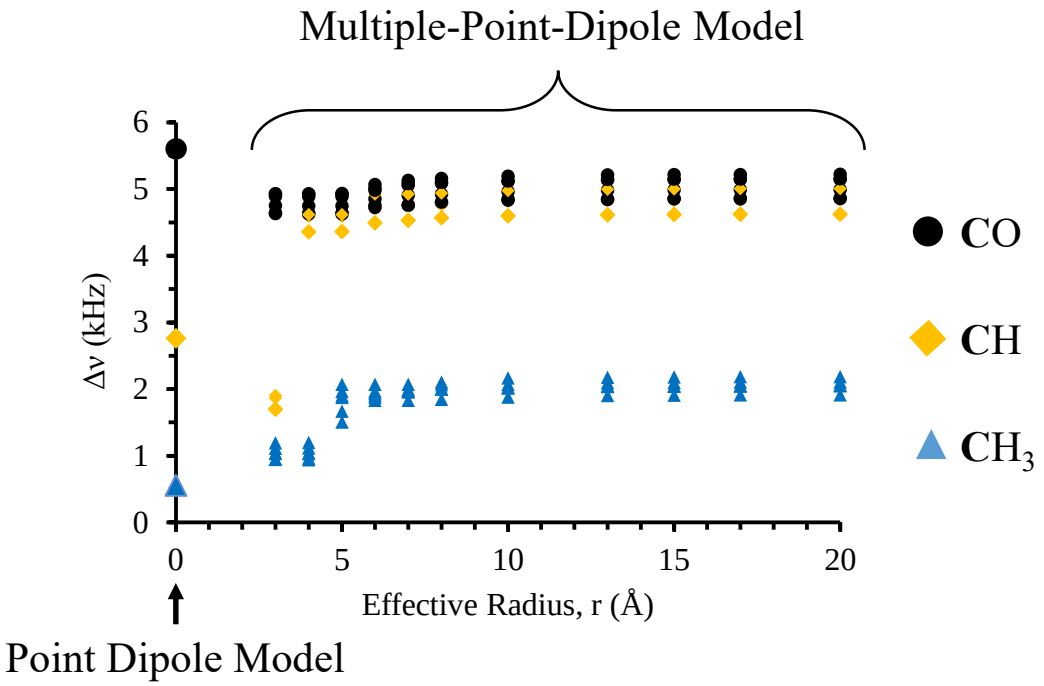

FIGURE 8.2: Modeling the dipolar paramagnetic contribution to isotropic ^{13}C signal width in $Cr(acac)_3$. Comparison between point-dipole and multiple-point-dipole models.

8.2 Modeling NMR signal width in $Ti(acac)_3$

The signal width of the isotropic resonance in solid-state NMR of a paramagnetic solid is intrinsically tied to their electron and nuclear relaxations. Electron relaxation acts as a scaling factor in both the Fermi and electron-nuclear dipolar mechanisms of nuclear transverse relaxation, equations 2.29 and 2.33, which is related to the signal width via $(\pi T_2)^{-1}$. The inverse dependence between the two relaxation parameters makes EPR and NMR techniques complementary in the study of the hyperfine-coupling interactions. For the purposes of this work, short relaxation times for the electron are desired as they lead to increased transverse nuclear relaxation, which ultimately leads to narrower NMR lines and greater signal resolution. By implication, broad EPR peaks at low experimental temperatures can be considered promising for solid-state NMR experiments as they imply favorable relaxation for nuclear magnetic resonances, and have improved NMR resolution (Chapter 2 [5]).

8.2.1 ^{13}C MAS NMR

According to our previous discussion of ^{13}C MAS NMR of $Ti(acac)_3$, Chapter 4, the ^{13}C signal has a significant Fermi-contact interaction and broadening of resonances. The Fermi-contact shift is attributed to singly occupied metal orbitals and can be estimated from the observed NMR shift, assuming that the pseudocontact shift is negligible. Figure 8.3a gives a comparison of the measured and DFT-calculated Fermi-couplings for the observed resonances. This figure shows that the calculated Fermi-couplings agree consistently with the experimental values. NMR- derived Fermi-coupling constants are used to express the Fermi contribution to the signal width according to equation 2.29. The NPA calculation together with the known crystal structure is sufficient to provide an expression for the dipolar contribution to the paramagnetic

width via equation 8.1. As both Fermi and dipolar expressions share a common parameter, the electronic relaxation time T_e, its value is fitted to obtain the best agreement among all signal widths in ^{13}C MAS NMR. The fit is defined by the equation:

$$\Delta\upsilon_{1/2} = \frac{1}{\pi T_{2F}} + \frac{1}{\pi T_{2D}} + \Delta\upsilon_{1/2}^{dia}$$

where the diamagnetic contributions to the width, $\Delta\upsilon_{1/2}^{dia}$, are approximated from ^{13}C{^{1}H} CP MAS NMR of Al(acac)$_3$, Table 8.1(Appendix). Using the experimental Fermi contact coupling for all calculations, the only remaining variable in the fitting procedure is the electronic

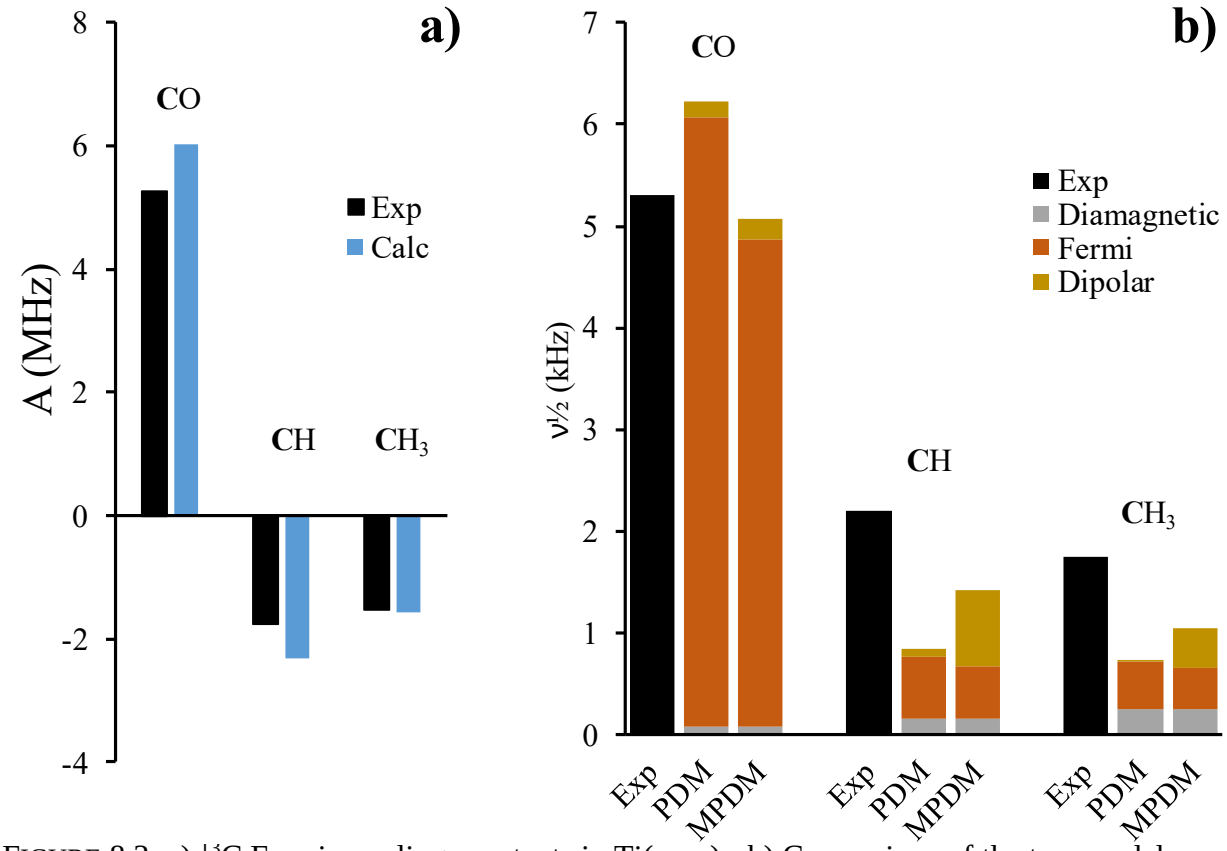

FIGURE 8.3: a) ^{13}C Fermi coupling constants in Ti(acac)$_3$. b) Comparison of the two model schemes for the signal width in ^{13}C MAS NMR of Ti(acac)$_3$. Presented widths are from the experiment (Exp), point-dipole model (PDM) and multiple-point-dipole model (MPDM). Detailed values are given in Table 4.2 and Appendix Table 8.1.

relaxation time. T_e values evaluated using both models - PDM and MPDM - are compared in the Appendix tables.

Figure 8.3b compares of two fitting models for signal width in ^{13}C MAS NMR of $Ti(acac)_3$. The point-dipole model (PDM) is governed by the distance between a single metal and the nucleus of interest. The multiple-point-dipole model (MPDM) is our proposed extension of PDM that incorporates additional delocalized spin-density on the ligand and from nearby molecules in a solid. The degree of the delocalization is calculated with NPA within the same energy calculation that was used to find the Fermi-coupling constants in Figure 8.3a. Signal widths in Figure 8.3b and the following figures are averaged for individual functional groups for visual clarity. Actual fits per experimentally observed signal are given in Appendix tables. According to Figure 8.3b, both theoretical methods agree on the Fermi-coupling contribution as being the major source of ^{13}C MAS NMR signal width in $Ti(acac)_3$ of the carbonyl group, which may seem counterintuitive at first as the carbonyl group is the closest to the transition metal and therefore one might assume it to have a strong contribution from electron-nuclear dipolar interaction. However, the combination of the large Fermi-coupling, that boosts the Fermi contribution according to equation 2.26, and low magnetogyric ratio of ^{13}C (compared to ^{1}H, see below), that lowers the dipolar contribution according equation 8.1, leads to the dominant contribution of the Fermi coupling to ^{13}C peak width.

The overall order of signal widths is estimated correctly by both models: the carbonyl-group signals have the largest width, followed by the methine and methyl signals. This is attributed to the small impact of the dipole contribution to signal broadening, which is the major difference between the two models. The dipolar contribution from the MPDM has an overall greater magnitude than that of the simple point-dipole model, which is expected as MPDM

includes contributions from molecules within the 20 Å radius. Nevertheless, both methods provide a relatively close fit for the electron-relaxation parameter, on the order of 55 – 65 ps. This is considerably shorter compared to the linewidth estimate from EPR in a frozen solution at 77 K, where T_e is estimated to be on the order of a nanosecond [59]. However, the estimate provided by EPR may not agree with our high temperature/high field-based value, as these conditions are known to shorten the electronic relaxation by introducing additional spin relaxation pathways [96].

8.2.2 ^{1}H MAS NMR

The signal width of the ^{1}H MAS NMR resonances of $Ti(acac)_3$ can be fitted by analogy with ^{13}C MAS NMR. Both ^{1}H and ^{13}C MAS NMR spectra are expected to show identical electronic relaxation, as this parameter is independent of the choice of the NMR nucleus. The diamagnetic width of the ^{1}H resonances is approximated from the ^{1}H MAS NMR of $Al(acac)_3$ under similar experimental conditions. Figure 8.4a presents a summary of the experimentally estimated (in the absence of the pseudocontact shift) Fermi-contact couplings that are used in the evaluation of the Fermi contribution to the signal width. Fermi couplings from individual protons on methyl groups are scaled accordingly to provide the appropriate averaged-shift, while retaining their relative magnitude, as there is no practical way to experimentally determine Fermi couplings of individual ^{1}H signals due to the rapid rotation of the methyl group. This rotation can also lead to partial averaging of the paramagnetic dipolar coupling if the rotational frequency is on the order of the dipolar-coupling frequency. According to Figure 8.4a the Fermi coupling of ^{1}H shows close agreement with experimentally derived values, consistent with the accuracy of ^{13}C-coupling predictions, Figure 8.3a. An accurate account of the spin-density distribution is

essential for modeling its effects on the dipolar contribution to the isotropic width with the MPDM according to equation 8.1.

Figure 8.4b compares the signal widths in ^{1}H MAS NMR of Ti(acac)$_3$ for the two models. The PDM model does surprisingly well and estimates the electronic relaxation to be on the order of 55 ps based on ^{13}C NMR and 65 ps based on ^{1}H NMR experiments, which suggests that the long-range interaction does not play a significant role in this system. The MPDM model significantly overestimates the dipolar width for the methine group. The cause of this discrepancy is the predicted presence of the large spin-density at the aromatic orbital of the

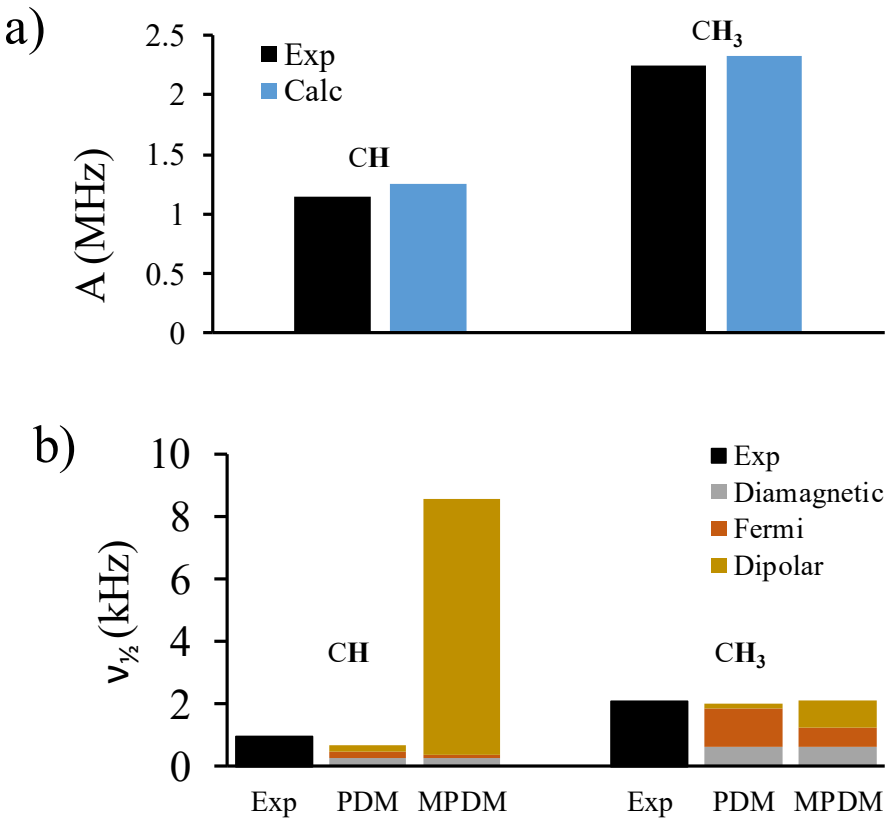

FIGURE 8.4: a) ^{1}H Fermi-coupling constants in Ti(acac)$_3$ and b) the comparison of the two modeling schemes for the signal width, $\upsilon_{½}$, in ^{1}H MAS NMR of Ti(acac)$_3$. Detailed values are given in Table 4.2 and Appendix Table 8.2.

methine carbon, which dominates the predicted width of the ^{1}H as its next-nearest neighbor. A detailed NPA gives the pseudoaromatic methine spin-density as $\rho_{\alpha\beta}$ = - 0.01, which is almost an order of magnitude greater than the total spin-density at the methyl carbon, where $\rho_{\alpha\beta}$ = - 0.002. The dipolar contribution from the spin-density at the methine carbon dominates the contribution from the metal center due to the difference in their proximity. The scaling factor $\rho(\rho+2)/r^6$ for the methine-carbon dipolar contribution to the methine ^{1}H width is found to be three orders of magnitude greater than that from Ti^{3+}. This shows the level of accuracy required to model the signal width in solid-state paramagnetic NMR: an accurate account of the spin density distribution is crucial. Despite having a computational model that does well at predicting Fermi-coupling constants at each nuclear site, the spin density at other atomic orbitals with $l > 0$ may still have significant error, which will affect the anisotropic hyperfine-coupling.

8.3 Modeling NMR signal width in β - $V(acac)_3$

Analysis of signal widths in ^{13}C and ^{1}H MAS NMR spectra of β-$V(acac)_3$ is similar to that of $Ti(acac)_3$. A comparison of averaged computed and experimental ^{13}C and ^{1}H Fermi-coupling constants of $V(acac)_3$ is given in Figure 8.5, with the detailed values available in Tables 8.5 – 8.8 (Appendix). The overall quality of the computational modeling is satisfactory, as the calculated Fermi-couplings are in a close agreement with those derived from NMR experiments.

Figure 8.5b shows comparisons of the ^{13}C signal widths in β-$V(acac)_3$ calculated by the two models. The results of both methods are similar due to the low significance of the paramagnetic dipolar coupling to the signal width of ^{13}C resonances. Both methods give the electronic relaxation on the order of 20 ps, which is even shorter than that of $Ti(acac)_3$. Despite having a larger number of unpaired electrons, $V(acac)_3$ resonances are narrower than those of

$Ti(acac)_3$ due to a shorter relaxation time and a smaller magnitude of the Fermi coupling, Figures 8.5a and 8.3a. Low values of Fermi coupling in methine and methyl groups ensure that the signal width is dominated largely by the electron-nuclear dipolar coupling and other diamagnetic couplings. This finding is a similar to that of $Ti(acac)_3$ in that the width of the carbonyl group is once again heavily dominated by the Fermi interaction and not the dipolar term.

Figure 8.5d shows a comparison of the ^1H NMR peak widths, which again shows inconsistent results for the dipolar coupling of the methine group by the MPDM. The lack of

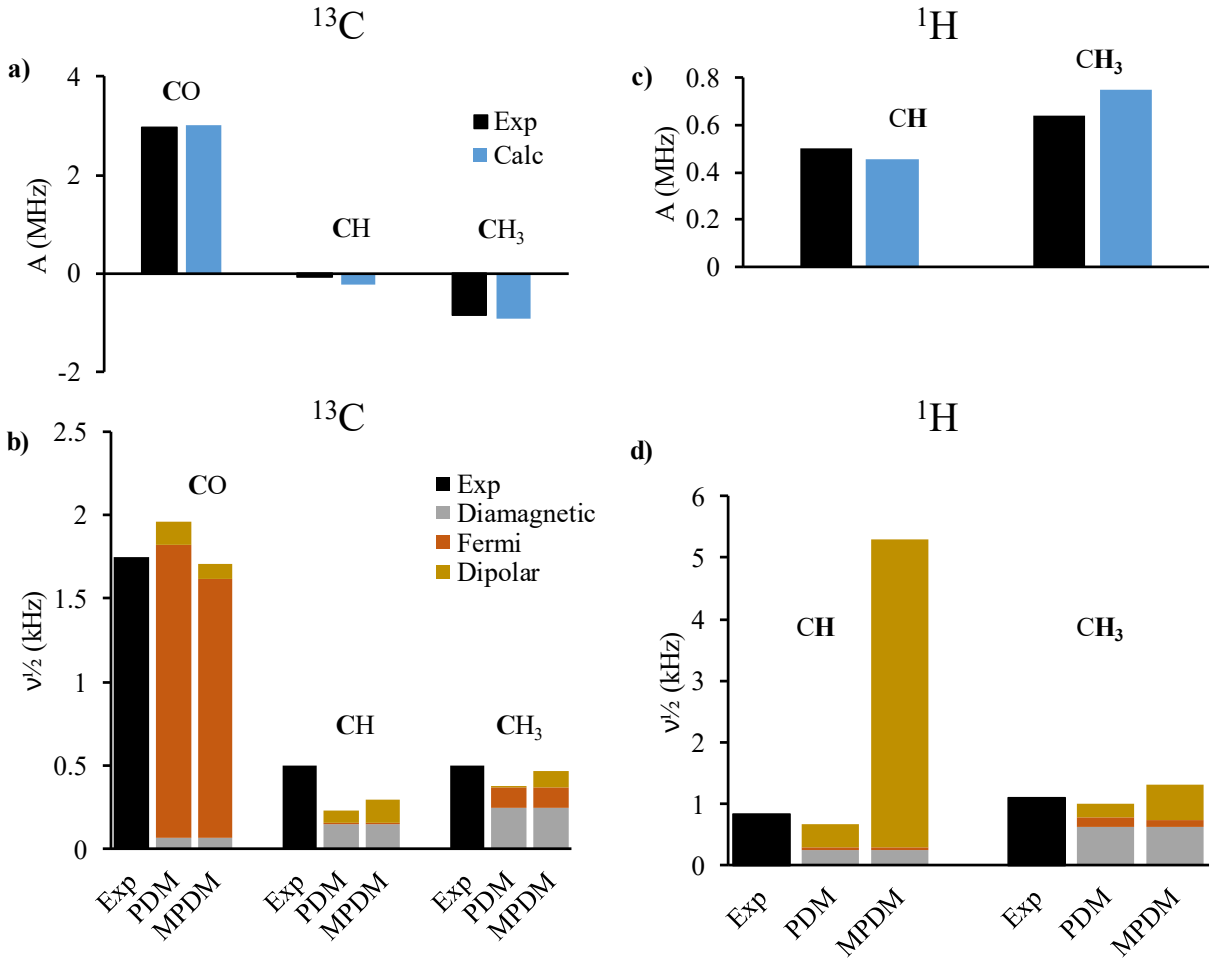

FIGURE 8.5: a) ^{13}C and c) ^1H Fermi-coupling constants in β-$V(acac)_3$ and a comparison of the two models for the signal width in b) ^{13}C and d) ^1H MAS NMR of β-$V(acac)_3$. Detailed values are given in Table 4.4 and Appendix Table 8.3.

agreement is attributed to the large spin-density in the pseudoaromatic orbital of the methine carbon, which is on the order of -0.01 electrons. This is a smaller value than that calculated for $Ti(acac)_3$, and thus the error in the dipolar component is also smaller in magnitude for $V(acac)_3$, Figures 8.4b and 8.5a. Nevertheless, both ^{1}H and ^{13}C peak-widths show overall agreement with the electronic relaxation time for $V(acac)_3$, which is within the 20-30 ps under the experimental conditions used here.

8.4 Modeling NMR signal-width in $Cr(acac)_3$

Figure 8.6a,c gives a summary of the calculated and experimentally derived Fermi couplings of ^{13}C and ^{1}H in $Cr(acac)_3$. The signs of the Fermi-coupling constants and their relative magnitudes are predicted reliably with the hybrid functional calculation, however the coupling at the methine ^{13}C lacks in accuracy (Figure 8.6a). However, this does not significantly compromise the analysis of the signal width in ^{13}C MAS NMR, Figure 8.6b, as both MPDM and PDM indicate the dominance of dipolar coupling to the nuclear relaxation. Acceptable agreement of signal widths for both observed ^{13}C resonances confirms the overwhelmingly broad resonance of the carbonyl group, which is experimentally unobserved, Figure 4.18. As both fitting models clearly indicate in Figure 8.6b, the dominant contribution to the signal width of this group is the Fermi-coupling interaction, despite the proximity to the metal center.

^{1}H MAS NMR of $Cr(acac)_3$ in Figure 4.20 shows a broad featureless resonance, which is strongly affected by paramagnetic broadening. Figure 8.6c shows good agreement between the averaged calculated methyl ^{1}H Fermi-coupling and the observed average resonance, which is attributed primarily to the methyl groups as they have most protons in the structure. The resonance-width agreement of ^{1}H in this case is highly uncertain due to a severe overlap of all

resonances, but even in these conditions, both fitting models give results similar to previous cases. The PDM indicates the dominant effect of the electron-nuclear dipolar contribution and estimates the width of the methine signal to be on the order of that of the methyl group. Whereas the methine signal from MPDM is highly overestimated, judging from the significant occupancy of the p_z-orbital at the methine carbon, + 0.007, its similar to the trend in the titanium and vanadium cases.

The signal of the EPR resonance is narrow, implying a relatively long electronic-relaxation time, on the order of nanoseconds [144]. This is in accord with our NMR spectra having appreciable signal-widths due to electron-nuclear interactions and long electron-

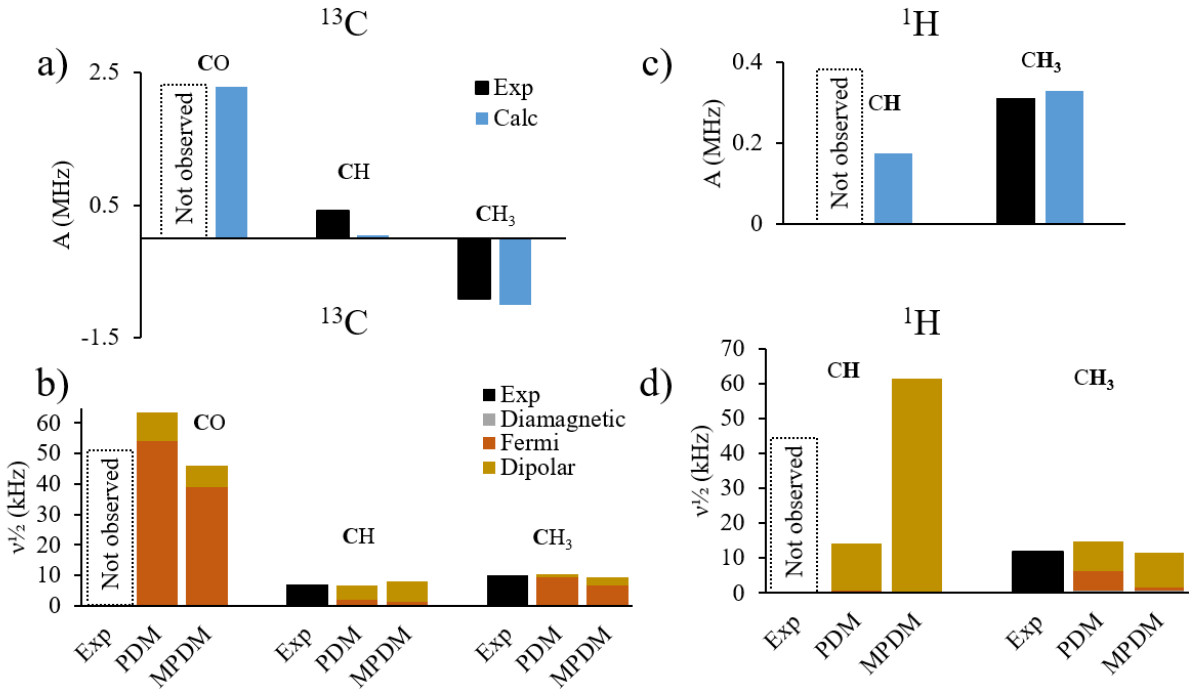

FIGURE 8.6: a) ^{13}C and c) ^{1}H Fermi-coupling constants in Cr(acac)$_3$ and comparison of the two models for the signal width in b) ^{13}C and d) ^{1}H MAS NMR of Cr(acac)$_3$. Detailed values are given in Table 4.5 and Appendix Tables 8.5 and 8.6.

relaxation times found from ^{13}C NMR (500-700 ps) and ^{1}H NMR (350 - 950 ps) (see Tables 8.5, 8.6 in Appendix for details).

8.5 Modeling the NMR signal-width in γ-$Mn(acac)_3$

The electron-relaxation time in $Mn(acac)_3$ was estimated from a solution ^{1}H NMR experiment on a $Mn(acac)_3$/acetone mixture in magnetic fields of up to 1.1 T [58]. The electronic relaxation was 8(2) ps in the temperature range 215-303 K. Such a low and temperature-independent relaxation time is consistent with the lack of signal resolution in EPR experiments [65, 145], and suggests that fast electronic-relaxation will lead to sharp solid-state NMR signals, as observed in the ^{13}C MAS NMR spectrum of $Mn(acac)_3$, Figure 5.4.

A breakdown of the Fermi couplings and contributions to the signal widths of ^{13}C and ^{1}H resonances is given in Figure 8.7. Manganese has four unpaired electrons in a highly Jahn-Teller-distorted pseudo-octahedral coordination, which produces a significant variation in Fermi-contact shifts among the same functional groups of the ligand. From Figure 8.7a, c, it can be seen that the calculation provides an overall correct distribution of Fermi-coupling constants, but the relative magnitudes of these couplings do not agree as well as in systems with fewer unpaired electrons due to the increased complexity of modeling systems with a large number of unpaired electrons [93].

Modeling ^{13}C and ^{1}H signal widths is given in Figure 8.7b, d, where the fits follow experimental values qualitatively in both NMR spectra. The ^{13}C peak-widths are dominated largely by substantial Fermi coupling, as opposed to the ^{1}H signals, where Fermi coupling is relatively small, and the electron-nuclear dipolar coupling dominates the signal width. All models of relaxation indicate electronic-relaxation times in the 5 – 45 ps range, which is a large

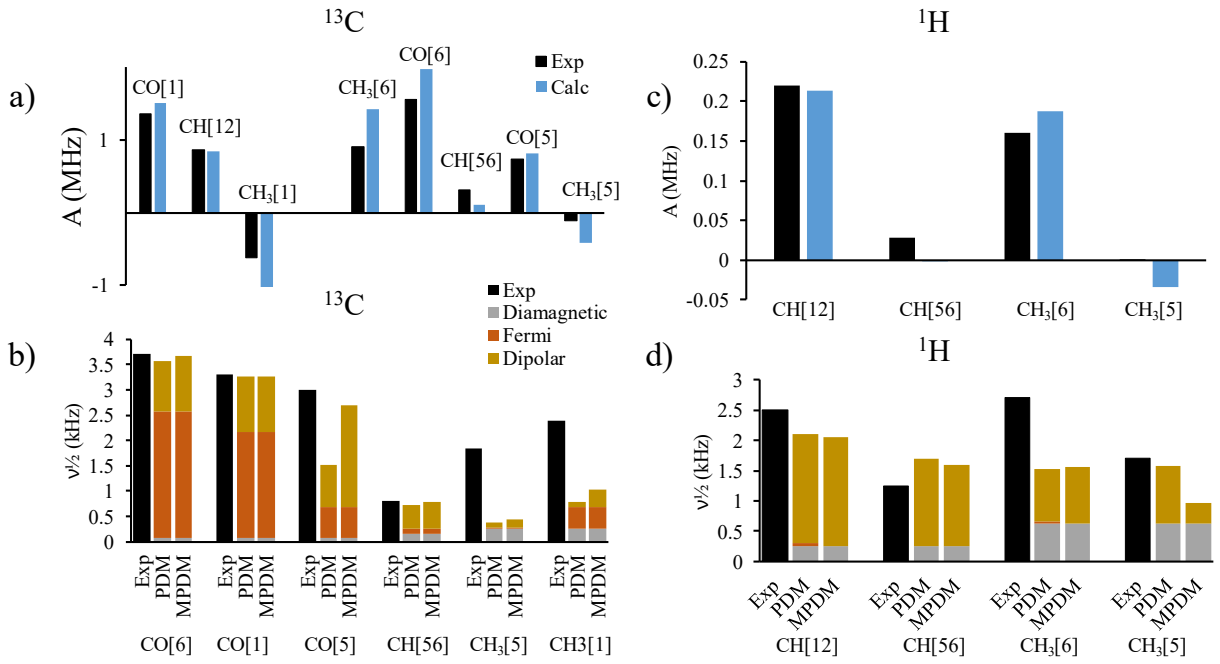

FIGURE 8.7: a) ^{13}C and c) ^{1}H Fermi-coupling constants in $Mn(acac)_3$ and a comparison of the two models for the signal widths in b) ^{13}C and d) ^{1}H MAS NMR spectra of $Mn(acac)_3$. Detailed values are given in Table 5.2 and Appendix Tables 8.7 and 8.8.

variation but includes the previously reported estimate of 8(2) ps [65]. Modeling a short relaxation-time requires greater knowledge of other possible signal-width contributions, such as variations due to signal overlap, sample temperature, degree of sample crystallinity, an accurate account of the diamagnetic contribution to the width, and possible effects of an anisotropic magnetic-moment of the rotor packed with a sample having a large magnetic-moment [105]. With all these considerations and based on our previous modeling results for the Ti, V and Cr acac complexes, the model provides a general order-of-magnitude estimate of the electronic-relaxation, which may be sufficient to rationalize the relative contributions to the observed signal-widths and indicate possible issues with the signal detectability in NMR and EPR.

8.6 Modeling NMR signal width in $Fe(acac)_3$

No ^{13}C MAS NMR signal could be obtained for solid $Fe(acac)_3$, and a single featureless broad peak was obtained in the ^{1}H MAS NMR spectrum. Here, we use calculated results to attempt to explain the lack of a ^{13}C signal through modeling of the signal width of the observed ^{1}H resonance. As we have seen previously, both ^{1}H and ^{13}C NMR have the same electronic-relaxation time which can be used as a fitting parameter to interpret observed-resonance widths. In this example, I shall use both PDM and MPDM to estimate the electronic-relaxation time, and using the calculated ^{13}C Fermi-coupling of $Fe(acac)_3$, provide estimates of signal widths for the ^{13}C MAS NMR spectrum.

Figure 8.8a shows the averaged experimental and calculated Fermi-coupling constants. Although the absolute error in the coupling is not significant, on the order of 0.1 MHz, the difference between the calculated and the experimental values indicates that the fit is not satisfactory. Widths of ^{1}H signals are estimated in Figure 8.8b where both models indicate the dominance of the dipolar mechanism. The PDM estimates the electronic relaxation to be on the order of a nanosecond, whereas MPDM gives a much smaller value of 80 ps. The most likely explanation for such a difference is the lack of accuracy in estimates of the spin-density distribution in the ligand orbitals. Experimental EPR suggests a long relaxation time for $Fe(acac)_3$ with an isotropic g-value of 2 [56], and thus the PDM seems more reliable in this scenario.

Figure 8.8c shows predictions of ^{13}C signal-widths for $Fe(acac)_3$ estimated from electronic-relaxation times from ^{1}H width-fitting. PDM clearly indicates that all ^{13}C resonances are expected to have widths exceeding 25 kHz, which would not be detectable under my

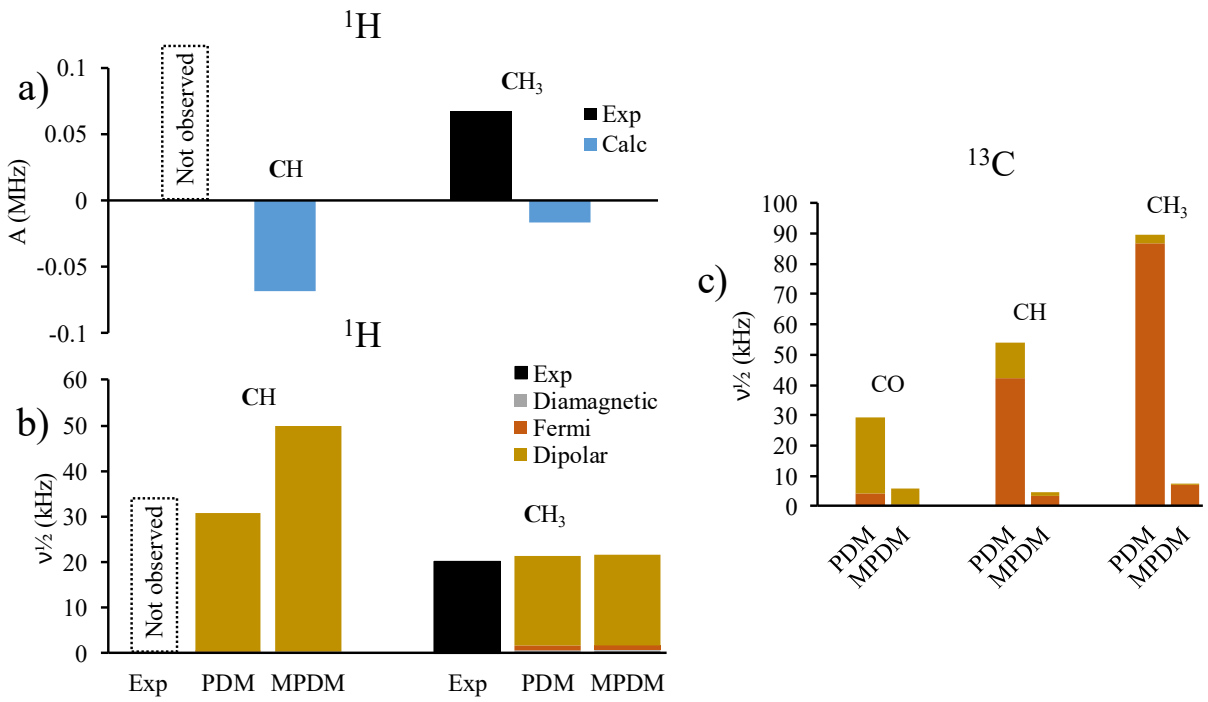

FIGURE 8.8: a) ^{1}H Fermi-coupling constants in Fe(acac)$_3$ and the comparison of the two models for the signal width in b) ^{1}H and c) ^{13}C MAS NMR of Fe(acac)$_3$. Detailed values are given in the Appendix Tables 8.9 – 8.11.

experimental conditions. Predictions from MPDM give values in the range 5 – 7 kHz, which should be detectable, but with low signal intensity. A good example of such a spectrum is ^{13}C MAS NMR of Cr(acac)$_3$ (Figure 4.18). Despite the large discrepancy in electronic relaxation-time, both fitting methods indicate that the ^{13}C resonances of Fe(acac)$_3$ are expected to be either broad or not detectable. Additional experimental data from EPR should provide a better indication of the expected magnitude of the electronic relaxation.

8.7 Modeling signal-widths in Co(acac)$_2$·2H$_2$O

The cobalt complex has a significant anisotropy in its g-tensor and an appreciable zero-field splitting, therefore, any reliable theoretical treatment of the observed shifts requires

consideration of these effects. The values of the Fermi-coupling constants that were derived experimentally using these formulations are given in Tables 8.12 and 8.14 (Appendix) where the range of the Fermi coupling includes the difference between the two methods of evaluation of the pseudocontact shift as discussed in Chapter 6. Luckily, for the evaluation of the signal widths in ^{13}C and ^{1}H NMR, the discrepancy between the two methods is small, Figure 8.9, where all the signal widths, apart from the methyl ^{13}C, are dominated by dipolar coupling. The variation in the methyl ^{13}C Fermi-coupling between the two methods of evaluation is on the order of 10%, Table 8.12, which is insufficient to cause major changes to the overall fit of the electron-relaxation parameter.

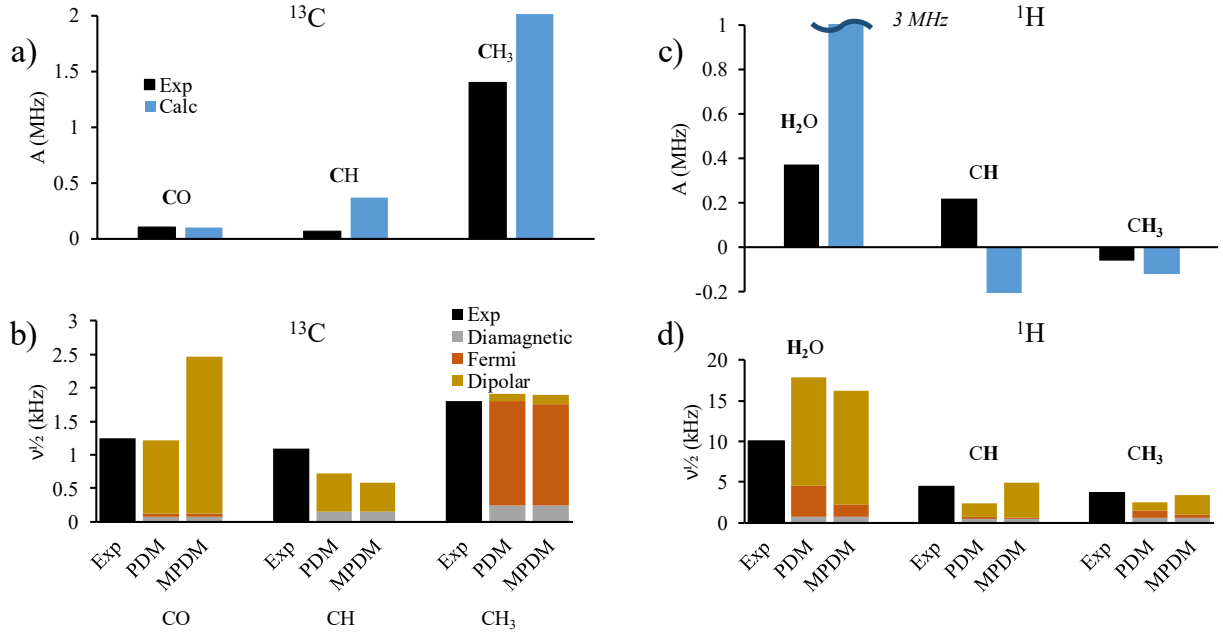

FIGURE 8.9: a) ^{13}C and c) ^{1}H Fermi-coupling constants in $Co(acac)_2 \cdot 2H_2O$ and comparison of the two models for the signal width in b) ^{13}C and d) ^{1}H MAS NMR of $Co(acac)_2 \cdot 2H_2O$. Detailed values are given in Appendix Tables 8.20 – 8.23.

Both models for fitting the widths of the NMR signals indicate that the electronic-relaxation time of the cobalt complex is short, on the order of 20-50 ps. Such a short relaxation-

time can be rationalized by the presence of multiple electronic microstates, as the d^7 system has a highly uneven occupancy of the electronic-energy levels, Figure 6.15. This accessibility of multiple electronic states promotes electron-spin relaxation [96]. The same was observed in $Ti(acac)_3$ and $V(acac)_3$ complexes, where short electron-relaxation times were estimated from ^{13}C and ^{1}H NMR (see above). Whereas in the $Cr(acac)_3$ and $Fe(acac)_3$ complexes, the complete occupancy of degenerate states by unpaired electrons, Figures 1.4 and 1.7, restraints electrons from accessing excited states at room temperature, as a result these complexes show broad ^{13}C and ^{1}H NMR resonances and long electron-relaxation times (see above).

8.8 Modeling NMR signal-width in $Ni(acac)_2{\cdot}2H_2O$

$Ni(acac)_2{\cdot}2H_2O$ has a short electronic-relaxation time at room temperature, which was measured to be on the order of 10 ps and attributed to relaxation due to zero-field splitting [134].

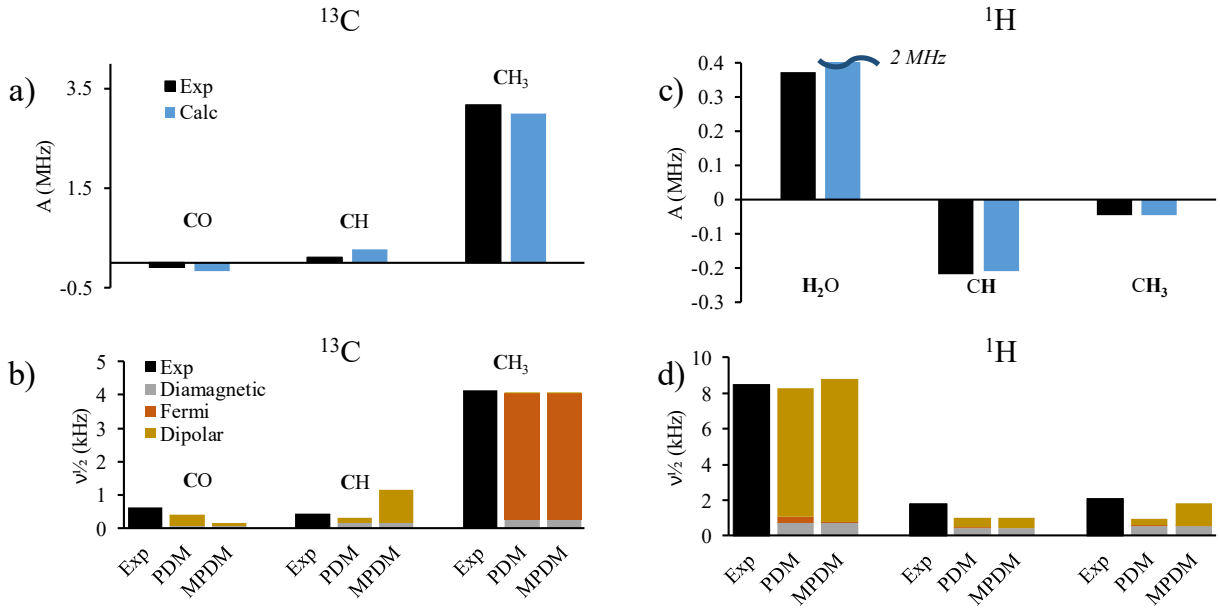

FIGURE 8.10: a) ^{13}C and c) ^{1}H Fermi-coupling constants in $Ni(acac)_2{\cdot}2H_2O$ and comparison of the two models for the signal width in b) ^{13}C and d) ^{1}H MAS NMR of $Ni(acac)_2{\cdot}2H_2O$. Detailed values are given in Table 6.2 Appendix Tables 8.16 and 8.17.

Figure 8.10 shows the fits for the ^{13}C and ^{1}H resonance widths that can be achieved with the two models for the dipolar contribution. In each case for both nuclei, the widths are fit to acceptable accuracy allowing the estimation of electronic relaxation time to be on the order of 10-45 ps, which is in agreement with the literature value [134].

8.9 Modeling NMR signal-width in $Cu(acac)_2$

Model fitting can provide insight into the paramagnetic relaxation of the $Cu(acac)_2$, which can provide an additional justification for the lack of an observable ^{13}C methyl signal in Figure 6.1. Figure 8.11 gives a summary of the ^{1}H and ^{13}C signal-widths and the Fermi-contact couplings. The performance of the MPDM in this case is poor as the signal widths are poorly

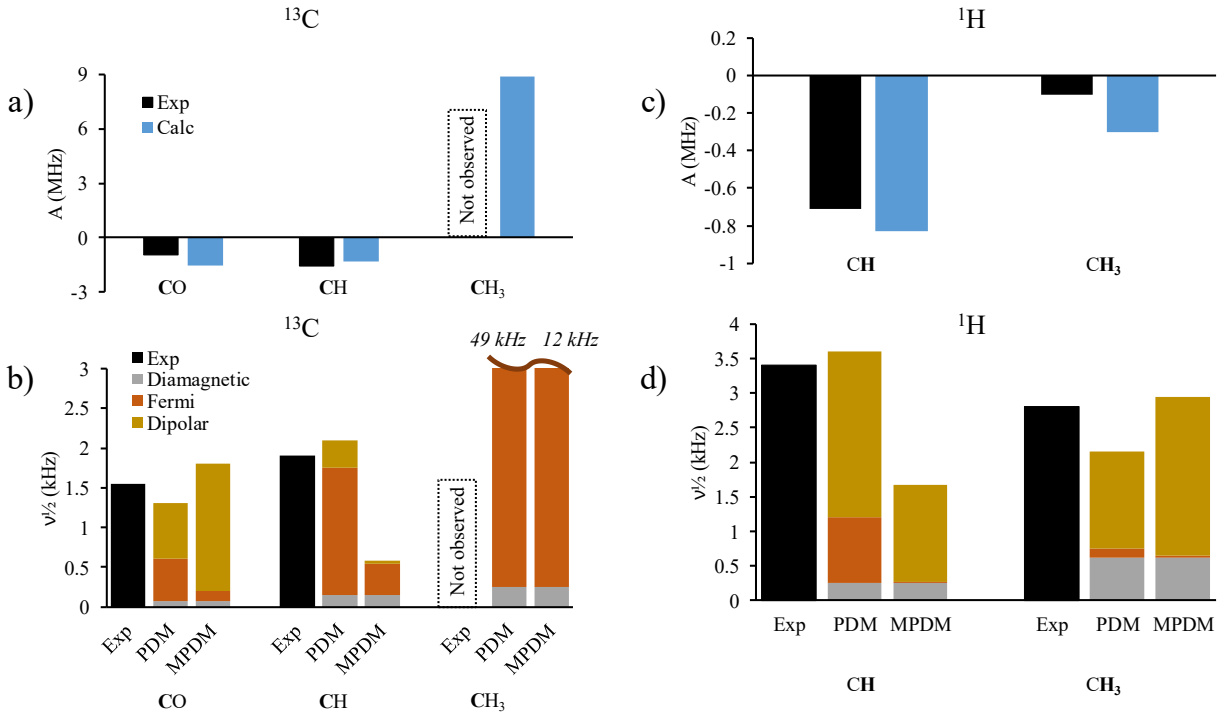

FIGURE 8.11: a) ^{13}C and c) ^{1}H Fermi-coupling constants in $Cu(acac)_2$ and a comparison of the two models for the signal width in b) ^{13}C and d) ^{1}H MAS NMR of $Cu(acac)_2$. Detailed values are given in Table 6.1 and Appendix Tables 8.18 and 8.19.

predicted in both ^{1}H and ^{13}C NMR. This model yields a low value of the electronic relaxation to be on the order of 10 ps (^{1}H NMR) and 50 ps (^{13}C NMR), whereas the PDM provides a much greater estimates of 600 ps (^{1}H NMR) and 200 ps (^{13}C NMR). The agreement between either of these values is poor, which suggests an inadequate description of the electron-nuclear dipole interaction. Nevertheless, according to Figure 8.11b, the width of the methyl-carbon signal is predicted to be at least 12 kHz according to the low electron relaxation value of the MPDM, whereas the PDM calculates it to be on the order of 49 kHz. These estimates support the lack of observed ^{13}C NMR signal from the methyl group due to significant broadening from the Fermi interaction.

8.10 Modeling NMR signal-width in $VO(acac)_2$

Broad resonances in ^{13}C and ^{1}H MAS NMR experiments for $VO(acac)_2$ suggest a long electronic-relaxation time. Figure 8.12 gives the ^{13}C and ^{1}H MAS NMR signal widths with the two fitting models to identify the scale of this electronic relaxation. The modeling produces a reliable fit to the measured Fermi-coupling, and the order of the widths is predicted correctly by both the MPDM and PDM methods. The observable ^{1}H spectrum is dominated by dipolar broadening, whereas a significant contribution from the Fermi shift makes the methine signal too broad to be detected. Observed widths in ^{13}C NMR are largely dominated by the Fermi coupling and consequently, the largest contribution is expected in the carbonyl group, making the resonance too broad for detection. The electronic relaxation is on the order of 900-3300 ps depending on the fitting model and NMR nucleus, which is the longest electronic-relaxation time among all complexes in this thesis. ENDOR experiments performed on this complex in frozen

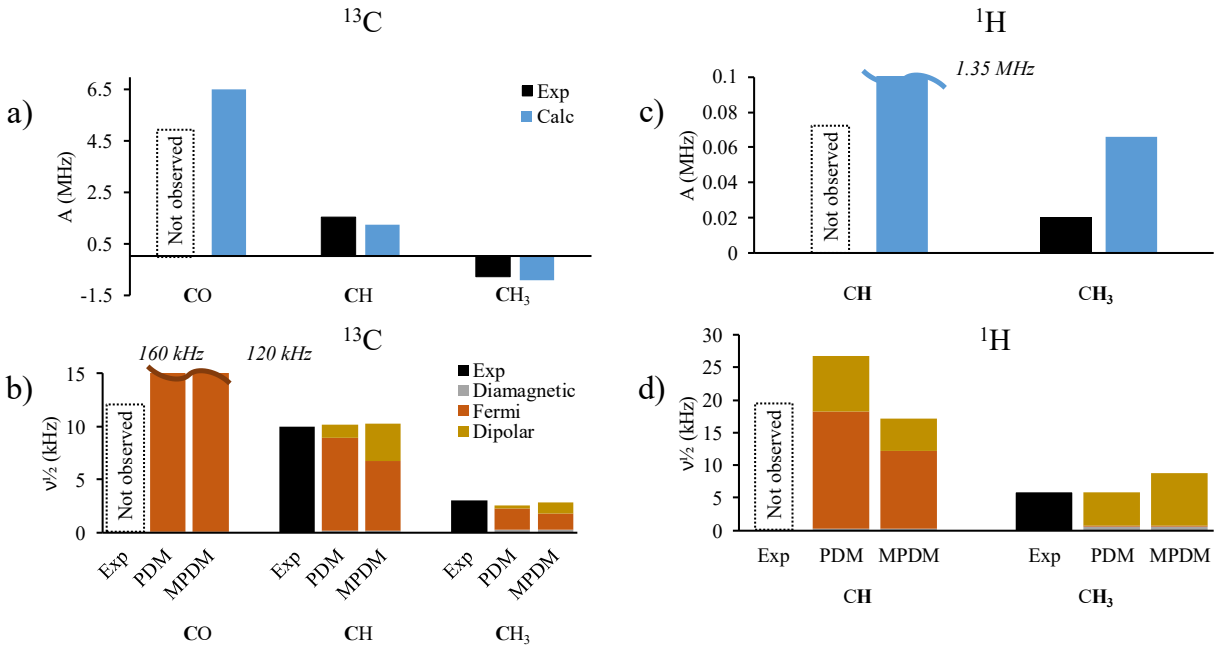

FIGURE 8.12: a) ^{13}C and c) ^{1}H Fermi coupling constants in $VO(acac)_2$ and the comparison of the two modeling schemes for the signal width in b) ^{13}C and d) ^{1}H MAS NMR of $VO(acac)_2$. Detailed values are presented in Table 7.1 and Appendix Tables 8.20 and 8.21.

solution at 30 K yield well-resolved hyperfine signals, suggesting relaxation times on the order of microseconds [146].

8.11 Modeling NMR signal-width in $[Cu(CH_3COO)_2]_2(H_2O)_2$

The coupled copper centers in $[Cu(CH_3COO)_2]_2(H_2O)_2$ have a reduced magnetic moment due to partial antiferromagnetic coupling at room temperature. This reduction in the effective-spin value affects the magnitude of both the Fermi and dipolar paramagnetic contributions to the nuclear resonance width. According to equations 2.29 and 2.33 both terms have the S(S+1) factor which is directly related to the effective magnetic moment of the complex. Figure 8.13 shows the fit of the nuclear relaxation with the two models for the dipolar contribution. Between the ^{13}C and ^{1}H NMR data, the MPDM does better at fitting the observed widths and provides a

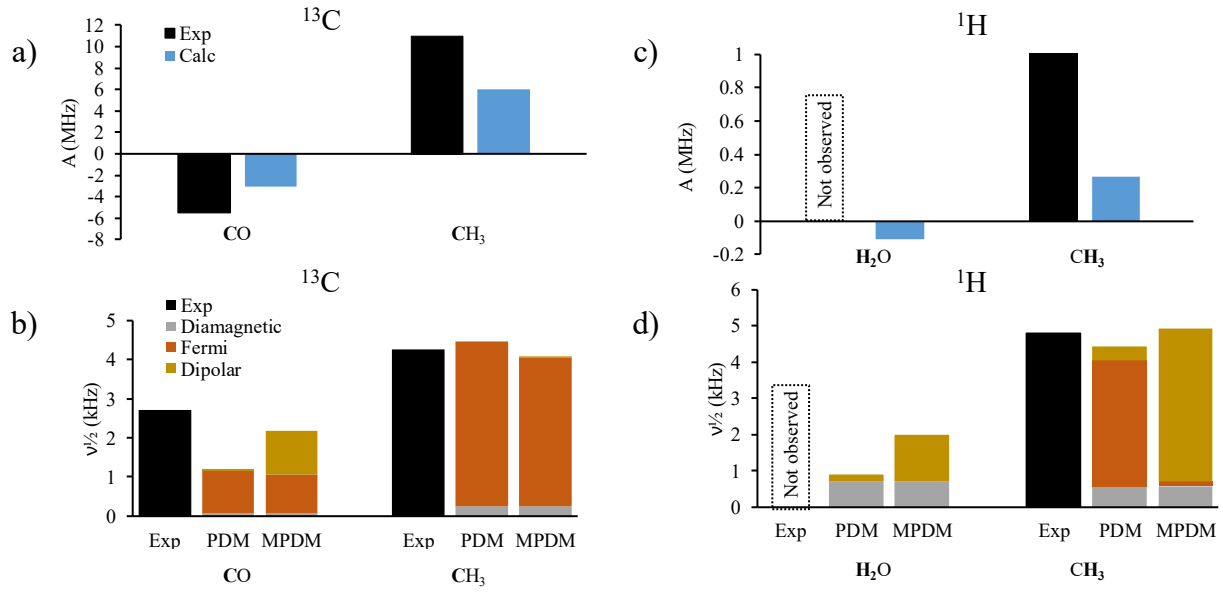

FIGURE 8.13: a) ^{13}C and c) ^{1}H Fermi-coupling constants in $[Cu(CH_3COO)_2]_2(H_2O)_2$ and comparison of the two model for the signal width in b) ^{13}C and d) ^{1}H MAS NMR of $[Cu(CH_3COO)_2]_2(H_2O)_2$. Detailed values are given in Table 7.3 and Appendix Tables 8.22 and 8.23.

small value for the electronic relaxation, on the order of 12-18 ps, whereas the PDM fit of the electronic relaxation varies between 20 ps for the ^{13}C fit and 250 ps for the ^{1}H fit. As the width of the ^{13}C resonances is consistently dominated by the Fermi contribution, as we have seen in the majority of the complexes, the relaxation time predicted from both models is expected to be more accurate for the ^{13}C experiment. Thus the most reliable value for the electronic relaxation in copper acetate hydrate is on the order of 12-20 ps.

8.12 Conclusion

The overall performance of the PDM is acceptable for approximating the magnitude of the electronic relaxation in solid paramagnetic M(acac)$_x$ complexes. The MPDM appears to be

heavily influenced by the quality of the computational prediction, i.e. the accuracy of the Fermi coupling prediction and the NPA, and needs further improvements before it is useful. A potential improvement could be to account for the distribution of the spin density around a given atom, thus moving away from the point charge approximation. Nevertheless, both models provide a general estimate of the relative magnitudes of the Fermi and dipolar contributions to the signal width. In addition, such estimates of electronic relaxation can be used as an initial guide to modeling NMR spectra of other nuclei in the analyzed molecule (e.g. ^{17}O), which may help identify potential benefits and limitations prior to the spectral acquisition.

Long electronic relaxation times are a serious limitation on the applicability of paramagnetic solid-state NMR, as they lower signal resolution and intensity. The current results suggest that without an experimental way of influencing the electronic environment, long electronic relaxation can be qualitatively predicted based on electronic environments and relevant EPR experiments. Such experiments would need to be performed under similar experimental conditions as NMR - such as high magnetic field, near-room temperature and in the solid state. Thus, a likely candidate would be high-field, room-temperature EPR measurements of a single crystal. A successful EPR experiment could then be used to estimate the magnitude of the electronic relaxation time, which could be applied in a preliminary NMR spectral simulation to assess its detectability.

Chapter 9: Spin-density arithmetics

Throughout this thesis, I have dealt with nearly every high-spin configuration of metal ions complexed to acetylacetonate ligands, and have provided a detailed explanation for the spin-density distribution with respect to the electronic configuration. I have used the spin-density contour-maps to show the dominant molecular-orbital-based mechanisms, that are responsible for the observed Fermi shifts in solid-state NMR spectra of paramagnetic coordination complexes. In order to illustrate the transferability of these principles to other paramagnetic systems, I propose a simplified model for understanding the Fermi spin-density in idealized metal-acetylacetonate complexes, i.e. in the absence of distortions between chemically equivalent functional groups. The proposal uses the general idea that the electronic occupancy at the transition metal may be understood as the sum of the contributions from the individual metal *d*-orbitals. This model is simplified as it does not provide an account of any degeneracy in t_{2g} electronic-energy states, nor does it account for the structural distortions present in different complexes.

9.1 Expressing spin-density of the d_{z2} orbital

Mechanisms of spin-distribution pathways were developed that involve in-plane t_{2g} orbitals (Ti, V, Cr), a combination of both e_g orbitals (Ni) and an individual d_{x2-y2} orbital (Cu). In this last section, an evaluation of the contributions from the d_{z2} orbital to Fermi coupling of the acetylacetonate ligand will be presented in order to complete the series. As was shown in Chapter 4, the occupancy of the unpaired spins in the in-plane t_{2g} orbital has a direct effect on the Fermi coupling at ^{13}C in the backbone of the ligand. Therefore, not only the metal-orbital

symmetry is responsible for the observed Fermi coupling, but also its degree of occupancy for sharing the unpaired spin-density with the ligand.

The unpaired electron-spin density at the nucleus can be considered a somewhat over-simplified definition for a description of the Fermi spin density. The orbital density changes as a function of the distance from the metal [147] and the size of the nucleus can play a part in affecting the Fermi spin-density. Equation 2.21 assumes that the nucleus can be treated as a point charge, thus the spin density is assumed to be constant throughout the core. The relativistic contraction of electron orbitals in high -Z atoms can cause admixture of L > 0 orbitals into the Fermi-coupling relation, essentially breaking the point-charge approximation [148]. To avoid this problem, the spin density at the nucleus will be expressed through the isotropic hyperfine coupling and the total electron spin. The term $A_{iso}S/g_{iso}$ retains the information about the unpaired spin-density for a given nucleus while keeping it independent of the total spin-state of the system; thus the term can be compared directly for different complexes.

With this normalization, the isolated contribution of the d_{z2} orbital to the xy-ligand can be expressed as the difference between the $Ni(acac)_2{\cdot}2H_2O$ and $Cu(acac)_2$ spin-densities. The nickel complex contains the aggregate effect of both orbitals on the Fermi coupling, therefore by subtracting the contribution from the d_{x2-y2} orbital, the remaining coupling is expected to originate from d_{z2}. This contribution can be expressed through experimentally derived Fermi-couplings and the g_{iso}, with the results given in Table 9.1. By analogy, the d_{z2} orbital contribution can be expressed as the difference between the Mn^{3+} and Cr^{3+} complexes. Mn^{3+} is known to have d_{xy}, d_{yz}. d_{xz} and d_{z2} orbitals occupied in the γ-phase, whereas Cr^{3+} has full occupancy of only the d_{xy}, d_{yz}, and d_{xz} orbitals. The difference between these complexes is also expected to give the

Spin-density arithmetics

Table 9.1: Estimation of d_{z2} orbital contribution to the Fermi-contact spin-density using the principles of spin arithmetics. When no experimental value is available, italicized calculated values are provided.

Group	$A_{exp} \cdot S / g_{iso}$ or ($A_{calc} \cdot S / g_{iso}$)					
	$t_{2g}(Cr^{3+})$	$t_{2g} + d_{z2}$ (Mn^{3+})	d_{z2} (Mn^{3+} - Cr^{3+})	$e_g(Ni^{2+})$	d_{x2-y2} (Cu^{2+})	d_{z2} (Ni^{2+} - Cu^{2+})
CH_3	-0.69	-0.62	0.07	1.6	*2.1*	*-0.5*
CH	0.31	0.86	0.55	0.055	-0.37	0.43
CO	*1.7*	1.36	*-0.3*	-0.045	-0.22	0.18

contribution of the d_{z2} orbital. However, their cases differ by the net metal charge, which is known to affect the energy levels of *d*-orbitals, and thus will have an effect on the magnitude of the *d*-orbital interaction with the ligand [15]. Table 9.1 gives the results of both evaluations of the d_{z2} orbital contribution. Unfortunately, not all signal coupling was observed experimentally, thus only the spin density at the methine carbon can be compared reliably. The methine indicates a small variation in the magnitude of the Fermi density, but the variation can be considered insignificant in light of the assumptions that were used here. This variation is of a similar magnitude to a good-fit hybrid DFT calculation. Values for the methyl and carbonyl groups had to be inferred in part from calculated Fermi-coupling constants as the carbonyl ^{13}C signal was not observed in $Cr(acac)_3$ and the methyl ^{13}C signal was not observed in $Cu(acac)_2$. Nevertheless, according to Table 9.1, both estimates of the d_{z2} orbital contribution agree that the methine Fermi-shift is expected to be larger than the Fermi shifts of both the carbonyl and the methyl groups, which has not yet been seen experimentally as none of our complexes has an isolated singly-occupied d_{z2} orbital.

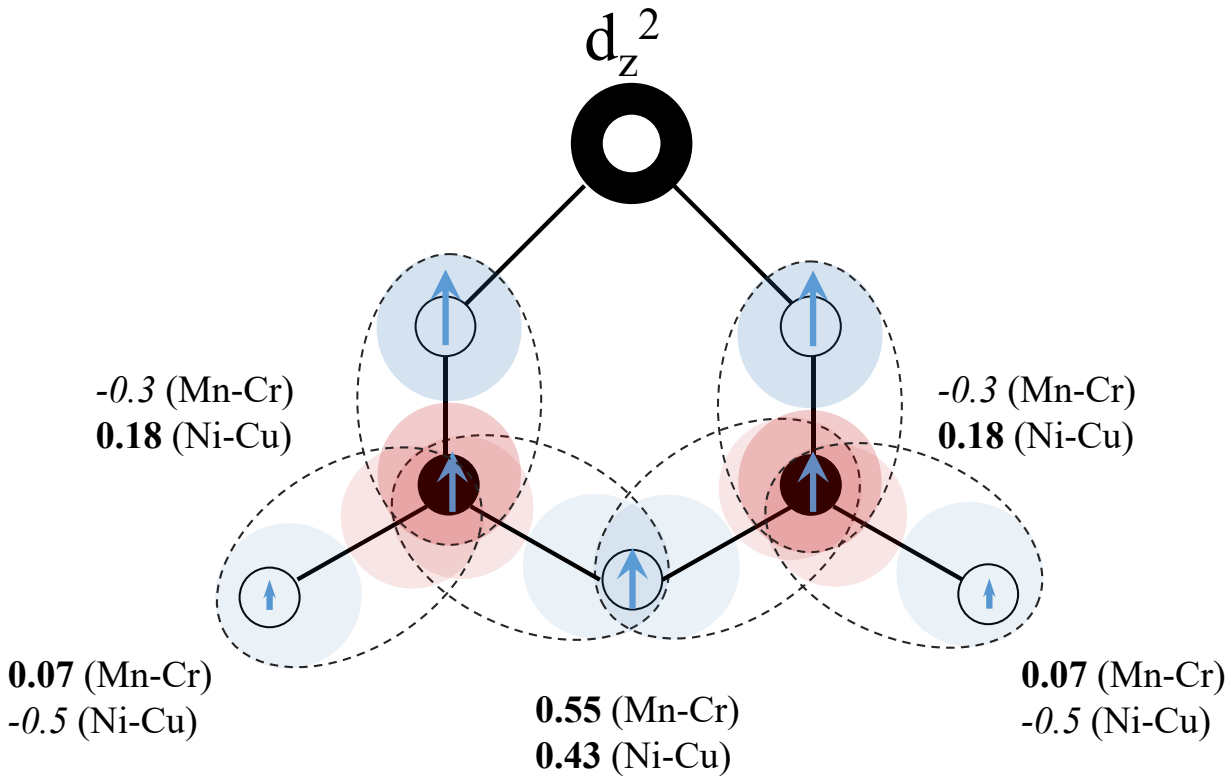

FIGURE 9.1: Pictorial representation of the d_{z2} orbital interacting with the ligand in the xy-plane. Values of $A_{iso} \cdot S/g_{iso}$ are from Table 9.1, where the values in bold are experimental and italicized values are calculated.

According to Table 9.1, a spin-density map can be made based on our understanding of molecular-orbital interactions and mechanisms of spin distribution. Figure 9.1 shows the delocalization pathway described previously in Chapter 5, Figure 5.14. In addition, the effect of polarization is introduced to rationalize the estimated Fermi-spin densities from the d_{z2} orbital. Delocalization between the d_{z2} and the oxygen leads to an abundance of positive spin-density at the latter. This is a similar effect to that observed in Figure 6.15 for $Cu(acac)_2$, where the oxygen interacts with the d_{x2-y2}, as both orbitals have the same σ* interaction symmetry. A significant difference between these interactions is the ligand-orbital phase between the two oxygens chelating to the same metal orbital. In the case of d_{x2-y2}, these phases are opposite, which eventually lead to destructive interference at the methine position. On the other hand, in d_{z2}, both

phases are the same, which leads to an increase in delocalization contribution at the methine. This is the significant difference between the two orbitals that can be used as a diagnostic tool to distinguish between occupied orbitals, as this relation is a direct probe of orbital symmetry.

9.2 Signal width and spin density in paramagnetic NMR

Upon establishing a firm understanding of the mechanisms of spin-density distribution in a paramagnetic system, the principle of perturbative analysis can be applied to expand the assignment capabilities to other paramagnetic systems with analogous molecular-orbital interactions. Chapters 4 through 8 provide the background for such an analysis, with the key examples provided in the previous section. Where a comparison is made between paramagnetic systems with equivalent molecular-orbital interactions but a differing total number of unpaired electrons, i.e. $A_1 \cdot S_1/g_{iso1} = A_2 \cdot S_2/g_{iso2}$, it is important to note that the magnitude of the Fermi-coupling constant, A_{iso}, is expected to scale inversely with the total spin-number, S, for the same $\rho_{\alpha\beta}$ value. Thus, systems with low number of unpaired electrons have a Fermi coupling constant of a larger magnitude. This has a significant consequence on the detectability and resolution of NMR spectra. As shown in Figure 9.2, the overall contribution of the Fermi coupling to the nuclear relaxation (equation 2.29) and thus the signal width, increases as a function of the magnetic moment. However, if the spin-density mechanism is able to produce the same number of unpaired electron spins tunneling the nucleus, i.e. $S_1 \cdot A_1 = S_2 \cdot A_2$ (assuming $g_{iso1}=g_{iso2} = g_e$), this same signal will appear narrower and shifted farther at high values of S. This condition is shown in Figure 9.2 with the solid line passing through SA = 4, which is arbitrarily selected to illustrate a hypothetically fixed condition of the influence of a spin distribution mechanism on the Fermi spin-density. At S = 0.5, the line crosses the 10 – 30 kHz region at electron-relaxation

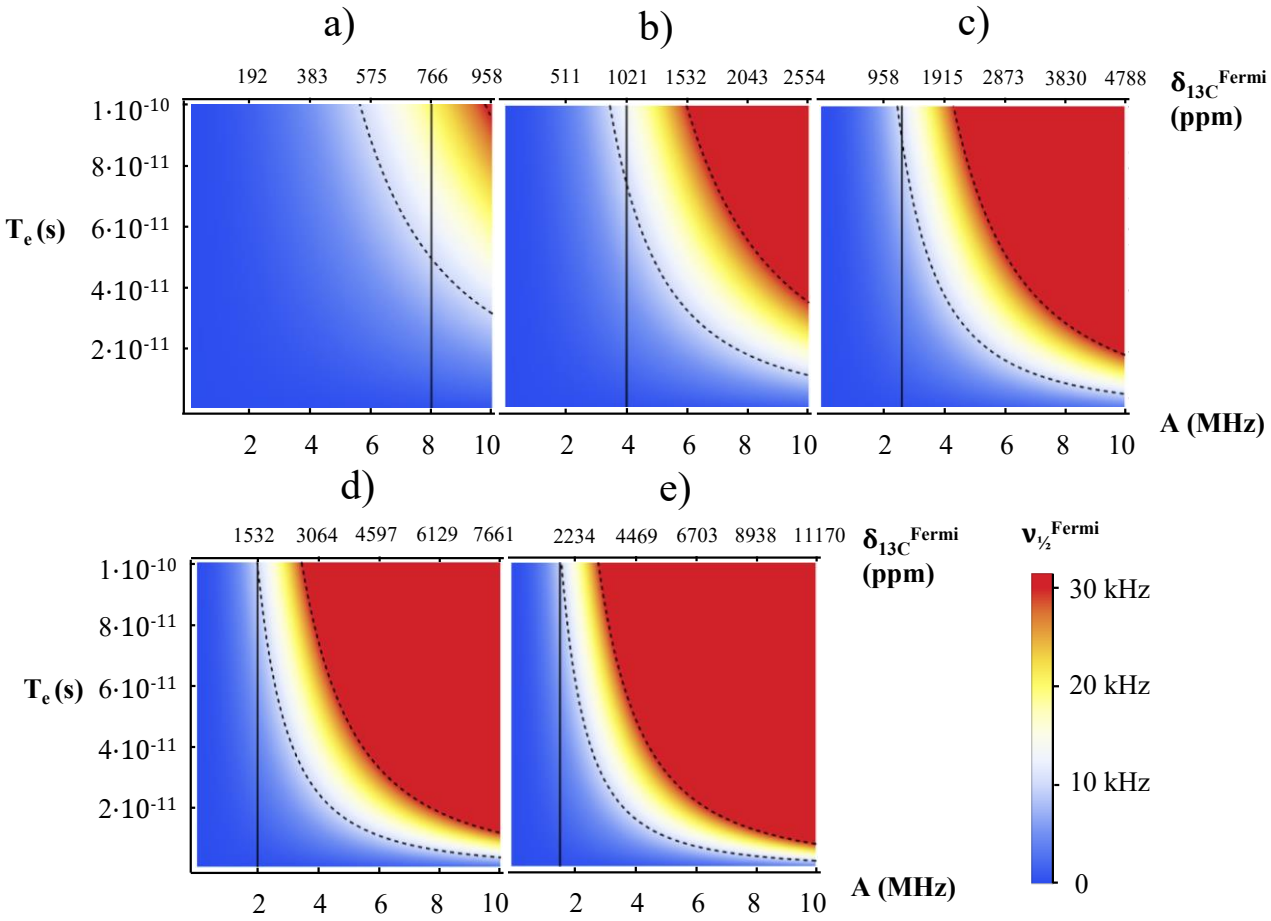

FIGURE 9.2: Fermi contribution to the isotropic signal width in a) S = 0.5; b) S = 1; c) S = 1.5; d) S = 2; e) S = 2.5 spin states in relation to the Fermi-coupling constant (A) and the electronic-relaxation time (T_e). Dashed contours indicate regions with 10 kHz and 30 kHz marks. Solid lines pass through SA = 4, which signifies equivalent $\rho_{\alpha\beta}$.

times above 50 ps, which would signify a potentially undetectable resonance at or above the specified electron-relaxation. The same crossing at S = 2.5 is past 100 ps, implying greater tolerance for longer electron relaxation. Thus, the presence of multiple unpaired electrons can significantly improve the capabilities of paramagnetic solid-state NMR to resolve and detect resonances a few bonds away from the source of the unpaired electrons.

Spin-density arithmetics

Figure 9.2 ignores the electron-nuclear dipolar contribution to the isotropic width, which should also scale as the total magnetic moment of the sample. The paramagnetic dipolar contribution can be significantly lowered with the observation of low-γ nuclei if there are such isotopes available for the atom.

I have now established general guidelines for the successful acquisition and interpretation of solid-state NMR spectra of paramagnetic coordination compounds under standard laboratory conditions. The ideal system must have known magnetic behavior ($\bar{\boldsymbol{g}}$, $\bar{\boldsymbol{D}}$, J, etc.) at experimental NMR temperatures, as this aspect is crucial for accurate interpretation of coupling magnitudes. The system should have a large number of unpaired spins as that ensures greater sensitivity to the hyperfine coupling, but there should be thermally accessible microstates that will reduce the electron-spin relaxation-time, a counterexample is $Fe(acac)_3$ in Chapter 8. A greater number of unpaired electrons in the system also leads to an overall lower magnitude of Fermi-coupling constant, as can be seen with the line of equivalent $\rho_{\alpha\beta}$ in Figure 9.2, provided the spin-distribution mechanism that creates the coupling does not vary significantly with the number of unpaired spins. This is beneficial as a smaller magnitude of the coupling reduces the Fermi contribution to nuclear relaxation, making NMR peaks narrower, Figure 9.2. The system should not have a significant contribution to signal width from the dipole mechanism, implying a larger distance from the paramagnetic center or/and the application of low-γ isotope for NMR. As shown in Chapter 8, NMR relaxation of a lower-γ nucleus, such as ^{13}C, is rarely dominated by dipolar broadening, even for carbonyl groups as close as 3 Å from the metal. Therefore, a beneficial system must have a MO mechanism by which a substantial amount of unpaired spin-density can be distributed throughout the ligand from the paramagnetic center. An additional benefit of such a system can be the presence of phonon-coupled modes of electronic relaxation,

which would improve the rate of relaxation and increase NMR resolution [96]. Another factor that influences electronic relaxation is a dipolar interaction between paramagnetic centers, as close paramagnetic centers can enhance electronic relaxation. The presence of low-lying accessible electronic-energy states creates possible microstates that reduce electronic relaxation, as seen for the $Ti(acac)_3$, $V(acac)_3$, $Mn(acac)_3$ and $Co(acac)_2 \cdot 2H_2O$ complexes. In contrast, systems with no accessible excited energy states, like $Cr(acac)_3$, $VO(acac)_2$ and $Fe(acac)_3$, show long electronic relaxation times.

Chapter 10: Conclusions and Outlook

10.1 Impact on solid-state NMR of paramagnetic materials

In this thesis I have provided a systematic study of Fermi coupling interaction on observed solid-state ^{13}C and ^{1}H NMR spectra with a series of related metal acetylacetonate coordination complexes. Effects of this coupling at short distances to the metal center have been established and linked to specific electronic configurations and individual orbital occupancies. Two major mechanisms that affect the distribution of spin density, polarization and delocalization, have been established and used to rationalize observed Fermi couplings. The interplay between these mechanisms has been illustrated in a series of near-isostructural tris(acac) complexes with t_{2g}^{1-3} configuration.

The effects of mixed orbital symmetries on NMR has been illustrated with the example of $Mn(acac)_3$ complex. It was also shown that ^{1}H NMR can serve as a sensitive probe for distinguishing a presence of mixed crystal phases.

The effect of local structural distortions on spin density and observed NMR spectra has been investigated with $VO(acac)_2$ structure, where the relation between the structure and mechanisms of spin distribution were identified. A bi-nuclear coupled system of copper acetate hydrate was investigated to provide an extension of the outlined principles of spin-density distribution to chemically-relevant systems. The effect of the anti-ferromagnetic coupling on the ^{13}C NMR spectrum was addressed in detail, providing guidelines for applications to more complex systems.

The effects of electronic spin relaxation on NMR signal widths have been systematically analyzed for all the complexes in the thesis, and general guidelines proposed to provide estimates on signal detectability, a common problem in paramagnetic NMR. An extension to the existing point-dipole model has been proposed in an attempt to generalize the through-space electron-nuclear coupling in the solid state. These results suggest a link between NMR peak widths of different nuclei in the same paramagnetic complex, and point towards the possibility of assessing NMR detectability of other nuclei in the system on the basis of a reliable NMR spectrum and/or relevant EPR measurements.

As a result of the systematic evaluation of metal-orbital contributions to the observed Fermi spin densities, a theory of spin-density arithmetics was proposed. Contributions from individual metal orbitals are considered to be independent, and can be co-added to predict Fermi spin densities from a specific electronic configuration. As the consequence of this spin-arithmetics approach on Fermi-spin-density contribution to the signal width, systems with a larger number of unpaired electrons and a fixed spin-density distribution pathway show the potential for narrower linewidths in solid-state NMR

10.2 Future studies

Efforts to decouple electron-nuclear dipolar coupling by the application of a decoupling pulse on the electron during acquisition with Dynamic Nuclear Polarization (DNP) MAS-NMR [149] are in the very early stages and have not yet produced promising results. An alternative approach is to attempt to control the electronic-relaxation time through physical influence on the mechanisms of its relaxation. For example, a possibility of the electron-phonon coupling implies that a rise in temperature, or far-IR – IR radiation, can enhance relaxation rate [96]. Another

possibility is a rapid (picosecond-length) excitation of the electron to a high-energy short-lived excited state for the duration of the NMR pulse sequence. The rapid exchange in electronic environment should lead to an adjustable electron correlation term in equations 2.26 and 2.30, thus allowing modulation of the paramagnetic broadening in solid-state NMR.

The contribution of the pseudocontact shift has been estimated in complexes that show a distinct anisotropy in the magnetic moment. An analytical assessment of this contribution is beyond the scope of this thesis, but remains under investigation.

Further development in this field includes extension to metal-organic frameworks, where the principles of analysis outlined in this thesis can be used to provide detailed electronic and structural characterization. The thesis has touched upon the method application to antiferromagnetically coupled spin systems, such as copper acetate hydrate, which are commonly used as linkers in MOFs and thus is able to provide analogous information on the local environment around these linkers in the solid state. These principles could be used to study electron paramagnetic-antiferromagnetic coupling behavior in solids. Systems that have a similar bonding configuration, such as derivatives of the "acac" ligand and moieties with a similar bonding symmetry (e.g. $Cu(acac)_2$ and copper acetate), can be studied successfully with this method as their electronic distribution and structural assignment have been well-established in this work. Application of double resonance experiments, such as 2D-CP and REDOR, can provide correlated spectra for signal assignment. Paramagnetic solid-state NMR can be used as a sensitive probe of electronic occupancy and aid in the evaluation of molecular-orbital interactions in solids. NMR sensitivity to electronic environment can resolve structural defects in solid systems, such as MOFs, perovskites, organometallic complexes, etc. This sensitivity to the electronic environment should allow the solid-state NMR to be used as a probe of metal-

oxidation states, as they have a direct dependence on the bonding configuration and the number of unpaired electrons in the system. As a general principle, this work provides a comprehensive guideline for a detailed structural interpretation of paramagnetic molecules with solid-state MAS NMR.

Bibliography

[1] K. MacKenzie, M. Smith, Multinuclear Solid State NMR of Inorganic Materials, Pergamon Press, Oxford, 2002.

[2] E.D. Becker, A brief history of nuclear magnetic resonance, Analytical Chemistry 65 (1993) 295A-302A.

[3] A.W. Overhauser, Paramagnetic relaxation in metals, Physical Review 89 (1953) 689.

[4] A.S.L. Thankamony, J.J. Wittmann, M. Kaushik, B. Corzilius, Dynamic nuclear polarization for sensitivity enhancement in modern solid-state NMR, Progress in Nuclear Magnetic Resonance Spectroscopy 102 (2017) 120-195.

[5] G.N. LaMar, W.D. Horrocks, R.H. Holm, NMR of paramagnetic molecules: principles and applications, Academic press, New York and London, 1973.

[6] N. Bloembergen, E.M. Purcell, R.V. Pound, Relaxation effects in nuclear magnetic resonance absorption, Physical Review 73 (1948) 679-712.

[7] W.D. Knight, Nuclear magnetic resonance shift in metals, Physical Review 76 (1949) 1259.

[8] I. Solomon, Relaxation processes in a system of two spins, Physical Review 99 (1955) 559.

[9] Web of Science, 2017 December 19th.

[10] B. Kozyrev, Paramagnetic resonance in solutions of electrolytes, Discussions of the Faraday Society 19 (1955) 135-140.

[11] H.M. McConnell, Indirect hyperfine interactions in the paramagnetic resonance spectra of aromatic free radicals, The Journal of Chemical Physics 24 (1956) 764-766.

[12] N. Bloembergen, L. Morgan, Proton relaxation times in paramagnetic solutions. Effects of electron spin relaxation, The Journal of Chemical Physics 34 (1961) 842-850.

[13] R. Golding, The theory of the temperature dependence of NMR spectra of paramagnetic octahedral complexes, Molecular Physics 8 (1964) 561-566.

[14] F. Loder, A.P. Kampf, T. Kopp, Superconductivity with Rashba spin–orbit coupling and magnetic field, Journal of Physics: Condensed Matter 25 (2013) 362201.

[15] J.S. Griffith, The theory of transition-metal ions, Cambridge University Press, 1964.

[16] D. Eaton, The nuclear magnetic resonance of some paramagnetic transition metal acetylacetonates, Journal of the American Chemical Society 87 (1965) 3097-3102.

[17] F. Rastrelli, A. Bagno, Predicting the NMR Spectra of Paramagnetic Molecules by DFT: Application to Organic Free Radicals and Transition-Metal Complexes, Chemistry-A European Journal 15 (2009) 7990-8004.

[18] R. Golding, L. Stubbs, NMR shifts in paramagnetic systems: A nonmultipole expansion method, Journal of Magnetic Resonance 33 (1979) 627-647.

[19] E.R. Andrew, A. Bradbury, R. Eades, Nuclear magnetic resonance spectra from a crystal rotated at high speed, Nature 182 (1958) 1659.

[20] I. Lowe, Free induction decays of rotating solids, Physical Review Letters 2 (1959) 285.

[21] A. Nayeem, J.P. Yesinowski, Calculation of magic-angle spinning nuclear magnetic resonance spectra of paramagnetic solids, The Journal of Chemical Physics 89 (1988) 4600-4608.

[22] J. Kowalewski, L. Nordenskiöld, N. Benetis, P.-O. Westlund, Theory of nuclear spin relaxation in paramagnetic systems in solution, Progress in nuclear magnetic resonance spectroscopy 17 (1985) 141-185.

[23] G.M. Clore, J. Iwahara, Theory, practice, and applications of paramagnetic relaxation enhancement for the characterization of transient low-population states of biological macromolecules and their complexes, Chemical Reviews 109 (2009) 4108-4139.

[24] V.I. Bakhmutov, Strategies for solid-state NMR studies of materials: from diamagnetic to paramagnetic porous solids, Chemical Reviews 111 (2010) 530-562.

[25] G. Pintacuda, G. Kervern, Paramagnetic solid-state magic-angle spinning NMR spectroscopy, Modern NMR Methodology, Springer, 2012, pp. 157-200.

[26] R.H. Contreras, High Resolution NMR Spectroscopy: Understanding Molecules and their Electronic Structures, Newnes, 2013.

[27] A. Bhaumik, C. Luchinat, G. Parigi, E. Ravera, M. Rinaldelli, NMR crystallography on paramagnetic systems: solved and open issues, CrystEngComm 15 (2013) 8639-8656.

[28] S.S. Yun, I.-H. Suh, S.-S. Choi, T.-H. Kim, S. Lee, Alternative Formation and Crystal Structure of Tris(Acetylacetonato)Titanium(III) from Titanocene and 2, 4-Pentanedione, Journal of Coordination Chemistry 47 (1999) 315-318.

[29] E. Arslan, R.A. Lalancette, I. Bernal, An historic and scientific study of the properties of metal (III) tris-acetylacetonates, Structural Chemistry 28 (2017) 201-212.

[30] K. Liu, J. Williams, H. Lee, M.M. Fitzgerald, G.M. Jensen, D.B. Goodin, A.E. McDermott, Solid-state deuterium NMR of imidazole ligands in cytochrome c peroxidase, Journal of the American Chemical Society 120 (1998) 10199-10202.

[31] Y. Ishii, N.P. Wickramasinghe, S. Chimon, A new approach in 1D and 2D ^{13}C high-resolution solid-state NMR spectroscopy of paramagnetic organometallic complexes by very fast magic-angle spinning, Journal of the American Chemical Society 125 (2003) 3438-3439.

[32] N.P. Wickramasinghe, Y. Ishii, Sensitivity enhancement, assignment, and distance measurement in ^{13}C solid-state NMR spectroscopy for paramagnetic systems under fast magic angle spinning, Journal of Magnetic Resonance 181 (2006) 233-243.

[33] N.P. Wickramasinghe, M.A. Shaibat, C.R. Jones, L.B. Casabianca, A.C. de Dios, J.S. Harwood, Y. Ishii, Progress in ^{13}C and ^{1}H solid-state nuclear magnetic resonance for paramagnetic systems under very fast magic angle spinning, Journal of Chemical Physics 128 (2008) 052210.

[34] G. Kervern, G. Pintacuda, L. Emsley, Fast adiabatic pulses for solid-state NMR of paramagnetic systems, Chemical Physics Letters 435 (2007) 157-162.

[35] D. Carlier, M. Ménétrier, C. Grey, C. Delmas, G. Ceder, Understanding the NMR shifts in paramagnetic transition metal oxides using density functional theory calculations, Physical Review B 67 (2003) 174103.

[36] J. Mao, Y. Zhang, E. Oldfield, Nuclear magnetic resonance shifts in paramagnetic metalloporphyrins and metalloproteins, Journal of the American Chemical Society 124 (2002) 13911-13920.

[37] V.K. Michaelis, B.J. Greer, T. Aharen, J.E. Greedan, S. Kroeker, Determining Electron Spin-Transfer Mechanisms in Paramagnetic Ba_2YMO_6(M = Mo, Re, Ru) Double Perovskites by ^{89}Y and ^{137}Ba MAS NMR Spectroscopy, The Journal of Physical Chemistry C 116 (2012) 23646-23652.

[38] E. Kermarrec, C.A. Marjerrison, C. Thompson, D.D. Maharaj, K. Levin, S. Kroeker, G.E. Granroth, R. Flacau, Z. Yamani, J.E. Greedan, Frustrated fcc antiferromagnet Ba_2YOsO_6: structural characterization, magnetic properties, and neutron scattering studies, Physical Review B 91 (2015) 075133.

[39] A.R. Brough, C.P. Grey, C.M. Dobson, Paramagnetic ions as structural probes in solid-state NMR: distance measurements in crystalline lanthanide acetates, Journal of the American Chemical Society 115 (1993) 7318-7327.

[40] F. Wehril, A.P. Marchand, S. Wehrli, Interpretation of carbon-13 NMR spectra, (1988).

[41] C. Luchinat, G. Parigi, E. Ravera, M. Rinaldelli, Solid-state NMR crystallography through paramagnetic restraints, Journal of the American Chemical Society 134 (2012) 5006-5009.

[42] B. Ramanan, W. Holmes, W. Sloan, V. Phoenix, Application of paramagnetically tagged molecules for magnetic resonance imaging of biofilm mass transport processes, Applied and Environmental Microbiology 76 (2010) 4027-4036.

[43] S. Ganapathy, P. Rajamohanan, P. Ganguly, T. Venkatraman, A. Kumar, Two-Dimensional Solid State NMR and Separation of ^{7}Li Quadrupolar Interactions in Paramagnetic Compounds, The Journal of Physical Chemistry A 104 (2000) 2007-2012.

[44] J. Kim, D.S. Middlemiss, N.A. Chernova, B.Y. Zhu, C. Masquelier, C.P. Grey, Linking local environments and hyperfine shifts: A combined experimental and theoretical ^{31}P and ^{7}Li solid-state NMR study of paramagnetic Fe (III) phosphates, Journal of the American Chemical Society 132 (2010) 16825-16840.

[45] J. Lee, I.D. Seymour, A.J. Pell, S.E. Dutton, C.P. Grey, A systematic study of ^{25}Mg NMR in paramagnetic transition metal oxides: applications to Mg-ion battery materials, Physical Chemistry Chemical Physics 19 (2017) 613-625.

[46] M. Mortuza, R. Dupree, D. Holland, Studies of the effect of paramagnetic impurity in the structure of sodium disilicate glass, Journal of Materials Science 35 (2000) 2829-2832.

[47] P.M. Aguiar, M.J. Katz, D.B. Leznoff, S. Kroeker, Natural abundance ^{13}C and ^{15}N solid-state NMR analysis of paramagnetic transition-metal cyanide coordination polymers, Physical Chemistry Chemical Physics 11 (2009) 6925-6934.

[48] W. Wang, X. Xu, W. Zhou, Z. Shao, Recent Progress in Metal-Organic Frameworks for Applications in Electrocatalytic and Photocatalytic Water Splitting, Advanced Science (2017) 1600371.

[49] J.J. Perry, S.L. Teich-McGoldrick, S.T. Meek, J.A. Greathouse, M. Haranczyk, M.D. Allendorf, Noble gas adsorption in metal–organic frameworks containing open metal sites, The Journal of Physical Chemistry C 118 (2014) 11685-11698.

[50] D.M. Dawson, L.E. Jamieson, M.I.H. Mohideen, A.C. McKinlay, I.A. Smellie, R. Cadou, N.S. Keddie, R.E. Morris, S.E. Ashbrook, High-resolution solid-state ^{13}C NMR spectroscopy of the paramagnetic metal–organic frameworks, STAM-1 and HKUST-1, Physical Chemistry Chemical Physics 15 (2013) 919-929.

[51] H. Lamprey, Properties and applications of metal acetylacetonates, Annals of the New York Academy of Sciences 88 (1960) 519-525.

[52] M. Seco, Acetylacetone: a versatile ligand, Journal of Chemical Education 66 (1989) 779.

[53] W.S. Seo, H.H. Jo, K. Lee, B. Kim, S.J. Oh, J.T. Park, Size-dependent magnetic properties of colloidal Mn_3O_4 and MnO nanoparticles, Angewandte Chemie International Edition 43 (2004) 1115-1117.

[54] A.L. Willis, Z. Chen, J. He, Y. Zhu, N.J. Turro, S. O'Brien, Metal acetylacetonates as general precursors for the synthesis of early transition metal oxide nanomaterials, Journal of Nanomaterials 2007 (2007) 1-7.

[55] K.J. de Almeida, A. Cesar, Z. Rinkevicius, O. Vahtras, H. Ågren, Modelling the visible absorption spectra of copper (II) acetylacetonate by Density Functional Theory, Chemical Physics Letters 492 (2010) 14-18.

[56] S. Hedewy, S. Hoffmann, Electron paramagnetic resonance of ferric acetyl acetonate, Physica Status Solidi (a) 97 (1986) 129-133.

[57] B. Pritchard, J. Autschbach, Theoretical Investigation of Paramagnetic NMR Shifts in Transition Metal Acetylacetonato Complexes: Analysis of Signs, Magnitudes, and the Role of the Covalency of Ligand–Metal Bonding, Inorganic Chemistry 51 (2012) 8340-8351.

[58] T. Bayburt, R.R. Sharp, Electron-and nuclear-spin relaxation in an integer spin system, tris-(acetylacetonato) Mn (III) in solution, The Journal of Chemical Physics 92 (1990) 5892-5899.

[59] G.-S. Lo, C. Brubaker, A new method for preparation and some properties of tris (acetylacetonato) titanium (III), Journal of Inorganic and Nuclear Chemistry 34 (1972) 2375-2377.

[60] S. Dilli, E. Patsalides, A convenient new Method for the preparation of vanadium (III) β-diketonates, Australian Journal of Chemistry 29 (1976) 2389-2393.

[61] L.S. von Chrzanowski, M. Lutz, A.L. Spek, alpha-Tris(2,4-pentanedionato-kappa O-2,O ')-chromium(III) at 290 and 110 K : a new delta phase at 110 K, Acta Crystallogr. Sect. C-Cryst. Struct. Commun. 63 (2007) M377-M382.

[62] J. Fackler Jr, A. Avdeef, Crystal and molecular structure of tris(2, 4-pentanedionato)manganese (III), $Mn(O_2C_5H_7)_3$, a distorted complex as predicted by Jahn-Teller arguments, Inorganic Chemistry 13 (1974) 1864-1875.

[63] P.K. Hon, C. Pfluger, The crystal and molecular structure of tris (acetylacetonato)-aluminum (III) and-cobalt (III), Journal of Coordination Chemistry 3 (1973) 67-76.

[64] B.R. Stults, R.S. Marianelli, V.W. Day, Distortions of the coordination polyhedron in high-spin manganese (III) complexes. 3. Crystal and molecular structure of γ-tris (acetylacetonato) manganese (III): a tetragonally elongated octahedral form, Inorganic Chemistry 18 (1979) 1853-1858.

[65] J. Krzystek, G.J. Yeagle, J.-H. Park, R.D. Britt, M.W. Meisel, L.-C. Brunel, J. Telser, High-frequency and-field EPR spectroscopy of Tris (2, 4-pentanedionato) manganese (III): investigation of solid-state versus solution Jahn− Teller Effects, Inorganic Chemistry 42 (2003) 4610-4618.

[66] S. Geremia, N. Demitri, Crystallographic study of manganese (III) acetylacetonate: An advanced undergraduate project with unexpected challenges, J. Chem. Educ 82 (2005) 460.

[67] J. Fackler Jr, Progress in Inorganic Chemistry, by FA Cotton, Interscience Publishers, John Wiley & Sons 7 (1966) 407.

[68] S.-S. Weng, C.-S. Ke, F.-K. Chen, Y.-F. Lyu, G.-Y. Lin, Transesterification catalyzed by iron (III) β-diketonate species, Tetrahedron 67 (2011) 1640-1648.

[69] V.D. Vreshch, J.H. Yang, H. Zhang, A.S. Filatov, E.V. Dikarev, Monomeric square-planar cobalt(II) acetylacetonate: mystery or mistake?, Inorganic Chemistry 49 (2010) 8430-8434.

[70] G. Bullen, The crystal structure of cobalt (II) bisacetylacetone dihydrate, Acta Crystallographica 12 (1959) 703-708.

[71] L.L. Lohr, J.C. Miller, R.R. Sharp, Electronic structure and magnetic properties of high-spin octahedral Co(II) complexes: $Co(II)(acac)_2(H_2O)_2$, The Journal of Chemical Physics 111 (1999) 10148-10158.

[72] G. Bullen, R.t. Mason, P. Pauling, The crystal and molecular structure of bis(acetylacetonato)nickel (II), Inorganic Chemistry 4 (1965) 456-462.

[73] X.-F. Zhou, A.-J. Han, D.-B. Chu, Z.-X. Huang, Electrochemical synthesis and a redetermination of $Ni(acac)_2(H_2O)_2 \cdot H_2O$, Acta Crystallographica Section E: Structure Reports Online 57 (2001) m506-m508.

[74] A. Mahmoudkhani, B. Casari, V. Langer, Refinement of the crystal structure of bis(2,4-pentanedionato-O,O')-oxovanadium(IV) at 183 K, $VO(C_5H_7O_2)_2$, Zeitschrift für Kristallographie-New Crystal Structures 216 (2001) 215-216.

[75] K. Bowers, Anomalous paramagnetism of copper acetate, Proc. R. Soc. Lond. A 214 (1952) 451-465.

[76] A. Ozarowski, The zero-field-splitting parameter D in binuclear copper (II) carboxylates is negative, Inorganic Chemistry 47 (2008) 9760-9762.

[77] A. Elmali, The magnetic super-exchange coupling in copper (II) acetate monohydrate and a redetermination of the crystal structure, Turkish Journal of Physics 24 (2000) 667-672.

[78] B.J. Walder, K.K. Dey, M.C. Davis, J.H. Baltisberger, P.J. Grandinetti, Two-dimensional NMR measurement and point-dipole model prediction of paramagnetic shift tensors in solids, Journal of Chemical Physics 142 (2015) 014201.

[79] L.L.P. Gwendal Kervern, Kevin Bernot, Nicholas Claiser, Mamoudou Diallo, Romain Coustel, Hella Boumaiza, Cedric Carteret, Erwan Andre, Arnaud Di Bitetto, Solid-state NMR as a probe for electronic structure in paramagnetic systems, The 10th Alpine Conference on Solid-State NMR, Chamonix Mont-Blanc, France, 2017.

[80] A. Abragam, A. Abragam, The Principles of Nuclear Magnetism, Oxford university press, 1961.

[81] K.S. Krane, D. Halliday, Introductory nuclear physics, Wiley New York, 1988.

[82] M.H. Levitt, Spin dynamics, Jon Wiley and Sons 196 (2001).

[83] The National High Magnetic Field Laboratory, 1800 E. Paul Dirac Drive Tallahassee, FL 32310.

[84] F. Bloch, Nuclear induction, Physical Review 70 (1946) 460.

[85] J. Mason, Conventions for the reporting of nuclear magnetic shielding (or shift) tensors suggested by participants in the NATO ARW on NMR shielding constants at the University of Maryland, College Park, July 1992, Solid State Nuclear Magnetic Resonance 2 (1993) 285-288.

[86] A. Carrington, A.D. McLachlan, Introduction to magnetic resonance: with applications to chemistry and chemical physics, (1967).

[87] I. Bertini, C. Luchinat, G. Parigi, E. Ravera, NMR of Paramagnetic Molecules: Applications to Metallobiomolecules and Models, Elsevier, 2016.

[88] J.L. Deutsch, S.M. Poling, The determination of paramagnetic susceptibility by NMR: A physical chemistry experiment, Journal of Chemical Education 46 (1969) 167.

[89] P. Viswanadham, Inexpensive gouy balance for magnetic susceptibility determination, Journal of Chemical Education 55 (1978) 54.

[90] E. Fermi, Über die magnetischen Momente der Atomkerne, Zeitschrift für Physik A Hadrons and Nuclei 60 (1930) 320-333.

[91] J. Autschbach, Orbitals: Some Fiction and Some Facts, Journal of Chemical Education 89 (2012) 1032-1040.

[92] L.W. Anderson, F.M. Pipkin, J.C. Baird Jr, Hyperfine structure of hydrogen, deuterium, and tritium, Physical Review 120 (1960) 1279.

[93] W. Koch, M.C. Holthausen, A chemist's guide to density functional theory, John Wiley & Sons, 2015.

[94] G. Gsaller, Visualizing atomic orbitals, (2008).

[95] F.X. Bronold, I. Martin, A. Saxena, D.L. Smith, Magnetic-field dependence of electron spin relaxation in n-type semiconductors, Physical Review B 66 (2002) 233206.

[96] G.E. Pake, T.L. Estle, Physical principles of electron paramagnetic resonance, Mass., WA Benjamin, Advanced Book Program, 1973.

[97] N.S. Barta, J.R. Stille, Bis (acetylacetonato) zinc (II), e-EROS Encyclopedia of Reagents for Organic Synthesis (2004).

[98] M.N. Bhattacharjee, M.K. Chaudhuri, D.T. Khathing, Direct Synthesis of Tris (acetylacetonato) manganese (III), Journal of the Chemical Society, Dalton Transactions (1982) 669-670.

[99] G. Morgan, H. Drew, C. Porter, Ber., 58, 333 (1925); C. R. Hauser and JT Adams, J. Am. Chem. Sac 66 (1944) 345.

[100] J.B. Ellern, R.O. Ragsdale, R.J. Allen, A.B. Chatterjee, D.F. Martin, Hexacoordinate Complexes of Bis (2, 4-Pentanedionato) Cobalt (II):[Bis (Acetylacetonato) Cobalt (II)], Inorganic Syntheses, Volume 11 (1968) 82-89.

[101] R.D. Peacock, The preparation and investigation of bis (acetylacetonato) copper (II), Journal of Chemical Education 48 (1971) 133.

[102] Bruker-AXS, APEX3 v2016.1-0, Madison,Wisconsin, USA, 2016.

[103] G.M. Sheldrick, A short history of SHELX, Acta Cryst A64 (2008) 112-122.

[104] A.L. Spek, Structure validation in chemical crystallography, Acta Cryst. D65 (2009) 148-155.

[105] A. Kubo, T.P. Spaniol, T. Terao, The effect of bulk magnetic susceptibility on solid state NMR spectra of paramagnetic compounds, Journal of Magnetic Resonance 133 (1998) 330-340.

[106] A. Bielecki, D.P. Burum, Temperature Dependence of ^{207}Pb MAS Spectra of Solid Lead Nitrate. An Accurate, Sensitive Thermometer for Variable-Temperature MAS, Journal of Magnetic Resonance, Series A 116 (1995) 215-220.

[107] E.L. Hahn, Spin echoes, Physical Review 80 (1950) 580.

[108] M. Leskes, C.P. Grey, Finite pulse effects in CPMG pulse trains on paramagnetic materials, Physical Chemistry Chemical Physics 17 (2015) 22311-22320.

[109] T. Gullion, Rotational-echo, double-resonance NMR, Modern Magnetic Resonance, Springer, 2008, pp. 713-718.

[110] K. Saalwachter, R. Graf, H.W. Spiess, Recoupled polarization-transfer methods for solid-state ^{1}H-^{13}C heteronuclear correlation in the limit of fast MAS, Journal of Magnetic Resonance 148 (2001) 398-418.

[111] J.-P. Amoureux, M. Pruski, Theoretical and experimental assessment of single-and multiple-quantum cross-polarization in solid state NMR, Molecular Physics 100 (2002) 1595-1613.

[112] F. Weigend, R. Ahlrichs, Balanced basis sets of split valence, triple zeta valence and quadruple zeta valence quality for H to Rn: Design and assessment of accuracy, Physical Chemistry Chemical Physics 7 (2005) 3297-3305.

[113] B. Martin, J. Autschbach, Kohn-Sham calculations of NMR shifts for paramagnetic 3d metal complexes: protocols, delocalization error, and the curious amide proton shifts of a high-spin iron(II) macrocycle complex, Phys Chem Chem Phys 18 (2016) 21051-21068.

[114] G.W.T. M. J. Frisch, H. B. Schlegel, G. E. Scuseria, M. A. Robb, J. R Cheeseman, V., J.A.M. G. Zakrzewski, Jr., R. E. Stratmann, J. C. Burant, S. Dapprich, J. M. Millam, A., K.N.K. D. Daniels, M. C. Strain, O. Farkas, J. Tomasi, V. Barone, M. Cossi, R. Cammi, B., C.P.

Mennucci, C. Adamo, S. Clifford, J. Ochterski, G. A. Petersson, P. Y. Ayala, Q. Cui, K., D.K.M. Morokuma, A. D. Rabuck, K. Raghavachari, J. B. Raghavachari, J. Cioslowski, J., A.G.B. V. Ortiz, B. B. Stefanov, G. Liu, A. Liashenko, P. Piskorz, I. Komaromi, R. Gomperts,, D.J.F. R. L. Martin, T. Keith, M. A. Al-Laham, C. Y. Peng, A. Nanayakkara, C. Gonzalez, M., P.M.W.G. Challacombe, B. Johnson, W. Chen, M. W. Wong, J. L. Andres, C. Gonzalez, M., E.S.R. Head-Gordon, J. A. Pople (1998) Gaussian 98 Revision A.7, Gaussian, Inc.,, Pittsburgh.

[115] C. Aleman, D. Curco, J. Casanovas, Reliability of the density functional approximation to describe the charge transfer and electrostatic complexes involved in the modeling of organic conducting polymers, Physical Review E, Statistical, Nonlinear, and Soft Matter Physics 72 (2005) 026704.

[116] C. Adamo, V. Barone, Exchange functionals with improved long-range behavior and adiabatic connection methods without adjustable parameters: The mPW and mPW1PW models, The Journal of Chemical Physics 108 (1998) 664-675.

[117] A.E. Reed, R.B. Weinstock, F. Weinhold, Natural population analysis, The Journal of Chemical Physics 83 (1985) 735-746.

[118] I. Wolfram Research, Mathematica Version 11.3, Champaign, IL, 2018.

[119] C. Bengs, M.H. Levitt, SpinDynamica: Symbolic and numerical magnetic resonance in a Mathematica environment, Magnetic Resonance in Chemistry (2017).

[120] M. Bak, J.T. Rasmussen, N.C. Nielsen, SIMPSON: a general simulation program for solid-state NMR spectroscopy, Journal of Magnetic Resonance 213 (2011) 366-400.

[121] K. Momma, F. Izumi, VESTA 3 for three-dimensional visualization of crystal, volumetric and morphology data, Journal of applied crystallography 44 (2011) 1272-1276.

[122] D. Massiot, F. Fayon, M. Capron, I. King, S. Le Calvé, B. Alonso, J.O. Durand, B. Bujoli, Z. Gan, G. Hoatson, Modelling one-and two-dimensional solid-state NMR spectra, Magnetic Resonance in Chemistry 40 (2002) 70-76.

[123] P.A. Beckmann, C.W. Mallory, F.B. Mallory, A.L. Rheingold, X. Wang, Methoxy and Methyl Group Rotation: Solid-State NMR ^{1}H Spin-Lattice Relaxation, Electronic Structure Calculations, X-ray Diffractometry, and Scanning Electron Microscopy, Chemphyschem 16 (2015) 1509-1519.

[124] C.J. Ballhausen, M.A. Weiner, Introduction to ligand field theory, Journal of The Electrochemical Society 110 (1963).

[125] G.R. Underwood, V.L. Vogel, J.-A. Iorio, The mechanisms of spin delocalization through sigma bonds delocalization to gamma protons, Molecular Physics 25 (1973) 1093-1101.

[126] X. Kong, V.V. Terskikh, R.L. Khade, L. Yang, A. Rorick, Y. Zhang, P. He, Y. Huang, G. Wu, Solid-state ^{17}O NMR spectroscopy of paramagnetic coordination compounds, Angew Chem Int Ed Engl 54 (2015) 4753-4757.

[127] D. Machin, K. Murray, The magnetism and spectra of some octahedral vanadium (III) complexes, Journal of the Chemical Society A: Inorganic, Physical, Theoretical (1967) 1498-1504.

[128] J. Krzystek, A.T. Fiedler, J.J. Sokol, A. Ozarowski, S. Zvyagin, T.C. Brunold, J.R. Long, L.-C. Brunel, J. Telser, Pseudooctahedral complexes of vanadium (III): electronic structure investigation by magnetic and electronic spectroscopy, Inorganic Chemistry 43 (2004) 5645-5658.

[129] T. Ikagawa, T. Otsuka, Y. Kaizu, Time-resolved ESR study of chromium (III) complexes in the ground state, The Journal of Physical Chemistry A 102 (1998) 649-653.

[130] B. McGarvey, Paramagnetic resonance in copper chelates, The Journal of Physical Chemistry 60 (1956) 71-76.

[131] C.P. Jaroniec, Structural studies of proteins by paramagnetic solid-state NMR spectroscopy, Journal of Magnetic Resonance 253 (2015) 50-59.

[132] B. Martin, J. Autschbach, Temperature dependence of contact and dipolar NMR chemical shifts in paramagnetic molecules, The Journal of Chemical Physics 142 (2015) 054108.

[133] B. Martin, J. Autschbach, Erratum:"Temperature dependence of contact and dipolar NMR chemical shifts in paramagnetic molecules"[J. Chem. Phys. 142, 054108 (2015)], The Journal of Chemical Physics 145 (2016) 049901.

[134] S.M. Abernathy, R.R. Sharp, Role of Zero-Field Splitting Interactions in the NMR Paramagnetic Relaxation Enhancements Produced by Ni(II)$(acac)_2 \cdot (H_2O)_2$, The Journal of Physical Chemistry A 101 (1997) 3692-3698.

[135] A. Lennartson, L.U. Christensen, C.J. McKenzie, U.G. Nielsen, Solid State ^{13}C and ^{2}H NMR Investigations of Paramagnetic [Ni (II)$(acac)_2L_2$] Complexes, Inorganic Chemistry 53 (2013) 399-408.

[136] S.A. Rouf, V.B. Jakobsen, J. Mareš, N.D. Jensen, C.J. McKenzie, J. Vaara, U.G. Nielsen, Assignment of solid-state ^{13}C and ^{1}H NMR spectra of paramagnetic Ni (II) acetylacetonate complexes aided by first-principles computations, Solid State Nuclear Magnetic Resonance 87 (2017) 29-37.

[137] Z. Tošner, R. Andersen, B. Stevensson, M. Edén, N.C. Nielsen, T. Vosegaard, Computer-intensive simulation of solid-state NMR experiments using SIMPSON, Journal of Magnetic Resonance 246 (2014) 79-93.

[138] H.N. Russell, F. Saunders, New regularities in the spectra of the alkaline earths, The Astrophysical Journal 61 (1925) 38.

[139] J. Herzfeld, A.E. Berger, Sideband intensities in NMR spectra of samples spinning at the magic angle, The Journal of Chemical Physics 73 (1980) 6021-6030.

[140] C.R. Cornman, E.P. Zovinka, Y.D. Boyajian, K.M. Geiser-Bush, P.D. Boyle, P. Singh, Structural and EPR studies of vanadium complexes of deprotonated amide ligands: effects on the ^{51}V hyperfine coupling constant, Inorganic Chemistry 34 (1995) 4213-4219.

[141] K. Eichele, R. Wasylishen, WSOLIDS NMR simulation package, Version 1 (2000) 26.

[142] J. Vaara, K. Oikarine, J. Jokisaari, J. Lounila, Anisotropy of the ^{1}H and ^{13}C shielding tensors in chloroform, Chemical Physics Letters 253 (1996) 340-348.

[143] J.K. Harper, Chemical Shift Anisotropy and Asymmetry: Relationships to Crystal Structure, eMagRes (2007).

[144] W. Andriessen, Electron paramagnetic resonance and thermodynamic measurements on a phase transition of tris (acetylacetonato) aluminium (III) and tris (acetylacetonato) cobalt (III), Journal of Physics and Chemistry of Solids 37 (1976) 189-196.

[145] S. Dexheimer, J.W. Gohdes, M.K. Chan, K.S. Hagen, W.H. Armstrong, M.P. Klein, Detection of EPR spectra in S= 2 states of trivalent manganese complexes, Journal of the American Chemical Society 111 (1989) 8923-8925.

[146] D. Mustafi, M.W. Makinen, Structure and Conformation of Bis(acetylacetonato)oxovanadium(IV) and Bis(maltolato)oxovanadium(IV) in Solution Determined by Electron Nuclear Double Resonance Spectroscopy, Inorganic Chemistry 44 (2005) 5580-5590

[147] A. Szabo, Contour diagrams for relativistic orbitals, Journal of Chemical Education 46 (1969) 678.

[148] J. Autschbach, S. Patchkovskii, B. Pritchard, Calculation of hyperfine tensors and paramagnetic NMR shifts using the relativistic zeroth-order regular approximation and density functional theory, Journal of Chemical Theory and Computation 7 (2011) 2175-2188.

[149] E.P. Saliba, E.L. Sesti, F.J. Scott, B.J. Albert, E.J. Choi, N. Alaniva, C. Gao, A.B. Barnes, Electron decoupling with dynamic nuclear polarization in rotating solids, Journal of the American Chemical Society 139 (2017) 6310-6313.

Appendix

Figure 5.1 shows experimental and simulated powder x-ray diffraction patterns for the two samples of $Mn(acac)_3$ present in this thesis. The purchased technical-grade sample can be identified primarily with the γ-$Mn(acac)_3$ phase (Figure 5.1a, b). This sample also contains δ -$Mn(acac)_3$ phase (Figure 5.1a,c) and a weak impurity signal. The synthesized sample is identified as a pure δ -$Mn(acac)_3$ phase (Figure 5.1c,d).

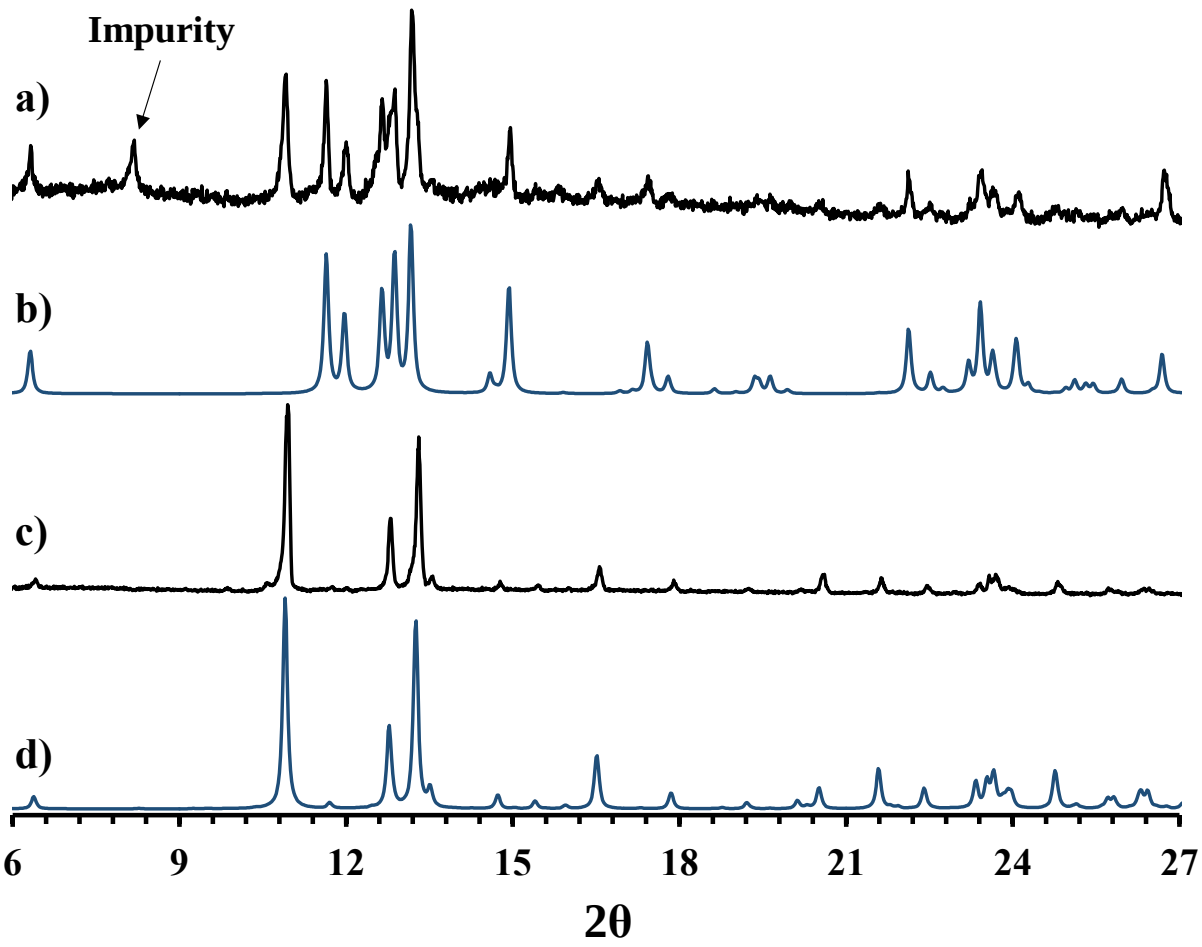

FIGURE 5.1: Powder x-ray diffraction of $Mn(acac)_3$. a) The reagent-grade sample as purchased from Alfa Aesar; b) the simulated powder pattern of γ-$Mn(acac)_3$ phase [27]; c) the synthesized sample of $Mn(acac)_3$; d) the simulated powder pattern of δ -$Mn(acac)_3$ phase [64].

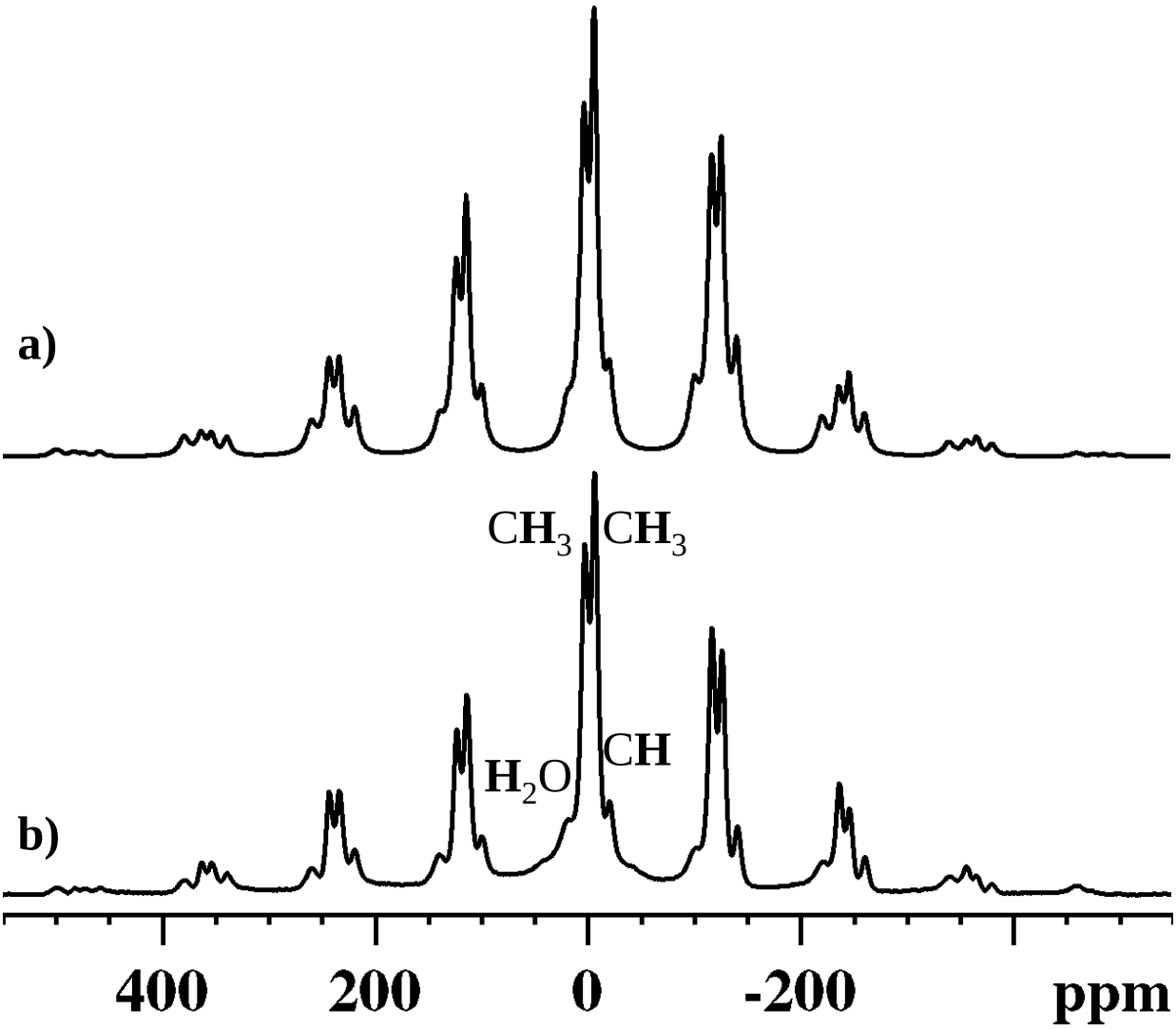

FIGURE 6.1: a) Fit of anisotropic ^{1}H MAS NMR signal of $Co(acac)_2 \cdot 2H_2O$ in comparison with the b) experiment. Signal spans for the functional groups are as follows: $\Omega(H_2O)$ = 900(50) ppm, Ω (CH) = 750(50) and $\Omega(CH_3)$ = 550(50) ppm.

Ti(acac)$_3$

TABLE 8.1: Modeling of signal widths in ^{13}C MAS MAS NMR of Ti(acac)$_3$. Fermi contribution, $\nu_{½}^{Fermi}$, uses A_{exp} from the above table 8.1. Widths are given in kHz.

Group	$\nu_{½}^{dia}$	PDM		MPDM		$\nu_{½}^{Exp}$
		$\nu_{½}^{Fermi}$	$\nu_{½}^{Dipolar}$	$\nu_{½}^{Fermi}$	$\nu_{½}^{Dipolar}$	
CO	0.07	6.1	0.15	4.8	0.20	5.3(5)
CH	0.15	0.61	0.08	0.52	0.75	2.1(1)
CH_3	0.25	0.46	0.02	0.40	0.40	1.8(2)
T_e		65 ps		55 ps		

TABLE 8.2: Modeling of signal widths in ^{1}H MAS NMR of Ti(acac)$_3$. Fermi contribution uses A_{exp} from the above table 8.3. Widths are given in kHz.

Group	$\nu_{½}^{dia}$	PDM		MPDM		$\nu_{½}^{Exp}$
		$\nu_{½}^{Fermi}$	$\nu_{½}^{Dipolar}$	$\nu_{½}^{Fermi}$	$\nu_{½}^{Dipolar}$	
CH	0.25	0.22	0.23	0.10	8.7	0.9(3)
CH_3	0.62	1.2	0.14	0.59	0.8	2.1(3)
T_e		55 ps		25 ps		

β - V(acac)$_3$

TABLE 8.3: Modeling of signal widths in ^{13}C MAS NMR of β -V(acac)$_3$. Fermi contribution uses A_{exp} from the above table 8.5. Widths are given in kHz.

Group	$\nu_{½}^{dia}$	PDM		MPDM		$\nu_{½}^{Exp}$
		$\nu_{½}^{Fermi}$	$\nu_{½}^{Dipolar}$	$\nu_{½}^{Fermi}$	$\nu_{½}^{Dipolar}$	
CO	0.07	1.8	0.14	1.6	0.09	1.8(3)
CH	0.15	<0.01	0.07	< 0.01	0.20	0.5(1)
CH_3	0.25	0.12	0.01	0.12	0.10	0.5(1)
T_e		20 ps		20 ps		

TABLE 8.4: Modeling of signal widths in ^{1}H MAS NMR of β -V(acac)$_3$. Fermi contribution uses A_{exp} from the above table 8.7. Widths are given in kHz.

Group	$\nu_{½}^{dia}$	PDM		MPDM		Experiment
		$\nu_{½}^{Fermi}$	$\nu_{½}^{Dipolar}$	$\nu_{½}^{Fermi}$	$\nu_{½}^{Dipolar}$	
CH	0.25	0.05	0.37	0.05	5	0.8(2)
CH_3	0.62	0.17	0.21	0.12	0.68	1.1(4)
T_e		30 ps		20 ps		

Cr(acac)$_3$

TABLE 8.5: Modeling of signal widths in ^{13}C MAS NMR of Cr(acac)$_3$. Fermi contribution uses A_{exp} from the above table 8.9. Widths are given in kHz.

Group	$\nu_{½}$ dia	PDM		MPDM		$\nu_{½}$ Exp
		$\nu_{½}$ Fermi	$\nu_{½}$ Dipolar	$\nu_{½}$ Fermi	$\nu_{½}$ Dipolar	
CO	0.07	55	9.5	39	7.0	Not observed
CH	0.15	1.8	4.6	1.3	6.6	7(1)
CH_3	0.25	9.2	0.93	6.5	2.6	10(1)
T_e		700 ps		500 ps		

TABLE 8.6: Modeling of signal widths in ^{1}H MAS NMR of Cr(acac)$_3$. Fermi contribution uses A_{exp} from the above table 8.11. Widths are given in kHz.

Group	$\nu_{½}$ dia	PDM		MPDM		Experiment
		$\nu_{½}$ Fermi	$\nu_{½}$ Dipolar	$\nu_{½}$ Fermi	$\nu_{½}$ Dipolar	
CH	0.25	0.4	13	0.15	61	Not observed
CH_3	0.62	2.9	8.5	1.1	9.9	12(1)
T_e		950 ps		350 ps		

γ - Mn(acac)$_3$

TABLE 8.7: Modeling of signal widths in ^{13}C MAS NMR of γ- Mn(acac). Fermi contribution uses A_{exp} from the above table 8.13. Widths are given in kHz.

Group	$\nu_{½}^{dia}$	PDM		MPDM		$\nu_{½}^{Exp}$
		$\nu_{½}^{Fermi}$	$\nu_{½}^{Dipolar}$	$\nu_{½}^{Fermi}$	$\nu_{½}^{Dipolar}$	
CO	0.07	2.9	1.0	2.9	1.0	3.7(1)
CO	0.07	2.1	1.0	2.1	1.0	3.3(1)
CO	0.07	2.5	1.0	2.5	1.1	3.0(1)
CH	0.15	0.11	0.47	0.11	0.53	0.80(3)
CH_3	0.25	<0.01	0.11	<0.01	0.15	1.6(1)
CH_3	0.25	0.03	0.11	0.03	0.21	2.1(1)
CH_3	0.25	0.42	0.11	0.42	0.36	2.3(1)
CH_3	0.25	0.45	0.11	0.45	0.33	2.5(1)
T_e		45 ps		45 ps		

TABLE 8.8: Modeling of signal widths in ^{1}H MAS NMR of γ- Mn(acac)$_3$. Fermi contribution uses A_{exp} from the above table 8.15. Widths are given in kHz.

Group	$\nu_{½}^{dia}$	PDM		MPDM		$\nu_{½}^{Exp}$
		$\nu_{½}^{Fermi}$	$\nu_{½}^{Dipolar}$	$\nu_{½}^{Fermi}$	$\nu_{½}^{Dipolar}$	
CH	0.25	0.05	1.8	<0.01	1.8	2.5(1)
CH	0.25	<0.01	1.4	<0.01	1.2	1.3(1)
CH	0.25	<0.01	1.5	<0.01	1.5	1.2(1)
CH_3	0.62	0.03-0.06	0.86	<0.01	0.90	2.7(1)
CH_3	0.62	<0.01	0.96	<0.01	0.34	1.7(1)
T_e		40 ps		5 ps		8(2) ps

Fe(acac)$_3$

TABLE 8.9: Fermi-coupling constants derived from ^{1}H MAS NMR of Fe(acac)$_3$ using equation 2.18 and obtained from the DFT calculation. Couplings from individual hydrogens from the same methyl group are scaled to match the average experimental shift.

Group	$^{1H}A_{calc}$ (MHz)	$^{1H}A_{exp}$ (MHz)
CH	-0.063	
	-0.096	
	-0.046	
CH_3	{0.021, -0.11, 0.027}	{-0.069, 0.36, -0.087}
	{0.0025, -0.032, -0.066}	{-0.0053, 0.069, 0.14}
	{0.018, 0.027, -0.11}	{-0.053, -0.082, 0.34}
	{0.034, -0.029, -0.0093}	{0.10, 0.039, 0.059}
	{0.056, -0.031, -0.026}	{0.12, 0.037, 0.042}
	{0.017, -0.14, 0.048}	{-0.050, 0.39, -0.14}

TABLE 8.10: Modeling of signal widths in ^{1}H MAS NMR of Fe(acac)$_3$. Fermi contribution uses A_{exp} from the above table 8.17. Widths are given in kHz.

Group	$\nu_{½}^{dia}$	PDM		MPDM		$\nu_{½}^{Exp}$
		$\nu_{½}^{Fermi}$	$\nu_{½}^{Dipolar}$	$\nu_{½}^{Fermi}$	$\nu_{½}^{Dipolar}$	
CH	0.25	0.11	30	< 0.01	50	Not observed
CH_3	0.62	1.2	19	0.09	20	20(2)
T_e		1000 ps		80 ps		

TABLE 8.11: Fit of the isotropic signal width in ^{13}C MAS NMR of Fe(acac)$_3$ and DFT calculation. Widths are given in kHz.

Group	$\nu_{½}^{dia}$	PDM		MPDM	
		$\nu_{½}^{Fermi}$	$\nu_{½}^{Dipolar}$	$\nu_{½}^{Fermi}$	$\nu_{½}^{Dipolar}$
CO	0.07	4.3	25	0.35	5.2
CH	0.15	42	12	3.3	0.88
CH_3	0.25	86	2.7	7.0	0.29
T_e		1000 ps		80 ps	

$Co(acac)_2 \cdot 2H_2O$

TABLE 8.12: Fermi-coupling constants derived from ^{13}C MAS NMR of $Co(acac)_2 \cdot 2H_2O$ using equation 2.18 and obtained from the DFT calculation.

Group	A_{calc} (MHz)	A_{exp} (MHz)*
CO	0.11	0.11 - -0.23
CO	0.09	0.09 - -0.29
CH	0.37	0.07 – 0.08
CH_3	2.10	1.51 – 1.47
CH_3	1.94	1.29 - 1.40

*The range of values signifies the uncertainty in the account of the pseudocontact-shift contribution from *D* between PDM and M-A formalism (see Chapter 6). Values on the left are determined with "PDM with *D*" correction, values on the right are determined with "M-A with *D*" correction (see table 6.4)

TABLE 8.13: Modeling of signal widths in ^{13}C MAS NMR of $Co(acac)_2 \cdot 2H_2O$. Fermi contribution uses A_{exp} that are found with the "PDM with *D*" model from the table 8.20. Widths are given in kHz.

Group	$\nu_{½}^{dia}$	PDM		MPDM		$\nu_{½}^{Exp}$
		$\nu_{½}^{Fermi}$	$\nu_{½}^{Dipolar}$	$\nu_{½}^{Fermi}$	$\nu_{½}^{Dipolar}$	
CO	0.07	0.05	1.1	0.05	2.3	1.2(1)
CH	0.15	<0.01	0.58	<0.01	0.43	1.10(5)
CH_3	0.25	1.5	0.11	1.5	0.15	1.8(1)
T_e		50 ps		50 ps		

TABLE 8.14: Fermi-coupling constants derived from ^{1}H MAS NMR of $Co(acac)_2 \cdot 2H_2O$ using equation 2.18 and obtained from the DFT calculation. Couplings from individual hydrogens from the same methyl group are scaled to match the average experimental shift.

Group	$^{1H}A_{calc}$ (MHz)	$^{1H}A_{exp}$ (MHz)*
H_2O	2.35 3.77	0.37 – 2.2
CH	-0.21	0.22 – 0.57
CH_3	-0.05, -0.60, 0.29	{-0.04, -0.46, 0.22} - {-0.16, -1.83, 0.86}
CH_3	0.003, -0.61, 0.23	{0.001, -0.16, 0.059} - {0.008, -1.65, 0.63}

*The range of values signifies the uncertainty in the account of the pseudocontact-shift contribution from *D* between PDM and M-A formalism (see Chapter 6). Values on the left are determined with "PDM with *D*" correction, values on the right are determined with "M-A with *D*" correction (see table 6.5)

TABLE 8.15: Modeling of signal widths in ^{1}H MAS NMR of $Co(acac)_2 \cdot 2H_2O$ and DFT calculation. Fermi contribution uses A_{exp} that were found using "PDM with *D*" model from table 8.22. Widths are given in kHz.

Group	$\nu_{½}$ dia	PDM		MPDM		$\nu_{½}$ Exp
		$\nu_{½}$ Fermi	$\nu_{½}$ Dipolar	$\nu_{½}$ Fermi	$\nu_{½}$ Dipolar	
H_2O	0.70	3.9	13.3	1.5	14	10.1(4)
CH	0.45	0.25	1.7	0.1	4.4	4.5(3)
CH_3	0.55	0.90	0.10	0.38	2.4	3.7(2)
T_e		50 ps		20 ps		

Ni(acac)$_2$·2H$_2$O

TABLE 8.16: Modeling of signal widths in ^{13}C MAS NMR of Ni(acac)$_2$ · 2H$_2$O and DFT calculation. Widths are given in kHz.

Group	$\nu_{1/2}^{dia}$	PDM		MPDM		$\nu_{1/2}^{Exp}$
		$\nu_{1/2}^{Fermi}$	$\nu_{1/2}^{Dipolar}$	$\nu_{1/2}^{Fermi}$	$\nu_{1/2}^{Dipolar}$	
CO	0.07	<0.01	0.34	<0.01	0.10	0.63(3)
CH	0.15	<0.01	0.17	<0.01	1.0	0.44(3)
CH_3	0.25	3.8	0.03	3.8	0.04	4.2(3)
T_e		45 ps		45 ps		> 10ps

TABLE 8.17: Modeling of signal widths in ^{1}H MAS NMR of Ni(acac)$_2$ · 2H$_2$O and DFT calculation. Widths are given in kHz.

Group	$\nu_{1/2}^{dia}$	PDM		MPDM		$\nu_{1/2}^{Exp}$
		$\nu_{1/2}^{Fermi}$	$\nu_{1/2}^{Dipolar}$	$\nu_{1/2}^{Fermi}$	$\nu_{1/2}^{Dipolar}$	
H_2O	0.70	0.36	7.3	0.08	8	8.5(4)
CH	0.45	0.02	0.57	<0.01	0.56	1.8(2)
CH_3	0.55	0.06	0.33	0.02	1.3	2.1(2)
T_e		45 ps		10 ps		> 10ps

Cu(acac)$_2$

TABLE 8.18: Modeling of signal widths in ^{13}C MAS NMR of Cu(acac)$_2$ and DFT calculation. Widths are given in kHz.

Group	$\nu_{½}^{dia}$	PDM		MPDM		$\nu_{½}^{Exp}$
		$\nu_{½}^{Fermi}$	$\nu_{½}^{Dipolar}$	$\nu_{½}^{Fermi}$	$\nu_{½}^{Dipolar}$	
CO	0.07	0.55	0.70	0.13	1.6	1.5(1)
CH	0.15	1.6	0.35	0.39	0.04	1.9(1)
CH_3	0.25	49	0.07	12	<0.01	Not observed
T_e		200 ps		50 ps		

TABLE 8.19: Modeling of signal widths in ^{1}H MAS NMR of Cu(acac)$_2$ and DFT calculation. Widths are given in kHz.

Group	$\nu_{½}^{dia}$	PDM		MPDM		$\nu_{½}^{Exp}$
		$\nu_{½}^{Fermi}$	$\nu_{½}^{Dipolar}$	$\nu_{½}^{Fermi}$	$\nu_{½}^{Dipolar}$	
CH	0.25	0.95	2.4	0.02	1.4	3.4(2)
CH_3	0.62	0.13	1.4	<0.02	2.3	2.8(2)
T_e		600 ps		10 ps		

VO(acac)$_2$

TABLE 8.20: Modeling of signal widths in ^{13}C MAS NMR of VO(acac)$_2$ and DFT calculation.

Widths are given in kHz.

Group	$\nu_{½}^{dia}$	PDM		MPDM		$\nu_{½}^{Exp}$
		$\nu_{½}^{Fermi}$	$\nu_{½}^{Dipolar}$	$\nu_{½}^{Fermi}$	$\nu_{½}^{Dipolar}$	
CO	0.07	160	2.5	120	3.4	Not observed
CH	0.15	8.8	1.2	6.6	3.5	10(1)
CH_3	0.25	2.0	0.27	1.5	1.0	3.0(1)
T_e		1200 ps		900 ps		

TABLE 8.21: Modeling of signal widths in ^{1}H MAS NMR of VO(acac)$_2$ and DFT calculation.

Widths are given in kHz.

Group	$\nu_{½}^{dia}$	PDM		MPDM		$\nu_{½}^{Exp}$
		$\nu_{½}^{Fermi}$	$\nu_{½}^{Dipolar}$	$\nu_{½}^{Fermi}$	$\nu_{½}^{Dipolar}$	
CH	0.25	18	8.5	12	4.7	Not observed
CH_3	0.62	<0.1	5.1	<0.1	8.1	5.7(2)
T_e		3300 ps		2200 ps		

$[Cu(Ac)_2H_2O]_2$

TABLE 8.22: Modeling of signal widths in ^{13}C MAS NMR of $[Cu(Ac)_2H_2O]_2$ and DFT calculation. Widths are given in kHz.

Group	$\nu_{½}^{dia}$	PDM		MPDM		$\nu_{½}^{Exp}$
		$\nu_{½}^{Fermi}$	$\nu_{½}^{Dipolar}$	$\nu_{½}^{Fermi}$	$\nu_{½}^{Dipolar}$	
CO	0.07	1.1	0.04	1.0	1.1	2.7(7)
CH_3	0.25	4.2	<0.01	3.8	0.04	4.3(2)
T_e		20 ps		18 ps		

TABLE 8.23: Modeling of signal widths in ^{1}H MAS NMR of $[Cu(Ac)_2H_2O]_2$ and DFT calculation. Widths are given in kHz.

Group	$\nu_{½}^{dia}$	PDM		MPDM		$\nu_{½}^{Exp}$
		$\nu_{½}^{Fermi}$	$\nu_{½}^{Dipolar}$	$\nu_{½}^{Fermi}$	$\nu_{½}^{Dipolar}$	
H_2O	0.70	< 0.01	0.20	< 0.01	1.3	
CH_3	0.55	3.5	0.38	0.16	4.1	4.8(2)
T_e		250 ps		12 ps		